UNIVERSIDADE DE SÃO PAULO
INSTITUTO DE FÍSICA DE SÃO CARLOS

MILLENA LOGRADO DOS SANTOS

Structural studies in aluminophosphosilicate glasses and in cold-pressurized borosilicate glasses by Nuclear Magnetic Resonance in the solid state

São Carlos
2023

MILLENA LOGRADO DOS SANTOS

STRUCTURAL STUDIES IN ALUMINOPHOSPHOSILICATE GLASSES AND IN COLD-PRESSURIZED BOROSILICATE GLASSES BY NUCLEAR MAGNETIC RESONANCE IN THE SOLID STATE

Thesis presented to the Graduate Program in Physics at the Instituto de Física de São Carlos, Universidade de São Paulo to obtain the degree of Doctor of Science.

Concentration area: Theoretical and Experimental Physics
Advisor:
Prof. Dr. Hellmut Eckert
Co-Advisor:
Prof. Dr. Marcos de Oliveria Jr.

Corrected Version
(original version available on the Program Unit)

SÃO CARLOS
2023

Santos, Millena Logrado dos
Structural studies in aluminophosphosilicate glasses and in cold-pressurized borosilicate glasses by Nuclear Magnetic Resonance in the solid state / Millena Logrado dos Santos; advisor Hellmut Eckert; co-advisor Marcos de Oliveira Júnior – corrected version -- São Carlos 2023.
165 p.

Thesis (Doctorate - Graduate Program in Theoretical and Experimental Physics) -- Instituto de Física de São Carlos, Universidade de São Paulo - Brasil , 2023.

1. Aluminophosphosilicate. 2. Borosilicate. 3. Glasses. 4. NMR. 5. Double Resonance. I. Eckert, Hellmut, advisor. II. de Oliveira Júnior, Marcos, co-advisor. III. Title.

Aos amados
Rosineyla Lograd, Zoraide Honório Lograd e José Amaro Lograd,
Que só amor me apresentaram.

ACKNOWLEDGEMENTS

Throughout the four years of doctoral studies, I counted on the support of my family, friends, colleagues, faculty staff and the community of students at the University of São Paulo. Undoubtedly, I am deeply grateful to everyone who was a part of my daily life, directly or indirectly. Among these, I owe special recognition to my colleagues in the NMR group. Our discussions, meetings, and the constructive criticism played a vital role in enhancing my work and nourishing my passion for research. Your scientific stimulation will always be appreciated.

Aos professores que cruzaram minha vida escolar e construíram toda uma base para o meu senso crítico, eu devo o meu mais profundo respeito. Gostaria de, dentre eles, prestar homenagens a três: à Sandra, minha professora de alfabetização, por me apresentar o mundo em sala de aula; ao Ari, professor que me ensinou a paixão pela matemática e geometria; ao Almir, meu primeiro professor de Física que, desde a primeira aula, me ensinou a amar o que viria a ser minha profissão. I would be remiss in not mentioning Alexandre Inforzato, the English teacher who has been helping me with patience and dedication in improving my English writing skills.

It is my great pleasure to have undertaken this journey with the support of my co-advisor, prof. Marcos de Oliveira Jr. Your enthusiasm for testing new pulse sequences and the amusement permeating the NMR discussions taught me how to learn in a good-humored way. The time you invested in helping me to grow will always be a cherished memory of my time during my PhD. Also, this endeavor would not have been possible without the support of my advisor, prof. Hellmut Eckert, who has been one of the cornerstones of my scientific development. Thank you for the constructive work environment that you provided. My growing scientific curiosity, as well as my interest in glass properties over the last four years, is a direct result of the scientific inspiration you have ignited in me. Thank you both for the professors you are!

To José Francisco Miras Domenegueti, a heartfelt thank you for the support during my PhD time and for being constantly available for the enlightening discussions exploring the enriching parallels between electronic resonance in optical contexts and nuclear magnetic resonance in solid-state. A você, acima de tudo, agradeço à vida que vale a pena ser dividida.

Profundo é o agradecimento ao amor que recebi da minha família, o meu maior farol. Agradeço ao meu irmão, Silmar Logrado dos Santos (em memória), pelas minhas melhores lembranças; a nossa amizade segue sendo cultivada. Aos meus avos, Zoraide Honório e José Amaro Logrado, e a minha mãe, Rosineyla da Silva Logrado, a quem eu apenas simbolicamente

dedico essa tese, mas aqueles que, em vias práticas, dedicaram suas vidas à família. Particularmente, um agradecimento à grande mulher que é minha mãe. Obrigada, por me fazer crescer em frente ao espelho do meu maior exemplo, o seu. À voces, meus mais devotos agradecimentos.

I would also like to express my gratitude to Dr. B. G. Aitken and Dr. R. E. Youngman for their valuable contributions to providing NAPS glasses, which greatly aided in my development. I am also deeply grateful to Dr. S. Nakane and Dr. Y. Kato for their invaluable scientific input and for their fruitful collaboration throughout my doctoral studies.

Finally, thanks are due to the foment agencies FAPESP, CNPq, CAPES (and further Brazilian agencies). Additionally, I am grateful to Nippon Electric Glass Co. for their financial support of my fellowship and for providing scientifically intriguing and well-characterized samples.

"Someone once asked Einstein, if he could only do one,
what experiment he would perform in a solid,
Einstein replied: 'I would measure the heat capacity of the solid.'
Well, I say he only answered that way because NMR had not been developed back then."
Hellmut Eckert

ABSTRACT

SANTOS, M. L. **Structural studies in aluminophosphosilicate glasses and in cold-pressurized borosilicate glasses by Nuclear Magnetic Resonance in the solid state**. 2023. 165 p. Thesis (Doctor in Science) - Instituto de Física de São Carlos, Universidade de São Paulo, São Carlos, 2023.

Technologically important glasses can have their properties fine-tuned by understanding the role of each element in the glass structure. However, elucidating properties, such as heat-, weathering- and crack-resistance, based on the glass structure is a challenging task due to the multiple factors influencing these macroscopic properties. In this study, we investigate the structure-property correlation for three distinct system: (i) an aluminophosphosilicate heat resistant optical fiber with composition: xNa_2O – $(22.50\text{-}x)Al_2O_3$ – $7.50P_2O_5$ – $70.00\ SiO_2$ (NAPS), $2.50 \leq x \leq 17.50$; (ii) an aluminophosphosilicate weathering resistant optical fiber, with composition $xSiO_2$ – $(59\text{-}x)P_2O_5$ – $13Al_2O_3$ – $28Na_2O$ (SPAN), $0 \leq x \leq 13$; and (iii) cold-pressurized glasses which can shed light on crack resistant properties, with the composition $20Na_2O$ – xB_2O_3 – $(70\text{-}x)SiO_2$, x = 10, 20, 30. The short- and medium-range order of the three distinct systems were investigated by ^{11}B, ^{23}Na, ^{27}Al, ^{29}Si, ^{31}P single and double resonance solid-state Nuclear Magnetic Resonance (NMR) spectroscopy. The glass structures are elucidated in terms of two terminologies: $X^{(n)}$, which refers to the atom X bonded to 'n' bridging oxygen atoms connected to like or unlike network former units, and X(N), which refers to the isotope X coordinated by 'N' atoms (N being a Roman numeral). (i) (NAPS glasses), the dual role of sodium, either as a charge balancer or as a network modifier was investigated. The structure of these glasses is dominated by a significant bonding preference between anionic four-coordinate Al(IV) species and cationic $P^{(4)}$ units (Al-O-P linkages). The gradual replacement of alumina by sodium oxide initially increases the number of Si-O-Al linkages, which are charge balanced by Na^+ introduced by Na_2O. Higher levels of *x* ([Na]/[P] > 1) lead to a partial depolymerization of Al-O-P linkages and to the formation of neutral $P^{(3)}$ and ionic $P^{(2)}$ and $P^{(1)}$ units strongly interacting with the sodium species. Furthermore, the presence of P-O-P linkages in the glasses with the highest sodium concentration was confirmed by ^{31}P double quantum excitation experiments. The overall scenario can be described by the dual role of sodium ions in the glass structure serving as a charge balancer for anionic Al(IV) network former, and as a neutralizer to the non-bridging oxygens of newly formed $P^{(n)}$ units ($3 \geq n \geq 1$). In the system (ii) (SPAN glasses), the spectra of ^{29}Si Magic Angle Spinning (MAS)-NMR indicates that no significant proportion of hexacoordinated Si, expected for glasses with high

[P]/[Si] ratios, was formed. This structure is likely suppressed by the strong interaction between phosphorus and aluminum, which was measured by ^{27}Al-^{31}P double resonance dipolar recoupling experiments. Dipolar recoupling techniques also facilitated the analysis of the ^{31}P MAS-NMR spectra in terms of two distinct components with different chemical shifts: one interacting more strongly with Na, the other one interacting more strongly with Al. The NMR-based structural information can provide insights about the non-linear composition dependence of the weathering resistance of the glasses. In (iii) the cold pressurized borosilicate glasses, ^{11}B MAS- and ^{23}Na MAS-NMR illustrated together a counterintuitive structural effect: the average B coordination number decreases upon compression. This effect exposes a behavior not previously reported in the literature: the applied pressure induces a closer approximation between Na^+ ions and oxygen species bridging between tetrahedral boron and silicon, causing a breaking in B(IV)-O-X (X = B, Si) linkages. As a result, new B(III) units are formed, as well as new non-bridging oxygens predominantly attached to silicon (later compensated by Na^+ ions). These results clearly document an insightful detailed structural picture provided by solid-state NMR, which was used to suggest possible and multiple structural origins for each macroscopic effect investigated.

Keywords: Aluminophosphosilicate. Borosilicate. Pressurized glasses. Solid-state. Double resonance. NMR.

RESUMO

SANTOS, M. L. **Estudo estrutural em vidros aluminofosfossilicatos e vidros borossilicatos pressurizados a frio por Ressonância Magnética Nuclear em estado sólido**. 2023. 165 p. Tese (Doutorado em Ciências) - Instituto de Física de São Carlos, Universidade de São Paulo, São Carlos, 2023.

Vidros tecnologicamente importantes podem ter as suas propriedades refinadas se associadas ao conhecimento do papel de cada elemento na estrutura do vidro. No entanto, elucidar propriedades, tais como a resistência ao calor, às intempéries e à formação de trincas, com base na estrutura do vidro é uma tarefa desafiadora, dado os múltiplos fatores que influenciam estas propriedades macroscópicas. Neste estudo, nós investigamos a correlação estrutura-propriedade para três sistemas distintos: (i) uma fibra ótica resistente ao calor de aluminofosfossilicato com a composição: xNa_2O - $(22.50\text{-}x)Al_2O_3$ – $7.50P_2O_5$ – $70.00\ SiO_2$ (NAPS), $2{,}50 \leq x \leq 17.50$; (ii) uma fibra ótica resistente às intempéries de aluminofosfossilicato, com composição $xSiO_2$ - $(59\text{-}x)P_2O_5$ - $13Al_2O_3$ - $28Na_2O$ (SPAN), $0 \leq x \leq 13$; e (iii) vidros pressurizados a frio que podem esclarecer propriedades de resistência à formação de trincas, com a composição $20Na_2O$ - xB_2O_3 - $(70\text{-}x)SiO_2$, x = 10, 20, 30. O ordem de curto e médio alcance dos três sistemas distintos foi investigada por espectroscopia de Ressonância Magnética Nuclear de estado sólido por meio de experimentos de ressonância simples de multinuclear de ^{11}B, ^{23}Na, ^{27}Al, ^{29}Si, ^{31}P. As estruturas vítreas são elucidadas em termos de duas terminologias: $X^{(n)}$, que se refere ao átomo X ligado a 'n' oxigênios conectados a átomos formadores de rede semelhantes ou distintos, e X(N), que se refere ao isótopo X coordenado por 'N' átomos (sendo N um numeral romano). No sistema (i) (vidros NAPS), o duplo papel do sódio, como compensador de carga ou como modificador de rede, foi investigado. A estrutura desses vidros é dominada por uma preferência significativa de ligação entre espécies tertracoodenadas e aniônicas de Al(IV) e unidades catiônicas de $P^{(4)}$ (ligações Al-O-P). A substituição gradual de óxido de alumínio por sódio inicialmente aumenta o número de ligações Si-O-Al, que são balanceadas pela introdução de íons Na^+ pelo Na_2O. Valores maiores de x ([Na]/[P] > 1) levam à despolimerização parcial das ligações Al-O-P e à formação de unidades neutras $P^{(3)}$ e iônicas $P^{(2)}$ e $P^{(1)}$, que interagem fortemente com as espécies de sódio. Além disso, a presença de ligações P-O-P nos vidros com maiores concentrações de sódio foi confirmada por experimentos de excitação de duplo quanta de ^{31}P. O cenário geral pode ser descrito pelo papel dual dos íons de sódio na estrutura vítrea, agindo como balanceador de carga para o formador de rede Al(IV) aniônico, e como um neutralizador para os oxigênios não

ligantes das novas unidades $P^{(n)}$ formadas ($3 \geq n > 1$). No sistema (ii) (vidros SPAN), os espectros de ^{29}Si medidos pela técnica de Rotação no Ângulo Mágico (*Magic Angle Spinning* - MAS)-RMN indicam que nenhuma proporção significativa de Si hexacoordenado, tipicamente esperado em vidros com altas razões [P]/[Si], foi formada. Essa estrutura é possivelmente suprimida pela forte interação entre fósforo e alumínio, quantificada pelos experimentos de ressonância dupla com reacoplamento dipolar ^{27}Al-^{31}P. Técnicas de reacoplamento dipolar também facilitaram a análise dos espectros de ^{31}P MAS-RMN em termos de duas componentes distintas, com deslocamentos químicos diferentes: uma interagindo fortemente com Na, outra mais fortemente com o Al. As informações estruturais baseadas em RMN podem esclarecer sobre a dependência composicional não-linear da resistência à intempérie dos vidros. Por fim, efeitos de pressurização a frio também foram investigados no sistema: No sistema (iii) de borossilicatos pressurizados, ^{11}B MAS e ^{23}Na MAS-RMN ilustram juntos um efeito estrutural contraintuitivo: o número de coordenação médio do B diminui com a compressão. Esse efeito expõe um comportamento ainda não reportado na literatura: a pressão aplicada induz uma aproximação entre os íons de Na^+ e espécies de oxigênio que ligam boro tetraédrico e silício, causando uma quebra em ligações B(IV)-O-X (X = B, Si). Como resultado, novas unidades B(III) são formadas, bem como oxigênios não-ligantes predominantemente conectados ao silício (e compensados por íons Na^+).

Keywords: Aluminofosfossilicato. Borossilicato. Vidros pressurizados. Estado sólido. Dupla ressonância. RMN.

LIST OF ABREVIATIONS AND ACRONYMS

BO(s)	Bridging Oxygen(s)
CPMAS	Cross Polarization Magic Angle Spinning
EFG	Electric Field Gradient
FID	Free Induction Decay
FT	Fourier Transform
HE	Hahn Echo
HF	High Frequency
IF	Intermediate Frequency
INADEQUATE	Incredible Natural Abundance DoublE QUAntum Transfer Experiment
IRO	Intermediate Range Order
LF	Local Frequency
LoF	Low Frequency
MAS	Magic Angle Spinning
MRO	Medium Range Order
NBO(s)	Non-Bridging Oxygen(s)
NFU(s)	Network Former Unit(s)
NMR	Nuclear Magnetic Resonance
PAF	Principal Axis Frame
REAPDOR	Rotational Echo Adiabatic Passage Double Resonance
REDOR	Rotational Echo Double Resonance
rf	Radio frequency
SOQE	Second Order Quadrupolar Effect
SRO	Short Range Order
ssNMR	solid-state Nuclear Magnetic Resonance
SSB	Spinning Side Bands
TQMAS	Triple Quantum Magic Angle Spinning

CONTENTS

1 INTRODUCTION

Vitreous materials have gained importance in the last two centuries and, currently, the term “Glass Age” was coined to refer to the major role that glasses have been playing in architecture, medicine, communication, and many other branches of great importance in civilization.[1–3] For instance, a man dropping a handheld electronic device, during a conversation with someone miles away, would be simultaneously benefitting from the technologies of crack-resistant glasses and optical fibers.

Crack resistance can be correlated with many observable properties, such as atomic packing density, Poisson’s ratio, and elastic moduli.[4] Specific atomic constituents are reported as enhancers of crack resistance, such as magnesium, calcium, aluminum and boron.[5–8] The enhancement of this property is frequently correlated with an increased molar volume for the glass.[8-9] Glasses with highly connected networks and high molar volumes tend to respond to Vickers indentation with densification instead of shear flow. This behavior minimizes the formation of shear loads, and the initiation/propagation of cracks.[5-6] Additionally, the study of room-temperature-pressurized samples has provided information regarding the structural changes in glasses that suffered an impact or were subjected to intense mechanical stress.[4,10,11] The glasses submitted to high-pressures might mimic the stress suffered by the glasses in experimentally-controlled situations. These studies might expand our knowledge of prominent glass ingredients and/or linkages that promote densification processes instead of shear deformation, nonetheless few high-pressures systems were studied under room-temperature.

Our example also concerns optical fibers. Phosphate and silicate glasses are frequently used as gain media optical fibers and optical fibers core in communication infrastructure, respectively.[12–15] Both systems can be benefited when co-doped with Al_2O_3, whether increasing the solubility to rare-earth elements - for silicate glasses or improving the weathering resistance – for phosphate glasses.[16-17] In order to guarantee their effective functioning, optical fibers must display a diverse combination of properties, such as durability, thermal robustness, and hydrolytic stability under ambient conditions.[12,18] Therefore, in order to attend specific demand applications, it is of great interest to understand non-linear behavior of macroscopic properties, such as the reflexive index, density, coefficient of thermal expansion, isokrom temperatures, among others.[19-20] In this regard, technologically impactful glasses with complex macroscopic properties can be made by combination Al_2O_3-P_2O_5-SiO_2 system. Nonetheless, investigations on structure-property relation on quaternary Na_2O-containing Al_2O_3-P_2O_5-SiO_2 optical fibers show to be poorly known. The addition of sodium in the system can deeply affect properties as

the coefficient of thermal expansion by depolymerizing the network and/or as hydrolytic stability by changing the dissolution rate.[16, 18, 21-24] All these changes shed light on which kind of bond connections, in the network, would reflect the macroscopic and thermodynamic properties.

Spectroscopic techniques have been used to investigate the mechanisms behind glass properties (such as crack, heat- and weathering-resistance) through network connectivity, angle distributions, and chemical compositions. During the 1970s, Magic Angle Spinning (MAS) NMR revolutionized the investigation of the short-range order of glasses, allowing for the determination of the coordination number of a specific nucleus.[3,25] Modern solid-state NMR techniques probe also glass structures at different length-scales (intermediate and medium-range order).[26] With the benefit of being an element-selective technique, NMR allows the investigation of single, double and triple resonances of a diverse range of chemical elements with non-zero magnetic moments.[27] Finally, the overall results of distinct experimental set-ups are important to analyze the glass structure through the selective determination of magnetic shielding, spin-spin interactions (dipolar coupling and J-coupling), and quadrupolar interactions.[28]

For instance, Nazamutdinova and co-authors explored the role of phosphate and aluminum in a quaternary SiO_2 - Na_2O - P_2O_5 - Al_2O_3 system using solid-state NMR (ssNMR). It has been suggested that the glass transition temperature correlates with the role of aluminum in the network via formation of sixfold coordinate cation. [29] Additionally, the effect of adding a small concentration of phosphorus in a glass system with [Na] / [Al] ratio of 1 was investigated through dipolar recoupling double resonance NMR experiments.[30] The results indicates that P-O-Si linkages do not seem to play a central role in the network, which aligns with the findings of Toplis, Schaller and collaborators, who studied the system via ^{31}P MAS NMR and Transfer of Population Double Resonance (TRAPDOR) experiments.[31-32] This result is attributed to phosphorus being integrated in the network mainly through the formation of P-O-Al linkages, which compensates mutually the formal positive charge of fully polymerized phosphorus and the formal negative charge of AlO_4^- polyhedra.[29] Furthermore, a detailed picture of the role of is described as depend on the ratio [Na]/[Al]; the higher the [Na]/[Al], the more depolymerized the phosphorus units.[30,32] Nonetheless, none of studies seek in shedding light in the role of sodium in the network, which seems a relatively unexplored system in NMR spectroscopy.

Furthermore, older solid-state NMR studies had already established how the addition of alumina into phosphate glasses enhances their chemical durability, namely via the formation of

Al-O-P linkages.[33–35] $^{27}Al/^{31}P$ two dimensional cross-polarization MAS (CPMAS-NMR) experiments were performed to unambiguously distinguish the isotropic chemical shifts of phosphorus environments characterized by P-O-P and P-O-Al linkages.[36] Lang *et al.* reported $^{31}P/^{27}Al$ and $^{31}P/^{23}Na$ TRAPDOR results for sodium aluminophosphate glasses; they were able to detect distinct distributions of aluminum and sodium cations in the vicinity of phosphorus units.[37] Other studies using $^{1}H/^{31}P$ CPMAS-NMR investigated and identified distinct hydroxyl groups in P-OH linkages due to hydrolytic corrosion.[38]

Regarding the structural characterization of cold-pressed samples, solid-state NMR studies have been less abundant. Various authors have argued that permanent effects caused by sample pressurization persist only after high pressures are applied (at least 10 to 15 GPa);[39–41] and, due to this contention, most cold-pressurization studies are conducted using *in-situ* Raman, inelastic X-ray scattering and Brillouin spectroscopy measurements (i.e. samples were measured while under pressure).[39,41–43] Because in-situ NMR studies at high pressures are not possible using standard instrumentation, many NMR studies have been conducted on hot pressurized samples that were decompressed at room temperature,[10,44–46] and relatively few studies have addressed the permanent effects of cold densification.[47–49] For hot- and cold-pressurized glasses, solid-state NMR studies show a general tendency of the coordination numbers of boron, oxygen, aluminum, silica and phosphorus to increase – whereas the bond lengths formed by this atoms with either oxygens or with network formers thought oxygen are shortened. However, these qualitatively similar results might not represent the same effect. Whereas hot-pressed glasses represent supercooled liquids under pressure at their glass transition temperatures, cold-pressed glasses were subjected to pressure in their frozen state. Therefore, cold pressurization promotes the decreasing of original volume of glasses and, further, represents the densification process. Due to that, sample pressurization via indentation at room temperature might mimic the stress suffered by the glasses in laboratory-emulated stress situations.[4,10-11]

Aiming to extend the knowledge existing in the literature about the above topics, in the present work, the structure-property relation of following glasses were investigated: (i) heat-resistant aluminophosphosilicate with composition $xNa_2O – (22.50\text{-}x)Al_2O_3 – 7.50P_2O_5 – 70.00 SiO_2$ (NAPS), $2.50 \leq x \leq 17.50$, (ii) weathering-resistance aluminophosphosilicate optical fibers, with composition $xSiO_2 – (59\text{-}x)P_2O_5 – 13Al_2O_3 – 28Na_2O$ (SPAN), $0 \leq x \leq 13$; and (iii) cold-pressurized glasses with the composition $20Na_2O – xB_2O_3 – (70\text{-}x)SiO_2$, x = 10, 20, 30. They were explored through solid-state NMR characterization of short- and medium-range network structures. Information about local structure was obtained from ^{11}B, ^{23}Na, ^{27}Al, ^{29}Si,

^{31}P element- and interaction-selective strategies, such as standard MAS-NMR, 2D Triple Quantum MAS (TQMAS)-NMR, Rotational Echo Double Resonance (REDOR) and Rotational Echo Adiabatic Passage Double Resonance (REAPDOR) experiments, among others. [50–52] Overall, the investigation has brought insights and helped to rationalize how the macroscopic properties of these materials might be interpreted thought their network structures.

The present thesis is divided into six main chapters. Chapter 2 entitled “Glasses: background” summarizes the principal features of glassy materials and their structural organization. Chapter 3 entitled “Theoretical aspects of solid-state NMR spectroscopy” presents the theoretical aspects of the NMR technique. Also, some basic aspects of the instrumental components and operating system of the spectrometer are discussed. Chapter 4 describes the “Advanced NMR techniques”. Here, it is highlighted how each technique acts on the magnetization of the spin system, and it is clarified how each physical quantity is extracted and interpreted. “Experimental details” are found in Chapter 5. Here the details of the sample preparations are described. The measurement parameters used in each NMR experiment, as well as the equipment employed for the development of this work, are also listed. Chapter 6 shows the “Results”. Structured as already presented in the introduction and abstract, this chapter is divided between the results obtained so far regarding the investigation of (6.1) NAPS: $xNa_2O – (22.50\text{-}x)Al_2O_3 – 7.50P_2O_5 – 70.00SiO_2$ ($2.50 \leq x \leq 17.50$); (6.2) SPAN: $xSiO_2 – (59\text{-}x)P_2O_5 – 13Al_2O_3 – 28Na_2O$ ($0 \leq x \leq 13$) and (6.3) the investigation of the cold-pressed borosilicate glasses $20\ Na_2O - (80\text{-}x)SiO_2 – x\ B_2O_3$ ($x = 10, 20, 30$). Chapter 7 summarizes the “Conclusions” including the discussion of the results in the context of previous literature, and with some perspectives for improvement and continuation of this not yet published work. The results presented here are being compiled and prepared for publication in international peer-reviewed scientific journals.

2 GLASSES: BACKGROUND

This chapter will provide a brief review of the main aspects of covalent inorganic glasses, such as the physicochemical aspects involved in their formation and the aspects of their structural organization. This chapter also dedicates an introductory subsection to NMR, where the advantageous features of the technique to glasses are explained.

2.1 General description

Glass is commonly defined as a non-crystalline frozen state of a supercooled liquid.[54] Its behavior can be better understood by considering the temperature dependence of a state function, such as molar volume, entropy, or enthalpy, as shown in Figure 1. Supercooled liquids are the melts, which can potentially crystallize or form a glass. When a liquid is cooled down rapidly, and its temperature transcends the melting point (T_m) without crystallization, the system enters the metastable supercooled liquid state.[53] The viscosity of the melt increases, preventing the formation of the seeds to initiate the crystallization process by a restriction of mobility in the molecular dynamics. As the temperature continues to decrease, the molecular dynamics of the material keep slowing down further, reaching the glass transition region.[53] The supercooled liquid now enters the frozen state, where structural reorganization is kinetically hindered such that the state of the metastable liquid is preserved. Figure 1 illustrate two glasses lines represented by fast and cold cooling. The intersection of these lines with the supercooled liquid line represents the fictive temperature T_f, where the value of T_f depends on the cooling rate.[54] For unspecified cooling rates one typically characterizes the glasses by the glass transition temperature (T_g), measured via differential scanning calorimetry, thermal expansion, or dynamic mechanical analysis. T_g depends on factors such as the glass composition, chemical bond density, and cooling rate.[53]

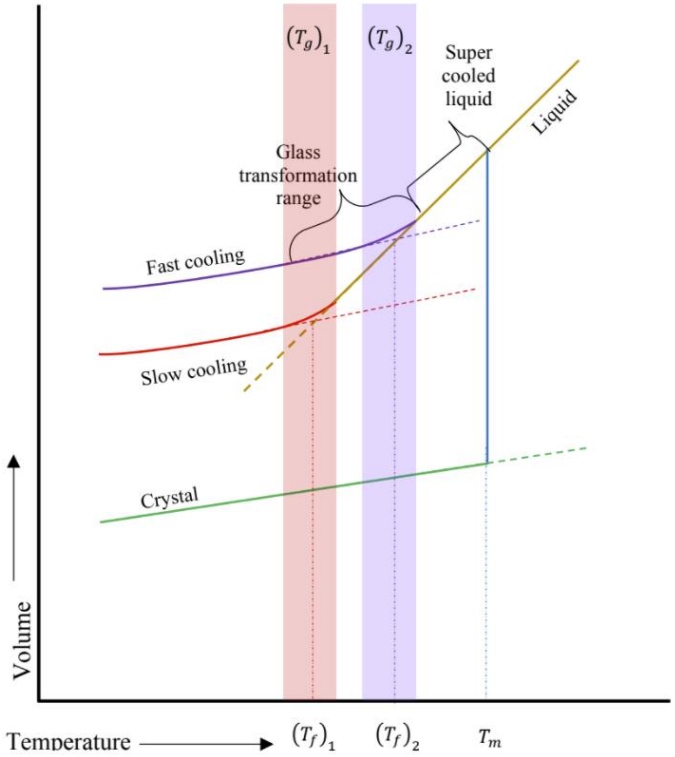

Figure 1 - Molar volume versus temperature illustration for the glass-forming transition.
Source: ECKERT; LENTZ.[44] Adapted from VARSHNEYA.[45]

While there is a wide compositional range of glasses resulting in a variety of physical properties, this work will focus on the so-called inorganic oxide glasses characterized by the prevalence of covalent bonds, such as those based on SiO_2, B_2O_3 and/or P_2O_5.[53] The role played by these oxides is illustrated in Figure 2. As the name suggests, the cations Si^{4+}, B^{3+} and P^{5+} are the "network formers": they are represented by the green and blue circles, and they form network connections through bridging oxygens (BOs), being oxygens represented by red circles.[54] Moreover, most industrially important glasses also have "network modifiers" in the composition.[54] In the current work, examples of them are the alkali elements, added as the oxides Na_2O. They act as charge balancers for atoms and structures with negative net charge. As represented in Figure 2, the charge balances (dark gray circles) will balance the network breaking linkages and will position themselves close to the negatively charged non-bridging oxygens (NBOs). Another group of oxides, called "intermediate oxides", can be either a network former or charge balancer.[54] In this work, this group is represented by Al_2O_3. Depending on the glass composition, aluminum can occur as either an anionic network former in tetrahedral symmetry, Al(IV), or as cationic Al(V) and Al(VI) units balancing the charges of anionic network formers.[55]

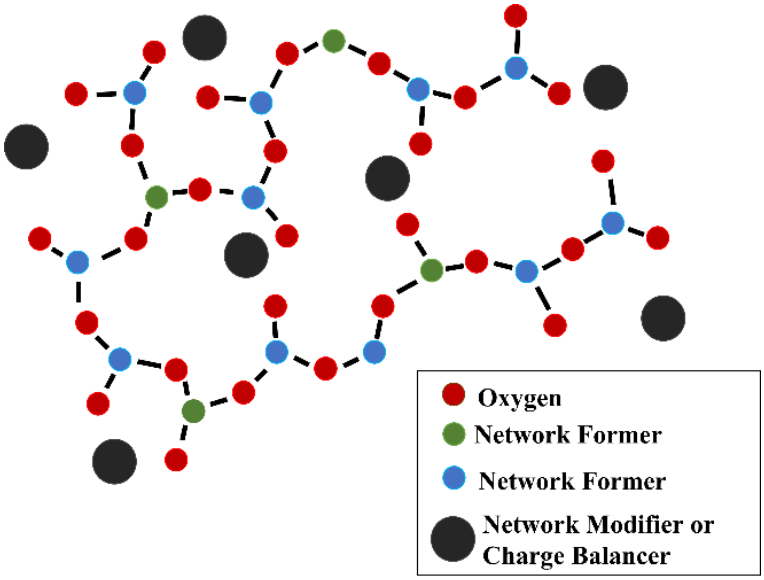

Figure 2 - Illustration of the structure of an amorphous material in a covalent network structure.
Source: By the author.

2.2 Phosphate, silicate, borate, and aluminum-containing glasses

The best structural description of the covalently bonded network is that done by the *Continuous random network model* of Zachariasen.[56] The model describes a glass as an aperiodic network of corner-sharing polyhedra randomly interconnected by bridging oxygens. In that context a glass might be discussed in terms of distinct distance domains on the length scale: short-range order (SRO) describing the first coordination sphere, intermediate-range order (IRO) describing details of the second and third coordination sphere and medium-range order (MRO), describing the spatial distribution of certain glass components and the formation of larger superstructural units such as clusters, chains, and rings.[54] Owing to the lack of translational symmetry, glasses show no long-range order.

The SRO (0.15-0.3 nm) describes the bonds between BOs or NBOs with a certain atom. The idea is summarized by Figure 3, which shows the types of network former units (NFUs) encountered in the glasses containing P_2O_5, SiO_2, B_2O_3, and/or Al_2O_3.[54] The nomenclature $X^{(n)}$ refers to the atom X with 'n' bridging oxygen atoms connected to network formers of either the same or of a different species. The $X^{(n)}$ terminology also adds the number of other network formers connected to the n bridging oxygen atoms as subscripts. For instance, in a $Si^{(4)}{}_{1B,2Si,1P}$ unit, the four bridging oxygen species of the $Si^{(4)}$ unit are connected to one boron, one phosphorus and two silicon atoms. The notation X(N), with 'N' is a number represented by a Roman numeral, means that the atom X is coordinated by 'N' atoms. This nomenclature is used for both aluminum and boron for which different coordination numbers may occur. The analysis

of SRO can then reveal structural information, such as the geometry in which the atoms are inserted and their coordination number.

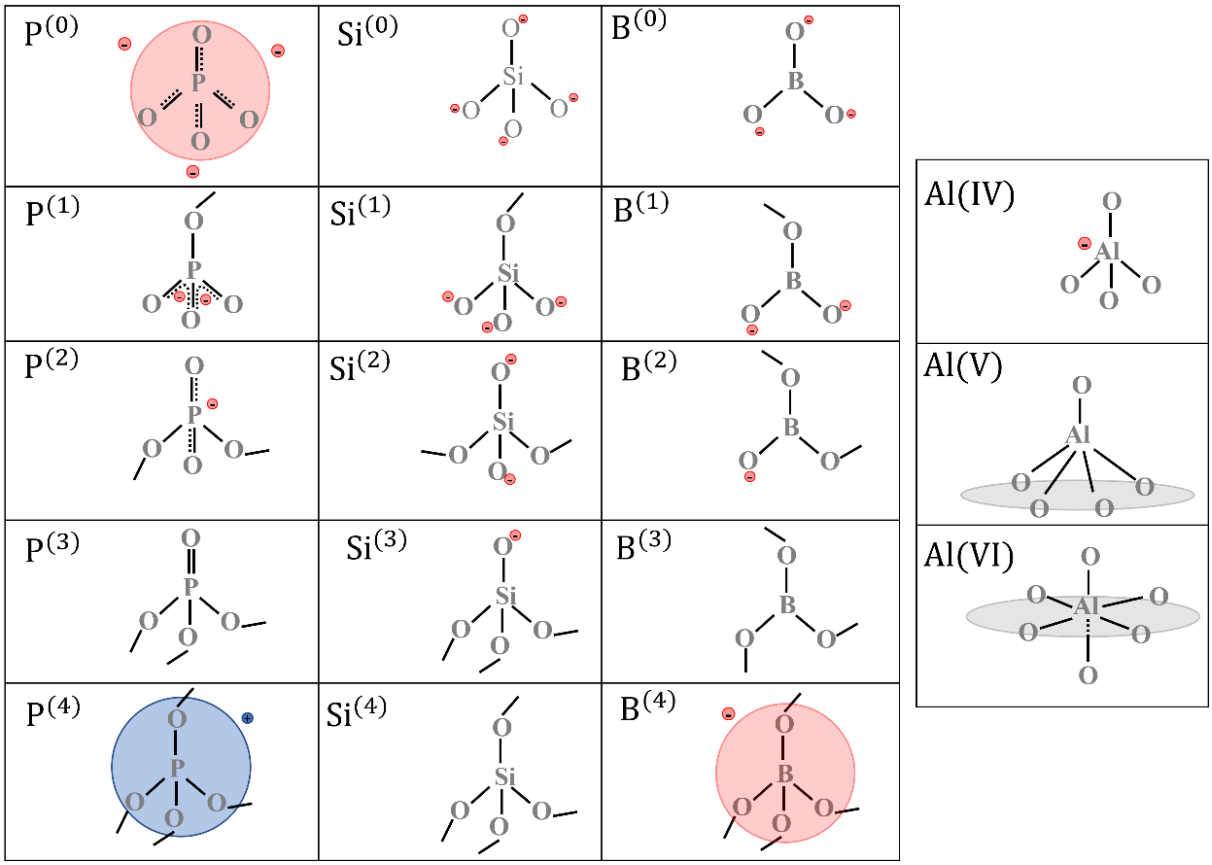

Figure 3 - Network former units in the nomenclature $X^{(n)}$, where 'n' is the number of bridging oxygens. For aluminum, the notation is Al(N), indicating the coordination number of Al.
Source: By the author.

IRO describes the bond connections and spatial relationships between the network formers and/or the network modifiers.[54] Particularly in the present work, the IRO will be explored by the average distance between the same or distinct species of network formers, also by the average distance between network formers and network modifiers. The combined study of SRO and IRO can provide insight into the structural origins of the physical properties of glasses, such as crack resistance, weathering stability and glass transition temperature.

2.3 Solid-state NMR and glasses

The principal technology mission of glass science is to tailor the physical and chemical properties of glasses to the demands of their application. For doing this, a deep understanding of glass structure is mandatory since this knowledge will facilitate compositional control of

glass properties. However, owing to the lack of periodic translational order of glasses, elucidating their structure is a challenging endeavor.

In this regard, solid-state NMR spectroscopy, because of its focus on local environments, has been playing a crucial role in structural investigation of glasses. Starting from the 1970s, the Magic Angle Spinning technique revolutionized this field of research and, since then, NMR techniques have been proven to be ideally suited for studying SRO, IRO, and MRO in amorphous materials.[25] The success achieved by NMR is attributed to its versatility. It is an element-selective technique, affording the study of a wide range of isotopes with non-zero nuclear spin, one at a time. Also, NMR is quantitative, as the nuclear magnetization of a bulk sample is directly proportional to the number of spins present in the sample. It is important to highlight that some experiments used in solid-state NMR might not me quantitative due to multiple factors, such as the inhomogeneous profile of excitation, excitation of groups inserted in certain environments – which might only partially select or fully eliminate the magnetization of other groups, among other reasons.[25-26] The non-quantitative nature of certain experiments is not always a disadvantage, as it can often be utilized as an important tool for spectral editing unresolved spectra. Additionally, various distinct interatomic interactions take part in characterizing the local environment. In this respect, NMR offers an interaction-selective experimental approach.[26] By properly manipulating the bulk magnetization, an experiment can select the interaction of interest and eliminate the others. Finally, NMR is a non-destructive technique, allowing reuse of the sample whenever necessary.

3 THEORETICAL ASPECTS OF SOLID-STATE NMR SPECTROSCOPY

This chapter is primarily concerned with understanding how and why solid-state NMR spectroscopy can serve as a key tool for examining the SRO and MRO in a glass. The first subsection, "Basic aspects of NMR", will summarize the Zeeman interaction as well as excitation pulses and relaxation effects. The second subsection, "Nuclear interactions", will summarize the local interactions that influence the Zeeman energy levels. It will also discuss the structural information that can be obtained by the interpretation of the local interactions. It is important to highlight that, in the current work, only diamagnetic effects were considered as the samples studied contain no unpaired electrons. The subsection titled "Instrumentation" will briefly describe how the spectrometer operates to extract information.

3.1 Basic aspects of NMR

3.1.1 Zeeman effect

NMR spectroscopy is fundamentally based on the Zeeman Hamiltonian, $\hat{H}_Z$, which describes an isolated single spin $\hat{\mathbf{I}}$, with its corresponding magnetic moment $\hat{\boldsymbol{\mu}}$, interacting with a magnetic flux density B_0. The Zeeman Hamiltonian is represented as the following:

$$\hat{H}_Z = -\hat{\boldsymbol{\mu}} \cdot \mathbf{B_0} = -\hbar\gamma\hat{\mathbf{I}} \cdot \mathbf{B_0} \quad (1)$$

where $\hbar$ is the Planck constant and γ is the gyromagnetic moment – an isotope-dependent constant, which makes NMR an element-selective technique.[57] The Hamiltonian can be expressed in units of energy (as Equation 1 shows) or in units of angular frequency, when the Hamiltonian is normalized by $\hbar$. In this work, the Hamiltonian is presented in the unit of angular frequency. The eigenstates of this Hamiltonian are represented by $|I, m\rangle$ and by the eigenvalues $E_{I,m}$, as shown by the equation below:

$$\hat{H}_Z|I, m\rangle = E_{I,m}|I, m\rangle \quad (2)$$

where $E_{I,m} = -m\gamma B_0$, being 'm' the magnetic quantum number assuming values of $m = -I, -I+1, \ldots, I-1, I$.[57] Therefore, the interaction between the magnetic field and the nuclear magnetic moment splits the degeneracy into $2I+1$ distinct energy levels. The energy equation can be rewritten as $E_{I,m} = -m\omega_0$, where:

$$\omega_0 = 2\pi\nu_0 = \gamma|\mathbf{B_0}| \quad (3)$$

and ω_0 is defined as the Larmor frequency. Figure 4 represents the splitting effect caused by the Zeeman interaction. Note that the states are equally spaced in terms of energy.

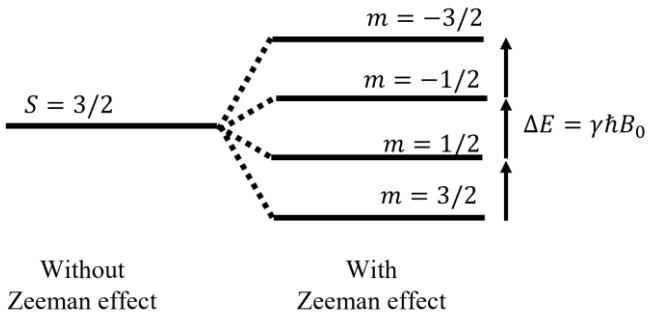

Figure 4 - Zeeman effect splitting for a spin-3/2 with a positive γ.
Source: By the author.

Using a semi-classical picture, it is convenient to analyze the behavior of the magnetization **M** (sum over all the magnetic moments $\boldsymbol{\mu}_I$ divided by the volume) under the influence of the magnetic field $\boldsymbol{B_0}$. The behavior is mathematically expressed by the equation of motion of the expectation value, shown in Equation (5): [57]

$$\mathbf{M} = \frac{1}{V}\sum \boldsymbol{\mu}_i \tag{4}$$

$$\frac{d\langle \mathbf{M} \rangle}{dt} = \langle \mathbf{M} \rangle \times \gamma \mathbf{B_0} \tag{5}$$

This equation predicts angular motion (precession) of **M** around $\mathbf{B_0}$ at a constant rate, then it is interpreted as the precession frequency of net nuclear magnetization around the magnetic flux density $\mathbf{B_0}$, with the Larmor frequency ω_0. Table 1 illustrates the Larmor frequency of some isotopes. In NMR spectroscopy, the magnetic flux density (measured in Tesla) is typically kept fixed at a particular value, defined by the current supplied to the superconducting coil upon initial charge-up. Spectrometers are usually labelled in terms of Larmor frequency of ^{1}H at that particular magnetic flux density; for instance, a spectrometer operating together with a 14.1 T magnet is usually called a 600 MHz spectrometer, as shown in Table 1.[57] This table also illustrates the precession frequencies of the other relevant nuclei studied in the present thesis. Negative values of gamma are interpreted, in semi-classical picture, as the net z-magnetization being oriented in the opposite direction (**-z**) of the magnetic field $\mathbf{B_0}$. In this case, Figure 2 would have inverted energy levels, where the more the negative the m-values, the lower the energy of the states, and vice versa.

Table 1 - Examples of gyromagnetic ratios (γ) and respective linear Larmor frequencies (ν_0) for a magnetic field strength of 14.1 T.

	γ (10^6 rad s^{-1} T)	ν_0 (10^6 s^{-1}) – 14.1 T
^{1}H	267.51	600.32
^{11}B	85.84	192.63
^{23}Na	70.76	158.79
^{27}Al	69.76	156.55
^{29}Si	-53.19	-119.36
^{31}P	108.29	243.014

Source: By the author.

3.1.2 Excitation pulses

When a sample is placed in the $\mathbf{B}_0 = B_0\mathbf{z}$ magnetic field, and thermal equilibrium is reached, the population of the spin states follows a Boltzmann distribution. In this scenario, the net z-magnetization is oriented in the (positive or negative) direction of the magnetic field (for $\gamma > 0$ and $\gamma < 0$), and the net transverse magnetization is zero.[57] In the presence of electromagnetic radio frequency (rf) waves the oscillating magnetic field component B_1 can interact with the nuclei on resonance ($\omega_{rf} \sim \omega_0$), mixing the Zeeman states and exciting the system.

The excitation radio wave means introducing a time-dependent oscillating field $\mathbf{B}_1(t)$ in the perpendicular xy-plane. Without loss of generality, let us assume that $\mathbf{B}_1(t) = B_1(t)\mathbf{x}$:

$$\mathbf{B_1}(t) = 2B_1 \cos(\omega_{rf} t)\,\mathbf{x} \tag{6}$$

where ω_{rf} are the angular radio frequency associated with the electromagnetic waves applied.[57] The factor of two in the linearly polarized $\mathbf{B_1}$ field corresponds to the sum of two circularly polarized waves with frequencies ω_{rf} and $-\omega_{rf}$. It is important to note that while one of these circularly polarized waves will efficiently excite the isotope (depending on the positive or negative sign of the gyromagnetic ratio) the other circularly polarized wave will be inefficient due to the large offset.

Next, follows a description of how the z-magnetization can be taken out of equilibrium and brought, partially or totally, to the transverse plane. For a simpler illustration of that effect, a mathematical procedure is adopted: The time dependence of $\mathbf{B}_1(t)$ is removed with the adoption of a new (and time-dependent) coordinate system, called *rotating frame*. This mathematical operation entails the rotation of the system's wavefunction $\mathbf{\Psi}$ around $\mathbf{B}_0$ with an angular radio frequency ω_{rf}:

$$\tilde{\mathbf{\Psi}} = \exp\{iI_z\omega_{rf}t\}\,\mathbf{\Psi} \tag{7}$$

where $\tilde{\boldsymbol{\Psi}}$ is the wavefunction in the rotating frame.[57] In this frame, Schrödinger's equation can be rewritten with a time-independent Hamiltonian (Equation (8)) and with time-dependent wavefunctions. Hence, in the rotating frame, during the excitation of the RF, the effective Hamiltonian is expressed by the equation below, and the magnetic field corresponding to the effective Hamiltonian is illustrated in Figure 5.[57]

$$\hat{\mathrm{H}}_{\mathrm{eff}} = \gamma(\mathrm{B}_0 - B_{\mathrm{rf}})\hat{\mathrm{I}}_{\mathrm{z}}\mathbf{z} + \gamma\mathrm{B}_1\hat{\mathrm{I}}_{\mathrm{x}}\mathbf{x} \qquad (8)$$

where $\omega_1 = \gamma \mathrm{B}_1$ and $\omega_{\mathrm{rf}} = \gamma \mathrm{B}_{\mathrm{rf}}$.

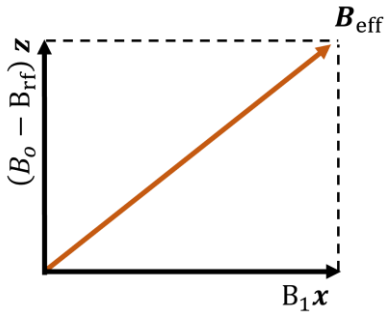

Figure 5 - Illustration of the effective field in the rotating frame.
Source: By the author.

Note that the effective Hamiltonian assumes a special form when the radio wave fulfills the following condition: $\omega_{\mathrm{rf}} = \omega_0$, where $\mathbf{B}_{\mathrm{eff}} = \mathbf{B}_1$. That picture summarizes the resonance condition, and it is used to excite the system with the highest efficiency.[57] Under this condition ($\omega_{\mathrm{rf}} = \omega_0$), the effective field (as well as the precession movement) would be pointed to the x-direction and the field in the z-direction would be zero. Under these circumstances, the rotation frequency of the rotating frame axis – in comparison with the laboratory frame axis – matches exactly the Larmor frequency. This means that, whereas all spins are precessing in the laboratory frame with their Larmor frequency, they appear static in the rotating frame.[57] An additional reason for doing so, as will be discussed in subsection 3.3, concerns the acquisition of the NMR data, which for technical reasons measures the frequency of the system subtracted by ω_{rf}; this means that the data is recorded as if the data were indeed in such a reference system.[57]

For analyzing the effect of pulse excitation, it is, again, convenient to use the equation of motion of the expectation value to analyze the behavior of magnetization **M**. According to Equation (5) and within the rotating frame under the resonance condition, the magnetization vector $\mathbf{M}(\mathrm{t})$ precesses around the excitation field $\mathbf{B}_1$ at a fixed rate of $\gamma \mathrm{B}_1$. If $\mathrm{t_p}$ is the time when the excitation field $\mathbf{B}_1$ is on, then $\mathbf{M}(\mathrm{t})$ rotates around $\mathbf{B}_1$ field for an angle θ defined as:

$$\theta = \gamma B_1 \cdot t_p \tag{9}$$

As shown in Table 2, the magnetization will always stay in the yz-plane of the rotating frame, but the orientation is dependent on the time during which the excitation is on.[57,58] There are many distinct pulses: shaped pulses, single and multiple quantum excitation pulses, adiabatic pulses, etc. [57,58,59] More about them, and how they are used to manipulate magnetization, will be further discussed in Chapter 3.

Table 2 - Examples of distinct pulses for $\gamma > 0$.

T_p	θ	$\langle\vec{M}\rangle$ direction
$\pi / 2\gamma B_1$	$\pi /2$	$\hat{y}$
$\pi / \gamma B_1$	π	$-\hat{z}$
$3\pi / 2\gamma B_1$	$3\pi /2$	$-\hat{y}$
$2\pi / \gamma B_1$	2π	$\hat{z}$

Source: By the author.

3.1.3 Relaxation of a spin system in the solid-state

The phenomenological relaxation in the NMR system is described by two main quantities: longitudinal or spin-lattice relaxation time (characterized by the time constant T_1) and transverse relaxation (characterized by the time constant T_2^*).[57,59] T_1 describes the behavior of a spin system returning to thermal equilibrium (recovering the magnetization along z-direction) and gradually approaching Boltzmann law distribution. T_2^* characterizes the decay of single quantum coherence, which means the loss of coherence after a $\Delta m = \pm 1$ excitation, within the xy-plane.[59] Equation (10) shows the Bloch equations with the terms accounting for the relaxation effects by phenomenologically adding them to the equations of motion:[59]

$$\frac{d}{dt}\mathbf{M}(t) = \gamma \mathbf{M}(t) \times \mathbf{B}(t) - R\,[\mathbf{M}(t) - \mathbf{M}(0)] \tag{10}$$

where:

$$R = \begin{pmatrix} 1/T_2^* & 0 & 0 \\ 0 & 1/T_2^* & 0 \\ 0 & 0 & 1/T_1 \end{pmatrix} \tag{11}$$

Although relaxation phenomena are not in the scope of this work, it is crucial to understand that transverse relaxation, which governs the width of the spectra, is based on two physically distinct effects, comprising homogeneous and inhomogeneous broadening: Homogeneous broadening is related to fluctuations of nuclear spin precession frequencies,

caused by internal interactions* producing fluctuating local magnetic fields. [60] This part of transverse relaxation is called "spin-spin" relaxation and associated with the relaxation time T_2. This effect can be understood in the basis of Heisenberg's uncertainty principle: the shorter the lifetime of the spin in a certain state, the larger the energetic uncertainty. In contrast, inhomogeneous broadening arises from distributions of temporally constant precession frequencies, caused e.g., by magnetic field inhomogeneities or (in powdered solids) orientationally dependent precession frequencies.[57,59-60] This part can be refocused by inversion pulses and characterized by the time constant T_2'. The relaxation rates from both processes are additive, i.e., $1/T_2 + 1/T_2' = 1/T_2^*$.[60]

Finally, the quantitative character of solid-state NMR measurements is directly associated with full recovery of magnetization via spin-lattice relaxation. If one sample contains distinct species with distinct T_1 relaxation times, it is crucial to wait for the full recovery of magnetization before exciting the sample again. Incomplete recovery of magnetization of some longer-T_1 species lead to incorrect measurement of relative intensities, resulting in wrong quantification of the distinct sites.[60]

3.2 Nuclear interactions

The nuclear precession frequencies are largely dominated by the strength B_0 of the externally applied magnetic field and additionally influenced by the chemical, electronic and magnetic environments of the nuclei.[57] In this work, the high-field approximation is valid, which means the spin interactions can be treated as perturbative interactions ($\hat{H}_{pert}$) to the Zeeman Hamiltonian ($\hat{H}_{pert} \ll \hat{H}_Z$) and they result in contributions to the energy levels. Relevant examples of perturbative interactions, in the current work, are magnetic shielding ($\hat{H}_{CS}$), J-coupling ($\hat{H}_J$), dipole-dipole coupling ($\hat{H}_{DD}$), and quadrupolar interaction ($\hat{H}_Q$): [57]

$$\hat{H} = \hat{H}_Z + \hat{H}_{CS} + \hat{H}_{DD} + \hat{H}_J + \hat{H}_Q \qquad (12)$$

In this subsection the contributions of these interactions to the energy levels will be discussed. In the solid state, each spin in a particular local environment and at a particular molecular/crystal orientation relative to the external magnetic field feels a specific local field that is characteristic for this environment/orientation. This anisotropy necessitates a

* Examples of internal interactions responsible for causing the fluctuation in nuclear spin precession frequencies are the dipolar interaction and the quadrupolar interaction.[60] Large chemical shift anisotropy might also have an influence in the spin-spin relaxation time nonetheless no example of large chemical shift anisotropy is present in the current work. More about the internal interactions seen in solid-state NMR in Section 3.2.

mathematical description in terms of tensor algebra. In polycrystalline or amorphous samples with different local environments distinct spin precession frequencies are thus present, whose superposition leads to coherence loss.

3.2.1 Magnetic shielding

The magnetic shielding interaction originates from perturbations caused by the interaction of the electronic cloud around the nucleus with the applied magnetic field $\mathbf{B}_0$. This interaction has an anisotropic character dictated by the interaction between the spin $\hat{\mathbf{I}}$, the magnetic shielding $\overleftrightarrow{\sigma}$, and the magnetic field $\mathbf{B}_0$, so that:

$$\hat{H}_{CS} = -\gamma_I \hat{\mathbf{I}} \cdot \overleftrightarrow{\sigma} \cdot \mathbf{B}_0 \tag{13}$$

where γ_I is the gyromagnetic factor associated with $\hat{\mathbf{I}}$. [57-58]

The magnetic shielding tensor can be viewed in terms of various distinct mechanisms leading to both: paramagnetic and diamagnetic contributions. Paramagnetic contributions arise from the van-Vleck paramagnetism associated with the angular momentum of admixed excited electronic state functions in covalently bonded compounds and from conduction electron Pauli paramagnetism in metallic compounds (Fermi-contact interaction, Knight shift).[58]A second contribution relevant only in metallic compounds arises from the conduction electron Pauli paramagnetism (Fermi-contact interaction, Knight shift).[57-58] Diamagnetic contributions arise from the orbital movement induced by any electronic charge assembly (closed shells, valence shells, conduction electrons), which generates a field opposite to $\mathbf{B}_0$ and depends only on the electronic ground state.[57] Because of that, the produced field tends to shield the nucleus with a magnitude of, approximately, 1 to 10^2 ppm of the Zeeman interaction.[57]

Experimentally only the sum of all contributions can be measured and described in terms of the usual tensor algebra. The tensor $\overleftrightarrow{\sigma}$ assumes a diagonal form within a special coordinate system, called the Principal Axis Frame (PAF): [57]

$$\begin{pmatrix} \sigma_{xx} & \sigma_{xy} & \sigma_{xz} \\ \sigma_{yx} & \sigma_{yy} & \sigma_{yz} \\ \sigma_{zx} & \sigma_{zy} & \sigma_{zz} \end{pmatrix} \xrightarrow{\text{Diagonalizing}} \begin{pmatrix} \sigma_{xx}^{PAF} & 0 & 0 \\ 0 & \sigma_{yy}^{PAF} & 0 \\ 0 & 0 & \sigma_{zz}^{PAF} \end{pmatrix} \tag{14}$$

The three principal axis components are expressed as the isotropic value (σ_{iso}), the asymmetry parameter (usual in two distinct notations η_{CS}^{a} and η_{CS}^{b}) and the anisotropic parameter (Δ), so that:[57]

$$\sigma_{iso} = \frac{\left(\sigma_{xx}^{PAF} + \sigma_{yy}^{PAF} + \sigma_{zz}^{PAF}\right)}{3} \quad (15)$$

$$\eta_{CS}^{a} = \frac{\left(\sigma_{XX}^{PAF} - \sigma_{YY}^{PAF}\right)}{\sigma_{ZZ}^{PAF}} \quad (16\ a)$$

$$\eta_{CS}^{b} = \frac{\left(\sigma_{XX}^{PAF} - \sigma_{YY}^{PAF}\right)}{\Delta} \quad (17\ b)$$

$$\Delta = \sigma_{ZZ}^{PAF} - \sigma_{iso} \quad (17)$$

To calculate the effect of magnetic shielding on the nuclear precession frequency, first-order perturbation theory is sufficient due to the above-mentioned reason of the small magnitude of magnetic shielding interaction (in comparison with the Zeeman interaction).[57] Formally, the first-order perturbation of shielding interaction Hamiltonian for $\mathbf{B}_0 = B_0\mathbf{z}$ is described as:

$$\hat{H}_{CS}^{(1)} = -\gamma \hat{I}_z \sigma_{zz}^{lab} B_0 \quad (18)$$

The angular precession frequency can be described by $\omega_{CS} = \sigma_{zz}^{lab}\gamma B_0$. The next steps involve describing σ_{zz}^{lab} in terms of components in the principal axis frame.[57] Thus, it is possible to write σ_{zz}^{lab} using the $\hat{z}$-versor in spherical coordinates (with θ and ϕ being, respectively, the polar and azimuthal angles defining the magnetic field B_0 in the PAF of the magnetic shielding tensor). Finally, the frequency $\omega_{CS} = \sigma_{zz}^{lab}B_0$ can be expressed as a function of (15), (16 a) and (17),[57] such that:[57,61]

$$\omega_{CS} = -\omega_0\sigma_{iso} - \frac{1}{2}\omega_0\Delta\left(3\cos^2\theta - 1 + \eta_{CS}^{b}\sin^2\theta\cos 2\phi\right) \quad (19)$$

where (a) $-\omega_0\sigma_{iso}$ is the angular frequency associated with the isotropic chemical shift – which means the displacement, or shift, caused by the magnetic shielding interaction if all the spins are in an isotropic environment – and (b) the second term represents the angular frequency associated with the chemical shift anisotropy.[57] According to equation (19), each crystallite in a polycrystalline sample has a distinct resonance frequency depending on the specific orientation θ, ϕ of its PAF relative to the magnetic field direction defining the laboratory frame. Therefore, the combination of signals from multiple possible orientations in a polycrystalline or amorphous material results in a broad pattern, known as *powder pattern*. Figure 6 illustrates the origin and shape of this anisotropic spectral pattern for the case of an axially symmetric tensor ($\eta_{CS} = 0$).[57]

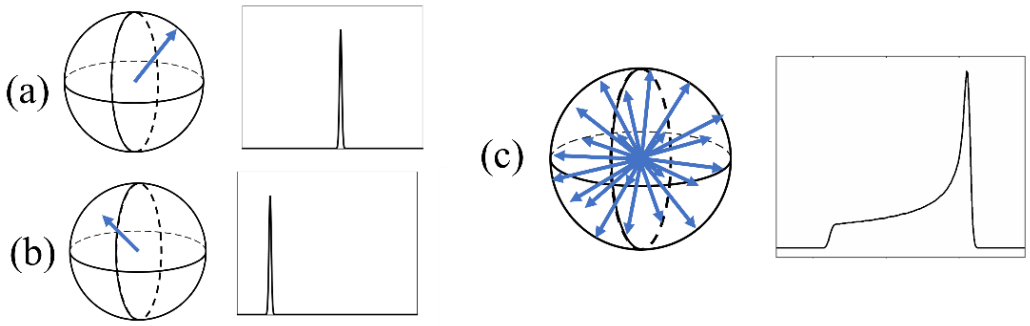

Figure 6 - Magnetic shielding anisotropy pattern for axial symmetry. In (a) and (b) we see the spectrum of single crystallites with distinct angular positions. The sum of these resonant frequencies generates the anisotropy pattern of the powder lineshape seen in item (c).
Source: By the author.

However, due to the frequencies being proportional to the strength of the magnetic field, the same sample responds with distinct frequencies for different field strengths B_0. Because of this, the absolute frequencies in NMR experiments are not usually reported. Instead, the frequencies are reported in relation to a reference sample, using the chemical shift scale defined by:[57]

$$\delta = \frac{\nu - \nu_{ref}}{\nu_{ref}} \cdot 10^6 [\text{ppm}] \tag{20}$$

With that, the magnetic field dependence is removed and δ can be rewritten as a function of equations similar to those found in shielding tensor equation (15), (16) and (17).[57] However, some conventions are used to label the principal values in order to report magnetic shielding anisotropy in lineshapes. The most used one is the Haeberlen convention [60]:

$$\left|\delta_{zz}^{PAF} - \delta_{iso}\right| \geq \left|\delta_{xx}^{PAF} - \delta_{iso}\right| \geq \left|\delta_{yy}^{PAF} - \delta_{iso}\right| \tag{21}$$

$$\delta_{iso} = \frac{\left(\delta_{xx}^{PAF} + \delta_{yy}^{PAF} + \delta_{zz}^{PAF}\right)}{3} \tag{22}$$

$$\delta_{aniso} = \delta_{ZZ}^{PAF} - \delta_{iso} \tag{23}$$

$$\eta_{Hae} = \left(\delta_{XX}^{PAF} - \delta_{YY}^{PAF}\right)/\left(\delta_{ZZ}^{PAF} - \delta_{iso}\right) \tag{24}$$

Applications of the chemical shift anisotropy as a source of structural information are highlighted in many studies,[20,62] however, the presence of multiple sites can result in insufficient resolution to resolve the broadband patterns for each of the resonant species. To improve the resolution of the spectra, the most widely used experimental technique in the spectroscopic investigation of polycrystalline materials and amorphous materials is sample rotation around an axis, which forms a specific angle of 54.7° (*magic angle spinning*) with the **z**-direction. This technique is used to average anisotropies out. More on these techniques will be presented in Chapter 4 – Section 4.1.

3.2.2 Indirect dipole-dipole interaction or J-coupling

J-coupling is also known as “through-bond spin-spin” or (less accurate) “indirect dipole-dipole” interaction. Under this interaction, two nuclei are coupled via spin polarization of bonding electrons: loosely speaking, one spin creates a local field, which magnetizes the bonding electrons; then, the magnetization thus generated perturbs the neighboring energy level of the spin. Thus, J-coupling can only be measured if two atoms are linked through one or more chemical bonds. For this work, let us assume a homonuclear through-bond interaction for a pair of spins $\hat{\mathbf{I}}_1$ and $\hat{\mathbf{I}}_2$, which can be expressed by the anisotropic interaction:

$$\hat{H}_J = 2\pi \hat{\mathbf{I}}_1 \cdot \overleftrightarrow{J} \cdot \hat{\mathbf{I}}_2 \tag{25}$$

where $\overleftrightarrow{J}$ is the coupling tensor, with an isotropic component, J_{iso}.[60]

Unlike the situation encountered with heavy atoms containing many electrons, this interaction is a source of only small perturbation amplitude, approximately on the order of 10-100 Hz and, therefore, frequently not observed in broad solid-state spectra due to more intense broadening caused by other interactions.[60] Consequently, this interaction is not often relevant employed in solid-state NMR studies. Nevertheless, there are methods specifically designed to investigate J couplings in solid-state NMR, which are used in some situations to unambiguously identify chemical connectivity, as it will be shown in the Chapter 4.

3.2.3 Direct dipole-dipole interaction

When two spins are close together, each one of them creates a field that influences its neighbor; in other words, there is a dipolar interaction between their magnetic moments.[57] The Hamiltonian of the dipole interaction can be obtained in analogy to the classical interaction energy of two-point dipoles; quantum mechanically the interaction between the spins $\hat{\mathbf{I}}$ and $\hat{\mathbf{S}}$ is expressed by:

$$\hat{H}_{DD} = -\left(\frac{\mu_0}{4\pi r^3}\gamma_I\gamma_S\right)\left(\hat{\mathbf{I}} \cdot \hat{\mathbf{S}} - 3\left(\hat{\mathbf{I}} \cdot \mathbf{u}\right)\left(\hat{\mathbf{S}} \cdot \mathbf{u}\right)\right) \tag{26}$$

where $\mathbf{u}$ is the versor (unit vector) in the direction of the internuclear distance ‘r’ between the spins $\hat{\mathbf{S}}$ and $\hat{\mathbf{I}}$.[57] For evaluating this equation, the coordinate system was defined as shown in Figure 7: θ is the polar angle subtended by the $\mathbf{B}_0$ field and the versor $\mathbf{u}$ and ϕ is the azimuthal angle in spherical coordinates.[57]

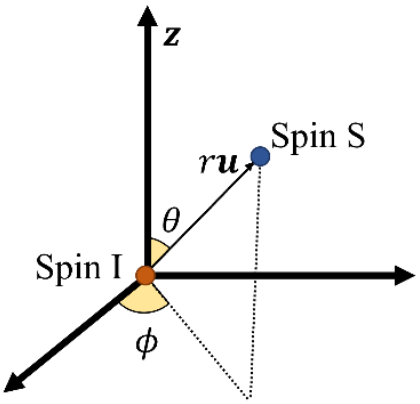

Figure 7 - Definition of spherical coordinates in relation with S-I internuclear vector, with $\mathbf{B_0} = \mathbf{B_0 z}$ field and the internuclear distance vector $\mathbf{r} = \mathbf{ru}$.
Source: By the author.

It is easy to see that the Hamiltonian depends also on the molecular orientation. Evolving the angular dependence terms of the equation above, it is possible to compute the terms like:[57]

$$\hat{\mathbf{I}} \cdot \hat{\mathbf{S}} - 3(\hat{\mathbf{I}} \cdot \mathbf{r})(\hat{\mathbf{S}} \cdot \mathbf{r}) = (\hat{A} + \hat{B} + \hat{C} + \hat{D} + \hat{E} + \hat{F}) \quad (27)$$

where:

$$\hat{A} = \hat{I}_z \hat{S}_z (3\cos^2\theta - 1) \quad (28)$$

$$\hat{B} = -\frac{1}{4}(\hat{I}_+ \hat{S}_- + \hat{I}_- \hat{S}_+)(3\cos^2\theta - 1) \quad (29)$$

$$\hat{C} = \frac{3}{2}(\hat{I}_z \hat{S}_+ + \hat{I}_+ \hat{S}_z)(\sin\theta\cos\theta\, e^{-i\phi}) \quad (30)$$

$$\hat{D} = \frac{3}{2}(\hat{I}_z \hat{S}_- + \hat{I}_- \hat{S}_z)(\sin\theta\cos\theta\, e^{i\phi}) \quad (31)$$

$$\hat{E} = \frac{3}{4}(\hat{I}_+ \hat{S}_+)\sin^2\theta\, e^{-2i\phi} \quad (32)$$

$$\hat{F} = \frac{3}{4}(\hat{I}_- \hat{S}_-)\sin^2\theta\, e^{2i\phi} \quad (33)$$

and, respectively, $\hat{I}_+$ and $\hat{I}_-$ are the raising and lowering operators for the spin $\hat{\mathbf{I}}$. The same notation is used for the spin $\hat{\mathbf{S}}$. Another important parameter of the dipolar Hamiltonian in (26) is the constant:

$$d = \left(\frac{\mu_0}{4\pi r^3}\gamma_I \gamma_S\right) \quad (34)$$

known as dipolar coupling constant.[57]

In all cases studied in this work the high-field approximation is valid for the dipolar Hamiltonian $\hat{H}_{DD}$, i.e., the Zeeman interaction is dominant ($\hat{H}_{DD}$ is approximately 100 ppm of Zeeman interaction) at the commonly used high magnetic field strengths.[57-58] This means that the next steps involve using perturbation theory to compute the first-order term, where the terms

C-F connecting different Zeeman energy levels can be truncated out. [57] On the other hand, the term $\hat{A}$ (which is dependent only on $\hat{I}_z$ and on $\hat{S}_z$) will affect the energy levels because it commutes with Zeeman interaction, thus, taking part of the secular form of the Hamiltonian. Therefore, the overall effect of this term is:

$$E_{DD}^{(1)} = -d \cdot m_I m_S (3\cos^2\theta - 1) \tag{35}$$

with $\hat{\mathbf{I}} = \hat{\mathbf{S}}$ in the case of homonuclear interaction. [57]

Furthermore, the term $\hat{B}$ should be analyzed separately for homo- and heteronuclear cases; for a two-spin system, the energy levels of both cases are illustrated in Figure 8. On the one hand, in Figure 8 (a), the Zeeman energy levels for two-like nuclei $|\pm\rangle$ and $|\mp\rangle$ are degenerate. The dipolar term $\hat{I}_+\hat{S}_- + \hat{I}_-\hat{S}_+$ flips one spin up and, simultaneously, flips the second spin down. This transition is known as *flip-flop* movement, [57] which is illustrated by the red double arrow in Figure 8 (a). On the other hand, in Figure 8 (b), the Zeeman energy levels for two unlike nuclei are split into $|\pm\rangle$ and $|\mp\rangle$ distinct energy levels, due to the distinct gyromagnetic constants. Thus, the flip-flop term does not anymore commute with Zeeman Hamiltonian. [57,58] Henceforth, for the heteronuclear dipolar interaction the term $\hat{B}$ does not contribute to the NMR lineshape.

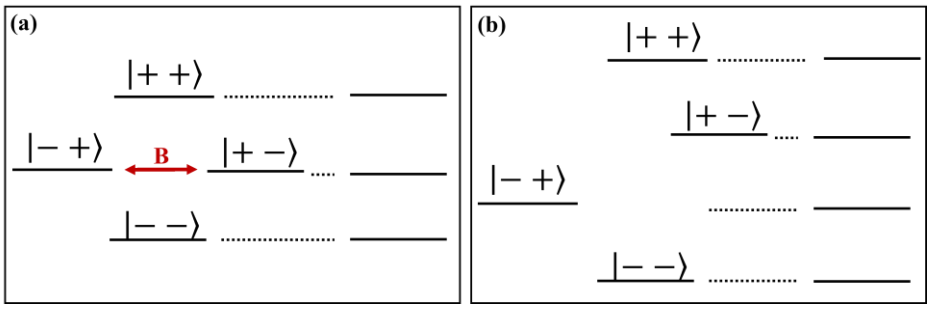

Figure 8 - Energy levels and eigenvectors for (a) a homonuclear and (b) a heteronuclear two-spin-1/2 system
Source: By the author.

Finally, taking into consideration the homo- and heteronuclear term of the first-order perturbation theory, respectively $\hat{H}_{I_1I_2}$ and $\hat{H}_{IS}$, they are expressed as: [57]

$$\hat{H}_{I_1I_2}^{(1)} = -\frac{\omega_{DD}}{2}(\theta)\left(3\hat{I}_{1z}\cdot\hat{I}_{2z} - \hat{\mathbf{I}}_1\cdot\hat{\mathbf{I}}_2\right) \tag{36}$$

$$\hat{H}_{IS}^{(1)} = -\omega_{DD}(\theta)\left(\hat{I}_z\cdot\hat{S}_z\right) \tag{37}$$

where $\omega_{DD}(\theta) = d(3\cos^2\theta - 1)$. Particularly in glasses, the distinct environment experienced by system with two like-spins is frequently considered as in as a heteronuclear case. In anisotropic systems, the energy levels of similar spins are perturbed by their local environment,

caused by, for instance, distinct components or orientation from the magnetic shielding PAF. [58] In such materials, the random variations in the orientations of the chemical shift tensors of neighboring spins can create significant differences in Larmor frequency, thereby preventing spin exchange. [58] As we are going to see in the Static Spin Echo Decay experiment, described in Section 4.3, the absence of spin exchange has a central role in the efficiency of this technique used to quantify the homonuclear interaction.

Figure 9 (a) illustrates the energy level diagram for the heteronuclear case, showing the perturbation caused by the operator $\widehat{A}$ of the dipolar Hamiltonian. Due to the energy dependence on the mirror "$\pm (3\cos^2\theta - 1)$" term, the transitions $\Delta M = 1$ will result in two mirrored powdered patterns with axial symmetry (like the axially symmetric shown in Figure 6), as illustrated in Figure 9 (b). [57,58] However, when the heteronuclear dipolar interaction involves N spins in a solid-state structure, a distribution of dipolar coupling constants should be considered, since they depend on the internuclear distances between the spins $\hat{\mathbf{I}}$ and $\hat{\mathbf{S}}$, r – as expressed in equation (34). Figure 10 illustrates the summation from the maximum dipolar coupling constant (when the spins $\hat{\mathbf{I}}$ and $\hat{\mathbf{S}}$ are as close as possible) to an assumed minimum dipolar coupling constant (the case in which spins $\hat{\mathbf{I}}$ and $\hat{\mathbf{S}}$ are very far apart from each other). Finally, the summation indicates that a broad band of several kHz (in a Gaussian function lineshape) is formed because of the distance distribution between the spins.

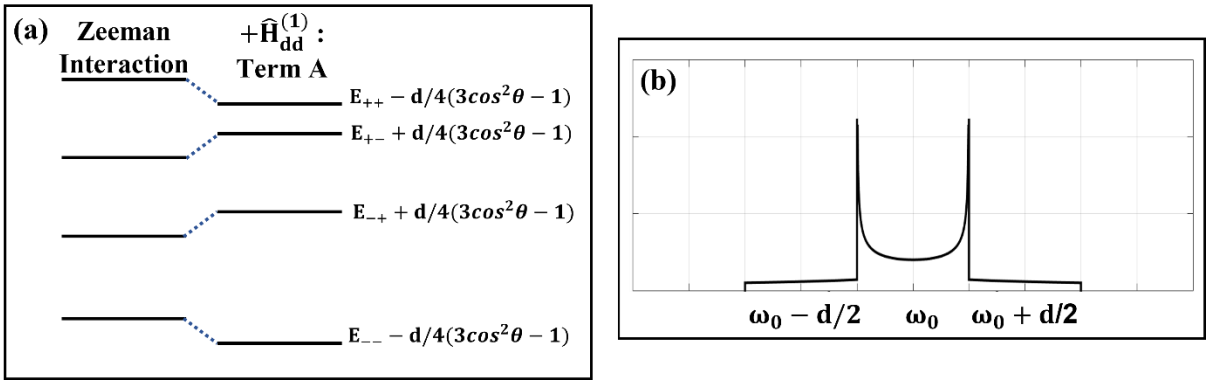

Figure 9 - (a) Energy level splitting for two unlike spins, only with the Zeeman interaction at first, and then with the addition of the term $\widehat{\mathbf{A}}$ of the dipolar interaction within the limit of first-order perturbation theory. (b) The theoretical spectra expected for the spin I in a two-unlike-spin system including the dipolar interaction. This pattern will also be observed (albeit with a wider splitting) for the case of a dominant interaction of two like spins (homonuclear case).

Source: By the author.

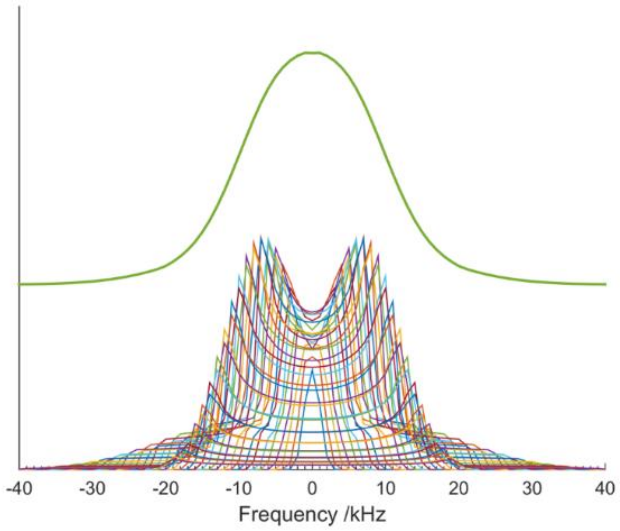

Figure 10 - The broadening of the heteronuclear spectra for the spin I caused by a distribution of dipolar coupling constants in a solid compound. In a multi-spin system, a similar pattern will arise originating from the summation of distinct two-spin interactions.
Source: Simulation done by prof. MARCOS DE OLIVEIRA JR.

A further step to complement the study of a dipolar interaction concerns the interpretation of the broadening caused by these interactions in multi-spin systems. Consider the function f(ω) as the absorption curve for the secular terms of the dipolar interaction in the case of a homo- or heteronuclear Hamiltonian. For either case, the broadening can be characterized by the mean square value of the dipolar field, expressed as the second moment (M_2), which is given in units of squared angular frequency (rad^2s^{-2}) and serves as a measure of the squared average field acting on the spins:[63-64]

$$M_2 = \int (\omega - \omega_0)^2 f(\omega) d\omega \quad (38)$$

Higher order moments could, in principle, be calculated as a contribution to the spectral width in the resonance signal. However, these terms would carry information about the non-secular perturbation terms of the dipolar Hamiltonian, which, as mentioned previously, are negligible in the high field approximation. Van Vleck derived an expression that correlated the second moment with the homo/heteronuclear secular terms, with the second moment proportional to the sum of the inverse sixth powers of all the internuclear distances involved.[63] Considering a spin I_1 interacting with multiple I_2 (similar among themselves and to I_1) or spin I interacting with multiple S (similar among themselves and different from I), Van Vleck's algebraic expression is given by: [58,63-64]

$$M_{2(I_1 I_2)} = \frac{3}{5}\left(\frac{\mu_0}{4\pi}\right)^2 I(I+1)\gamma_I^4 \sum_{I_1 \neq I_2} r_{I_1 I_2}^{-6} \quad (39)$$

$$M_{2(IS)} = \frac{4}{15}\left(\frac{\mu_0}{4\pi}\right)^2 S(S+1)\gamma_I^2\gamma_S^2 \sum_s r_{IS}^{-6} \quad (40)$$

Additionally, we should discriminate between the cases I = ½ and I > ½. For the homonuclear case, experimentally determined values of M_2 can be significantly smaller than their theoretical values, if the nucleus characterized by the spin quantum number I (coupled to S) is quadrupolar (I > ½), and not located at a site of cubic symmetry, as shown by VanderHart *et al.*[65] In the current work, no experiment investigating the homonuclear interaction between quadrupolar nuclei is presented. On the other hand, there are investigations concerning heteronuclear interactions involving a quadrupolar nucleus. The theoretical value of M_2 may be considerably lower than that determined experimentally from Equation (38) because it does not consider terms of second-order quadrupolar perturbation (for more about the quadrupolar interaction, next section 3.2.4).[64] More about the second moment investigation will be discussed in Chapter 4, which includes a discussion on how these values can be extracted experimentally and the calibration procedures to correct for underestimated values.

3.2.4 Quadrupolar interaction

In subsection 3.1.1, it was shown that the nuclei tend to orient themselves in the direction of B_0 due to their magnetic moments. However, the orientation of the nuclei can assume further dependencies when nuclei have spins quantum numbers I > ½. In this case, nuclear atomic charges are distributed non-spherically, and the asymmetry is described by a quantity known as electric quadrupole moment. [57]

The electric quadrupolar interaction is defined as the interaction between the electric quadrupole moments and an electric field gradient (EFG), which arises from charges produced by the spatial electronic distribution around the nucleus. [57] The Hamiltonian of this interaction can be obtained by the expansion of the classical interaction between a charge distribution of the nucleus and an electrostatic potential of the electric cloud. The symmetry of the molecule in which an atom is found, as well as the type of bonds formed by the atom with its neighbors, defines the EFG, which in turn determines the strength of quadrupolar interaction.[57] The interaction is mathematically expressed as:

$$H_Q = \frac{1}{2}\sum_{jk} Q_{jk}V_{jk} \quad (41)$$

where:

$$V_{jk} = \frac{\partial^2 V}{\partial x_j \, \partial x_k} \tag{42}$$

$$Q_{jk} = \int d^3x \, \rho(x) \, x_j x_k \tag{43}$$

and Q_{jk} is the electric quadrupole tensor defined as the integration of the electric nuclear density $\rho(x)$ and vector position x_I, and V_{jk} is the second order rank EFG tensor defined as the second derivative of potential V. [66] The quadrupolar moment is a constant for a given nuclei. Table 3 specifies some characteristic values to the nuclei investigated in the present work.[57]

Table 3 - Nuclear electric quadrupole moments Q.

Isotope	Spin	Quadrupole Moment (10^{-29} m^2)
^{11}B	3/2	0.4
^{23}Na	3/2	1.0
^{27}Al	5/2	1.5

Source: Adapted from DAUER.[57]

To analyze how this interaction impacts the Zeeman energy levels, we employ the Wigner-Eckart theorem that relates the matrix elements of each one of these two symmetric and traceless second order rank tensors (eQ_{jk} and V_{jk})[66] in cartesian space to a dependence in spin. In short, the nuclear quadrupole moment (related with the asymmetric charge distribution) is associated with an I spin and the electric field gradient tensor with a J spin. [64,67] Analogously to a spin-orbit coupling, [67] the influence of this interaction on the Zeeman energy levels can be calculated. Finally, Q_{jk} can be expressed as:

$$\widehat{Q}_{jk} = \frac{eQ}{6I(2I-1)}\left[\frac{3}{2}\left(\hat{I}_j\hat{I}_k + \hat{I}_k\hat{I}_j\right) - \delta_{jk}\hat{\mathbf{I}}^2\right] \tag{44}$$

where, δ_{jk} is the Kronecker delta. So far, the tensor is given in an arbitrary coordinate system.[64,66] The same can be performed for the Electric Field Gradient, but it is important to highlight that, in bulk-matter with diamagnetic properties, EFF is treated classically at the nucleus, so only it is expected values is considered in most of the literatures. [64,66] The tensor V_{jk} can be simplified by choosing an axis system in which the tensor is diagonal, named as principal axis frame (PAF of quadrupolar interaction). In a bulk diamagnetic matter, the tensor V_{jk} obeys Laplace's equation, therefore, it is traceless.[58,64] Following the convention $\left|V_{zz}^{PAF}\right| \geq \left|V_{YY}^{PAF}\right| \geq \left|V_{xx}^{PAF}\right|$, it is possible to define two parameters: [66]

$$\eta_Q = \frac{V_{XX}^{PAF} - V_{YY}^{PAF}}{V_{ZZ}^{PAF}} \tag{45}$$

$$eq = V_{ZZ}^{PAF} \tag{46}$$

where η_Q is the asymmetry parameter of quadrupolar interaction and eq is the magnitude of EFG tensor. Finally, re-writing the Hamiltonian in PAF system, it is found: [57]

$$\hat{H}_{Q-PAF} = \frac{e^2qQ}{4I(2I-1)}\left(3\hat{I}_z^2 - \hat{\mathbf{I}}^2 + \frac{\eta_Q}{2}\left(\hat{I}_x^2 + \hat{I}_y^2\right)\right) \tag{47}$$

The strength of Zeeman interaction is on the order of 10^2 MHz, whereas the strength of the quadrupolar interaction can vary between zero (in the case of cubic local symmetry) and values exceeding the strength of the Zeeman interaction. The case $\hat{H}_Q \ll \hat{H}_z$ is generally dealt with by first or second-order perturbation theory.[57] At the level of first-order perturbation theory the corrections to the energy levels are given by:

$$E_m^{(1)} = E_m^{(0)} + \langle m|\hat{H}_Q|m\rangle \tag{48}$$

where is the unperturbed Zeeman energy $E_m^{(0)} = m\gamma B_0$. At the level of second-order perturbation theory the calculation is done using the expression: [57]

$$E_m^{(2)} = \frac{\sum_{m'}\langle m|\hat{H}_Q|m'\rangle\langle m'|\hat{H}_Q|m\rangle}{E_{m'}^{(0)} - E_m^{(0)}} \tag{49}$$

Like what was done for the other interactions, the Hamiltonian will be rotated to the laboratory frame. Note that, for quadrupolar interaction, using the irreducible tensor formalism is a handier and more concise than explicating all the dependency terms of the same tensor in a particular basis, e.g., it would be laborious explicating the linear, bilinear, and quadratic spin operator, and the angles θ and ϕ of the EFG in the laboratory frame with respect to PAF. Moreover, the irreducible tensor operator formalism will help us with constructing further steps when talking about the pulse sequencies in the next chapter. [66,68]

The Hamiltonians affecting the Zeeman levels in the limit of first and second order perturbation theory can be expressed as:[68]

$$\hat{H}_Q^{(1)} = \frac{1}{3}\nu_Q' \cdot \left[3\hat{I}_z^2 - \hat{\mathbf{I}}^2\right], \tag{50}$$

$$\hat{H}_Q^{(2)} = \frac{\nu_Q^2}{9\nu_0} \cdot \left(2\hat{I}_z\left[2\hat{I}_z^2 - \hat{\mathbf{I}}^2 + \frac{1}{4}\right]\overleftrightarrow{V}_{-1}^{(2)}\overleftrightarrow{V}_1^{(2)} + \hat{I}_z\left[\hat{I}_z^2 - \hat{\mathbf{I}}^2 + \frac{1}{2}\right]\overleftrightarrow{V}_{-2}^{(2)}\overleftrightarrow{V}_2^{(2)}\right) \tag{51}$$

where $\nu_Q' = \frac{\nu_Q}{2}\left(3\cos^2\theta - 1 + \eta_Q\sin^2\theta\cos 2\phi\right)$ is the quadrupolar splitting and $\overleftrightarrow{V}_k^{(2)}$ is the tensor describing the strength and orientation dependence of the quadrupole coupling; it is obtained by rotations of the quadrupole tensor from the PAF to the laboratory reference frame using the spherical angles, θ and ϕ; ω_Q is quadrupolar frequency described as:

$$\nu_Q = \frac{3C_Q}{2S(2S-1)} = \frac{\omega_Q}{2\pi} \tag{52}$$

where:

$$C_Q = \frac{e^2qQ}{h} \tag{53}$$

and C_Q is the nuclear quadrupolar coupling constant, which measures the strength of the interaction in Hz.[68] Figure 11 depicts how Zeman energy levels vary due to the Hamiltonian of the quadrupolar interaction. The central transition (m = $\pm$1/2 → m = $\mp$1/2) remains unaltered under first-order perturbations (no anisotropy); however, this is not the case when second order perturbations are included.[57] In a polycrystalline or a disordered material, with non-zero EFG, powder patterns are observed for the central transitions arising from the anisotropy of the second order quadrupolar term. It is important to observe that the second order perturbative interaction has an inverse dependence on the Larmor frequency (Equation 51). This means that the higher the static field, the better the resolution, although even a high field will not completely remove the anisotropy of the central transition. [69]

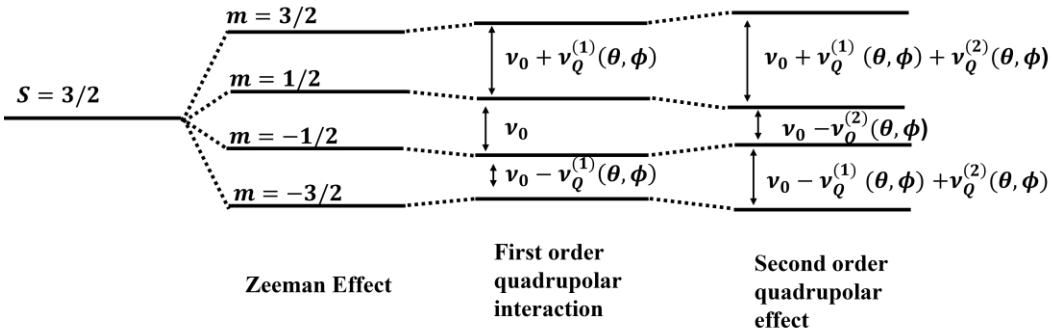

Figure 11 - (a) Splitting of energy levels under the quadrupolar perturbations predicted by first- and second order-order perturbation theory, where θ and ϕ are the polar and azimuthal angles describing the position of B_0 in PAF.

Source: By the author.

In Chapter 4, the consequence of the spectral dispersion on the lineshape of central transition and techniques for increasing the resolution of central-transition spectra for quadrupolar nuclei will be discussed in more detail.

3.3 Instrumentation

This subsection is dedicated to the operational aspects of a spectrometer. This knowledge is crucial to diagnose possible problems that might, for instance, influence the

spectra. Here, it is explained briefly the essential components of the duplexer, transmitter, receiver, and the probe to understand how they operate together.

3.3.1 Introduction

The main requirement for high-resolution NMR spectroscopy is a stable magnetic field, which is usually created by superconductive magnetic solenoids immersed in liquid helium, at 4K, as shown by Figure 12 (a). The liquid helium Dewar flask is enclosed by a vacuum shield, which is then surrounded by a liquid nitrogen reservoir, the latter also thermally insulated by vacuum.[60] A vertically oriented solenoid coil powered by several tens of Amperes creates the magnetic field responsible for the Zeeman effect. Any spatial inhomogeneity of the magnetic field creates a distribution of precession frequencies in the sample, producing a broadening of the NMR signals.[60] Therefore, a group of numerous small coils (shim coils) energized with currents are present to balance out these magnetic field imperfections. [60]

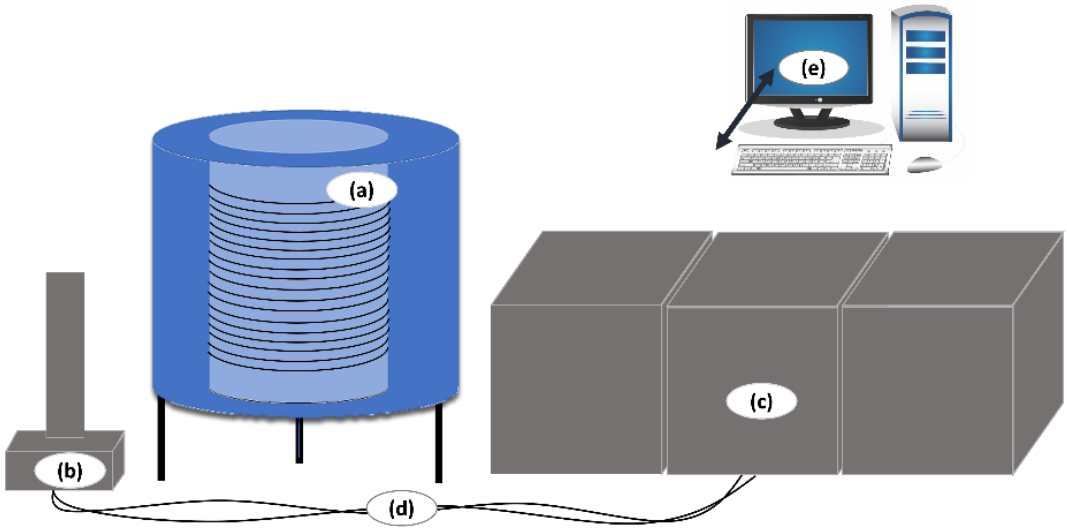

Figure 12 - Key elements of the spectrometer. (a) The supercooled magnetic coil, (b) the probe, (c) the transmitter, the duplexer, the pre-amplifier and, the receiver, (d) The transmission lines and I the computer.
Source: By the author.

The spectrometer component responsible for the signal generation is the probe (Figure 12 (b)), which serves to position the sample within the most highly homogeneous field region, apply the radio waves to the sample and collect the response of the sample.[60] The excitation mode is created in the transmitter, passes though the duplexer, then it is sent to the probe. The response signal produced by the nuclei is collected by the probe and sent to the duplexer, passes

through a pre-amplifier, and finally enters the receiver.[70] Figure 12 (c) illustrates the transmitter, the duplexer, the pre-amplifier, and the receiver.

Since the radio wavelength and the length of the cables are of the same order (~1 to 100 m), the cables act as transmission lines,[71] Figure 12 (d), and the proper choice of their characteristics is crucial for the conduction of the radio waves, minimizing eventual power losses. After digitalization of the receiver signal the data is stored in the computer for further processing.[60]

3.3.2 The duplexer and the transmission lines

Whereas the transmitter is responsible for the creation of pulsed radio waves with amplitudes on the order of kV, the receiver collects the radio waves emitted by the sample with amplitude on the order of μV.[70] The duplexer is the element accountable for the protection of the receiver, so it does not burn out by the high power coming directly from the transmitter. Two types of duplexers are found in NMR spectrometers: the passive one, which uses transmission lines, or active ones, switching the transmission or reception of the signal in an electronic way.[70] Going further in details of duplexer is not in the scope of this work, so the passive duplexer was chosen to illustrate the role of the duplexer in protecting the receiver. The working mechanism is depicted in Figure 13.

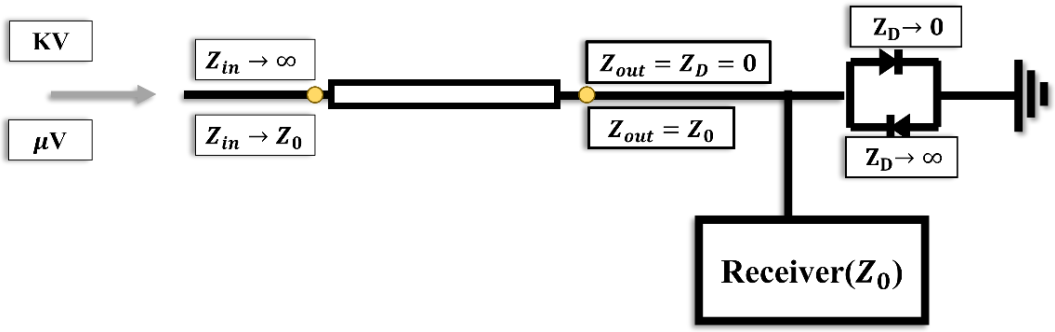

Figure 13 - Duplexer operating mode: High-power radio waves are reflected by the transmission line, whereas the low-power NMR signal is transmitted to the receiver. The boxes above and below the main circuit line correspond, respectively, to the effective impedance at that point of the circuit when high (kV) and low level (μs) power are applied.
Source: By the author.

The role of a passive duplexer is fundamentally based on the properties of the transmission lines, which are elements used to transport electrical current from one point to another.[71] For direct current, or low-frequency AC, electric conduits act as passive elements

with only resistive properties. However, when the wavelength of the excitation approaches the dimension of the conduit, the behavior of waves inside it becomes important; consequently, the voltage and current vary along the length of the conduit.[71] By considering a transmission line with a length corresponding to a multiple of λ/4 (quarter of the conducted wavelength), the input impedance of the transmission line (Z_{in}) will be related with the effective impedance of the components connected to its output (Z_{out}) by the equation:[71]

$$Z_{in} \cdot Z_{out} = Z_0^2 \tag{54}$$

where Z_0 is a characteristic impedance, which is constant, depending solely on the properties of the conduit. The work principle of the passive duplexer is based on the control of the Z_{out} (and consequently Z_{in}). This is done by associating the transmission line with a pair of crossed diodes connecting the λ/4-cable with the ground, as illustrated in Figure 13. When the transmitter conducts high voltage (kV), the crossed diodes ground the circuit ($Z_D = 0$).This causes Z_{out} to be $Z_D = 0$, and Z_{in} to tend to high values at the beginning of the transmission lines.[71] Therefore, the λ/4-cable act as an open circuit, protecting the receiver from the high voltage. Conversely, when low-frequency voltage is coming from the probe, the crossed diodes do not conduct ($Z_D \rightarrow \infty$), resulting Z_{out} being the impedance of the receiver ($Z_{out} = Z_0$).[71] Note that, by choice, the impedance of the receiver is equal to the characteristic impedance of the transmission line, in order to avoid signal reflections in the connections between components. Then, by Equation (54), the transmission line act as a closed circuit with $Z_{in} = Z_0$, matching impedances and conducting the low-voltage amplitude to the receiver.[71]

3.3.3 Transmitter

The transmitter is responsible for delivering the RF to the probe. To perform this task, first the radio wave needs to be synthesized and then shaped into pulses. The phases of the pulses need to be controlled, and, subsequently, the amplitude of the pulses needs to be enhanced by amplification. The whole scheme is summarized in Figure 14, which illustrates a heterodyne transmitter.[70]

To improve performance of the transmitter, it is desirable to select components that are optimized for a narrow frequency window. For instance, some components are constructed with transmission lines, which, as previously explained, have their impedance dependent on the length of the wave conducted.[70] Since the excitation frequencies in NMR cover a wide range, it is necessary for the transmitter to operate at a fixed intermediate frequency (IF) and subsequentially convert it into the desired excitation frequency.

Figure 14 shows the process in detail. Step (1) displays the radio wave synthesizer, which generates waves in a frequency corresponding to the sum of IF with the desired excitation on local frequency LF (typically equal or close to the Larmor Frequency). [70-72] In step (2), the IF wave is synthesized and synchronized with the radio wave generated in step (1). The IF wave is then modulated in amplitude and phase by a pulse generator.[70,72] In most experiments, the pulse phases are controlled and cycled to eliminate artifacts and/or eliminate undesired coherences during the experiment. In step (3), the mixer multiplied the IF pulses generated in (2) with the sum of LF and IF waves.[70,72] As a result, we have a sum of two periodic waves with frequencies corresponding to the addition and subtraction of the input frequencies, resulting in a high frequency (LF + 2IF) and one low frequency (LF + IF - IF = LF). In step (4), the output passes through a low-pass filter to select the radio wave. Finally, the signal is amplified to kV, and is ready to be delivered to the probe to excite the sample. While the sample is relaxing, the sample's magnetization will induce an alternating voltage in the coil of the probe, described by Faraday Law.[70,72] The magnetization is then sent to the receiver.

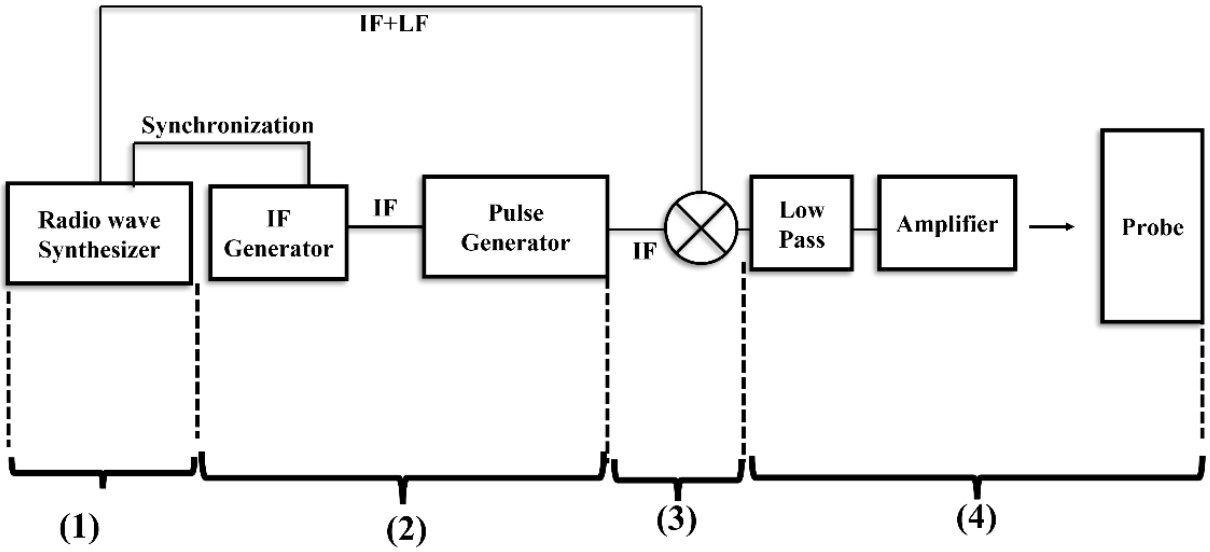

Figure 14 - Transmitter operating mode and its elements. In (1), the radio wave synthesizer; in (2), the wave generator in the frequency range labelled as "intermediate" (intermediate frequency – IF); in (3), pulse generator; in (4), the mixer and in (5), the low pass filter and pre-amplifier.
Source: By the author.

3.3.4 Receiver

As explained in the previous subsection, the Larmor frequencies fall within the 10^2 MHz range, whereas the perturbations interactions occur in the 10^2 kHz range. To focus on latter

range and (equally important) to facilitate digitalization of the emitted radio wave signal, it is desirable to subtract the Larmor frequency from the emitted signal. Figure 15 depicts the heterodyne receiver operating mode, distinguishing the emitted signal as LF + kHz.[70,72]

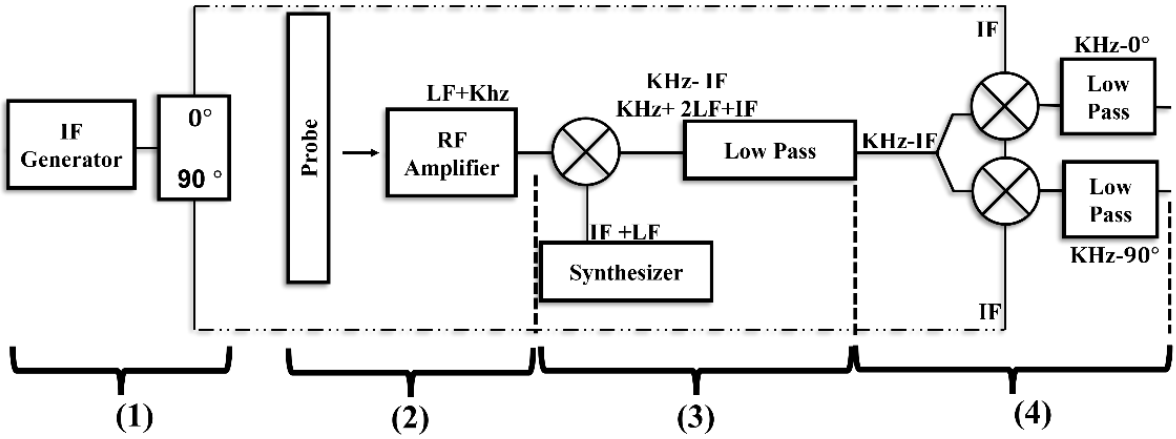

Figure 15 - The receiver operating mode and its elements. In (1), the IF generator; in (2), the probe and the amplifier; in (3), the RF synthesizer, the first mixer and the low-pass filter; in (4), the other two mixers and their respective high-pass filters.
Source: By the author.

Step (1) illustrates the division of the IF wave (same as used in the transmitter) into two 90º-dephased signals. In step (2), the signal exits the probe as a μV signal, and passes through a pre-amplifier. In step (3), the amplified signal (LF + kHz) is mixed with the IF + LF signal produced by the radio wave synthesizer (same as used in the transmitter). Then, the mixer output consists of a high frequency (kHz + 2LF +IF) and a low frequency (k–z - IF) signal, which passes through a low-pass filter to transmit only the k–z - IF low frequency signal.[70,72] In step (4), the output is split for two identical channels, each of which mixed with one of the two 90°-dephased signals from the IF generator (of step (1)).[70,72] After this mixing step, each channel comprises a low frequency (kHz) and a high frequency (k–z - 2IF) wave combination. The kHz component is then selected by a low-pass filter. In the end, two kHz signals dephased by 90°, called phase and quadrature signals result in the Quadrature detection scheme. It allows a differentiation between positive and negative frequency deviations from the excitation frequency.[70,72]

This mixing scheme results in the separation of the Larmor frequency signal from the kHz one. This detection mode is analogous to a direct detection in the rotating frame. Finally, the signal is ready for digitalization and transmission to the controller computer.

3.3.5 The probe

The probe is the unit responsible for irradiating the sample with the RF and for the detection of the response signal.[60] The excitation is performed through a single coil, which creates $\vec{B}_1(t)$ field. To have this system working properly, it is necessary to tune the probe to the transmitter frequency (also known as carrier frequency) and to match the impedance of the probe circuit with the impedance of the adjacent electronic components. Figure 16 (a) illustrates how a LC circuit with two capacitors would allow to tune and to match a single resonance system.[60] The capacitors C_T can be adjusted to have the circuit resonating in the transmitter frequency (tunning), whereas the capacitor C_M could be adjusted to maximize the power transfer (impedance matching). Equation (55) expresses the relevant mathematical relation between the inductance and the tuning capacitance, allowing to optimize the resonance condition.[60,70] Figure 16 (b) illustrates the similar idea but for a double-resonance system using a single coil typical of solid-state probes.[70,73] The system illustrates a circuit which has its sides isolated, either for low frequency wave (right side) or for higher frequency one (left side). The capacitors for matching (C_{MH} and C_{ML}) and for tuning (C_{TH} and C_{TL}) work analogously as in Figure 16 (a). Note that the quarter-wave lambda cable on the lower frequency side grounds the higher frequency wave and works as high impedance cable to the lower frequency one. The opposite is also true: the quarter-wave stub working on higher frequency side closes the circuit to the lower frequency wave and works as high impedance for the higher frequency one.[70,73]

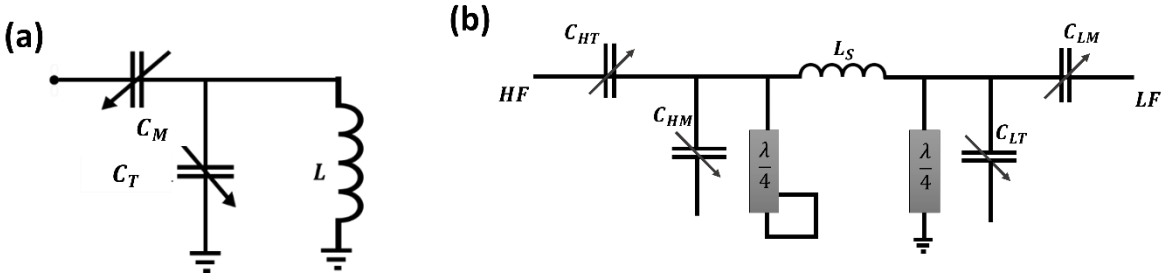

Figure 16: (a) The probe operating mode for a single resonance system; it is made by two capacitors and one inductor. (b) The probe operation mode for double resonance system. In addition to the two tunning and two matching capacitors, there are the two quarter-wave high frequency stubs, which isolate the higher frequency from the lower frequency side and vice-versa.
Source: Adapted from CROSS *et al.* [73]

$$\omega^2 = (LC_T)^{-1} \tag{55}$$

4 ADVANCED NMR TECHNIQUES

This section describes the magic-angle spinning technique along with the six distinct pulse sequences used in the present thesis, showing how each parameter can be extracted from the data. High-resolution techniques used to remove the anisotropies of higher-order perturbative terms are described as well as techniques for examining homo- and heteronuclear dipole-dipole couplings and connectivities.

4.1 Magic Angle Spinning (MAS)

The Magic Angle Spinning experiment has been a key factor responsible for the successful development of solid-state NMR as a structural technique in materials science. It averages out the anisotropy of the magnetic shielding ($\widehat{H}_{CS}$), heteronuclear dipolar ($\widehat{H}_{DD}$) and first-order quadrupolar ($\widehat{H}_{Q}^{(1)}$) interactions. In the current work, MAS also averages out the homonuclear dipolar interactions if stronger couplings (normally involving ^{19}F or ^{1}H in multi-spin systems)† are not present.[58] In the limit of first-order perturbation theory all of the above-mentioned interactions exhibit a dependence on $(3\cos^2\theta - 1)$, as demonstrated by equations (19), (36), (37) and (50). The underlying concept of technique is to rotate the PAF of the interactions and average the orientational dependences of the first-order perturbation terms; that is to say, the technique imposes a coordinate system where the polar and azimuthal angles are time dependent ($\theta = \theta(t)$), such that $\overline{3\cos^2\theta - 1}$ is zero on average, which means $\theta = 57°74'$, known as the *magic angle*.[64]

Figure 17 depicts the principle of the technique. The rotation axis represents the rotor; the green axis denotes the direction of the $\mathbf{B_0}$ static field and, the blue axis the direction of the PAF of a given interaction in a crystallite. These three axes in the spherical system of coordinates conform with the theorem of the sum of the spherical harmonics trigonometric relationship:[74]

$$\cos(\theta) = \cos(\alpha)\cos(\theta_{MA}) + \sin(\alpha)\sin(\theta_{MA})\cos(\omega_R t) \qquad (56)$$

† Homonuclear dipolar couplings involving ^{1}H and ^{19}F are in the range order of 10^2 kHz.[57,58] The magnitude of this interaction causes a large spectral broadening. Consequently, it would be required a large spinning speed to efficiently average out the spectral anisotropy. This is particularly true for systems in which the term $\hat{B}$, Equation (29), of dipolar expansion remains and the flip-flop interaction is present. However, homonuclear couplings involving other nuclei, named X, is relatively smaller due to the factor o $(\gamma_x/\gamma_H)^2$. [57-58]

where θ_{MA} is the angle between the rotation axis and the magnetic field, α is the angle between the rotation axis and the z-axis of the PAF, and the time-dependent argument of the cosine is the phase difference between the projection of the magnetic field and of the z-axis of the crystallite onto the traverse plane.[64]

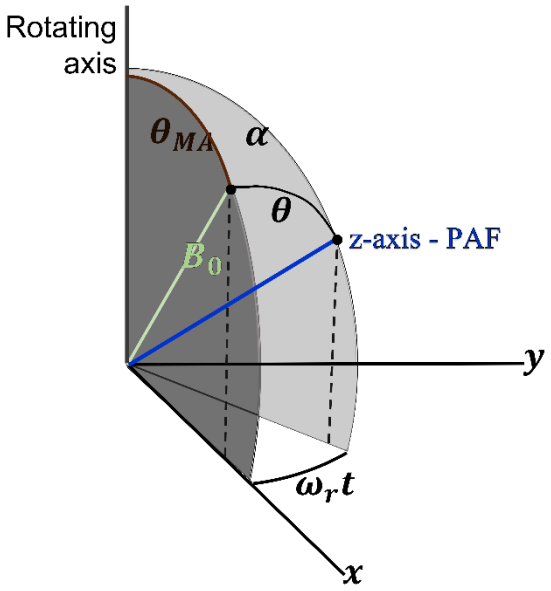

Figure 17 - MAS coordinate system. The cartesian axes represent the rotor frame, the green axis represents the position of the static magnetic field vector, and the blue axis represents the z-axis of a sample crystallite.

Source: By the author.

For a polycrystalline sample, the orientation of θ can take on many possible orientations, which assume a time dependence when the sample is under rotation. Under this scenario, interactions with the angular dependence $3\cos^2\theta - 1$ can be averaged out if θ_{MA} is adjusted to $\theta_{MA} = 57°74'$, as is demonstrated by the equations:[64]

$$\langle 3\cos^2\theta - 1\rangle = (3\cos^2\alpha - 1)(3\cos^2\theta_{MA} - 1)$$
$$(3\cos^2\theta_{MA} - 1) = 0 \rightarrow \theta_{MA} = 57°74' \quad (57)$$

where θ_{MA} is defined as magic angle.[57,64] For the above-mentioned case (first-order perturbative Hamiltonians), Figure 18 illustrates the impact of rotating the sample at distinct spinning speed (ω_r) around the magic angle. In (a) the static broad Gaussian lineshape is observed. In (b) the case $\omega_R < |H_{per}|$ is found. Here, the time evolution of the magnetization from a perturbative interaction has not decayed in a period of the rotation. Then, the lineshape of the perturbative term, of the first-order perturbative interactions, can be expressed as:

$$\hat{H}_{aniso}(t) = \omega(\theta(t)) \cdot f(\hat{I}, \hat{S}, \hat{I} \cdot \hat{S})$$
$$\omega(\theta(t)) \sim \omega_{aniso}(3\cos^2\theta - 1 + \eta\sin^2\theta\cos 2\phi) \quad (58)$$

(η = 0 in the dipolar case), can be written as a sum of sigmoidal functions with arguments proportional to $\omega_r t$, as expressed below:

$$\omega(t) = g_1 \cos(\omega_r t + \psi_1) + g_2 \cos(2\omega_r t + \psi_2) \quad (59)$$

where g_1 and g_2 are dependent on the PAF of the interaction analysed.[57] During the rotation, the modulation of the perturbative interaction with this angular dependence produces echoes, in the time domain, at the end of each rotor cycle while there is still magnetization signal present. The Fourier transformation (FT) of the decay with its rotational echoes results in the spectra with spinning side bands (SSB) appearing at integer multiples of the spinning frequency.[57] In that case the components of the anisotropic tensor can be determined by an intensity analysis of the spinning sidebands. In (c) the case $\omega_R > |H_{per}|$ the anisotropy is completely removed.[57]

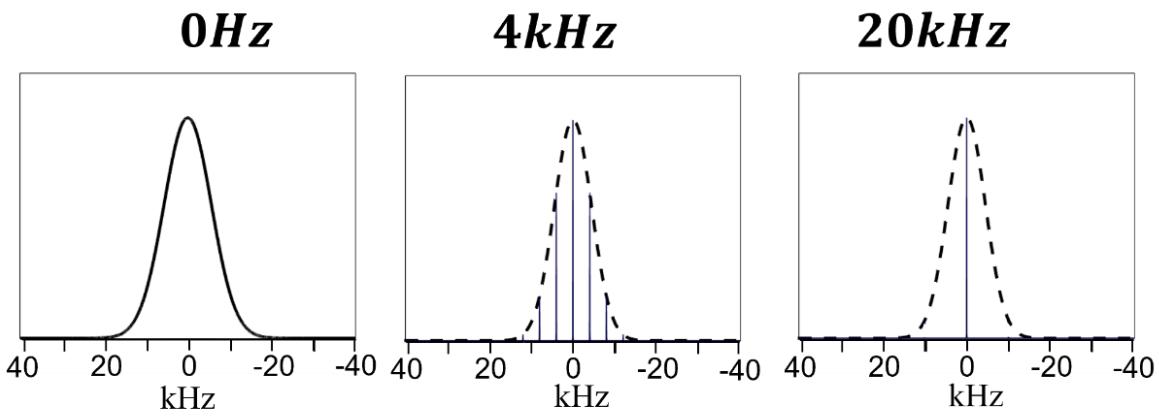

Figure 18 - Effect of the rotation about the magic angle for different rotation speeds upon the lineshape of a nucleus with a static line width of ca. 10 kHz.
Source: By the author.

4.1.1 Additional features of quadrupolar nuclei

Although the first order quadrupolar interaction can be averaged out by MAS, the same conclusions do not hold for the second-order expansion, which has a significant impact on the lineshapes of the central transition. As discussed in the previous chapter, the second-order term perturbs the central transition, which under fast spinning, can be described as:

$$\nu_{\frac{m}{2},-\frac{m}{2}} = \sum_{l=0,2,4} \nu_Q^{(l)}(\theta,\phi) \cdot C_l(I,m) \cdot P_l(\cos\theta_{MA}) \quad (60)$$

where $\nu_Q^{(l)}$ is the term with angular dependence on (θ,ϕ) describing the location of the PAF within the spinning frame; $C_l(I,m)$ are rank zero, two and four tensors dependent on the spin operators and, $P_l(\cos\theta)$ is the order l Legendre polynomial, which represents the spatial part of

the second order quadrupolar Hamiltonian under fast spinning.[68,75] Note that orientational dependence of the second Legendre polynomial can be averaged out by MAS, but the fourth Legendre polynomial, which describes the spatial dependence of the second-order perturbation cannot. Figure 19 shows that there is no simultaneous root for Legendre polynomials of orders two and four. Therefore, with only the MAS technique it is not possible to eliminate the spectral dispersion caused by the angular dependence of the second-order quadrupole perturbation. Some other techniques can be used with this porpoise, such as Double Rotation (DOR), Double Angle Rotation (DAR) and Multiple Quantum -MAS (MQMAS), last of which will be discussed in Subsection 4.6 and used along this work.[76-80]

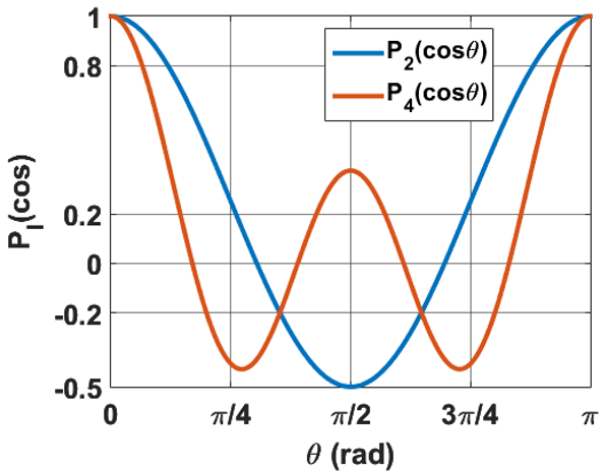

Figure 19 - Dependence of the Legendre polynomials $P_l(\cos\theta)$ on θ for l = 2 and 4.
Source: By the author.

One additional aspect to consider is the excitation behavior of quadrupolar nuclei. The nutation behavior of a quadrupolar nucleus depends on the relation of the nutation frequency to the quadrupolar frequency. Equation (9), discussed in Section 3.1.2, introduces the idea of the nutation frequency (γB_1). By measuring the intensity of the observable magnetization as a function of the duration of the radiofrequency pulse, a periodic modulation can be observed, known as nutation curve. The nutation behavior of spin-½ nucleus is a sinusoidal function with the detected signal oscillating at the frequency $\omega_{nut} = \gamma B_1$, as qualitatively illustrated in Table 2. On the other hand, the behavior of quadrupolar nuclei must be studied under specific conditions. As the central transition depends on $\nu_Q^{(1)}(\theta, \phi)$ (Equation (60)), the angular pairs (θ, ϕ) show different responses in a distinct regime of excitation, leading to a spectral distortion in the lineshape.

Figure 20 illustrates two regimes of nutation curves for a quadrupolar nucleus. The first regime, depicted in blue, is when $\gamma B_1 \gg \omega_Q$, representing the non-selective excitation or a *hard pulse* profile of excitation. In this case, a wide spectral window is excited, meaning that all the spins behave uniformly, in other words, their evolution under the Hamiltonian shows the same behavior. Under a weak quadrupolar interaction, the nutation curve behaves similarly to that of a spin-½ with $\omega_{nut} = \gamma B_1$. In the solid-state, this regime is found in cubic symmetries where the electric field gradient is close to–zero - thus, the small quadrupolar interaction conforms to the regime: $\gamma B_1 \gg \omega_Q$.[68] Liquid samples also follow this relationship in general. Depicted in red, the second regime happens when $\gamma B_1 \ll \omega_Q$ and represents the totally selective excitation, also called *soft-pulse* excitation profile. In this case, only the central-transition (½ ↔ $^{-}$½) is excited due to the narrow excitation frequency band limited by the nutation frequency γB_1. The modulation in this scenario is given by $\omega_{nut} = \left(I + \frac{1}{2}\right)\gamma B_1$.[68] In the current thesis, the frequency ω_Q was frequently found in the range of some units of MHz, whereas the γB_1 is in the range of 100 kHz (for hard pulses). Clearly, this excitation is found to be in the intermediate regime of those discussed above. This profile of excitation is hard to predict and affects the signal intensity, compromising the quantitative character of the experiment. To avoid this, the yellow line in Figure 20 illustrates for spin-3/2 nuclei that for $\sin(x) \sim x$, both nutation curves are similar, meaning that in this approximation, the quantitative character of selective excitation is not lost for the non-selective excitation.[68] For a generical spin I, the yellow line is analytically expressed by: [68,81]

$$\omega_{rf}\tau_{pulse} \leq \frac{\pi}{6\left(I + \frac{1}{2}\right)} \tag{61}$$

which corresponds to:

$$\tau_{pulse} \leq \frac{t_{\frac{\pi}{2}}^{selective}}{3\left(I + \frac{1}{2}\right)} \tag{62}$$

This condition will be applied to every quadrupolar nucleus of spin-I as we will see in the experimental section.

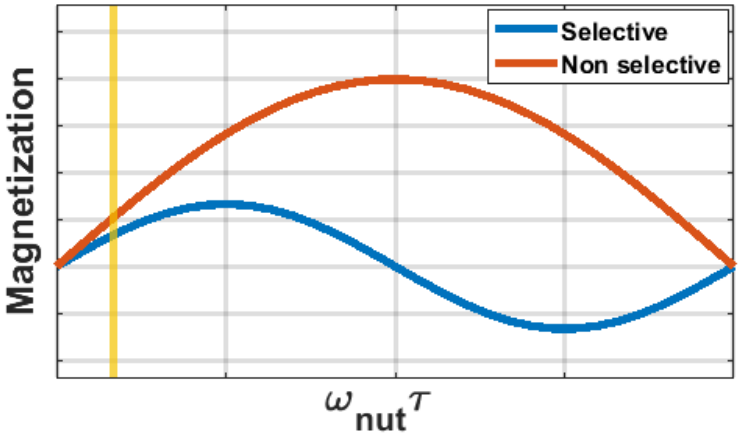

Figure 20 - Comparison between selective and non-selective nutation curves for I=3/2.
Source: By the author.

Finally, Figure 21 illustrates the systematic broadening observed in a system with C_Q = 5 MHz and δ_{iso} = 0. Figure 21(a), from the bottom to the top: spectra in yellow illustrate a static quadrupolar pattern; purple spectra illustrate a second order quadrupolar interaction being partially averaged by MAS; blue spectra show the sum of a continuous distribution of C_Q values, varying from 4.0 MHz to 5.8 MHz. These components are illustrated in Figure 21 (b). Finally, in Figure 21 (a), the red spectra show the lineshape formed by a continuous distribution of C_Q. This lineshape with the appearance of a tail-like shape towards lower frequencies is used for modeling the response of disordered material as glasses, known as *Czjzek model*.[82] It will be used for simulating some quadrupolar nucleus spectra, as further described in Chapter 5 and 6.

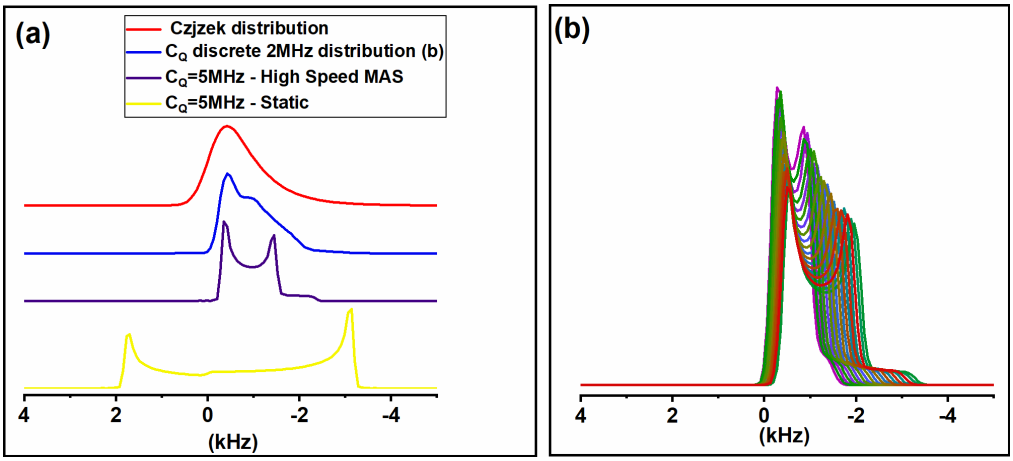

Figure 21 - (a) From the bottom to the top: in yellow, static S = 5/2 quadrupolar lineshape pattern with δ_{iso} = 0 ppm, C_Q = 5 MHz and η = 0 at; in purple, same parameters as those in (a) but under infinite spinning speed at the magic angle; in blue, the sum of equally weighted discrete C_Q contributions from 4.0 MHz to 5.8 MHz (shown in figure (b)); and, in red, the Czjzek distribution with EFG distribution width of 1 MHz, corresponding to $< |C_Q| > = 2$ MHz.
Source: By the author.

4.2 1D Refocused Incredible Natural Abundance DoublE QUAntum Transfer Experiment (Refocused-INADEQUATE)

The refocused-INADEQUATE experiment is a pulse sequence based on the excitation of double-quantum coherences using the J-coupling interaction.[83] The technique was developed to detect ^{13}C-^{13}C linkages present in natural abundance and has a wide range of applications today. In the present study, this pulse sequence is used for spectral editing of unresolved MAS-NMR spectra of spin-½ ^{31}P nuclei, involved in P-O-P linkages.

Figure 22 displays the pulse sequence at the top, and the coherence path at the bottom. The sequence of pulses basically records the amplitude modulation of the double quantum coherence selected by appropriate phase cycling as t_1 is incremented.[84] The corresponding signals, acquired in the detection period t_2, are stored, resulting in a two-dimensional dataset. Following double Fourier Transformation, a correlation plot is generated between the two frequency domains of resulting two dimensional datasets.[84] In the one-dimensional version of this experiment (Refocused-INADEQUATE), t_1 is fixed at short values, meaning that double quantum coherence is converted to single quantum and recorded, but not its modulation.[84] In this application, the 1D refocused INADEQUATE can selectively detect species coupled by $^2J(^{31}P$-$^{31}P)$ coupling, because only in that case a double quantum coherence can be excited owing to the J-coupling between the two nuclei involved. The major advantage of the 1D technique is to provide crucial information with a truly less time-consuming pulse sequence. Multiple couplings can, however, not be revealed by this sequence.

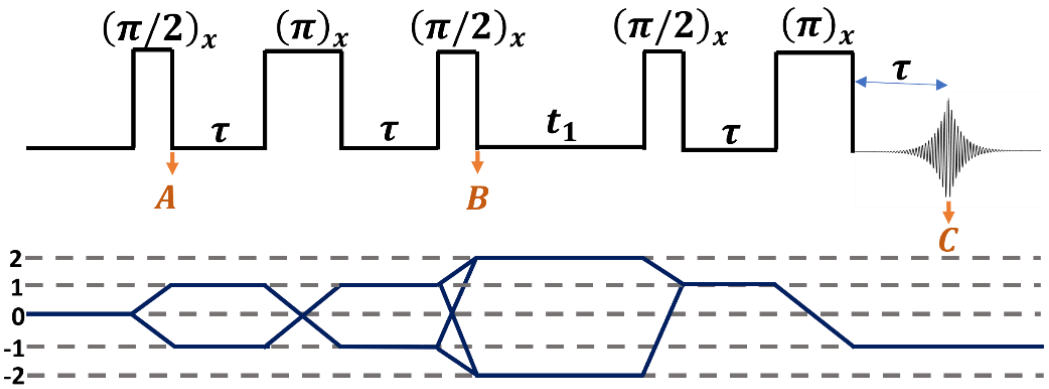

Figure 22 - Pulse sequence scheme on the top. On the bottom, the coherence pathway for Refocused INADEQUATE.

Source: By the author.

The beginning of the pulse sequence (point A) starts with the transverse magnetization, described by the operators $\hat{I}_{1y} + \hat{I}_{2y}$. It is followed by a $\tau - \pi_x - \tau$ sandwich, which removes the chemical shift effect and creates an anti-phase spin alignment if τ is chosen to be 1/4J. The magnetization is converted to a double quantum excitation via the third pulse. At the point B, for a two spin-½ system, this coherence oscillates according to: [59,84]

$$\left(\hat{I}_{1z} + \hat{I}_{2z}\right)\cos(2\pi J\tau) + 2\left(\hat{I}_{1x}I_{2y} + \hat{I}_{1y}I_{2x}\right)\sin(2\pi J\tau) \qquad (63)$$

From this equation, it is defined $\tau = 1/(4J)$, resulting in a magnetization proportional to $2\left(\hat{I}_{1x}\hat{I}_{2y} + \hat{I}_{1y}\hat{I}_{2x}\right)$. Theoretically, the coherence includes the term $\left(\hat{I}_1^+\hat{I}_2^+ + \hat{I}_1^-\hat{I}_2^-\right)$, representing double quantum (DQ) excitation. However, in practice, the signal detected usually also contains single-quantum coherence, due to the hardly predictable scalar interaction distribution of coupling constants. [59,84] This contribution is eliminated by appropriate phase cycling. The distribution of $^2J(^{31}P\text{-}^{31}P)$ coupling constants in a glass is challenging to determine. The interaction is dependent on the nature of the bonding electrons and their electron density at the nuclei; thus, it can vary with the angle and lengths of the P-O-P linkages. Studies in the literature have shown that ^2J ($^{31}P\text{-}^{31}P$) is on the order of 20-30Hz.[85,86] During t_1 evolution, the dominant single-quantum coherences are removed though proper phase cycling. The final $\tau - \pi_x - \tau$ creates an in-phase J-signal while converting the DQ back into the observable coherence with $p = -1$ and refocused at point C.[59,64]

Finally, to run a 1D refocused INADEQUATE experiment, t_1 is set as the initial value in a 2D experiment, around 5-10μs. Another fixed parameter is the evolution time between echoes ($\tau = 1/4J$), whose optimal value is around 8.3-12.5ms (J = 20-30Hz).[85-86] However, spin-spin relaxation may impose a limit of the evolution times that can be used, without suffering significant signal decay. To mitigate this undesired effect in the experiments, shorter evolution times (corresponding to longer J-coupling) are often used, such as $\tau = 1/6J$, $\tau = 1/8J$, etc.[85]

It is worth noting that INADEQUATE is not a quantitative experiment. It is hard to know whether a phosphorus site with no contribution to the final spectrum has indeed no P-O-P linkages or whether the missing signal results only from short T_2 relaxation time, leading to complete spin-spin relaxation before the signal being acquired. Moreover, the distributions of J-couplings may affect the lineshapes, emphasizing contributions that are better matched to the evolution time chosen than others. Finally, in the refocused INADEQUATE spectra, it is important to note that the spinning side bands are often observed with severe distortions and not purely absorptive in-phase signal, which may arise from imperfect rotor synchronization.

However, this is not a problem if the samples are spun sufficiently fast to minimize the spinning sidebands. [85-86]

4.3 Static Spin Echo Decay (Static SED)

The Spin Echo decay (SED) method, also known as Hahn Echo (HE) decay, is a pulse sequence that can be represented by $\left(\frac{\pi}{2}\right)_x - \tau - \pi_x - \tau$, as shown in Figure 23.

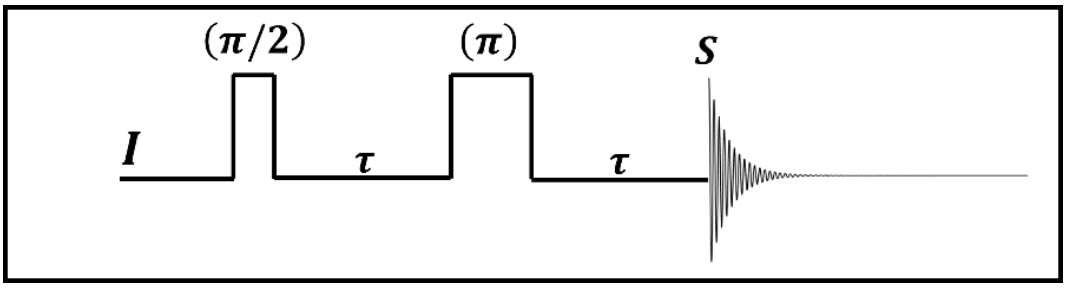

Figure 23 - Static Spin Echo Decay pulse sequence. The total evolution time 2τ increases.
Source: By the author.

In this sequence, the mixing time τ is incremented systematically. The HE sequence is a widely used and straightforward pulse sequence to eliminate the effect of inhomogeneity equivalent to the spread in temporally constant precession frequencies, such as occurring under the effect of internal interactions whose Hamiltonians scale linearly with the operator I_z. [58] For instance, that is the case of chemical shifts which have offset frequencies caused by distinct chemical environments.

In the present study, this versatile technique is being used to obtain information about dipole-dipole interactions measured under static conditions for spin-½ nuclei. There, the interactions as magnetic shielding and heteronuclear dipolar interaction are being refocused due to their linear dependence on $\hat{I}_z$. Therefore, in this case (spin-½ nuclei), the decay of static echo will depend solely on the homonuclear interaction, as the bilinear dependence on $\hat{I}_z$ (in terms of the product $\hat{I}_{z1}\hat{I}_{z2}$) will affect both spins, preventing the interaction to be refocused. As the contribution from evolution of the spin system due to homonuclear interaction is not refocused, the signal diminishes with increasing evolution time 2τ.[26,87]

The magnetization accumulates a phase dependent on the dipolar frequency during the evolution of the time 2τ. "Accumulate a phase" means a diminution of echo intensity at the end the time 2τ.[68] The resulting signal diminution can be analyzed in terms of a sum of pairwise

dipolar interactions with powder averaging. For multiple spin interactions the refocused magnetization intensity I as a function of 2τ is given by:[26,87]

$$I = I_0 \cdot \exp\left[-\frac{(2\tau)^2 M_2}{2}\right] \quad (64)$$

where I_0 is the initial intensity obtained by back-extrapolation in $t_1 = 0$. Note that the second moment M_2 can be experimentally extracted from such experiments. It is important to note that, even dealing with like spins, in the case of highly disordered system, the flip-flop interaction was assumed as negligible. If there is an exchange between two nuclei, the line broadening would not be caused only by the homonuclear $\hat{I}_z\hat{S}_z$ operator ($\widehat{A}$ term) but also the by flip-flop ($\widehat{B}$) term, respectively, in Equations (28) and (29). This assumption is quite realistic, particularly talking about disordered material with wide frequency dispersion, where the random variations in the mutual orientations of the chemical shift tensors of two neighboring like spins are likely to create a sufficient difference in Larmor frequency forestalling the spin exchange.[26]

4.4 Rotational Echo Double Resonance (REDOR)

REDOR is a double resonance MAS-NMR technique that enables a quantitative determination of average distances between two different nuclear isotopes through the measurement of heteronuclear dipolar interaction strengths.[51] The sequence consists of a combination of a rotor-synchronized spin-echo applied to the observe-nuclei spin I, which average out the magnetic shielding and homonuclear interaction through MAS, while recoupling the heteronuclear dipolar interaction through the application of a π-pulse applied on spin S.[88,89] Figure 24 shows the overall design of the REDOR pulse sequence.[51]

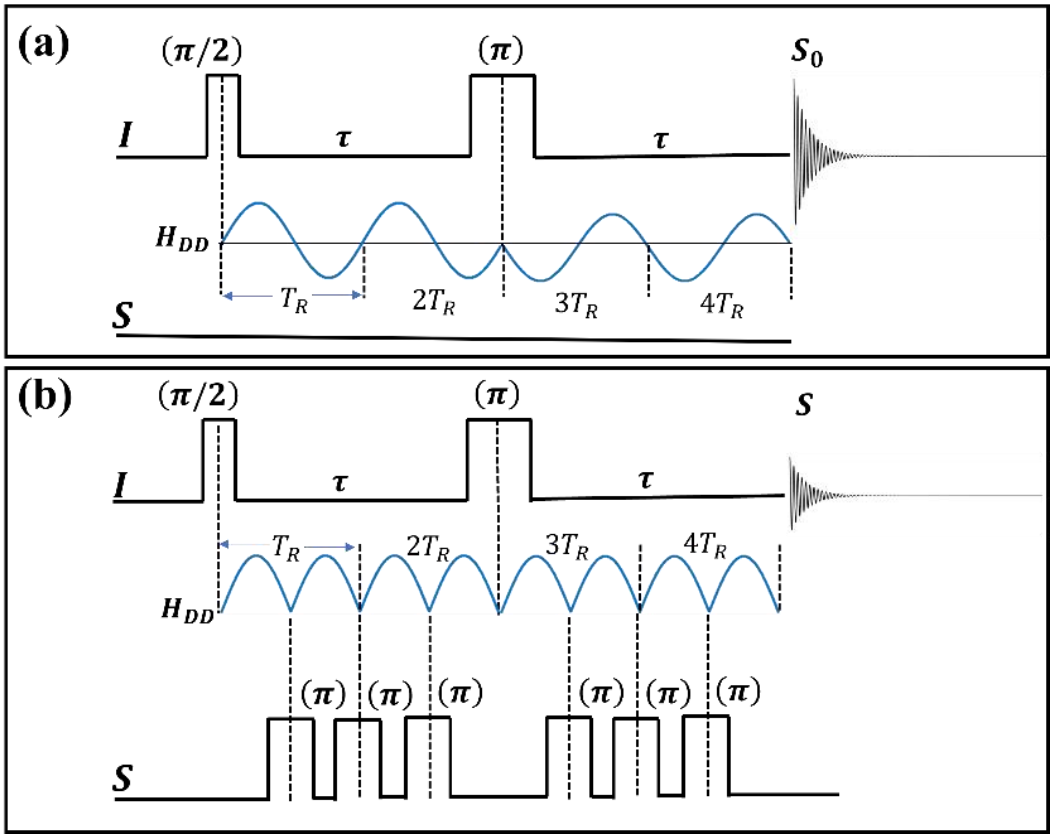

Figure 24 - REDOR pulse sequence. In (a) there is refocusing of the dephasing from magnetic shielding and heteronuclear dipole interactions. In (b) there is refocusing only from magnetic shielding.
Source: By the author.

In Figure 24 (a), the pulse sequence is a synchronized spin-echo experiment ($\frac{\pi}{2} - \tau - \pi - \tau$ as discussed in Section 3.2). Synchronized MAS conditions mean that the time τ is an integer multiple of the MAS rotation period, or $\tau = NT_r$. This condition is adopted to ensure that the I nuclei are in the same local field and interact with the same S spins while revolving in the same space trajectory until they refocus. In Figure 24 (b), the pulse sequence from the part (a) is repeated, but with the addition of π-pulses applied on the spin I each half period of the rotor. This inverts the sign of the heteronuclear dipole Hamiltonian and results in the bilinear interaction between coupled S-I spins (Equation (37)) not being refocused.[89] The total signal loss due to the heteronuclear contribution is given by the difference between the signals without (S_0) and with (S) heteronuclear recoupling normalized by the S_0 signal:

$$\frac{\Delta S}{S_0} = \frac{S_0 - S}{S_0} \tag{65}$$

Equations (37) and (59) express the average of the dipole-dipole coupling under MAS. Like the case of the static SED, the magnetization evolving in REDOR experiments accumulates a phase dependent on the heteronuclear dipolar frequency during the evolution time 2τ, which implies in the diminished refocused signal intensity. The recoupling pulse

prevents the refocusing of heteronuclear interaction, leading to the propagation of phase that is observed as a decreased signal intensity when the observed coherence is acquired. Finally for calculating the signal intensity, a powder average over all the orientation(α, β values) considering the random orientations of the PAF in the rotor axis system must be performed. The magnetization intensity function over time is given by:[88–90]

$$S \sim \int_0^{\pi} \int_0^{2\pi} d\alpha d\beta \sin\beta \cdot \cos(\langle \omega_{DD} \rangle N T_r) \quad (66)$$

In the regime where the dephasing caused by the dipolar coupling is still small, $0 \leq \langle \omega_{DD} \rangle N T_r \leq 0.2$, Bertmer *et al.* showed that it is possible to study internuclear distances without previous knowledge of the local geometry. Approximating the coupling dephasing to short evolution times, one can find through the cosine expansion:[90]

$$\frac{\Delta S}{S_0} = \frac{S_0 - S}{S_0} = f \frac{4}{3\pi^2} (N T_r)^2 M_2. \quad (67)$$

Here, M_2 is the dipolar second moment specifying the average mean square dipolar coupling strength of a multispin system as defined in (40). In the same study it is demonstrated that this approximation tends to underestimate the M_2 values slightly. Aside from this, effects arising from the chemical shift anisotropy as well as experimental imperfections (pulse missed, finite pulse length in relation to the rotor period, etc.) accumulate in a systematic diminution of the difference signal. To address this issue, a multiplicative factor f was introduced into the Equation (67) as a calibration factor. This dipole coupling adjustment factor is determined by analyzing a model compound for which the theoretical value of M_2 is known from the crystal structure. The experimental value obtained from the REDOR experiment is compared to the theoretical M_2 value calculated by the Van Vleck equation, equation (40). The standard compounds used in this study and their theoretical M_2 values are listed Table 4.[91-93]

Table 4 - Theoretical M_2 values predicted by the Van Vleck equation (40) for crystalline compounds.

Sample	S-nucleus (I-nucleus)	Theoretical M_2 (10^6 rad^2/s^2)
$(AlPO_3)_3$	^{27}Al(^{31}P)	7.7
$Na_5B_2P_3O_{13}$	^{23}Na(^{31}P)	6.2(Na1), 3.7(Na2), 3.7(Na3), 5.8(Na4), 5.9(Na5)

Source: By the author.

4.5 Rotational Echo Adiabatic Passage Double Resonance (REAPOR)

As for REDOR, REAPDOR is a double resonance technique that allows the investigation of heteronuclear dipolar coupling between S and I spins by manipulation of the

states of both spins.[94] The REAPDOR technique is used when a quadrupolar nucleus S is coupled to the observed spin I. As discussed in the section on quadrupolar nuclei excitation, the condition $\gamma B_1 \ll \omega_Q$ is the often observed when exciting quadrupolar nuclei of a polycrystalline material. Therefore, a π-pulse used in the REDOR sequence would excite only a small fraction of nuclei, resulting in an inefficient method of dipolar recoupling.[94]

As expressed by Equations (50), (59) and (**60**) the quadrupolar splitting of a single crystallite assumes different values during the rotation period under MAS and, it might take on the value zero twice or four times during a single period of rotation. When an excitation is on while a crystallite is passing through the zero-crossing, it might either induce or avoid an energy level crossing corresponding to the "sudden" and "adiabatic" regimes, respectively. [89,95]

Figure 25 illustrates the adiabatic regime case.[51,96] Far from zero crossing, the radiofrequency has no greater influence on the energy levels. When γB_1 is much greater than ω_Q (close to zero-crossing), the RF perturbs the eigenstates of the system, causing the spins to briefly exist in a mixed state. Afterwards, the spin eigenstates interconvert, as well as their populations.[96] This is called an adiabatic passage. In order of the zero-crossing to be considered an adiabatic passage, it must meet the following condition:[96]

$$\alpha = \frac{\nu_1^2}{\nu_Q \nu_R} > 1 \qquad (68)$$

Note that if the RF is continuously kept on, the quadrupolar nucleus with half-integer spin would pass through the second zero-crossing and due to the second interconversion, no net change takes place. To ensure the maximal occurrence of an even number of zero-crossings, the optimal pulse length needs to be calculated. As reported in the literature, this length is $\tau = T_r/3$.[89,94–96]

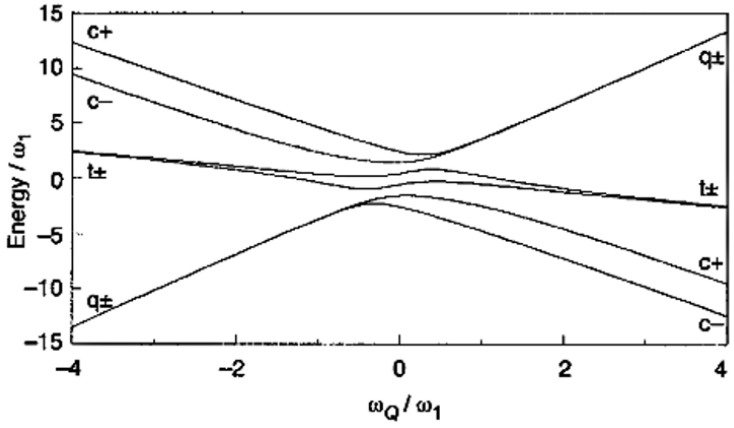

Figure 25 - The eigenenergy of a spin S = 5/2 passing through a zero-crossing along the period of a rotor under an adiabatic regime.

Source: ASHBROOK; DUER.[96]

Finally, Figure 26 illustrates the REAPDOR pulse sequence.[51] In (a) similarly to the REDOR manipulation of the magnetization, the π-pulses are responsible for refocusing the dephasing caused by magnetic shielding and heteronuclear dipolar interaction in a spin S = ½. Again, the signal S_0 is more intense due to the refocusing of the interactions. In (b) the same pulses are applied to spin S = ½, while a continuous wave (cw) excitation (γB_1) sweeps the transition frequency of the non-observed I nuclei.[51] If this radio wave is applied for at least of $T_R/3$, it affects the first zero-crossing, where pure states do no longer exist, but only the coexistence of mixed states. During this time span there is a population transfer between the levels, making the recoupling of the dipolar interaction between S and I more effective and, therefore, successfully re-introducing the heteronuclear interaction into the MAS Hamiltonian.[57,89] As expressed in Equation (65), the signal loss is given by the difference with and without dephasing normalized by the full signal, $\Delta S/S_0$.

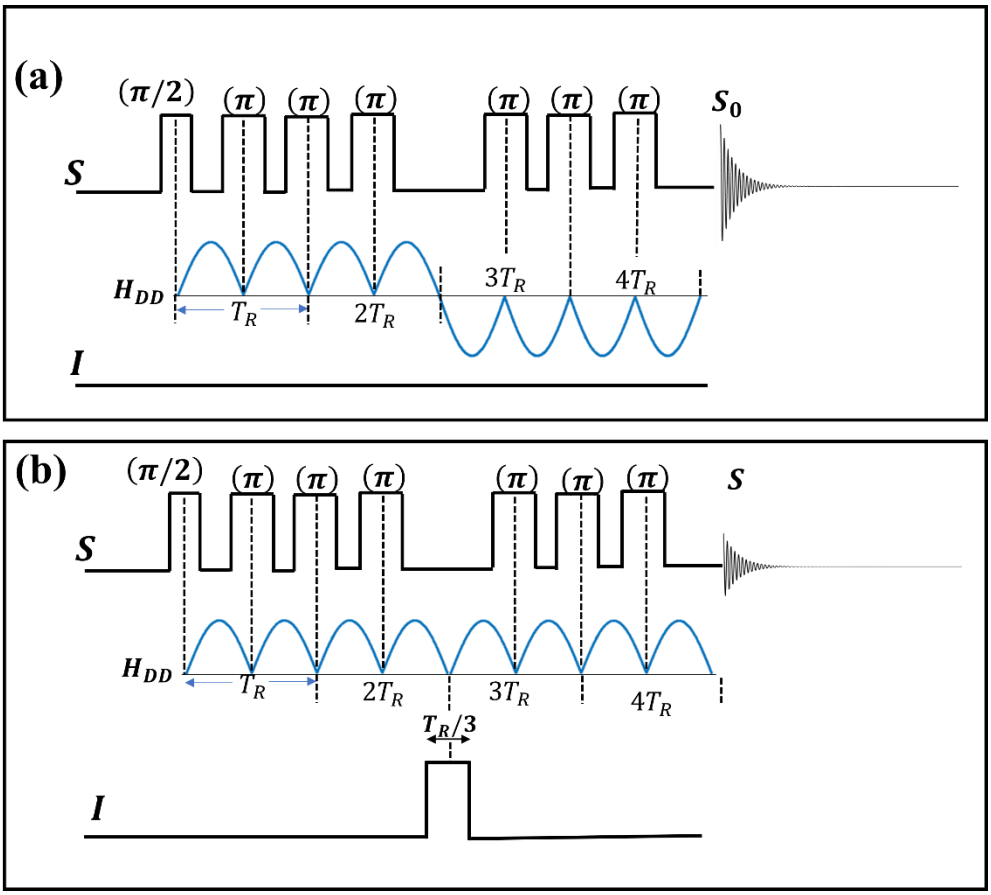

Figure 26 - REAPDOR pulse sequence. In (a) there is refocusing of the dephasing from magnetic shielding and heteronuclear dipole interactions. In (b) there is refocusing only from magnetic shielding.
Source: By the author.

It is important to observe that, as well as REAPDOR experiment, Transfer Population Double Resonance (TRAPDOR) technique is an alternative to recouple dipolar interactions of

quadrupolar nuclei that does not present an ultra-wide band.[89] However, TRAPDOR had fallen in disuse due to a strong dependence between the dephasing evolution curve and parameters as quadrupolar coupling, asymmetry parameter and relative orientation between quadrupolar and dipolar tensor,[97-98] as evidenced by Kalwei and Koller.[99] READOR experiment, on the other hand, shows a relatively weak dependence on these parameters,[97-98] therefore it provides a more independent dephasing curve that can be simulated without complicated simulations.[89]

4.6 Multiple Quantum Magic Angle Spinning (MQMAS)

As mentioned in Subsection 4.1.1, some techniques, such as Double Rotation (DOR), Double Angle Rotation (DAR) and Multiple Quantum -MAS (MQMAS), can be used to acquire high resolution of nuclei under second-order quadrupolar interaction.[76-80] DOR and DAR achieve the high resolution through mechanical rotations, which demands a sophisticate probe engineering and several limitations.[75] MQMAS, on the other hand shows a big advantage of manipulating the spin coherence under regular MAS in order to average the broadening coming from second order quadrupolar interaction.[79-80]

MQMAS is a 2D experiment designed to resolve the anisotropy in the spectra of quadrupolar nuclei whose Zeeman energy levels are perturbed by the quadrupolar interaction to an extent requiring second-order perturbation theory for the theoretical treatment, as described in subsection 3.2.4.[79-80]

Figure 27 displays the z-filtered Triple-Quantum Magic Angle Spinning (TQMAS) pulse sequence at the top and the coherence path below.[50,68] Although the same approach can be applied for higher multiple-quantum excitation, only triple-quantum (TQ or 3Q) spectroscopy was applied in this work. The pulse p_1 is a hard pulse designed to the convert the magnetization into TQ coherence, the harder the pulse, the more efficient the conversion. During t_1, the TQ coherence evolves freely, then the pulse p_2 converts it back to zero quantum coherence. Unwanted coherences are eliminated by suitable phase cycling. Finally, a soft $\pi/2$-pulse selectively excites only the central transition to the observable magnetization, and during the detection period t_2, the signal is acquired while the echo of the magnetization is refocused.[79,80] The correlation of the single- and triple-quantum coherences eliminates the anisotropies caused by first- and second order quadrupolar perturbations in a 2D MQMAS spectra. Under MAS, the second rank order of quadrupolar interaction is averaged out, while the fourth rank order is eliminated by Fourier Transforming the amplitude modulation during t_1 time evolutions. [68,75,79-81]

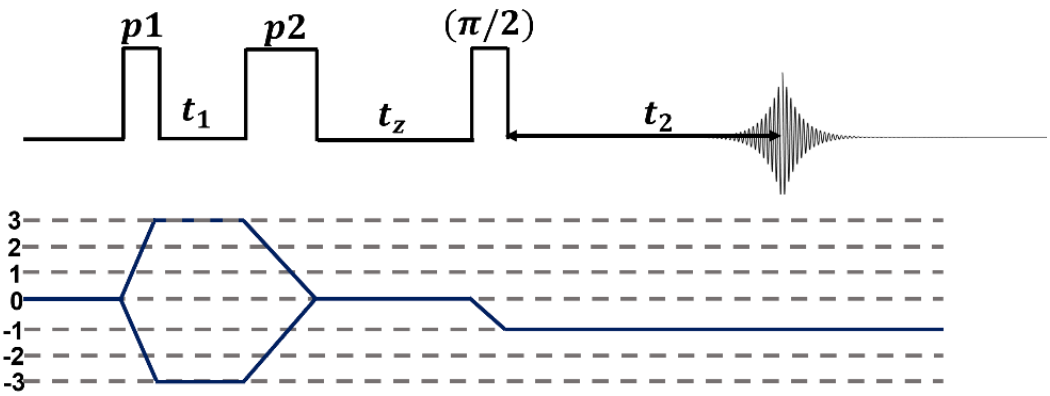

Figure 27 - Schematics of the pulse sequence used in z-filter TQMAS or 3QMAS technique: p1 and p2 are, respectively, the excitation and reconversion pulses, and the third pulse (π/2) is the soft pulse, used to convert the magnetization evolved to the observable coherence.
Source: By the author.

To demonstrate the echo, equation (60) can be expanded under the MAS conditions. Note that the total phase accumulated during the TQMAS experiment should be zero in order to average out the fourth rank tensor.[75]

$$\Delta\phi = (\nu_{3/2,-3/2})t_1 + (\nu_{1/2,-1/2})t_2 = 0 \tag{69}$$

As $\nu_Q^{(4)}(\theta,\phi)$ is independent on the transition, and $P_2(\cos\theta_{MA}) = 0$, the echo condition is expressed as:[75]

$$t_2^{echo} = \left|\frac{C_4(I,3)}{C_4(I,1)}\right| t_1 \tag{70}$$

where $C_4(I,m)$is defined by Equation (60). However, due to the proportionality of the two axes, it is necessary to perform a linear transformation on the tilted axis, so that it appears perpendicular to the first. This is known as the "shearing" transformation, which allows the visualization of a high-resolution spectrum along two perpendicular axes.[75] The first of them displays the Fourier transform of magnetization detected along t_2, which represents the MAS detection, and is referred to as the direct dimension, f_2; the second of them displays the Fourier transform of the isotropic evolution along t_1, which represents the isotropic spectrum, and is referred to as the indirect dimension, f_1.

By analyzing the center of gravity of the spectra in both dimensions, sheared δ_{F1} and δ_{F2}, two parameters can be extracted: the isotropic chemical shift (δ_{iso}) and the second order quadrupolar effect (P_Q or SOQE), as shown above: [100]

$$\delta_{iso} = \frac{17}{27}\delta_{F_1} + \frac{10}{27}\delta_{F_2} \tag{71}$$

$$P_Q = \sqrt{\left(\delta_{iso} - \delta_{F_2}\right)\nu_0^2\left(\frac{10}{3}\right)\left(\frac{(2I)^2(2I-1)^2}{I(I+1)-\frac{3}{4}}\right)10^{-6}} \quad (72)$$

where P_Q is given by: [68]

$$P_Q = C_Q\left(1+\frac{\eta^2}{3}\right)^{\frac{1}{2}} \quad (73)$$

It is important to note that the efficiency of TQMAS is strongly dependent upon the ratio of the nuclear electric quadrupolar interaction to the RF strength (ν_Q/ν_1). For nuclei with large average C_Q, the efficiency of the TQMAS might be low. Nevertheless, as discussed in the Results Chapter, significant constraints can still be obtained for modeling the glass structure.[101]

5 EXPERIMENTAL DETAILS

In this chapter the experimental conditions used to perform the experiments are described, as well as the sample fabrication methods. Bellow, Figure 28 illustrates the quaternary phase diagram comparing the compositional region of NAPS and SPAN glasses.

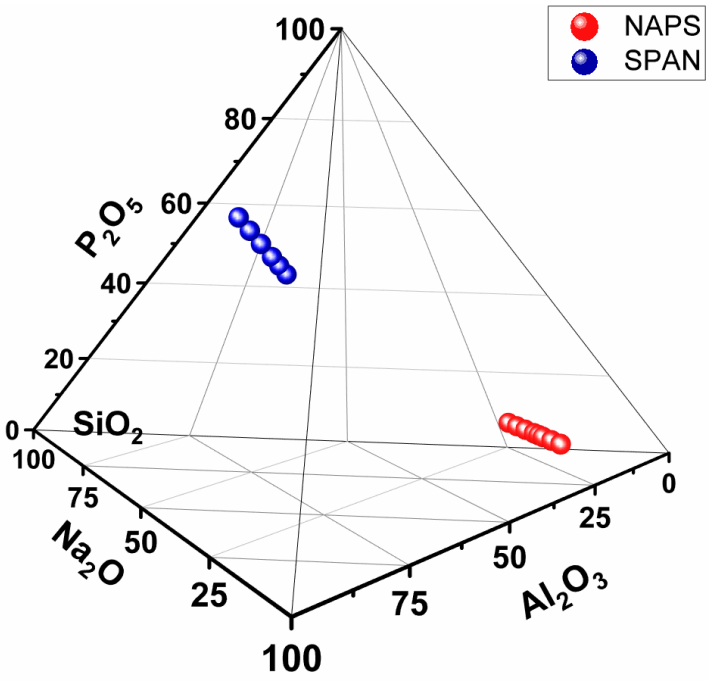

Figure 28 - Quaternary phase diagram of the sodium phosphoaluminosilicate glasses under study in the current thesis.

Source: By the author.

The experiments were recorded on Agilent DD2 and Bruker Avance Neo 600 spectrometers, operating with magnets of flux densities of 5.7 (240 MHz) and 14.1 T (600 MHz), respectively. Both machines were equipped with MAS probes. The chemical shifts are reported relative to liquid TMS, aqueous solution of 1M $Al(NO_3)_3$, 0.1M NaCl, 85% H_3PO_4, and BF_3Et_2O solution for ^{29}Si, ^{27}Al, ^{23}Na, ^{31}P and ^{11}B respectively. In the latter three cases, secondary references of AlF_3 (-16 ppm), NaCl (7.2 ppm), and BPO_4 (-29.3 and -3.5 ppm for ^{31}P and ^{11}B, respectively) were used.

Double resonance REDOR and REAPDOR experiments were performed in a 2.5 mm probe using the Bruker Avance Neo 600 equipment. TQMAS spectra were obtained in the same spectrometer with either a 2.5- or 1.3-mm probe. As illustrated in Figure 21, ^{23}Na and ^{27}Al MAS-central transition spectra exhibit quadrupolar patterns with a broad distribution of

quadrupolar coupling constants. They were analyzed with the Czjzek model implemented within the DMfit and Ssnake data processing and simulation programs.[82,102,103]

5.1 NAPS glasses

Corning Incorporated collaborators prepared the glasses with a composition of $70.00SiO_2 – 7.50P_2O_5 – (22.50\text{-}x)Al_2O_3 – xNa_2O$, $(2.50 \leq x \leq 17.50)$. The starting materials used were SiO_2, Al_2O_3, $Al(PO_3)_3$ and Na_2CO_3, which were ball-milled and melted in a 650cc Pt crucible at 1650°C for 24 hours. The resulting melts were quenched onto a steel plate and subsequently annealed at 750°C for 1 hour and then cooled to room temperature at furnace rate.

For single-pulse experiments, the parameters are expressed in Table 5. Table 5 also lists the experimental conditions of Spin Echo Decay on ^{31}P, which were measured with 4.0 mm probe. The spectra of ^{27}Al and ^{23}Na were obtained using 2.5 mm probes, and the spectra of ^{29}Si and ^{31}P spectra were, respectively, collected with a 7.5- and a 4.0 mm probe. For quadrupolar nuclei, a tip angle of less than or equal to 30º was used in the excitation, while, for spin-½ nuclei, the tip angle is 90º.

Table 5 - Frequency of Larmor ($\boldsymbol{\nu_0}$), time of pulse (t_p), relaxation delay (D1), rotation frequency ($\boldsymbol{\nu_R}$) and number of scans (NS). (*) For samples x = 17.50 and x = 15.00.

Nucleus	ν_0 / MHz	t_p / µs	D1 / s	ν_R/ kHz	NS
^{31}P	98.1	5.3 -One Pulse	420, 16*	8	46
		4.1/8.2 -SED	110, 4*	-	16
^{23}Na	158.8	0.7 (30º)	1.0	20	4000
^{27}Al	156.4	0.375(25º)	1.0	25	4000
^{29}Si	48.2	8.8	600	5	52

Source: By the author.

The optimizations were often performed using the initial saturation of the magnetization.[59] By using multiples pulses with distinct phases and short relaxation delay between them, the magnetization is fully destroyed. The objective of this pulse sequence is to start at the same point of built magnetization. For instance, in T_1 measurements (Figure A1 - Appendix A) and in the nutation curve behavior (data not shown), the saturation of the signal guarantees that, in a signal vs. time experiment, the intensities collected from the bulk magnetization are acquired in the same built-magnetization point. Therefore, the intensities in the signal vs. time experiment are comparable one to each other. Also, the pre-saturation is implemented at the beginning of REDOR, REAPDOR and MQMAS pulse sequence.

For $^{23}Na(^{31}P)$ REDOR experiments, the power used when irradiating the nuclei corresponded to a nutation frequency of (a) 62.5 kHz for ^{23}Na nuclei in NaCl and (b) 125 kHz for ^{31}P using the x = 17.50 glass as a calibration sample. This sample was used because of its short relaxation time (T_1 = 6s; Figure A1 - Appendix A). For $^{27}Al(^{31}P)$ REDOR experiments, the nutation frequencies measured were (a) 58 kHz for ^{27}Al in AlF_3 and (b) 156 kHz measured also on the x = 17.50 glass sample. The other parameters are listed below in Table 6.

Table 6 - For $^{23}Na(^{31}P)$ and $^{27}Al(^{31}P)$ REDOR experiments, the table specifies the parameters used in the pulse sequence. To run these experiments, a 2.5 mm probe was used.

	$^{23}Na(^{31}P)$ REDOR	$^{27}Al(^{31}P)$ REDOR
MAS speed (kHz)	10	15
$^{23}Na/^{27}Al$ exciting pulse length (μs)	2.2	1.7
$^{23}Na/^{27}Al$ refocusing pulse length (μs)	4.8	3.4
^{31}P recoupling pulse length (μs)	4.0	3.2
D1(s)	0.3	1

Source: By the author.

The parameters used in the REAPDOR experiments are listed in Table 7. Additionally, for $^{31}P(^{23}Na)$ REAPDOR, the power used in the irradiation of the nuclei showed a nutation frequency of (a) 132 kHz for ^{31}P and (b) 100 kHz for ^{23}Na in NaCl. For $^{31}P(^{27}Al)$ REAPDOR, the nutation frequencies assumed the values of 156 kHz for ^{31}P (sample x = 17.50) and 58 kHz for ^{27}Al using AlF_3.

Table 7 - For $^{23}Na(^{31}P)$ and $^{27}Al(^{31}P)$ REAPDOR experiments, the table specifies the parameters used in the pulse sequence. To run these experiments, a probe 2.5 mm was used. (*) Conditions used for the samples x = 15.00 and x = 17.50.

	$^{31}P(^{23}Na)$ REAPDOR	$^{31}P(^{27}Al)$ REAPDOR
MAS speed (kHz)	15	15
^{31}P exciting pulse length (μs)	1.9	1.6
^{31}P refocusing pulse length (μs)	3.8	3.2
$^{23}Na/^{27}Al$ adiabatic pulse length (μs)	22.2	22.2
D1(s)	200/5*	200/5*

Source: By the author.

The TQMAS experiments of ^{23}Na and ^{27}Al were acquired with the 1.3 mm or 2.5 mm probes, respectively. The excitation /conversion /soft pulses used for ^{23}Na and ^{27}Al, respectively, were 3 μs/ 1 μs/ 19 μs and 8.1 μs/ 2.1 μs/ 17 μs with a spinning speed of 20 kHz and 25 kHz. The power used to excite/convert the magnetization corresponded to a nutation frequency of 192 kHz for NaCl and of 58 kHz for AlF_3.

For the INADEQUATE experiment, the J-evolution time used between the pulses was $\tau = 6.25$ms, which would correspond $\tau = 1/8J_{P\text{-}P}$. Decreasing the time between pulses below the theoretically optimal value of $\tau = 1/4J_{P\text{-}P}$ is a strategy used to reduce coherence loss due to spin-spin relaxation.[85]

5.2 SPAN glasses

Nippon Electric Glass Co. collaborators produced the glasses with composition $xSiO_2 – (59\text{-}x)P_2O_5 – 13Al_2O_3 – 28Na_2O$, $(0 \leq x \leq 13)$ using standard melt-cooling.[104] The starting materials, SiO_2, $Al(PO_3)_3$, $(NaPO_3)$, Na_3PO_4, were melted in a Pt crucible at 1150^{o}C for 2h. The resulting melts were rapidly quenched by casting them into graphite molds. A relatively large block (400g) of these samples were fabricated to evaluate their optical properties. Since phosphate glasses normally do exhibit low-crack resistance and low heat conductivity, these glasses are very fragile and prone to cracking.[105] Consistently, deep cracks appeared in just a short amount of time after the samples had been fabricated, caused by the large temperature distribution within the blocks. To mitigate this effect, the samples were submitted to a second heating treatment to minimize the internal stress: these samples were re-heated until T_g + 100 ^{o}C and uniformly cooled down. This empirical procedure shows a satisfactory result, attenuating the internal stress of the structure. It is fundamental to highlight that no signal of crystallization was observed after the second heat-treatment, except for the sample x = 13. For this sample experiments were conducted on purely quenched sample, and no second heating was performed.

The parameters are listed in Table 8 for the single pulse experiments, and for Spin Echo Decay on ^{31}P, which were measured with a 3.2 mm probe. The spectra of ^{27}Al and ^{23}Na were obtained using 2.5 mm probes, and the spectra of ^{29}Si and ^{31}P spectra were collected with a 7.5- and 3.2-mm probe respectively. For quadrupolar nuclei the tip angle was less than or equal to 30^o and under the power used to obtain the single-pulse spectra, the nutation frequency of NaCl was 47 kHz and AlF_3 was 46 kHz. For spin-1/2 nuclei the tip angle is 90^o.[104]

Table 8 - Frequency of Larmor (ν_0), time of pulse (t_p), relaxation delay (D1), rotation frequency (ν_R) and number of scans (NS). (*) For samples x = 13.

Nucleus	ν_0 / MHz	t_p / µs	D1 / s	ν_R/ kHz	NS
^{31}P	98.1	2.4 -One Pulse	80	8	80
		2.4 /4.8 -SED	110	-	16
^{23}Na	158.8	0.3	0.5	20	5000
^{27}Al	156.4	0.2	0.02	25	80000
^{29}Si	48.2	5.5/6.2*	600/1000*	5	400/140*

Source: LOGRADO *et al.* [81]

For $^{23}Na(^{31}P)$ REDOR, the power used when irradiating the nuclei corresponded to a nutation frequency of (a) 63 kHz for ^{23}Na nuclei in NaCl and (b) 132 kHz for ^{31}P using $Na_5B_2P_3O_{13}$ as a sample. For the $^{27}Al(^{31}P)$ REDOR experiment, the nutation frequencies measured were (a) 63 kHz for ^{27}Al in AlF_3 and (b) 151 kHz measured with $Al(PO_3)_3$. The other parameters are listed below in Table 10.[104]

Table 9 - For $^{23}Na(^{31}P)$ and $^{27}Al(^{31}P)$ REDOR experiments, the table specifies the parameters used in the pulse sequence. To run these experiments, a 2.5 mm probe was used.

	$^{23}Na(^{31}P)$ REDOR	$^{27}Al(^{31}P)$ REDOR
MAS speed (kHz)	10	10
^{23}Na exciting pulse length (µs)	2.2	2.0
^{23}Na refocusing pulse length (µs)	4.5	6.0
^{31}P recoupling pulse length (µs)	3.8	3.3
D1(s)	1	0.2

Source: By the author.

The parameters used in the REAPDOR experiments are listed in Table 10. Additionally, for $^{31}P(^{23}Na)$ REAPDOR, the power used in the irradiation of the nuclei showed a nutation frequency of (a) 132 kHz for ^{31}P (measured with $Na_5B_2P_3O_{13}$) and (b) 100 kHz for ^{23}Na in NaCl. For $^{31}P(^{27}Al)$ REAPDOR, the nutation frequency assumed the values of 156 kHz for ^{31}P (sample $Al(PO_3)_3$) and 58 kHz for ^{27}Al using AlF_3.[104]

Table 10 - For $^{23}Na(^{31}P)$ and $^{27}Al(^{31}P)$ REAPDOR experiments, the table specifies the parameters used in the pulse sequence. To run these experiments, a 2.5 mm probe was used.

	$^{31}P(^{23}Na)$ REAPDOR	$^{31}P(^{27}Al)$ REAPDOR
MAS speed (kHz)	10	10
^{31}P exciting pulse length (µs)	1.9	1.6
^{31}P refocusing pulse length (µs)	3.8	3.2
^{23}Na adiabatic pulse length (µs)	33.3	33.3
D1(s)	80	80

Source: By the author.

The TQMAS experiments of ^{27}Al were acquired with the 2.5 mm probe. The excitation/ conversion/ soft pulses used for ^{27}Al were 3.8 μs/ 1.3 μs/ 14 μs with a spinning speed of 25 kHz. The power used to excite/convert the pulses corresponded to a nutation frequency of 64 kHz for AlF_3.[104] For the INADEQUATE experiment the time used between the pulses was τ = 8.33 ms, which would correspond to $1/8J_{P\text{-}P}$.

5.3 Cold-pressurized borosilicate glasses

The samples $20Na_2O - xB_2O_3 - (80\text{-}x)SiO_2$ glasses (x = 10, 20, 30) were prepared by standard melt-cooling by Nippon Electric Glass Co. and details of the fabrication are reported by Kato *et al.*[8] In order to pressurize the samples, they were processed to cylindrical samples with ~3 mm in diameter and ~3 mm height. The 6-8 type double-stage compression method was used to compress these samples with a 3000-ton hydraulic press apparatus (Orange-3000, Sumitomo Heavy Industries, Ltd., Japan). Octahedral pressure transmitting medium, which is semi-sintered (Mg, Co), was compressed with 8 cubic anvils made of tungsten carbide with 4 mm truncated edge length (TEL). The samples were subject to a 7-hour compression up to 25 GPa, followed by one hour hold, and a subsequent 7-hour decompression. The whole process was performed at room temperature. Upon recovery from the pressurization apparatus, the samples were light purplish-colored, indicating the presence of some impurities of unknown origin. As explained in the Result section, the high pressurized samples were annealed to track the recoverability of the structure of unpressurized samples. The annealing of the samples was performed in a DSC machine in an attempt to also trace possible calorimetric events (other than the relaxation of glass structure) that could be correlated with the dark color of the samples. After annealing, the sample recovers the expected white color for the powdered glasses. No additional peak was observed in this heat treatment as illustrated by Figure A2 - Appendix A. Still regarding the color of the samples, some studies on hot pressurized ceramics describes changes in their color due to change in the oxidation number of some elements.[106-107] However, not yet in the literature this phenomenon had been observed for cold-pressurized glasses. Although, in this study, the change in the color of the glasses during the densification process was not credited to a specific reason, the researchers in this work believe that the change of color might have occurred during the densification process, and it is unrelated with contaminations.

The parameters for the NMR measurements are listed in Table 11 for the single pulse experiments. The spectra of ^{11}B were obtained using 7.5 mm and 4.0 mm probes at 5.7 T and 2.5 mm at 14.1 T. The spectra of ^{23}Na were collected with 7.5- and 2.5-mm probes, respectively in low- and high-field, and finally ^{29}Si spectra were collected with a 7.5 mm and a 4.0 mm probe only in low field. The nutation frequency of ^{23}Na for NaCl was 47 kHz and AlF_3 was 46 kHz. For spin-1/2 nuclei the tip angle is 90º. All the measurements conducted in the 7.5 mm probes were done on the solid-piece samples without further grinding. This was done to examine whether crushing the samples could induce some structural changes. No such change was observed within the limits of experimental error.

Table 11 - Typical measurement conditions used for the glasses under study: resonance frequency ν_0, excitation pulse length t_p, relaxation delay D1, MAS spinning frequency ν_R - the values between brackets represents the frequency interval in which each spectrum was acquired, number of scans NS.

Nucleus	Pulse Sequence	Rotor Diameter	ν_0 /MHz	t_p /µs	D1 /s	ν_R/kHz	NS
^{11}B	MAS – Single Pulse	2.5	192.68	0.6 (30º)	1.0	15.0	2000
	MAS – Single Pulse	4.0	77.77	0.7 (30º)	2.0	8.0	2000
	MAS – Single Pulse	7.5	77.77	1.35 (30º)	2.0	[5.3, 6]	1200
	Static Hahn Echo	7.5	77.77	1.35/2.70 (30º/60º)			2000
^{23}Na	MAS – Single Pulse	2.5	156.51	0.68	1	20	3000
	Static Hahn Echo	7.5	64.12	2.0/4.0 (30º/60º)	1	5	3400
^{29}Si	MAS – Single Pulse	4.0	48.16	4.80 (90º)	1400	5	64
	MAS – Single Pulse	7.5	48.16	8.80 (90º)	1400	[4.5,5]	64

Source: By the author.

The TQMAS experiments of ^{11}B were acquired with the 2.5 mm probe. The excitation/ conversion/ soft pulses used for ^{11}B were 5.3 µs/ 1.9 µs/ 19 µs with a spinning speed of 25 kHz. The power used to excite/convert the pulses corresponds to a nutation frequency of 100 kHz for BPO_4.

6 RESULTS

As mentioned in the Chapter two (Section 2.2), the structural characterization of the glasses will be based on the following nomenclatures: network former units (NFUs) are denoted with the symbol $X^{(n)}$, indicating an atom X linked to 'n' oxygen atoms, which are bridging it to other NFUs of either the same or a different kind. This nomenclature is further expanded to show the connections with other network formers by subscripts (i.e., $P^{(4)}_{2P,2Al}$). Furthermore, the terminology 'X(n)' is used, where 'n' is a Roman numeral indicating the coordination number. Additionally, the acronyms BO and NBO are used to refer to 'bridging oxygen' and 'non-bridging oxygen', respectively.

6.1 NAPS glass system

As mentioned in the Introduction, the investigations on structure-property relation on quaternary Na_2O-containing Al_2O_3-P_2O_5-SiO_2 optical fibers shows to be poorly known. The addition of sodium in the system conspicuously affects the coefficient of thermal expansion by depolymerizing the network.[18, 21,22] Consistently, the glass samples labelled as NAPS, with nominal composition of $x Na_2O - (22.50 - x)Al_2O_3 - 7.50\ P_2O_5 - 70.00\ SiO_2$ in molar percentage, shows this effect. Figure 29 shows the coefficient of thermal expansion (in blue) increases as a function of the increase in sodium oxide concentration. This result is expected and represents the network being globally depolymerized by sodium ions. Figure 29 also shows characteristic glass temperatures: in yellow, strain temperature; in orange, annealing temperature and in brown softening temperature, which, respectively corresponds to a viscosity of $10^{7.6}$, $10^{13.4}$ and $10^{14.6}$ Pa-s.[108] It is observed that the characteristic glass temperatures seems show distinct regimes: (I) the temperatures decreases monotonically and slightly with the initial addition of sodium; (II) the temperature for the samples x = 10.00, 11.25 and 12.50 shows a dramatic decrease and they surround the minimum, finally regime (III) shows that the temperature increases again for $x \geq 15.00$. These distinct regimes pose the question whether the network structure could help to rationalize these thermodynamic properties.

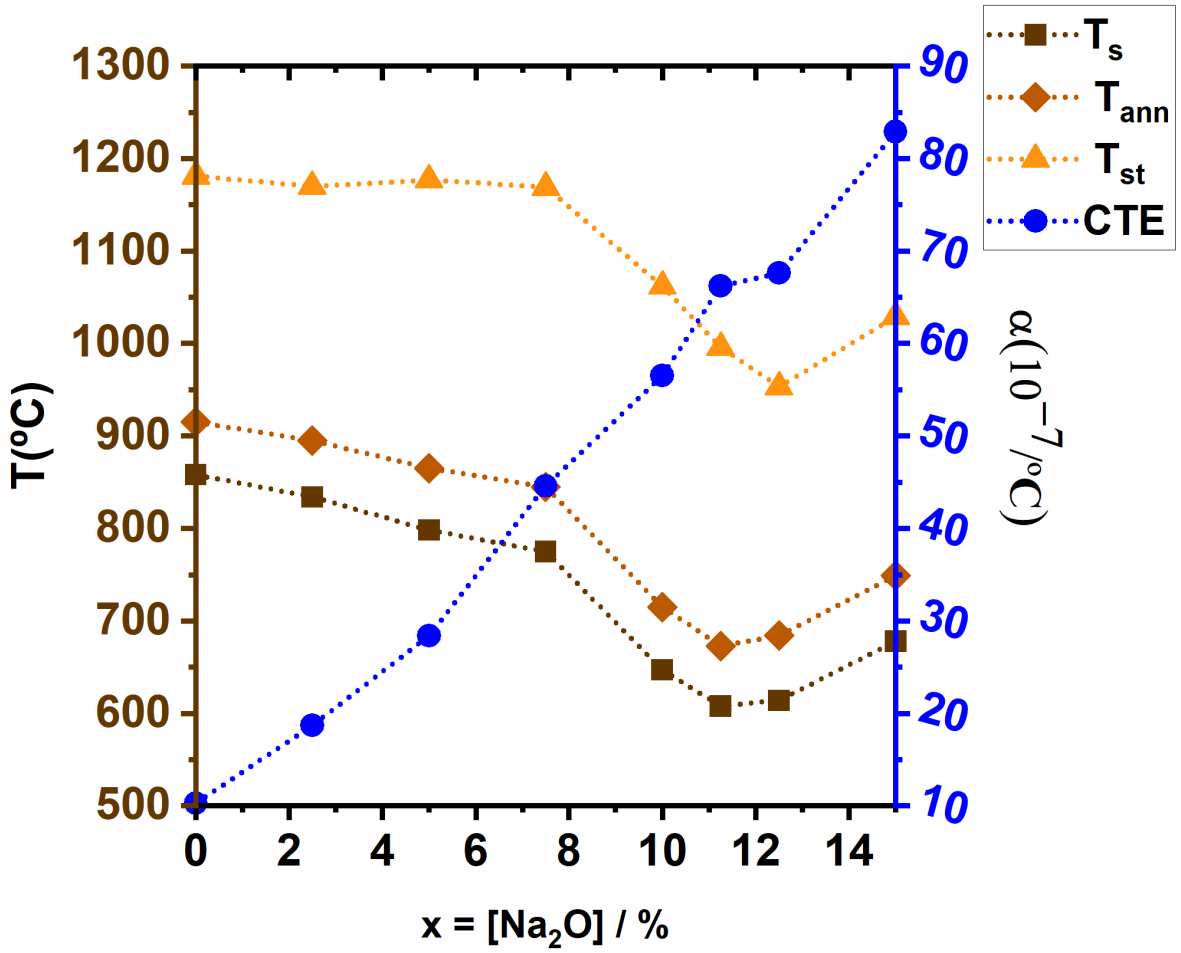

Figure 29 - Thermal expansion (in blue) and characteristic glasses temperature (T_s is temperature of softening, T_{ann} is the temperature of annealing and T_{st} is the temperature of strain) as a function of the concentration of sodium oxide in the glasses. This data was acquired using parallel plate, for softening temperature, and beam-bending viscometry, for annealing and strains temperatures. The coefficient of thermal expansion (CET) was measured by dilatometry from room to 500ºC relative to a fused silica standard.

Source: Corning Incorporated.

6.1.1 ^{23}Na MAS-NMR

The results of the Fourier Transform of Free Induction Decay (FID) for ^{23}Na MAS-NMR analysis are shown in Figure 30. Only the central peak of the central transitions ½ → -½ are displayed in this figure. They show broadbands attributed to interaction between EFG and quadrupolar moment of the nuclei, described by the quadrupolar interaction. The curves are fitted by Czjzek distributions (see more about in subsection 4.1.1). For the two samples with highest content of Na, more than one site can be identified due to the presence of a partially resolved components, giving rise to shoulders in the spectra. On the other hand, the bands for the other six samples appear broad and unresolved. For samples in the range between x = –2.50

and x = –12.50, a single Czjzek distribution cannot describe the spectra with appearance of tail-shape towards lower frequencies and, therefore, more than one single component must be present.

There are multiple possibilities of deconvoluting the spectra with two or more Czjzek curves, resulting in erroneous simulation and erroneous data interpretation. To avoid this, some constraints to the deconvolutions were considered. To develop suitable deconvolution constraints, $^{23}Na(^{31}P)$ REDOR and ^{23}Na TQMAS experiments were performed, which will be explained in detail below. Based on the constraints, the ^{23}Na spectra could be deconvoluted. The deconvolution parameters are summarized in Table 12and shown as dashed curves in Figure 30.

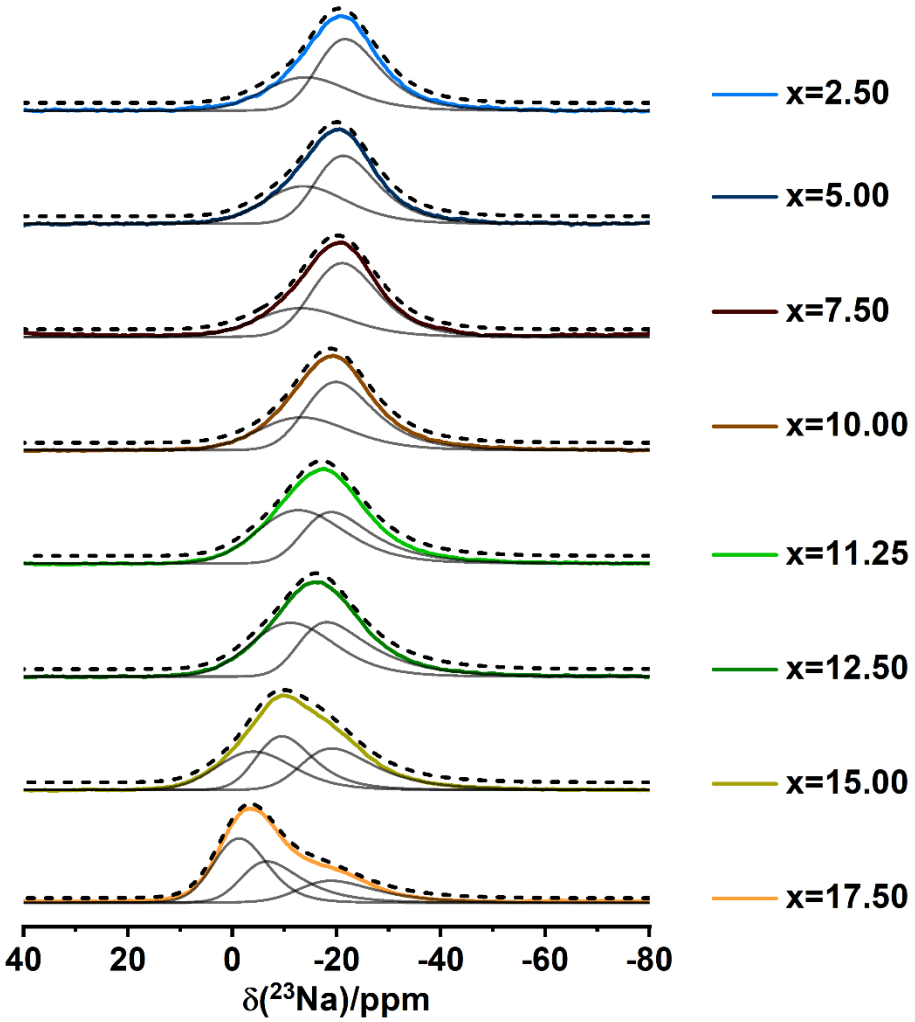

Figure 30 - ^{23}Na MAS-NMR spectra of xNa_2O - $(22.5-x)Al_2O_3$ - $7.5P_2O_5$ - $70SiO_2$, $2.50 \leq x \leq 17.50$. The coloured lines represent the FT of the FID. The solid lines under the coloured curved represent the deconvolution and the dash lines slightly above the coloured curves represent the sum of the proposed deconvolutions.

Source: By the author

Table 12 - Average Isotropic ^{23}Na Chemical Shift, Average Magnitude of the Quadrupolar Coupling Constant $<|C_Q|>$, relative area occupied by the distribution A. Each parameter is reported for one pulse experiment and synchronized Hahn Echo (HE - first S_0 spectra extracted from the REDOR evolution curve). Second moments $M_{2(Na-P)}$ of each site and second moment $M_{2(Na-P)}{}^t$ obtained from total dephasing came from the simulation of smaller evolution times of REDOR data points. Inside the parenthesis in the column of second moments are the experimental values obtained and out of the parentheses the values with the calibration factor calculate using $Na_5B_2P_3O_{13}$ model compound, as discussed by Equation (67).

Sample	Pulse Sequence	$\delta_{iso}/\pm1$ (ppm)	$\langle\lvert C_Q\rvert\rangle/\pm0.2$ (MHz)	A/±1 (%)	$M_{2(Na-P)}/\pm10\%$ (10^6 rad^2/s^2)	$M_{2(Na-P)}{}^t/\pm10\%$ (10^6 rad^2/s^2)
2.50	One Pulse	-9	2.3	38	-	-
		-17	2.3	62	-	
	HE*	-10	2.4	34	0.95 (0.49)	0.66 (0.34)
		-18	2.4	66	0.54 (0.28)	
5.00	One Pulse	-8	2.4	42	-	-
		-17	2.3	58	-	
	HE	-7	2.4	35	0.95 (0.49)	0.78 (0.41)
		-17	2.3	65	0.77 (0.40)	
7.50	One Pulse	-7	2.4	48	-	-
		-16	2.3	51	-	
	HE	-7	2.4	34	1.06 (0.55)	0.89 (0.46)
		-16	2.3	66	0.83 (0.43)	
12.50	One Pulse	-7	2.5	47	-	-
		-15	2.5	53	-	
	HE	-7	2.5	39	2.32 (1.20)	1.49 (0.77)
		-15	2.4	61	1.16 (0.60)	
11.25	One Pulse	-7	2.5	56	-	
		-14	2.7	44	-	-
	HE	-7	2.5	55	2.40 (1.24)	1.81 (0.94)
		-13	2.7	45	1.04 (0.54)	
10.00	One Pulse	-6	2.4	53	-	-
		-12	2.9	47	-	
	HE	-5	2.4	58	3.17 (1.64)	2.04 (1.06)
		-12	2.9	42	1.02 (0.53)	
15.00	One Pulse	1	2.2	32	-	-
		-5	2.2	34	-	
		-13	2.8	34	-	
	HE	1	2.2	37	4.67 (2.41)	3.40 (1.76)
		-5	2.5	31	3.44 (1.78)	
		-13	2.8	31	1.43 (0.74)	
17.50	One Pulse	2	1.9	51	-	-
		-2	2.5	29	-	
		-13	2.8	20	-	
	HE	2	1.8	44	5.16 (2.67)	4.6 (2.38)
		-2	2.5	33	2.05 (1.58)	
		-13	2.8	23	0.31 (0.16)	
$Na_5B_2P_3O_{13}$	-	-	-	-	-	6.20 (2.70)

Source: By the author

To improve the resolution in ^{23}Na MAS-NMR, we conducted a TQMAS experiments for three of the samples (x = 7.50, x = 15.00 and x = 17.50), as shown in Figure 31. The choice of the samples was based on the possible distinct regimes (Regime I and III) of the system and the possibility of obtaining higher resolution in distinct sodium environments. Sample x = 17.50 shows a high-resolution spectrum, in which two sites were able to be resolved. Although sample x = 15.00 and sample x = 7.50 suggest a distribution due to the tail-appearance in the Gaussian distribution, no higher resolution was obtained. Therefore, no other ^{23}Na MQMAS spectra was measured for the other samples. The parameters, P_Q and isotropic chemical shifts extracted from the experiments, are summarized Table 13. Although the experiments did not yield new information, TQMAS experiments were helpful to constrain the fits to the MAS-NMR spectra, which means to fix the chemical shift and quadrupolar coupling constant values. This leaded to a consistent analysis, which indicates the dual role of the sodium ions, as the displacement of Na isotropic chemical shift may be linked to Na-O distances to bridging and non-bridging oxygens,[109,110] as further explained when introducing the double resonance experiment results.

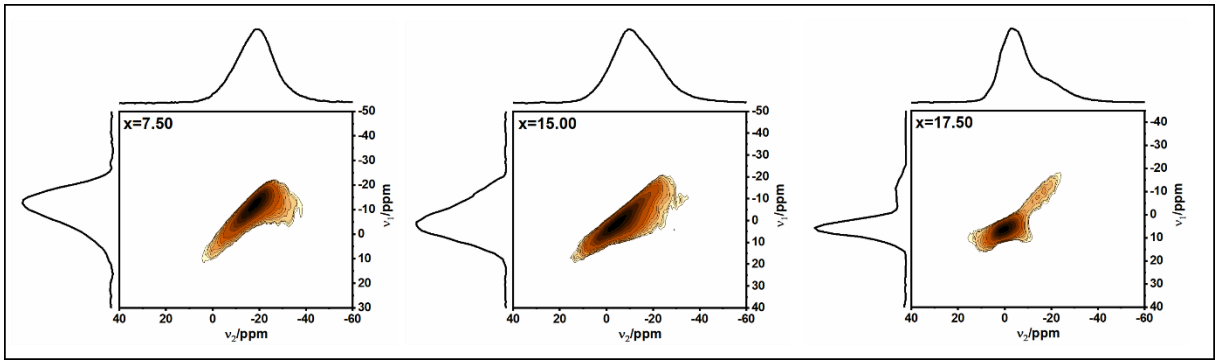

Figure 31 - Triple Quantum ^{23}Na MAS-NMR spectra of $70SiO_2$-$7.5P_2O_5$-$(22.5-x)Al_2O_3$-xNa_2O glasses for x = 7.50, x = 15.00, x = 17.50.

Source: By the author.

Table 13 - Average isotropic ^{23}Na chemical shift and quadrupolar product P_Q obtained by MQMAS experiment.

Sample	δ_{iso} / ±1 (ppm)	P_Q / ±0.5(MHz)
7.50	-15	2.0
15.00	0	2.4
	-13	2.6
17.50	3	2.1
	-15	2.1

Source: By the author

While average ^{23}Na quadrupolar coupling constants in glasses are not typically very sensitive to changes in the glass compositions (typically values of 1.5 to 2.5 MHz are found in oxide glasses), the distinct sodium local environments can influence the isotropic chemical

shifts. Figure 32 (a) displays the mean isotropic chemical shift datapoints measured by synchronized Hahn Echo (HE – first S_0 spectra extracted from REDOR experiment), in blue, and regular single pulse under MAS, in red, as a function of the molar concentration of sodium. The mean isotropic chemical shift values were calculated by weighted average of components of Table 12. These datapoints were adjusted to a quadratic fitting curve, which indicates a monotonic behavior: the greater the concentration of Na, the higher the resonance frequencies. Figure 32 (b) provides the same information as in Figure 32 (a), but as a function of the composition parameter [Al]/([Al]+[Si]). This change in the ^{23}Na chemical shift might be attributed to the average Na-O bond distances and/or the nature of the O species (bridging or non-bridging) in the first coordination sphere of sodium. Angeli *et al.* showed the influence of the Na-O bond lengths in the chemical shifts of sodium in glasses;[109] they showed Na-O average distance increasing when aluminum oxide was added in sodium silicate glasses. This result can be rationalized as an association of sodium ions in charge-compensating positions near $[AlO_4]^-$ units rather than sodium ions compensating non-bridging oxygen atoms. As will be discussed later, the trend observed in the spectra of ^{27}Al spectra reinforce the changes seen for the ^{23}Na environment adding consistency to the Na-O distance interpretation.

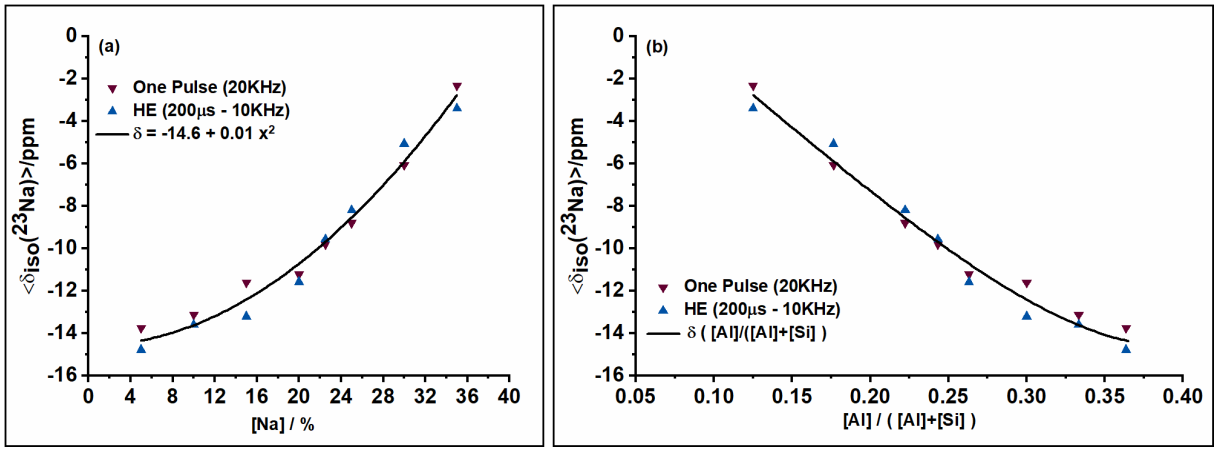

Figure 32 - (a) Average chemical shift datapoints versus molar percentage of sodium in NAPS glasses. The mean chemical shifts were calculated with weight average. The red inverted triangles show the parameters obtained with one pulse experiment; the blue triangles show the parameters obtained with synchronized HE experiments; and the black curve represents a parabolic fit to the non-linear behavior. (b) Average chemical shift as a function of [Al]/([Al]+[Si]). The black curve represents the parabolic fit as a function of [Al]/([Al]+[Si]).

Source: By the author.

Lee and Stebbins, as well as Angeli *et al.*, proposed a quantitative trend by fitting a linear equation that correlates Na-O bond distances, $d_{(Na-O)}$, and the chemical shift of ^{23}Na for crystallized aluminosilicates.[109, 110] The trends proposed are summarized in Figure 33. The

dashed lines correlate the minimum and maximal average chemical shifts found in NAPS glasses to, respectively, the maximal and minimum $d_{(Na-O)}$, according to their works. The correlation suggests that Na-O bond distances are found in the range 257 pm - 289 pm.

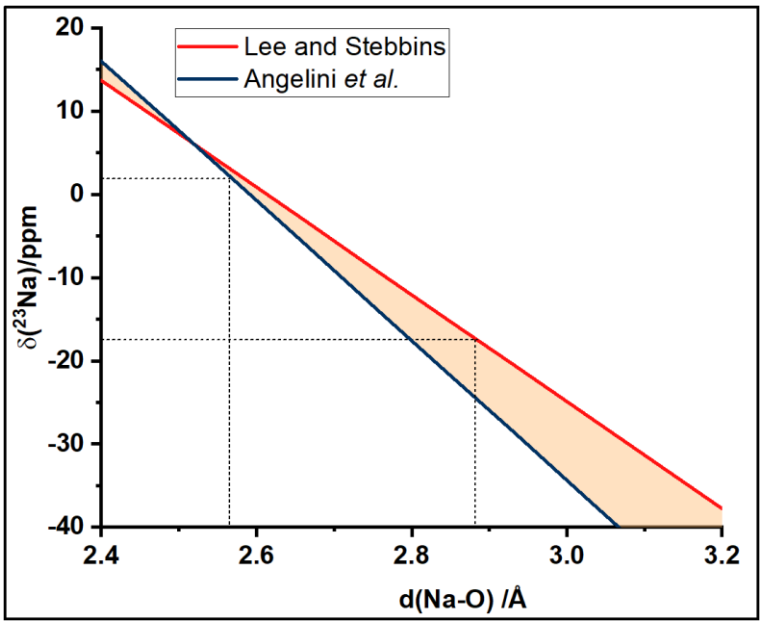

Figure 33 - The plot shows the correlation between the chemical shift of ^{23}Na and the Na-O bond length, $d_{(Na-O)}$. The blue trend line represents the data obtained by Angeli *et al.*, while the red trend line represents the data obtained by Lee *et al.* The dashed lines indicate the highest and lowest average chemical shifts, which were obtained in NAPS glasses and correlated with the minimum and maximum $d_{(Na-O)}$ values found in these two studies.[109-110]

Source: By the author.

In NMR terms, Na-O bond length can be only indirectly investigated in samples with natural abundance ^{17}O. However, indirect ways to study Na-O bond length can be tested using NMR. To test if sodium ions play a role as charge compensator of tetrahedra $(AlO_4)^-$ units, the structure Na^+ - $(AlO_4)^-$ should be tested by, for instance, probing ^{23}Na-^{27}Al homonuclear interaction. However, ^{23}Na-^{27}Al double resonance experiments have proven to be challenging due to the proximity of their Larmor frequencies.[111-112] On the other hand, increased Na concentration can act as network-modifiers, creating NBOs in phosphate network and forming units as $P^{(n)}$ - O^- ^+Na, which is easily possible to be investigated with $^{23}Na(^{31}P)$ REDOR experiment.

Figure 34 (a) shows the results of $^{23}Na(^{31}P)$ REDOR for all the samples. The first points of dephasing curve were adjusted to a parabolic fit from which the $M_{2(Na-P)}^t$ values were extracted (Equation (67)). Table 12 includes the second moment values. As explained in Section 4.4 and discussed in Equation (67), the parabolic fit approximation for lower evolution time tends to underestimate the M_2 values, as well as the accumulated experimental imperfections

(pulse missed, finite pulse length in relation to the rotor period, etc.). Therefore, a multiplicative factor f was introduced into the Equation (67) as a calibration factor. In $^{23}Na(^{31}P)$ REDOR experiments, the REDOR evolution curve of estequiometric $Na_5B_2P_3O_{13}$ was measured, from which the experimental $M_{2(Na\text{-}P)}{}^{t}$ value was obtained. Also, the theoretical $M_{(Na\text{-}P)}{}^{t}$ was calculated based on the crystallographic ^{23}Na - ^{31}P distances.[91] Comparing the theoretical and experimental value, the factor of calibration 'f' was calculated. Therefore, Table 12 shows in parenthesis the experimental value and outside the value counting with the calibration.

Figure 34 (b) displays the second moment values plotted against [Na_2O] concentration. The increased [Na]/[P] ratio correlates with the increase in the $M_{2(Na\text{-}P)}{}^{t}$ values, which means increased strength of ^{23}Na-^{31}P dipolar interaction. This result indicates that Na ions preferentially interact with the phosphate NFUs.

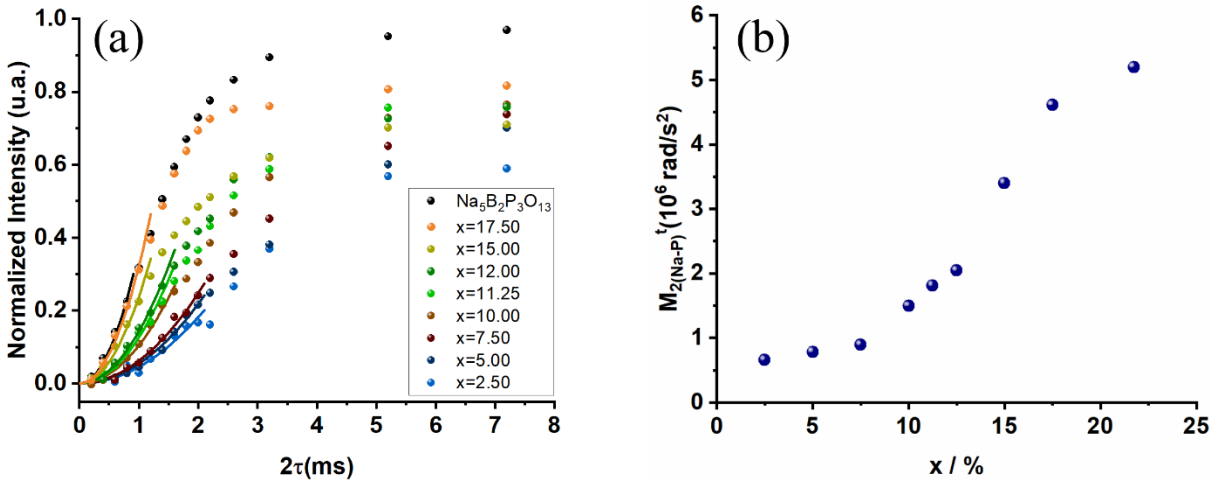

Figure 34 - $^{23}Na(^{31}P)$ REDOR total dephasing of the spectra of each xNa_2O - $(22.5\text{-}x)Al_2O_3$ - $7.5P_2O_5$ - $70SiO_2$ glass. The parabolic curves were fitted within the range $\Delta S/S_0 < 0.3$ to yield the $M_{2(Na-P)}$ values.
Source: By the author.

Additionally, the comparison between the S and S_0 spectra obtained by Fourier transforming the echoes for longer evolution times in the $^{23}Na(^{31}P)$ REDOR experiments resulted in distinct lineshapes for samples with higher Na concentration, as shown in Figure 35. The image displays the real intensity spectra on the left and the re-normalized ones, on the right. Based on the changes in the lineshape, the average quadrupolar coupling constant and the isotropic chemical shift from Czjzek distributions were obtained. The spectra of samples x = 15.00 and x = 17.50 were deconvoluted with three sites, whereas the spectra of samples x = 12.50 and x = 10.00, which have a tailing shape towards lower frequencies, were satisfactorily explained using just two curves. Samples $x < 10.00$ showed smaller lineshape changes between the S and S_0 spectra even for longer dipolar evolution time. In general terms, the

constraints were made based on the minimal variations among the parameters of simple pulse MAS, S and S_0 spectra, also on the minimal variations in the spectral simulations of the glasses compositionally similar. The parameters are included in Table 12.

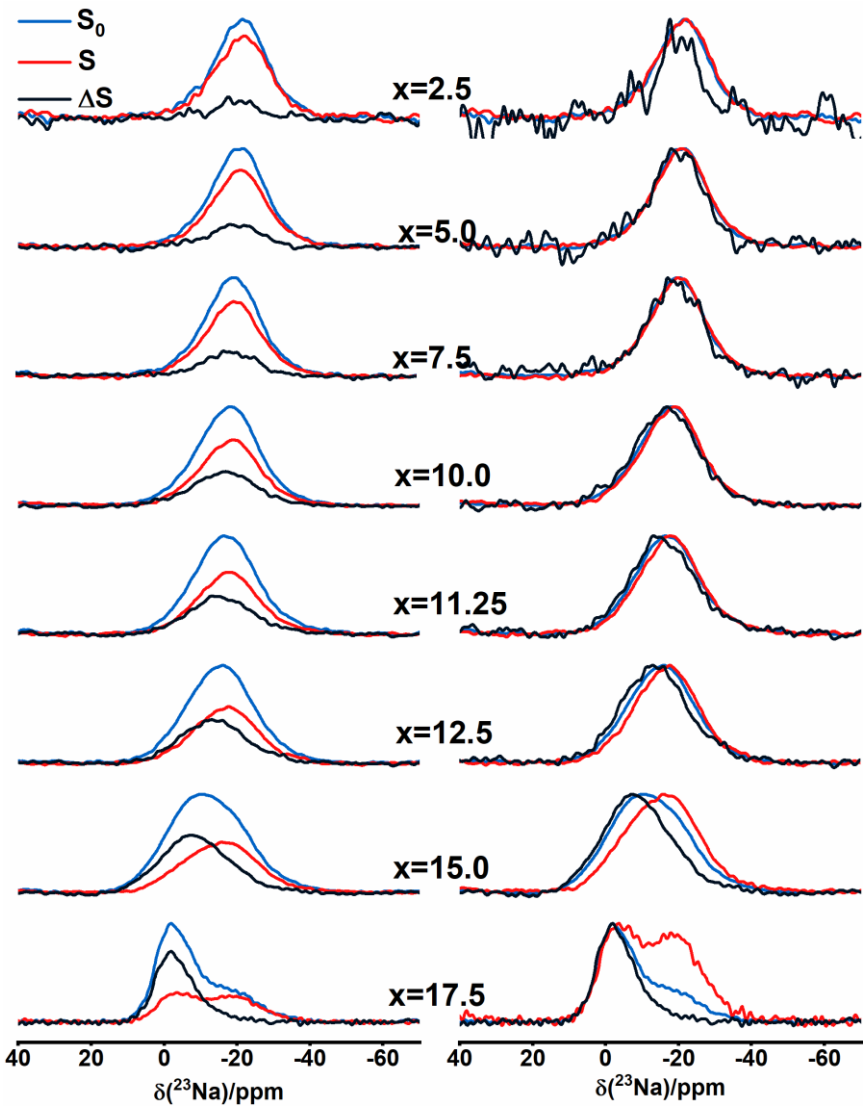

Figure 35 - FT of the REDOR result with S0, S and ΔS documenting the REDOR under dipolar evolution time of 2.00ms – based deconvolution. On the left, spectra as obtained experimentally. On right, re-normalized spectra, making the lineshape differences more visible.
Source: By the author.

These set of parameters (average quadrupolar coupling constant and the isotropic chemical shift) obtained from single-point REDOR deconvolutions were used to deconvolute all the other S and S_0 spectra of REDOR experiment, where the relative intensities were the only adjustable parameter of the Czjzek distributions. Figure 36 illustrates the $^{23}Na(^{31}P)$ REDOR dephasing curve for each individual ^{23}Na spectral component. In the graph, (a) blue color represents the ^{23}Na resonating at low frequencies, which are weakly bonded to ^{31}P in

comparison with those ^{23}Na resonating at medium frequencies, red color, which are moderately bonded to ^{31}P. Additionally, in green, there is the ^{23}Na resonating at high frequencies and strongly bonded to ^{31}P.

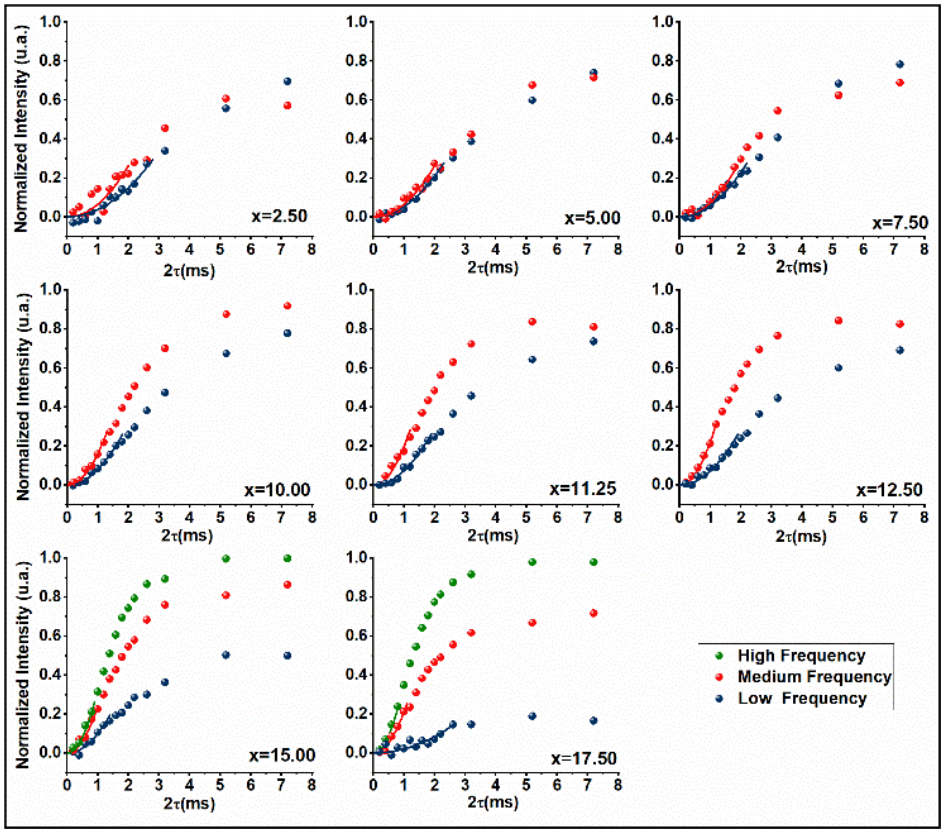

Figure 36 - $^{23}Na(^{31}P)$ REDOR dephasing of the Czjzek distributions used to deconvolute each spectrum of xNa_2O - $(22.5\text{-}x)Al_2O_3$ - $7.5P_2O_5$ - $70SiO_2$ glasses. The parabolic curves were fitted within the range $\Delta S/S_0 < 0.3$ to yield the $M_{2(Na-P)}$ values.

Source: By the author.

Clearly, the higher the Na concentration in a particular glass, the more distinct the evolution of the dephasing curves among themselves and, particularly, the dephasing curves seem to divide in three distinct regimes. First, Regime (I), $2.50 \leq x < 10.00$: the dephasing behavior of each individual ^{23}Na spectral components does not present considerable difference between low and medium frequency, which characterize no significative difference between ^{23}Na environment in relation to ^{31}P dipolar interaction. Second, Regime (II), $10.00 \leq x < 15.00$: the dephasing behavior of low and medium frequency components shows a difference in the evolution dipolar recoupling time, indicating one of Na sites interacts more strongly with the phosphate NFUs in one site (medium frequency) and weakly in the second site (low frequencies). The second site might be attributed to Na^+ ions balancing the $(AlO_4)^-$ structure, as the discussion of ^{27}Al-NMR will clarify. Last, Regime (III), $15.00 \leq x \leq 17.50$: the preferential

interaction of sodium in interacting with phosphate units is reinforced with the clearly strong dipolar interaction between ^{23}Na-^{31}P seen in the spectral components resonating at high frequencies.

These three behaviors observed in the $^{23}Na(^{31}P)$ REDOR results were validated with a cluster analysis. The cluster analysis verifies the similarities/dissimilarities among the ^{23}Na spectral components, then clustering of variables is a direct result of distinct Na groups. Two variables were used in the analysis: the isotropic chemical shift extracted from the FT from one pulse experiment and the $^{23}Na(^{31}P)$ heteronuclear dipolar second moment of each site, $M_{2(Na-P)}$. Each site was labeled before the cluster analysis, as Table 14 shows. The parameters were grouped based on their normalized Euclidian distance using the ward.D method for the hierarchization.[113] In this method, each datapoints starts and corresponds to one cluster. Then, a pair of clusters are grouped such that the increase in variance is minimized. The process happens recursively until all the data points are merged into a single cluster. The dendrogram is illustrated in Figure 37. The dataset was divided into three clusters (blue, red, and green), which might correspond to three Na behaviors exposed above. The numbers labelled in the clusters correspond to the spectral components labeled in Table 14.

Table 14 - Label of each site for the cluster analysis, average 23Na chemical shift extracted from the deconvolution of the FT of the FID and Second Moment extracted from the parabolic fitting of short evolution time of REDOR experiments.

Sample	Label	$\delta_{iso}/\pm1$ (ppm)	$M_{2(Na-P)} / \pm10\%$ (10^6 rad^2/s^2)
2.50	1	-9	0.95 (0.49)
	2	-17	0.54 (0.28)
5.00	3	-8	0.95 (0.49)
	4	-17	0.77 (0.40)
7.50	5	-7	1.06 (0.55)
	6	-16	0.83 (0.43)
12.50	7	-7	2.32 (1.20)
	8	-15	1.16 (0.60)
11.25	9	-7	2.40 (1.24)
	10	-14	1.04 (0.54)
10.00	11	-6	3.17 (1.64)
	12	-12	1.02 (0.53)
15.00	13	1	4.67 (2.41)
	14	-5	3.44 (1.78)
	15	-13	1.43 (0.74)
17.50	16	2	5.16 (2.67)
	17	-2	2.05 (1.58)
	18	-13	0.31 (0.16)

Source: By the author

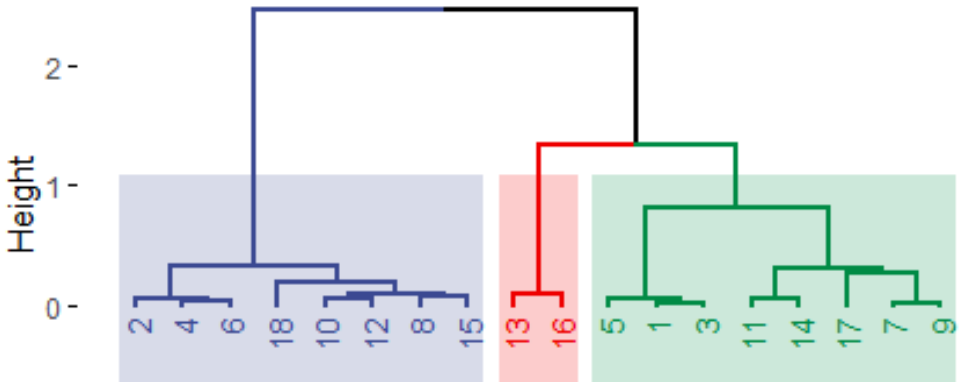

Figure 37 - Classification dendrogram of hierarchical clustering calculated with the ward.D method. Purple/green, red, and blue groups represent, respectively, the ^{23}Na ions that are highly, moderately, and poorly connected with ^{31}P. Height in the y-axis represents the Euclidian distances between two clusters,
Source: By the author.

Finally, Figure 38 summarizes the result of the dendrogram. Figure 38 (a) shows that the cluster analysis empirically confirms the discussion on the three Na environments. The clusters division is interpreted as: ^{23}Na resonating in the range -18 to -12 ppm are weakly bonded to ^{31}P, whereas ^{23}Na showing moderate dipolar interaction strength resonates at frequencies between -10 and 0 ppm. Strong ^{23}Na-^{31}P interaction represents ^{23}Na completely dominated by phosphorus NFUs.

The cluster division of the ^{23}Na moderately connected to ^{31}P (in red) seems to be less homogeneous than the other clusters, which is attributed to a strong difference in M_2 values inside this cluster. Consistently, higher frequency spectral components of samples x = 2.50, 5.00 and 7.50 (samples integrating Regime I) seem to be the most inhomogeneous data in this cluster, and could be interpreted as a sub-cluster, with chemical shift as high as ^{23}Na moderately connected to ^{31}P, but with second moment compatible with ^{23}Na poorly connected to ^{31}P.

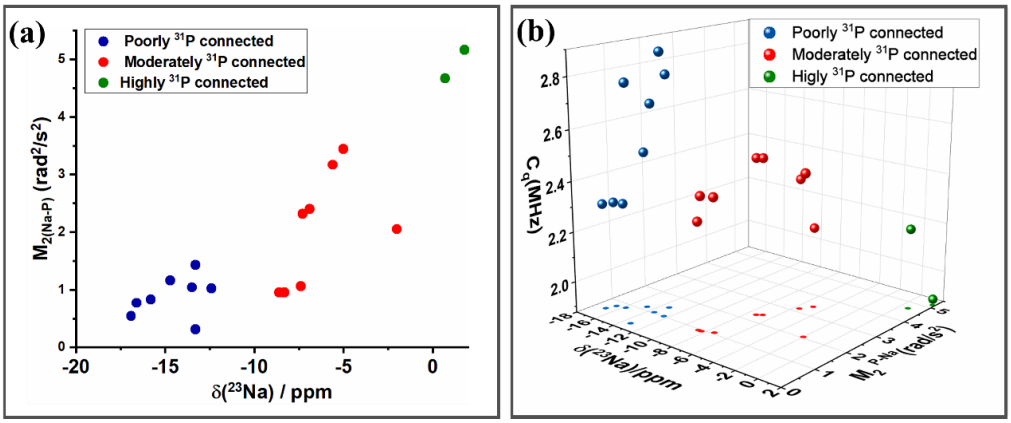

Figure 38 - (a) Plot of the ^{23}Na REDOR and MAS-NMR observables represents the result obtained from the hierarchical clustering, showing three different groups: ^{23}Na highly, moderately, and poorly connected to ^{31}P. (b) Same plot as (a), but inclusion in the third dimension the quadrupolar coupling constants.
Source: By the author.

It is also interesting also to pay some attention to whether quadrupolar coupling constant can be described as a function of the compositional line. Figure 38 (b) shows the result of cluster analysis with the addition of $\langle|C_Q|\rangle$ values as the third axis in a 3D plot. In this regard, Koller and Engelhardt showed clearly how the quadrupolar coupling constant can be affected by the coordination number of sodium and by the symmetry of the sodium local environment.[114] For a systematic study in P-bearing NAS glasses, Zhao *et al*. presented the coordination number of sodium and the chemical composition as interdependent.[115] Also, some studies indicate that fully polymerized $[AlO_4]^-$ tetrahedral units are coordinated to a Na^+ with higher Na-O bond length, which may be compatible with a higher sodium coordination number.[116–119] Kobera *et al*. studied the relation between EFG and the nature of the chemical bonds in Lewis adducts by analysis of Electron Localization Function.[120] They found that the weakening of Al-O polarized donor-acceptor bonds results in an increase in C_Q values. Therefore, the change of composition can change the nature of the bond as well as changing the coordination number of sodium. It may cause the environment to be less or more symmetric, resulting in the increase or decrease of quadrupolar coupling constant. Nonetheless, as discussed, a direct relationship between quadrupolar coupling constant involves many distinct factors and is hard to establish.

As observed, the role of sodium is strongly linked to the Na-O bond length, as demonstrated in numerous studies,[109-110,117,119] and supported by the findings in this thesis. The three compositional regimes detected showed to be in close connection with the interaction between ^{23}Na and ^{31}P. The next step of this work is, therefore, to explore ^{31}P environment and verify if the results obtained in for ^{31}P will reinforce the found in this work until now.

6.1.2 ^{31}P MAS-NMR and Static-NMR

The ^{31}P (a) static and (b) MAS-NMR spectra in Figure 39 reveal broad bands that reflect ^{31}P isotropic chemical shift distributions, which appear to be governed by three distinct regimes. The samples with $x < 10.00$ resonate at approximately -28.5 ppm and, according to the literature, the chemical shifts of these glasses provide evidence of a preponderance of $P^{(4)}$ coordinated with Al(IV).[62,121] The cationic $P^{(4)}$ NFU has a symmetric charge distribution, resulting in an anisotropy forming a Gaussian lineshape, as observed in the static spectra. The increase in sodium concentration in the three aluminum-rich glasses having the lowest sodium contents ($x = 2.50$, 5.00, and 7.50) does not significantly affect the ^{31}P chemical shifts. A similar behavior was reported by Aitken *et al*. in a modifier-free ternary aluminophosphosilicate system, suggesting that the ^{31}P chemical shift is, in aluminum-rich samples, less dependent on

the concentration of aluminum[20]. For samples with x = 10.00 and above, the static spectra show asymmetries in the lineshapes. The MAS spectra depicts the ^{31}P chemical shifts displaced slightly towards higher frequencies, suggesting that the addition of sodium leads to the depolymerization of P units, forming neutral $P^{(3)}$, anionic $P^{(2)}$ and a minority of di-anionic $P^{(1)}$ units. In the richest-Na containing glass, it was observed a sharp peak consistent with the chemical shift of $Na_4P_2O_7$. An X-Ray diffraction was performed in this sample and illustrated in Figure A3 – Appendix A. The partial crystallization of $Na_4P_2O_7$ indicates the limit of the glass-forming region.

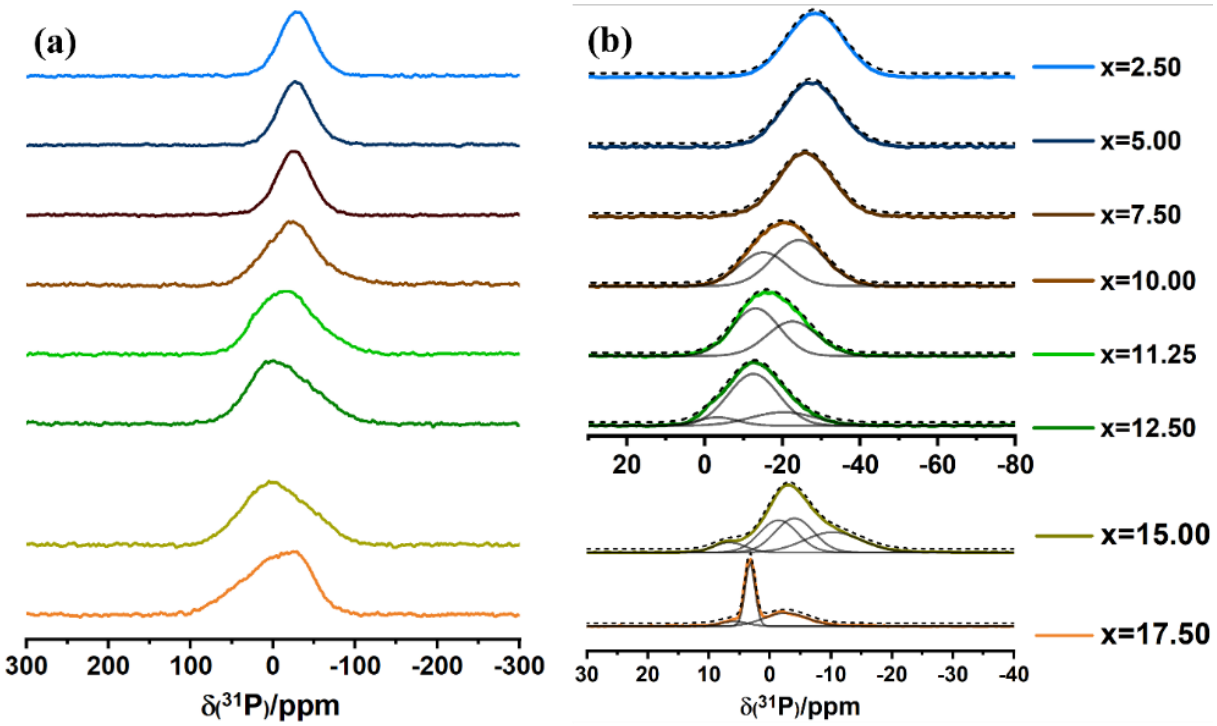

Figure 39 - (a) ^{31}P static and (b) MAS spectra of $xNa_2O – (22.5\text{-}x)Al_2O_3 – 7.5P_2O_5 – 70SiO_2$. The coloured lines represent the FT of (a) the first echo of Static SED experiment and (b) the FT of FID under MAS condition. Solid lines under the coloured curved represent the deconvolution and the dash lines slightly above the coloured curves represent the sum of the proposed deconvolutions.

Source: By the author.

Due to the presence of pyrophosphate structure ($Na_4P_2O_7$) in the sample x = 17.50, the existence of P-O-P linkages was investigated to the other glasses. In order to do so, the second moments values ($M_{2(P\text{-}P)}$) were measured via the static Spin Echo Decay (SED) experiment. Figure 40 (a) shows the simulation of Gaussian decay fit to the set of points obtained with each experiment. Figure 40 (b) reinforces the relationship of $M_{2(P\text{-}P)}$ values versus the sodium molar concentration. The decays show that only samples x = 17.50 and 15.00 possess a significant amount of proximity, is attributed to the existence of P-O-P connectivity in the sample x =

17.50. Based on this, the question of whether high second moments are attributed to through-space proximity or though-bond connectivity can be posed to sample x = 15.00.

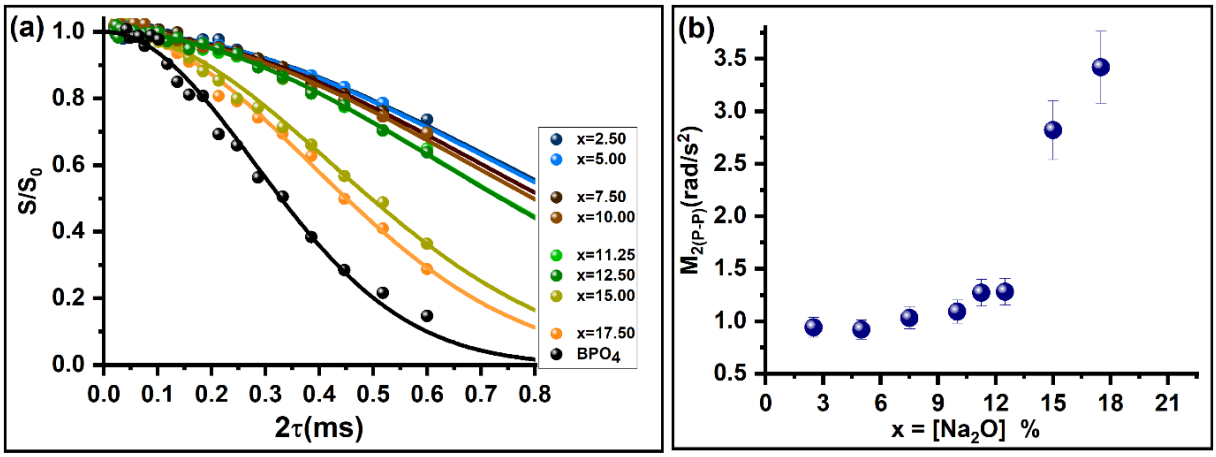

Figure 40 - (a) the ^{31}P Static Spin Echo Decay (SED) curves of $xNa_2O - (22.5-x)Al_2O_3 - 7.5P_2O_5 - 70SiO_2$ glasses. (b) the $M_{2(P-P)}$ values obtained from SED against x. Stochiometric BPO_4 was used to calibrate the M_2 values to obtain their quantitative result.
Source: By the author.

To answer this, an INADEQUATE experiment was performed to verify whether P-O-P connections were present in the two Na-richest samples, as illustrated by Figure 41. Consistently, the presence of P-O-P linkages was detected; for the sample x = 17.50, this connection represents the formation of a crystalline $P^{(1)}{}_{1P}$ unit ($Na_4P_2O_7$), observed at around 3 ppm, as expected by X-ray diffraction (Figure A3).[20,122] Therefore, for the two Na-richest samples, the high second moments reflects the formation of P-O-P bonds, which, as further discussed in this section, correlates well with the formation of sodium site resonating at high frequencies. This structure in these two samples is associated with the characteristic behavior of Regime III: the formation of P-O-P bonds seems be in closer connection with the existence sodium sites resonation in high frequency, which balance the non-bridging oxygen bonded to the $P^{(1)}$ units.

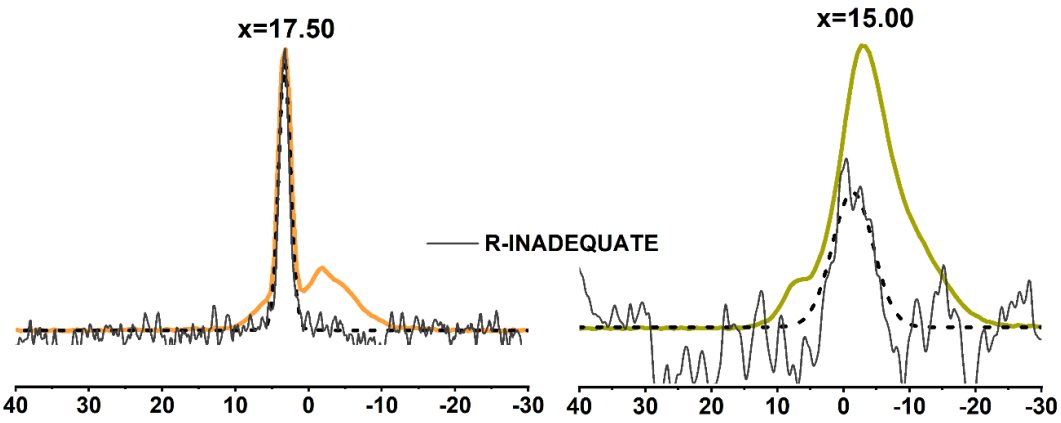

Figure 41 - Comparison of single-pulse ^{31}P MAS-NMR spectra (in yellow) and ^{31}P Refocused INADEQUATE spectra (in dark color), which corresponded to double quantum excitation signal from species with P-O-P linkages in glasses with x = 15.00 and x = 17.50.
Source: By the author.

Finally, deconvolutions shown in Figure 39 (b) were performed based on the spectral editing, considering the information from Static SED and INADEQUATE experiments, as well as ^{31}P(^{23}Na) and ^{31}P(^{27}Al) REAPDOR, which will be discussed in the sequence. The values of the deconvolution parameters and second moment are summarized in Table 15.

Table 15 - ^{31}P isotropic chemical shifts obtained from deconvolution of single-pulse MAS-NMR spectra, area percentages A and $M_{2(P-P)}$ values measured by spin echo decay.

	2.50	5.00	7.50	10.00	11.25	12.50	15.00	17.50	BPO_4
A	100	100	100	42	56	9	8	10	
±1 / (%)				58	44	68	30	47	
						23	33	43	
							29		
δ_{iso}	-28.4	-27.4	-25.9	-15.1	-13.1	-3.2	6.7	5.9	
±1 / (ppm)				-24.2	-23.5	-12.5	-1.4	3.3	
						-20.2	-4	-2.6	
							-10.3		
$M_{2(P-P)}$ ±10% / (10^6 rad^2/s^2)	0.97	0.92	1.03	1.09	1.26	1.28	2.82	3.42	6.41

Source: By the author.

To facilitate the deconvolution of the ^{31}P MAS-NMR spectra, complementary information extracted from ^{31}P(^{27}Al) REAPDOR and ^{31}P(^{23}Na) REAPDOR experiments were used. Due to the long spin-lattice relaxation time of ^{31}P, only single-point experiments with a fixed dipolar mixing time of 1.2 ms were done. Figure 42 illustrates the results of these ^{31}P(^{23}Na) REAPDOR experiments (on the left), and of the ^{31}P(^{27}Al) REAPDOR experiments (on the right) for three samples. One sample from each one of the three distinct Regimes was chosen: x = 2.50, x = 11.25 and x= 15.00. For sample x = 2.50, the recoupling of ^{27}Al-^{31}P

dipolar interaction shows phosphorus to be a $P^{(4)}$ unit dominated by aluminum in the second coordination sphere and almost unaffected by the recoupling of ^{23}Na-^{31}P dipolar interaction. For sample x = 11.25, recoupling the dipolar interaction between ^{23}Na and ^{31}P, causes the higher-frequency part of the signal to dephase more strongly than the part at lower frequencies, creating a change in lineshape. This result indicates that the increased amount of sodium in the network leads to breaking linkages of $P^{(4)}$ units, which form new NBOs compensated by the sodium ion, causing sodium to be more closely connected to anionic $P^{(n)}$ units (n = 1,2). A complementary effect is observed by recoupling of the dipolar interaction between ^{27}Al and ^{31}P, in which phosphorus resonates at low frequency dephase more intensely. Based on these constraints, a consistent deconvolution model can be developed. The results obtained on the sample with x = 15.00 also shows that phosphorus resonating at higher frequencies is strongly charge balanced by sodium, whereas the component at lower frequencies is connected to aluminum.

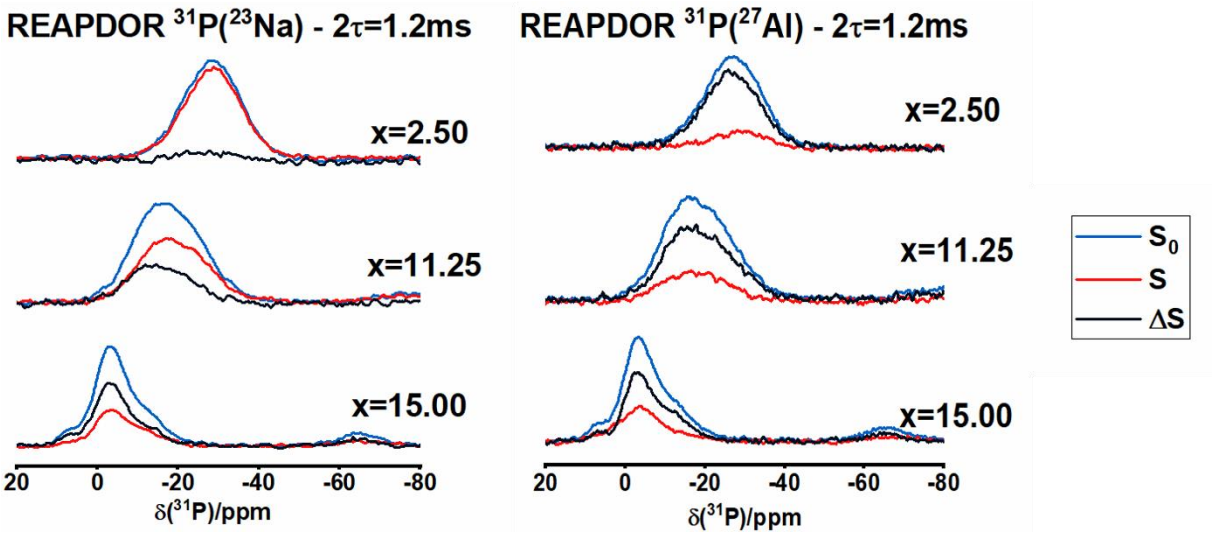

Figure 42 - $^{31}P(^{23}Na)$ REAPDOR spectra on the left and $^{31}P(^{27}Al)$ REAPDOR spectra on the right of samples x = 2.50, x = 11.25, x = 15.00 and x = 17.50 of the glasses $xNa_2O – (22.5\text{-}x)Al_2O_3 – 7.5P_2O_5 – 70SiO_2$.
Source: By the author.

In summary, the MAS-NMR spectra were deconvoluted based on the constraints extracted by $^{31}P(^{27}Al)$ REAPDOR, $^{31}P(^{23}Na)$ REAPDOR and INADEQUATE experiments. The combination of these experiments allows identifying three regimes. At low x-values, sodium ions do not attack $P^{(4)}$ groups in Al-rich samples (x < 10.00). The static spectra show no anisotropy and a single distribution, interpreted as $P^{(4)}$ mainly connected to aluminum network formers, can explain the MAS lineshape. For samples with $10.00 \leq x < 15.00$, sodium acts on phosphorus vicinity as a network modifier when depolymerizing $P^{(n)}$ groups with the

formation of NBOs. Thus, due to the network modification effected by Na^+, new $P^{(3)}$, $P^{(2)}$ and $P^{(1)}$ units containing NBOs are successively formed as x is increased. Finally, $P^{(4)}$ and/or $P^{(3)}$ structures are completely eliminated for the sample x = 15.00. The line shape clearly presents three distributions, one more being revealed by the double-quantum excitation of P-O-P linkages. For the sample with x = 17.50 the partial crystallization of $Na_4P_2O_7$ indicates the limit of the glass-forming region. Additionally, the result of single point $^{31}P(^{27}Al)$ REAPDOR experiment for all the glasses can be encountered in Figure A4 – Appendix A.

Figure 43 (a) summarizes these trends described above. Regime (I) shows the small changes in the average chemical shift as the concentration of sodium changes. In the regime (II) the chemical shift changes as the function of x, as the concentration of sodium is more pronounced. Finally, the regime (III) shows the sample approaching the limit of the glass forming region. On the right side, the image shows the measured dipolar strength ($\Delta S/S_0$) at a fixed dipolar mixing time for each site against sodium concentration for (b) $^{31}P(^{23}Na)$ REAPDOR and (c) $^{31}P(^{27}Al)$ REAPDOR experiments. Phosphorus reveals an expected increased interaction with sodium as the ratio Na/P increases, while its interaction strength with ^{27}Al tends to decrease, which can be explained by the combination of both, the decreased Al/P ratio with increasing x, and the systematic changes in the network structure as discussed above. The parameters used in Figure 43 are summarized in Table 16.

For understanding better this glass system and add consistency to the model, ^{27}Al-NMR will be explored in the next subsection.

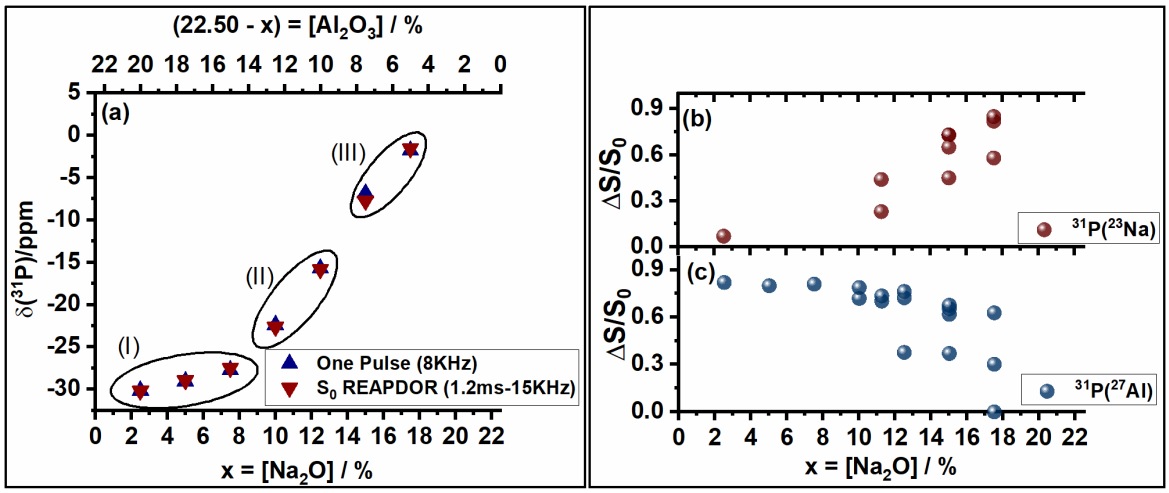

Figure 43 - (a) ^{31}P MAS-NMR average chemical shift of $xNa_2O – (22.5\text{-}x)Al_2O_3 – 7.5P_2O_5 – 70SiO_2$ glasses plotted as a function of x. In blue, the FT of FID and in red the FT of induced echo measured with first S_0 REAPDOR spectra. (b) Dephasing under ^{23}Na dipolar recoupling of each deconvolution plotted as function of x.(c) Dephasing under ^{23}Al dipolar recoupling of each deconvolution plotted as function of x.

Source: By the author.

Table 16 - ^{31}P MAS-NMR average isotropic chemical shifts (±0.5 ppm) $<\delta_{iso}>$ of the spectra, average chemical shift of each site δ_{iso}, magnitude of single-point dipolar dephasing $\Delta S/S_0$ for $^{31}P(^{23}Na)$ and $^{31}P(^{27}Al)$ REAPDOR measured at dipolar mixing times of 1.2 ms.

	$<\delta_{iso}>$ (ppm)	δ_{iso} (ppm)	(^{31}P-^{23}Na) REAPDOR Norm – $\mathbf{\Delta}S/S_0$	(^{31}P-^{27}Al) REAPDOR Norm – $\mathbf{\Delta}S/S_0$
2.50	-28.4	-28.4	0.07	0.82
5.00	-27.4	-27.4	-	0.80
7.50	-25.9	-25.9	-	0.81
10.00	-20.4	-15.1/-24.2	-	0.72/0.79
11.25	-17.7	-13.1/-23.5	0.44/0.23	0.70/0.74
12.50	-13.4	-3.2/-12.5/-20.2	-	0.38/0.72/0.76
15.00	-4.2	6.7/-1.4/-4.0/-10.2	0.73/0.73/0.65/0.45	0.37/0.62/0.65/0.68
17.50	1.0	5.9/3.3/-2.6	0.82/0.85/0.58	0.30/0.00/0.63

Source: By the author.

6.1.3 ^{27}Al MAS-NMR

The results of the ^{27}Al MAS-NMR analysis are shown in Figure 44, which displays broad and unresolved lines in the spectra. Minor features around 18 and -4 ppm indicating Al(V) and Al(VI) were observed in the samples with the highest sodium content (x = 15.00 and 17.50), according to the literature.[33-34,123] The multiple deconvolutions seen in the MAS-spectra will be explained more in details in this text. The pieces of information collected by regular MAS, and further explained by TQMAS and $^{27}Al(^{31}P)$ REDOR experiments are the sources of the deconvolution constraints exposed in Figure 44, in other words, from these experiments, many insights could be obtained in order to limit the variation of parameters as average chemical shift, number of sites and quadrupolar coupling contact. The parameters extracted from each deconvolution are expressed in Table 17.

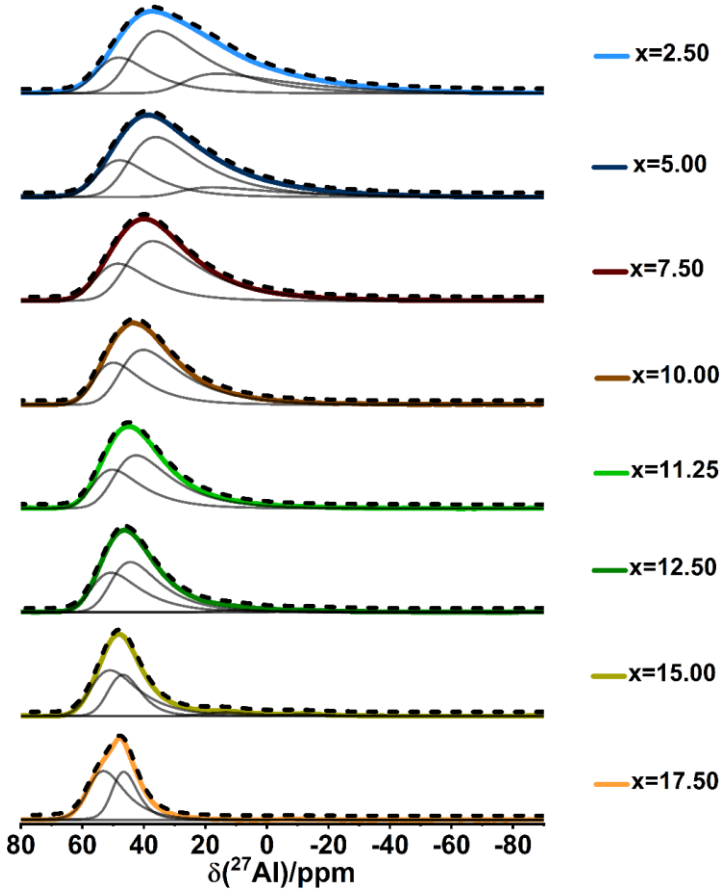

Figure 44 - FT of FID of ^{27}Al MAS-NMR spectra for samples $xNa_2O - (22.5-x)Al_2O_3 - 7.5P_2O_5 - 70SiO_2$. The coloured lines represent the FT of the FID. The solid lines under the coloured curved represent the deconvolution and the dash lines slightly above the coloured curves represent the sum of the proposed deconvolutions.

Source: By the author.

Table 17 - Average Isotropic ^{27}Al Chemical Shift, Magnitude of the Quadrupolar Coupling Constant C_Q, Sigma value simulated in Czjzek model, Quadrupolar Product P_Q, Total area occupied by the distribution A, Site-specific Second Moment $M_{2(Al-P)}$ and $M_{2(Al-P)}{}^t$ obtained by analyzing total dephasing. *HE = rotor synchronized Hahn echo. *Poor signal-to-noise ratio

Sample	Pulse Sequence	δ_{iso} ±1 (ppm)	σ (MHz)	$\langle\lvert C_Q\rvert\rangle$ ±0.2 (MHz)	A ±1 (%)	$M_{2(Al-P)}$ ±10% (10^6 rad^2/s^2)	$M_{2(Al-P)}{}^t$ ±10% (10^6 rad^2/s^2)
2.50	SP	29.0	5.05	10.0	23	-	-
		45.5	4.10	8.0	54	-	
		55.8	3.30	6.5	23	-	
	Echo/	28.0	5.05	10.0	21	0.9 (0.4)	3.0(1.26)
	REDOR	44.9	4.41	8.5	58	4.0 (1.7)	
		54.7	3.30	6.5	21	2.4 (1.0)	
5.00	SP	30.0	4.80	9.5	13	-	-
		46.0	4.00	7.9	59	-	
		55.5	3.00	6.5	28	-	
	Echo/	28.7	4.80	9.5	12	0.0 (0.0)	3.5 (1.47)
	REDOR	44.7	4.00	7.9	59	4.9 (2.1)	
		54.3	3.00	6.5	29	2.4 (1.0)	

(continued)

(continuation)

Table 17 - Average Isotropic ^{27}Al Chemical Shift, Magnitude of the Quadrupolar Coupling Constant C_Q, Quadrupolar Product P_Q, Total area occupied by the distribution A, Site-specific Second Moment $M_{2(Al-P)}$ and $M_{2(Al-P)}{}^t$ obtained by analyzing total dephasing. *HE = rotor synchronized Hahn echo. *Poor signal-to-noise ratio

Sample	Pulse Sequence	δ_{iso} ±1 (ppm)	σ (MHz)	$\langle\lvert C_Q\rvert\rangle$ ±0.2 (MHz)	A ±1 (%)	$M_{2(Al-P)}$ ±10% (10^6 rad^2/s^2)	$M_{2(Al-P)}{}^t$ ±10% (10^6 rad^2/s^2)
7.50	SP	44.9	4.00	7.9	68	-	-
		56.0	3.30	6.5	32	-	
	Echo/	46.1	3.90	7.7	67	4.7 (2.0)	3.5 (1.50)
	REDOR	55.2	3.30	6.5	33	2.1 (0.9)	
10.00	SP	48.1	3.70	7.3	62	-	-
		56.0	3.20	6.3	38	-	
	Echo/	48.3	3.60	7.1	64	4.7 (2.0)	3.4 (1.43)
	REDOR	56.2	3.20	6.3	36	1.4 (0.6)	
11.25	SP	50.4	3.54	6.9	61	-	-
		57.1	3.20	6.3	39	-	
	Echo/	49.9	3.42	6.8	61	5.4 (2.3)	3.3 (1.39)
	REDOR	56.1	3.20	6.3	39	0.7 (0.4)	
12.50	SP	-6.5	2.95	5.9	1	-	-
		16.0	2.95	5.9	2	-	
		51.2	3.70	7.3	54	-	
		57.5	3.20	6.3	43	-	
	Echo/	-6.5	2.95	5.9	1	-	3.3 (1.41)
	REDOR	16.0	2.95	5.9	2	-	
		50.2	3.70	7.3	56	5.4 (2.3)	
		56.0	3.20	6.3	41	0.9 (0.4)	
15.00	SP	-4.5	3.00	6.0	2	-	-
		20.3	3.00	6.0	5	-	
		50.6	2.15	4.3	35	-	
		57.9	3.10	6.1	58	-	
	Echo/	-6.5	3.00	6.0	2	-	3.0 (1.28)
	REDOR	18.0	3.00	6.0	4	8.2 (3.5)*	
		49.8	2.10	4.2	35	6.8 (2.9)	
		56.6	3.00	6.0	59	0.7 (0.3)	
17.50	SP	-3.5	2.20	4.0	<1	-	-
		49.5	1.80	3.5	40	-	
		57.9	2.49	4.2	60	-	
	Echo/	-3.5	2.20	4.0	<1	-	2.4(1.01)
	REDOR	49.4	2.03	3.8	45	4.8 (2.1)	
		57.2	2.50	4.3	55	0.05 (0.02)	
$AlPO_4$	REDOR	-	-	-	-	-	8.7 (3.7)

Source: By the author.

The curves, influenced by second order quadrupolar interaction, can have improved resolution in ^{27}Al TQMAS experiments. The results are illustrated in Figure 45 and the parameters extracted from the experiments are expressed in Table 18. Once again, the samples

were selected for MQMAS experiments based on choosing at least one sample of each regime. For the sample x = 2.5, two sites resonating at the isotropic chemical shifts of 26 and 51 ppm were observed and assigned respectively as Al(V) and Al(IV); the latter showing predominantly a SOQE distribution, characterized by the broadening towards the horizontal direction. Note that the amount of Al(V) in the MQMAS data is small compared to the prediction obtained from the deconvolution shown in Figure 44. The confirmed existence of higher coordinate units in the poor-Na glass was hypothesized as the formation of $Al(V)^{+3}(AlO_4)^{-}$ structural balance unit. In the absence of sodium ions, the higher coordinate ion is formed and acts as a balancer to the remaining aluminum tetrahedra units. This difference might be due to the non-quantitative nature of the MQMAS experiment. The considerable larger quadrupolar coupling constant predicted to Al(V) compared to Al(IV) interferes with the efficiency, leading to an underestimation of Al(V) site in MQMAS experiments. The same broadening type as the one observed for sample x = 2.50, was observed for sample x = 11.50. Improved resolution was found for the sample x = 15.00, for which signals near -5, 16 and 54 ppm are found and assigned to Al(VI), Al(V) and Al(IV), respectively. Samples x = 15.00 and 17.50 show a broadening towards the diagonal direction, meaning that the isotropic chemical shift distribution was the predominant source of spectral dispersion. For sample x = 17.50, three sites resonating near -3, 50 and 58 ppm were obtained.

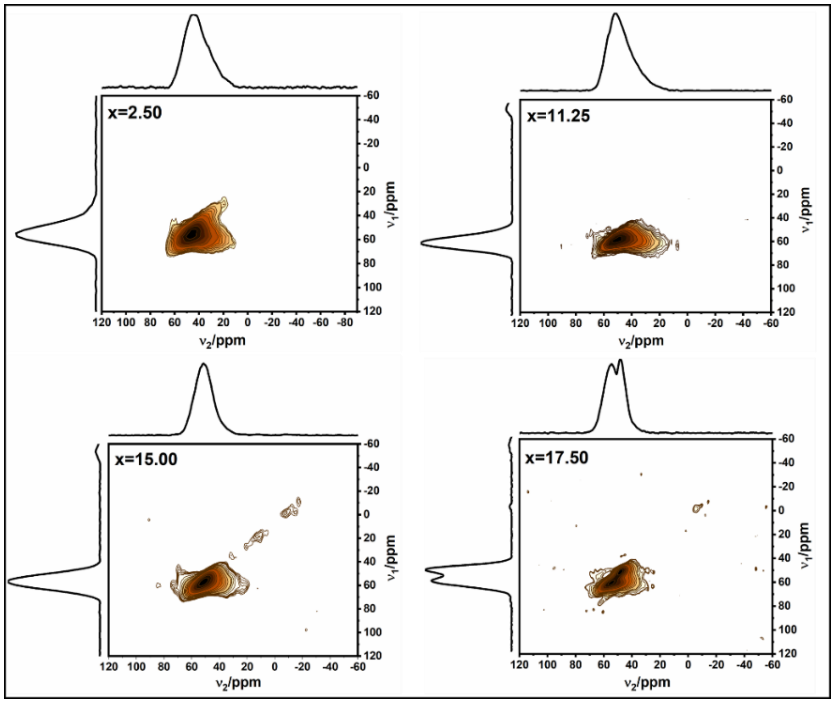

Figure 45 - ^{27}Al Triple Quantum MAS NMR spectra of $xNa_2O – (22.5-x)Al_2O_3 – 7.5P_2O_5 – 70SiO_2$ glasses for x = 2.50, 7.50, x = 15.00, x = 17.50.

Source: By the author.

Table 18 - Average isotropic ^{27}Al chemical shift and quadrupolar product extracted by MQMAS.

Sample	δ_{iso} / ±1 (ppm)	P_Q / ±0.5 (MHz)
2.50	25.8	5.8
	50.8	5.2
11.25	55.2	5.0
15.00	-5.1	3.9
	16.1	3.9
	54.2	4.5
17.50	-3.4	3.0
	49.6	3.0
	58.2	4.2

Source: By the author.

The chemical shift of ^{27}Al is influenced by its coordination number and surrounding ligands, as demonstrated in previous studies.[55,124] This sensitivity makes the chemical shift a useful parameter to investigate the local environment of the nucleus. Many studies have observed correlations between ^{27}Al chemical shifts and glass composition lines.[34,104,125-126]

In the current study, Figure 46 shows that the mean chemical shifts of single pulse spectra, in blue, and of HE, in red, decreases monotonically as the x = $[Al_2O_3]$ content increases.[‡] The chemical shifts of the components used to deconvolute synchronized HE (first S_0 spectra of REDOR) and regular single pulse spectra under MAS (see Table 17) were averaged according to their weights, and this was used to calculate the mean chemical shifts of each glass. In Na-rich glasses, the ^{27}Al MAS-NMR spectra exhibit an average chemical shift of 54 ppm, indicating Al(IV) units connected to silicon (rather than phosphate units). As the [Al] content gradually increases, the average resonance shifts increasingly towards the low-frequency direction. In Al-rich networks, the average chemical shift is 38 ppm, indicating Al(IV) units connected to phosphorus (rather than silicon units).

[‡] Spectra obtained by Hahn echo might be affected by T_2 relaxation. However, a study, which is not exposed in this Thesis, was done to investigate the T_2 values. For short values of evolution times (50 to 100μs), the FT of the echo Hahn shows the same lineshape and the same parameters as those of the single pulse experiment. On the other hand, for longer evolution time, sites with higher quadrupolar coupling constant decays faster that the sites with smaller values.

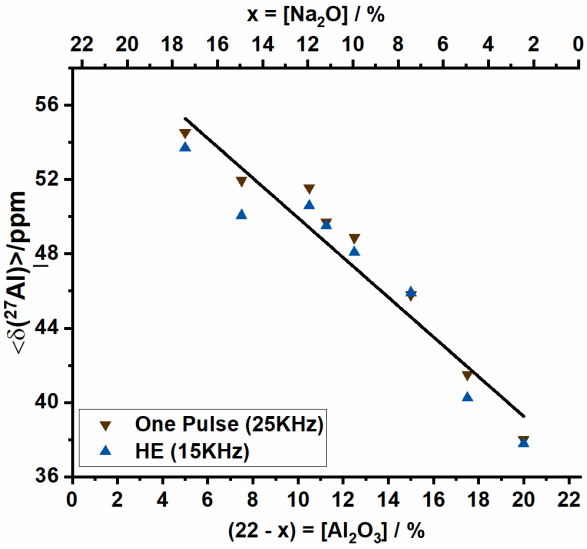

Figure 46 - Molar Percentage of aluminum (bottom) and sodium (top) in the network per weighted mean chemical shift. The red inverted triangles show the parameters obtained with one pulse experiment; the blue triangles show the parameters obtained with HE (first S0 spectra of REDOR); and the black line represents the fitting of linear behavior.

Source: By the author.

Previous studies also addressed attention to the width of ^{27}Al MAS-NMR spectra in Al-rich silicate and phosphosilicate glasses and have attributed this broadening to Al(V) units, which resonate at lower frequency.[20,127] In the current study, the MAS-NMR spectra of Al-rich glasses also exhibit increased peak widths, which may be ascribed to a combination of multiple sites, as the above discussed Al-O-P and Al-O-Si.

To investigate the correlations between ^{27}Al and ^{31}P, ^{27}Al(^{31}P) REDOR experiments were performed. Figure 47(a) shows the dephasing curve of each sample. The datapoints of the range $0 \leq \Delta S/S_0 \leq 0.3$ were adjusted to a parabolic curve (see Equation (67)), from which $M_{2(Al-P)}^{t}$ where obtained; the second moments are summarized in Table 17. Figure 47(b) shows $M_{2(Al-P)}^{t}$ as a function of the [Na_2O] concentration, on the bottom, and [Al_2O_3], on the top.

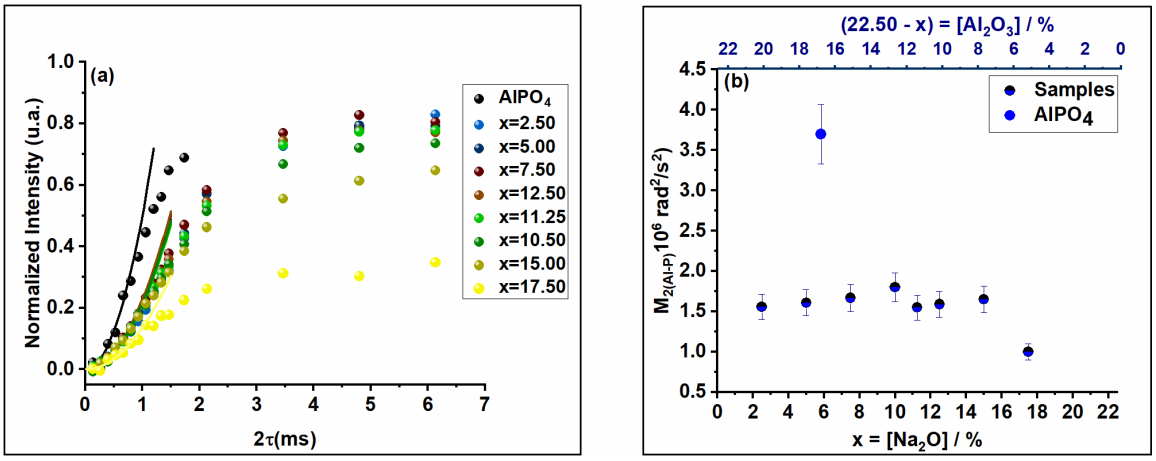

Figure 47 - (a) $^{27}Al(^{31}P)$ REDOR total dephasing of the spectra of each $xNa_2O - (22.5\text{-}x)Al_2O_3 - 7.5P_2O_5 - 70SiO_2$. The parabolic curves were fitted within the range $\Delta S/S_0 < 0.3$ to yield the $M_{2(Al\text{-}P)}$ values. (b) [Na] (bottom) and [Al] (top) vs. $M_{2(Al\text{-}P)}{}^t$ values, extracted from $^{27}Al(^{31}P)$ REDOR experiments. Note that $AlPO_4$, in blue circle, is associated exclusively with the blue axis corresponding to aluminum concentrations.

Source: By the author.

In sample x = 17.50, a strong decrease in Al-P interaction strength is observed. Aside from this exception, no clear compositional dependence was found in second-moment values, indicating a constant interaction strength between ^{27}Al and ^{31}P. This conclusion may appear contradictory with the compositional dependence discussed earlier, which suggested a partial substitution of Al(IV)-O-P by Al(IV)-O-Si bonding when Na is added into the network. This inconsistency is explained by two counteracting effects: on the one hand, $M_{2(Al\text{-}P)}$ is expected to increase with increasing x, because the P/Al ratio increases; on the other hand, the Al-O-P linkages are successively broken with increasing x, giving rise to four-coordinated aluminum (AlO_4) bonded to silica, hence resulting in a decrease in the dipolar ^{27}Al-^{31}P interaction. These two effects appear to balance each other maintaining the average level of Al-O-P connectivity per Al-unit more and less independent of the composition.

Further insights can be obtained from a more detailed inspection of the lineshape obtained by Fourier transforming the S_0, S, and ΔS signals in the REDOR experiments for longer dipolar mixing times, as the dephasing curves do not show a homogeneous behavior when looking at the lineshape, as revealed by Figure 48. The changes in the lineshape under the recoupling of dipolar interaction were used as constraints for the deconvolution of the ^{27}Al MAS-NMR spectra. Figure 48 compares S and S_0 spectra for dipolar evolution of 2.13 ms, on the left, the real intensity spectra and, on the right, the re-normalized ones.

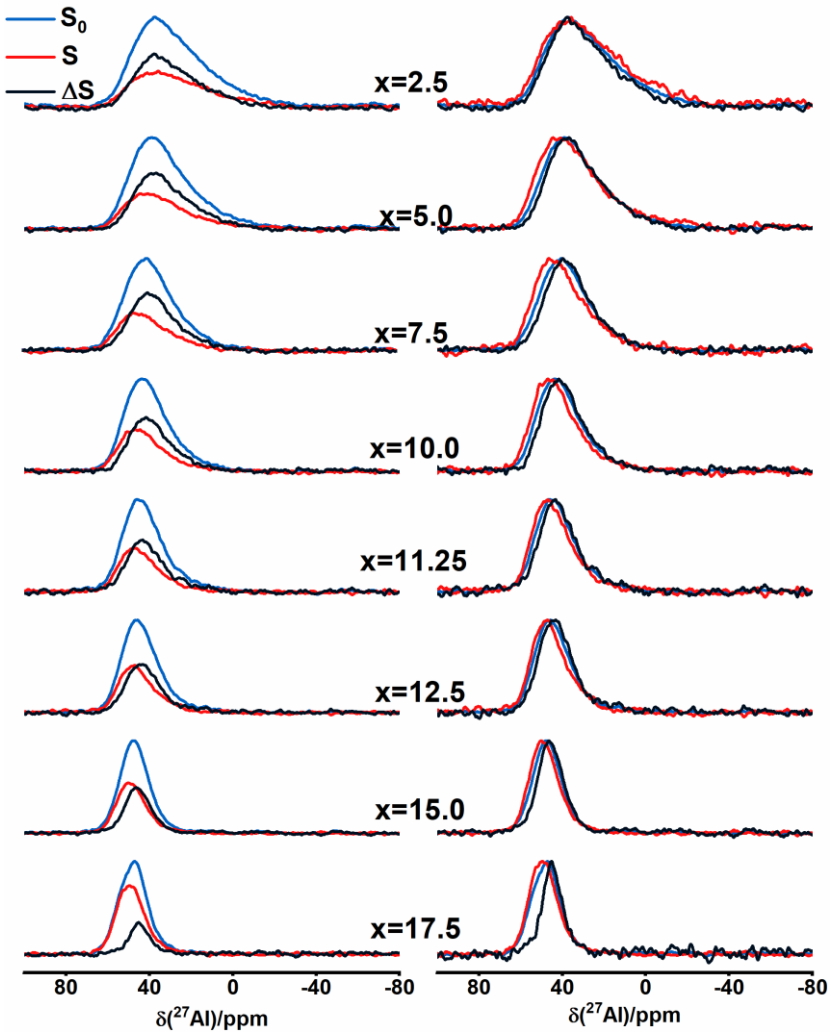

Figure 48 - Fourier transform of the REDOR result with S_0, S and ΔS documenting the REDOR under dipolar evolution time of 2.13 ms – based deconvolution. On the left, the spectra as obtained. On the right, re-normalized spectra making the lineshape changes more visible.
Source: By the author.

We attribute the broad ^{27}Al NMR spectra observed particularly at low x-values to multiple overlapping sites.[126,128] Our simplified approach was to deconvolute the spectra into four distinct sites. Two distinct Al(IV) sites were imposed for the MAS and $^{27}Al(^{31}P)$ REDOR spectra, one species named as "higher coordinate" and one Al(V) at 20 ppm: (i) the first site was assigned based on its chemical shifts in the range of 45-50 ppm and interpreted as a NFU interacting with phosphorus and silica and represented by the unit $Al^4_{2P,2Si}$; (ii) the second site was assigned as a network former unit dominantly interacting with silica isotropic chemical shifts between 55-58 ppm, Al^4_{4Si}. Additionally, (iii) samples x = 15.00 and x = 17.50 show smaller amounts of Al(V) and Al(VI) and were assigned as "higher coordinated" units. Finally, as previously discussed, in the poor-Na glass, the formation of $Al(V)^{+3}(AlO_4)^-$ structural balance unit was hypothesized. These units are represented by (iv) the notation Al^5_{Al}.

Figure 49 shows the dephasing evolution for each component under the $^{27}Al(^{31}P)$ REDOR experiment. The result indicates that the two Al(IV) components show different interaction strengths between ^{27}Al and ^{31}P nuclei. Using the approximation of shorter evolution times, the parabolic curves were fitted to the data points and the site-selective $M_{2(Al-P)}$ parameters are summarized in Table 17. Sites with small concentrations, such as Al(V) and Al(IV) for samples x = 15.00 and x = 17.50, shows a large experimental error in the second moment calculation and, therefore, they were omitted from the Figure 49.

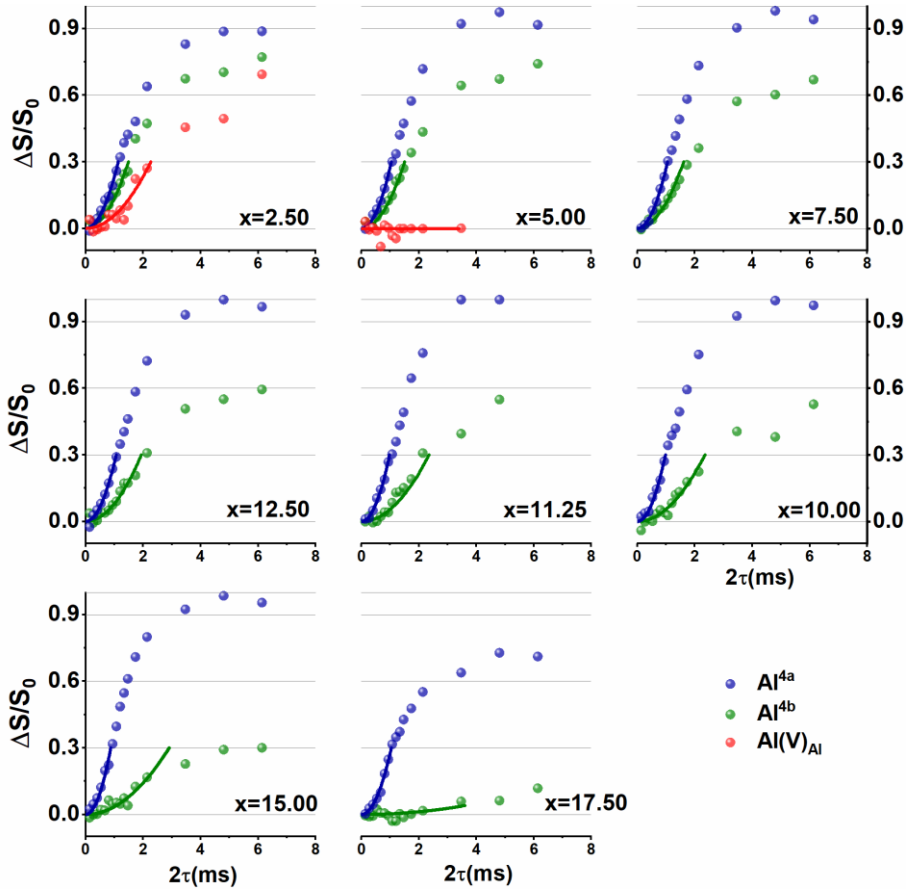

Figure 49 - $^{27}Al(^{31}P)$ REDOR dephasing of the Czjzek distributions used to deconvolute each spectrum of $xNa_2O - (22.5-x)Al_2O_3 - 7.5P_2O_5 - 70SiO_2$ glasses. The parabolic curves were fitted within the range $\Delta S/S_0 < 0.3$ to yield the $M_{2(Al-P)}$ values.

Source: By the author.

Aluminum environments appear to exhibit two distinct regimes: $x \leq 7.50$ and $x > 7.50$. The first one (Regime I) is defined by smaller concentration of sodium and by the existence of cationic $P^{(4)}$ units. Despite these positive charges, they are still insufficient to balance the charge of the aluminum tetrahedra. As a result, the remaining aluminum acts as charge balancer in the $Al(V)^{+3}(AlO_4)^-$ structure, gradually being replaced by the addition of sodium. In sample x = 7.50, all Al(V) is converted in newly formed Al(IV) units, which are balanced by sodium.

In the second regime of behavior of aluminum (Regime II and Regime III), a growing disparity in the second moment between the two sites is observed, primarily due to the decreasing M_2 values of $Al^4_{2Si,2P}$ component. This result implies that the increased [Si]/[Al] ratio, as a function of increased sodium concentration, increases the proportion of Al-O-Si bonding from the perspective of aluminum.[§] However, the same argument cannot be applied to phosphorus, as the increased [P]/[Al] accompanied by the depolymerization of Al-O-P in Regime II and Regime III.

Like the approach taken in the ^{23}Na study, the similarity among the various aluminum sites is determined through clustering of the variables obtained from the experiments and deconvolutions discussed previously. The second moment $M_{2(Al-P)}$ values and the chemical shifts were labeled, as shown in Table 19, and the clustered using the ward.D method (same as the one used in ^{23}Na cluster analysis).[113]

Table 19 - Label of each site, average ^{27}Al chemical shift extracted from the deconvolution of the FT of the FID and second moment extracted from the parabolic fitting of short evolution time of REDOR experiments.

	Label	δ_{iso} / ±1 (ppm)	$M_{2(Al-P)}$ / ±10% (10^6 rad^2/s^2)
2.50	1	29.0	0.9 (0.4)
	2	45.5	4.0 (1.7)
	3	55.8	2.4 (1.0)
5.00	4	30.0	0.0 (0.0)
	5	46.0	4.9 (2.1)
	6	55.5	2.4 (1.0)
7.50	7	44.9	4.7 (2.0)
	8	56.0	2.1 (0.9)
10.00	9	48.1	4.7 (2.0)
	10	56.0	1.4 (0.6)
11.25	11	50.4	5.4 (2.3)
	12	57.1	0.7 (0.4)
12.50	13	51.2	5.4 (2.3)
	14	57.5	0.9 (0.4)
15.00	15	20.3	8.2 (3.5)*
	16	50.6	6.8 (2.9)
	17	57.9	0.7 (0.3)
17.50	18	49.5	4.8 (2.1)
	19	57.9	0.05 (0.02)

Source: By the author.

§ The global Al-O-Si bonds decreases because of systematic decrease of aluminum proportion in the network. However, in the aluminum perspective, the proportion of this linkages increases as a function of the increased amount of sodium in the network.

Finally, Figure 50 shows that the colored horizontal division in the dendrogram creates four clusters. The groups created are: (i) the purple group, which represents the resolved higher-coordinated aluminum units (detected by TQMAS in x = 15.00 and x = 17.50), (ii) the green group, which represents Al(V) (detected by TQMAS in the x = 2.50 sample and also present in the MAS-NMR spectrum of the x = 5.00 sample), (iii) the red group which represents $Al^{4}_{2Si,2P}$ and (iv) the blue group, which represents Al^{4}_{4Si}.

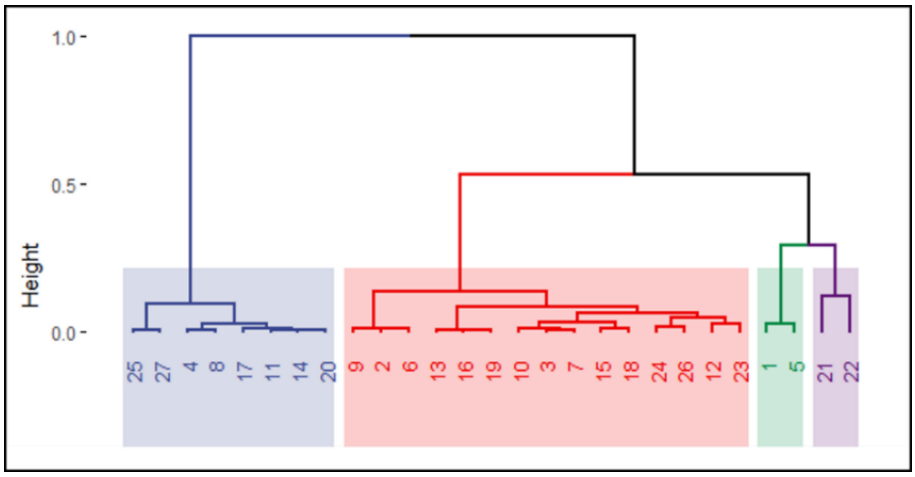

Figure 50 - Classification dendrogram of hierarchical clustering calculated with ward.D method. Al^{4a} aluminum species are represented by the blue group, Al^{4b} e Al^{4c} species by the red group, Al(V) species by the green group and "higher coordinate" groups is represented by the purple group.
Source: By the author.

Figure 51 shows the result of the clustering in a 2D graph. The 'higher-coordinated' aluminum group was the most strongly connected to phosphorus, showing chemical shifts in a wide range spanning five- and six-coordination aluminum: 20 to -10 ppm. The $Al^{4}_{2Si,2P}$ group corresponds to the cluster with the second highest $M_{2(Al-P)}$ values. As the experimental value measured in $AlPO_4$ is $3.70 \cdot 10^6$ rad^2/s^2 (four Al-O-P linkages – see Table 17) and the second moment of these glasses fall into the range $1.7 \cdot 10^6$ rad^2/s^2 to $2.3 \cdot 10^6$ rad^2/s^2 these sites correspond to Al(IV) units moderately strongly connected to phosphorus but having fewer than 4 Al-O-P linkages. Finally, the last two groups, with low $M_{2(Al-P)}$ values, represent species weakly bonded to phosphorus, and can be distinguished by their chemical shifts. The group labeled Al(V) resonates at around 21.7 ppm, therefore it might represent the $Al(V)^{+3}$ units in a charge balance $Al(V)^{+3}(AlO_4)^-$ structure, whereas the group resonates at approximately 58 ppm and can be categorized as an Al(IV)-O-Si, i.e., an $Al^{(4)}_{4Si}$ site.

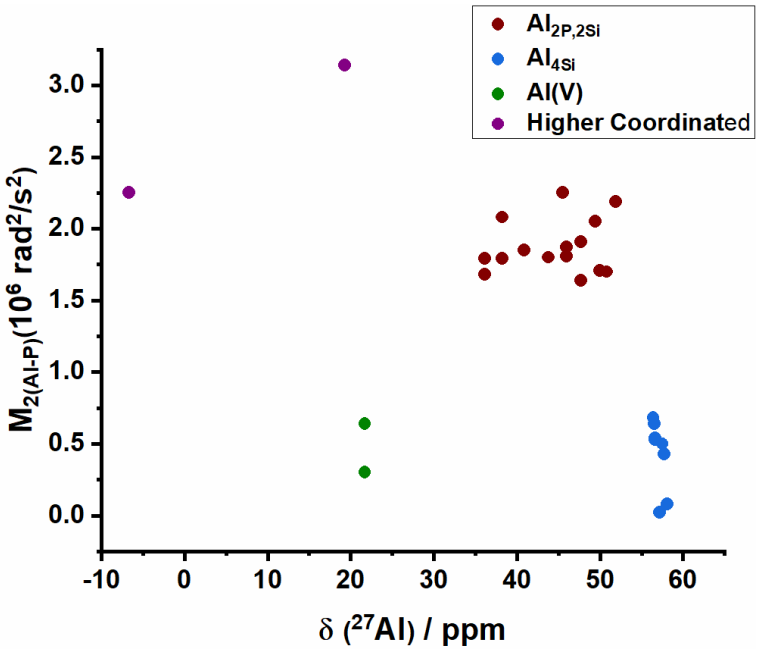

Figure 51 - The result obtained from the hierarchical clustering, showing four groups labeled as: ^{27}Al high, medium, low frequency and higher-coordinated aluminum.
Source: By the author.

Note that some discussions have taken place regarding the Al-O-Si bonds in the network and how this connectivity evolves with the systematic addition of sodium into the network. Therefore, ^{29}Si NMR studies provide valuable complementary information to the studies conducted on other nuclei so far.

6.1.4 ^{29}Si MAS-NMR

Figure 52 (a) shows the result of ^{29}Si MAS-NMR experiments, and Table 20 lists the parameters extracted from the Gaussian simulations. First moment calculation (data not shown) was also calculated and shows a good agreement with the values obtained by the Gaussian. In Figure 52 (b), the average chemical shifts are plotted as function of x, and the data is divided into three distinct regimes. Silica is well-known to be sensitive to changes in its nearest neighbors: while Si-O-Al bonds produce more positive chemical shifts, Si-O-P bonds have the opposite effect, both in relation to silicate glass chemical shift displacements. [121] In Regime (I), the displacement towards the high frequency indicates the formation of Si-O-Al linkages. Al(V) units disappear, and new tetrahedral Al(IV) units form a corner-sharing oxygen with tetrahedral $Si^{(4)}$ units. In Regime (II) the shift towards the lower frequencies suggests that Si-O-Si and/or Si-O-P connectivities become increasingly predominant. This can be seen as a consequence of the decreasing Al/Si ratio with increasing x. No Si^3 or Si^2 units, containing NBOs bonded to

silicon can be found. Sample x = 17.50 in regime (III) illustrates another trend breaking possibly due to the formation of crystalline phase $Na_4P_2O_7$. In this sample, phosphorus is predominantly integrated to the crystalline phase, causing silicon to connect in the network through Si-O-Si linkages. The Si-O-Al linkages may also happen, but due to the low amount of aluminum, their effect on the average ^{29}Si chemical shift is minor. Overall, based on the chemical shift positions, it can be concluded that silica is mainly tetrahedral $Si^{(4)}$ along the entire compositional line.

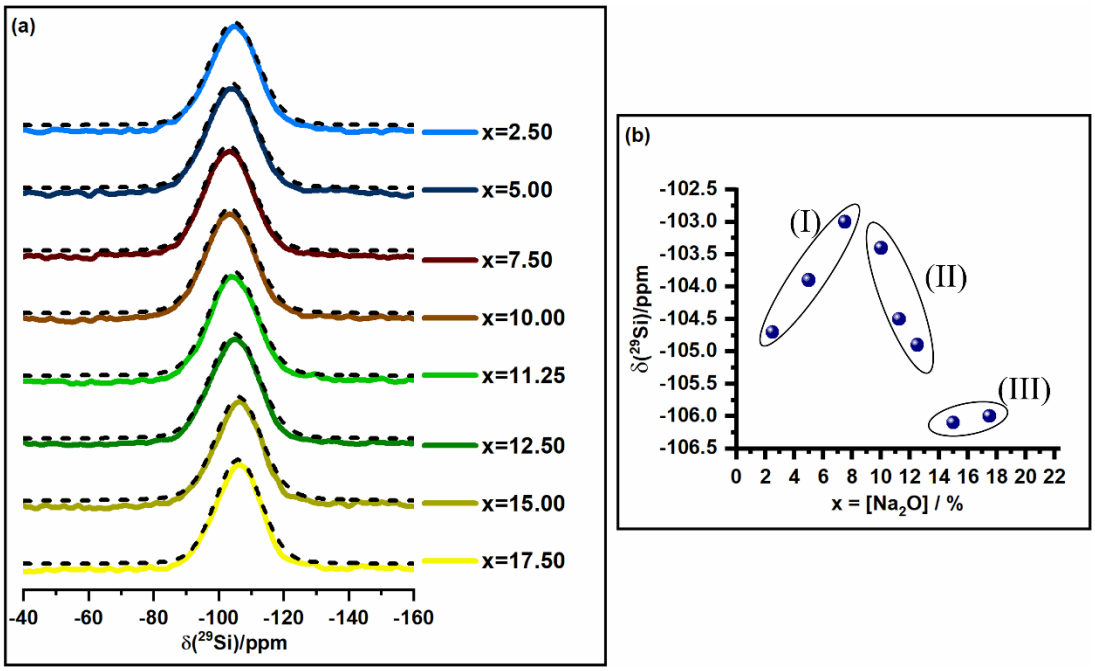

Figure 52 - (a) ^{29}Si MAS-NMR spectra of $xNa_2O - (22.5\text{-}x)Al_2O_3 - 7.5P_2O_5 - 70SiO_2$ glasses. (b) the variation of chemical shift against x. The coloured lines represent the FT of the FID. The dash lines, slightly above the coloured curves, represent the deconvolutions.
Source: By the author.

Table 20 - For single pulse MAS experiment the ^{29}Si isotropic chemical shift of each curve and it the respective width.

Sample	δ_{iso} / ppm (± 1)	FWHM / ppm (± 1)
17.50	-106.0	16.6
15.00	-106.1	17.0
12.50	-104.9	17.8
11.25	-104.5	17.7
10.00	-103.4	18.2
7.50	-103.0	18.1
5.00	-103.9	18.1
2.50	-104.7	18.0

Source: By the author.

6.1.5 Discussion

The NMR results detailed above convey a comprehensive description of xNa_2O – $(22.50\text{-}x)Al_2O_3$ – $7.50P_2O_5$ – $70.00SiO_2$ glasses. The compositional dependence of the observables can be rationalized in three distinct regimes based on the role of sodium in the network.

Regime (I) concerns the region where $2.50 \leq x < 10.00$. First, the replacement of Al by Na leads to the conversion of higher-coordinated aluminum Al(V) into tetrahedral Al(IV) units. In this regime, all phosphorus is found in cationic $P^{(4)}$ structure. Assuming that $(AlO_4)^-$ balances all $(PO_4)^+$ and Na^+ in the network, the remaining aluminum might also form higher-coordinated Al^{3+} species able to balance three $(AlO_4)^-$ NFUs. The equation bellow expresses this balance:

$$[Al^{+3}(V)] = \frac{1}{n+1}\left(1 - \frac{[P_2O_5] + [Na_2O]}{[Al_2O_3]}\right) \quad (74)$$

where 'n' is the charge devoted to compensated other units. For instance, if $Al^{+3}(V)$ is closely connected with an oxygen O^{-2}, the formal charge of this unit will result in n = +1. For samples with x = 2.50, 5.00 and 7.50, the theoretically predicted concentration of higher-coordinated Al for n = +1 would be 25.00%, 14.3% and 0%, which would show a good agreement with the 23%, 13% and 0% obtained by ^{27}Al NMR. Figure A5 – Appendix A shows that the charge balance of the network seems also consistent with this hypothesis (n = +1). Nonetheless, no experimental result evidence the formal charge of Al(V). The constraints, gathered with $^{27}Al(^{31}P)$ REDOR and ^{27}Al MQMAS, provided powerful indications not only of the presence of Al(V) unit but also of the isotropic chemical shift and quadrupolar coupling constant of its distribution. Additionally, our attempt to characterize Al(IV) in two distinct distributions shed light into two distinct environments: $Al^{(4)}_{2P,2Si}$ and $Al^{(4)}_{4P}$ units detected by site-selective $^{27}Al\{^{31}P\}$ REDOR. The gradual increase of sodium within this regime breaks the $(Al^{3+})(AlO_4)_n$ associations. As 'x' increases Al(IV) units linking to P and/and Si become dominant. The formation of Si-O-Al linkages is also clearly indicated by the ^{29}Si chemical shifts, and particularly their trends observed in glasses with low x-values.

Regime (II) concerns the region where $10.00 \leq x < 15.00$ In the absence of Al(V), the increased sodium ion concentration simultaneously balances the charge of Al(IV) and modifies the network by breaking P-O-Al linkages, thus creating anionic NBOs on the phosphate NFUs that are charge compensated by the cation Na^+. The ^{31}P chemical shifts move towards higher frequencies, reflecting the conversion of some units from $P^{(4)}_{4Al}$ unit to $P^{(3)}$ and $P^{(2)}$ and possibly

$P^{(1)}$. Breakage of Al-O-P linkages is also reflected in the ^{27}Al NMR chemical shifts, which increase systematically with increasing x, indicating a systematic formation of Al-O-Si (in substitution of Al-O-P) linkages. Additionally, $^{23}Na(^{31}P)$ REDOR experiments show that the high frequency component observed in the ^{23}Na MAS NMR spectra is, due to their association with NBO, bearing phosphate species (Na^+ $^-$O-P), while the lower frequency component of the ^{23}Na spectra represents sodium ions more strongly connected with $(AlO_4)^-$ units.

Regime (III) concerns the region where $15.00 \leq x \leq 17.50$. In the sample with x = 15.00, no significant amount of $P^{(4)}$ units is observed, meaning that these units are completely converted to a less connected structure. This sample presents half of the Na content balancing the $(AlO_4)^-$ structure, and the other half interacting with NBOs in $P^{(3)}$, $P^{(2)}$ and possibly $P^{(1)}$ units. The latter unit was expected to increase its proportion in the network for the sample x = 17.50, at which point the limit of the glass forming region is reached, and crystalline $Na_4P_2O_7$ is formed. For this sample a large fraction of the phosphorus is present in this form. Thus, a sharp peak is seen in the ^{31}P NMR shows a strong dipolar interaction with the high frequency site in ^{23}Na MAS-NMR spectra, detected by the expected high $M_{2(Na-P)}$ -value measured in the ^{23}Na (^{31}P) REDOR experiment. Likewise, the $^{31}P(^{23}Na$)REAPDOR single point experiment reveals strong dipolar dephasing as expected.

The clustering method applied for sodium distributions resulted in a consistent model with clear distinction between a site associated with stronger connection with phosphorus and a second site hypothesized as the connection between Na^+ and $(AlO_4)^-$. In a similar vein, the cluster analysis permitted a differentiation between $Al^{(4)}{}_{4Si}$ ($\delta_{iso} > 55$ ppm) and ($Al^{(4)}{}_{2Si,2P}$ and $Al^{(4)}{}_{4P}$) units. The next step is to use a single Czjzek distribution to simulate the distributions $Al^{(4)}{}_{2Si,2P}$ and $Al^{(4)}{}_{4P}$ as a single entity.

In this study, the concentration of sodium in the network and the role that this ion assumes have played a central role in distinct network regimes. The ability of ^{23}Na NMR to distinguish Na^+ ions with these distinct roles is based on the correlation of ^{23}Na chemical shifts with average Na-O bond lengths: sodium ions balancing the anionic charges of NFUs established by bridging oxygen species (such as AlO_4^- units)$^-$ tend to be more ionic, having longer Na···O distances (and possibly higher coordination numbers, producing lower isotropic chemical shifts). In contrast, sodium ions interacting with NBOs tend to be more covalently bonded, having shorter Na···O distances (and lower coordination numbers, producing higher isotropic chemical shifts).

6.2 SPAN glasses

The glass samples labelled as SPAN have the nominal composition of $28Na_2O$ – $13Al_2O_3$ – (59-x) P_2O_5 – x SiO_2 in molar percentage. Figure 53 shows the non-linear behavior of the coefficient of thermal expansion (in blue) and of the glass transition temperature (in red), with a maximum and minimum for the glass x = 6, respectively. Moreover, an improved weathering stability was observed at around this concentration, as shown in Figure 54. Studies suggest that the higher the polymerization degree of the network, the higher the glass transition temperature and the lower the coefficient of thermal expansion. [38,129–131] Some studies also indicate that chemical durability is affected not only by the chemical composition but also by the proportion of linkages that are susceptible to hydrolysis.[22,131,132] For instance, well-established studies showed that the addition of alumina to phosphate glasses can strengthen their chemical durability due to the formation of Al-O-P linkages.[33–36] Additionally, the weathering of a glass is commonly initiated by the interaction of network modifiers, such as Na^+ ion, with neutral water from the atmosphere. The reactions of the Na^+ cation with H_2O trigger the glass deterioration process.[22,130]

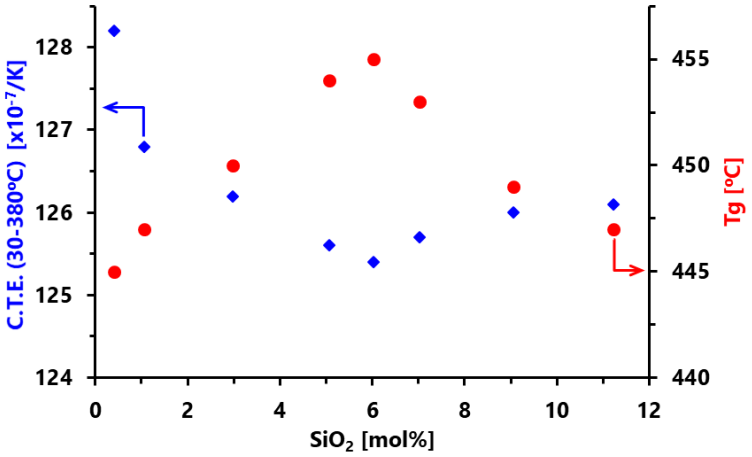

Figure 53 - Coefficient of thermal expansion (C.T.E), in blue, and glass transition temperature (T_g), in red, against the concentration of silica in the network in the glasses $28Na_2O$ – $13Al_2O_3$ – (59-x)P_2O_5 – xSiO_2. The graph shows the non-linear trend of the properties.

Source: LOGRADO *et.al.*[104]

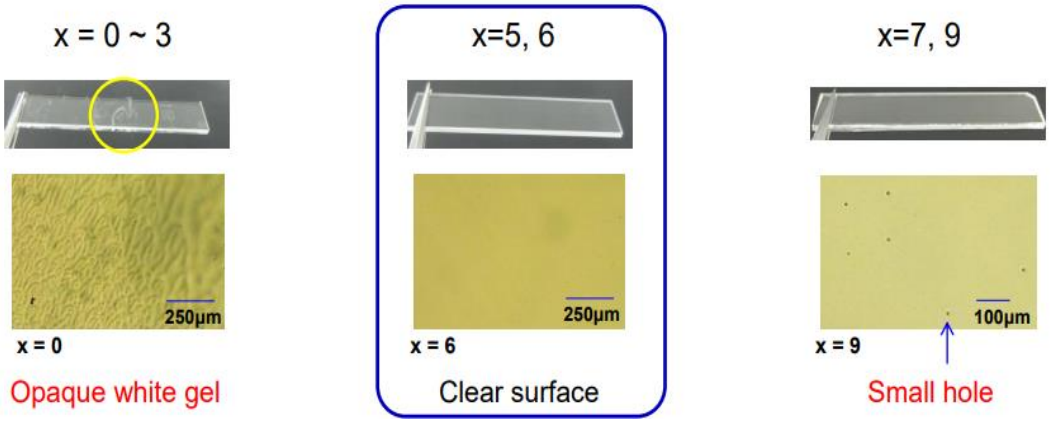

Figure 54 - Electron micrographs of glasses following exposure for 30 days to a humidity chamber. The highest weathering resistance could be observed for glasses with x = 5 and x = 6.
Source: NIPPON ELECTRIC GLASS Ltd.

Therefore, it is hypothesized that the observed non-linear trend might correlate with non-linear trends in the network connectivity and/or the local environment of the sodium ions. To shed light on the origins of the glasses' chemical stability, a detailed NMR study was undertaken to elucidate the effect of silica on the structural organization of these glasses.

6.2.1 ^{29}Si MAS-NMR

Figure 55 shows the ^{29}Si MAS-NMR spectra of the five Si-containing glasses. The spectrum of the sample x = 3 did not yield any signal, even after a three-days long measurement owing to the low amount of silica (in this sample) combined with the low sensitivity of the ^{29}Si isotope (natural abundance 4.7% and long longitudinal relaxation times) to NMR measurements.[133] The ^{29}Si MAS spectra of the other samples were successfully acquired. The spectra of four other samples (x = 6, 9, 11 and 13) were fitted with Gaussian lineshapes, and the results of the simulations are summarized in Table 21.

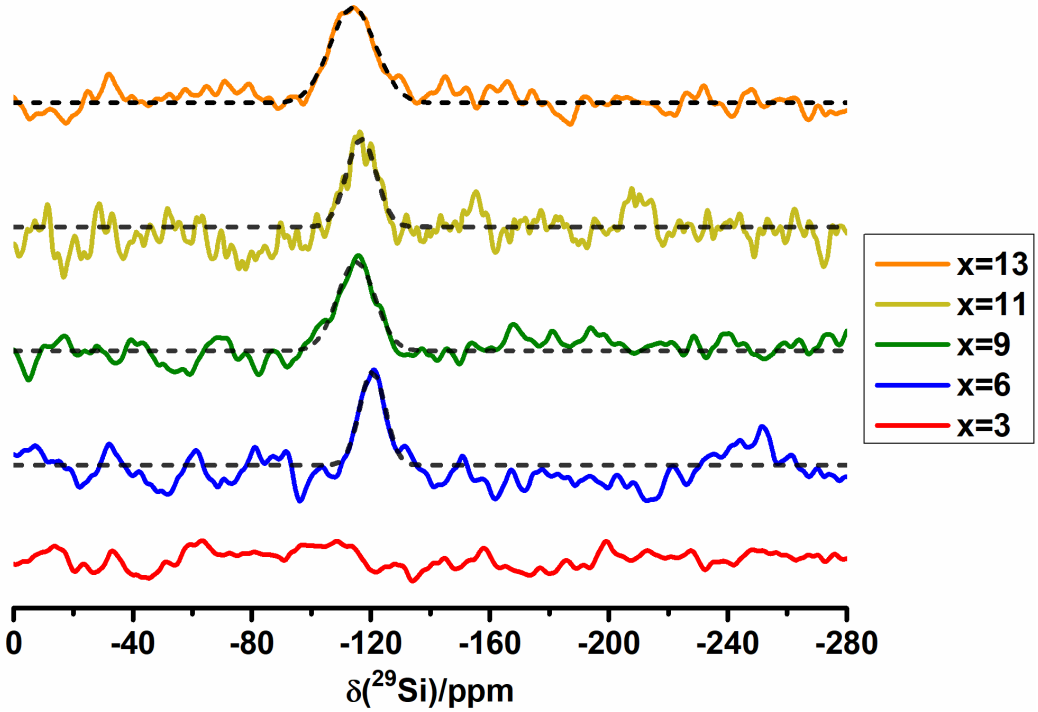

Figure 55 - ^{29}Si MAS spectra of $xSiO_2$ $(59-x)P_2O_5$ – $13Al_2O_3$ – $28Na_2O$ glasses. The dash lines represent the deconvolutions whereas the coloured curves represent the spectra.
Source: LOGRADO *et.al.*[104]

Table 21 - ^{29}Si isotropic chemical shift of each curve and the respective full width at half maximum.

Sample	δ_{iso} / ± 1 (ppm)	FWHM / ± 1 (ppm)
x = 6	-121	10
x = 9	-115	15
x = 11	-117	12
x = 13	-114	18

Source: LOGRADO *et al.*[104]

A broad peak maximum near approximately -115 to -121 ppm is observed, providing structural information about the ^{29}Si surroundings in the glasses. The isotropic chemical shift clearly indicates that all the Si atoms are fully polymerized, forming only Si^4 units. Based on the composition of these glasses, silica could be forming various linkages, including Si-O-P, Si-O-Si, or Si-O-Al units. Linkages such as Si-O-P produce shifts towards lower resonance frequencies,[121] while Si-O-Al linkages cause higher frequency shifts[127], both in comparison to the silica found in silicate glasses.[134]

For low x samples, the spectra unambiguously indicate that the Si^4 units are mostly connected to phosphorus, due to the considerably lower range of the resonance frequencies. However, with increasing x, we observe a shift towards higher frequencies, which can be attributed to the formation of Si-O-Al and/or Si-O-Si linkages. The evidence for the formation

of Si-O-Al and Si-O-Si linkages will be reinforced further in this work by the ^{27}Al NMR and ^{31}P NMR results.

In certain ternary sodium phosphosilicate and in some quaternary alkali silica-aluminophosphate glasses, with a [Si]/[P] ratio similar to the ones studied here, $Si^{(5)}$ and $Si^{(6)}$ species have been observed.[135–137] In principle, the presence of these units in the phosphorus-rich glasses in this study could be hypothesized. Nonetheless, the presence of significant amounts of aluminum creates an unfavorable chemical environment for the formation of these superstructural higher-coordinated silica units. The addition of aluminum into the network competes successfully for the connections with phosphorus polyhedra, as reported by Nizamutdinova *et al.* [29] They showed that the decreased amount of $Si^{(6)}$ is due to the addition of aluminum into the network, consequently $Si^{(6)}$ units vanish. In the current study, the competition is already well established in favor of Al-O-P connections and, despite the fact that phosphorus dominates silica's first neighborhood, no $Si^{(6)}$ is observed.

6.2.2 ^{27}Al MAS-NMR

The results of ^{27}Al MAS NMR are shown in Figure 56, and the corresponding parameters are summarized in Table 22. The MAS NMR spectra in Figure 56 (a) exhibit three resonance lines in the central transition, corresponding to Al(IV) resonating at near 40 ppm, Al(V) at around 9 ppm and Al(VI) resonating at -14 ppm, dominating the spectrum. These peaks are characteristic of resonance frequencies found in sodium aluminophosphate glasses.[34]

TQMAS provided improved resolution for the ^{27}Al spectra, as shown by Figure 56 (b) and yielded consistent results for the chemical shift and SOQE values, as shown in Table 23. Both regular ^{27}Al MAS NMR and TQMAS showed that the proportion of Al(IV) and Al(V) increases at the expense of Al(VI) as the amount of silica in the network increases. Although TQMAS is not a quantitative technique, this trend was also observed, indicating that the addition of Si into the network leads to a change in aluminum's role from charge balancer (as an Al(VI) unit) to network former (in the Al(IV) unit).

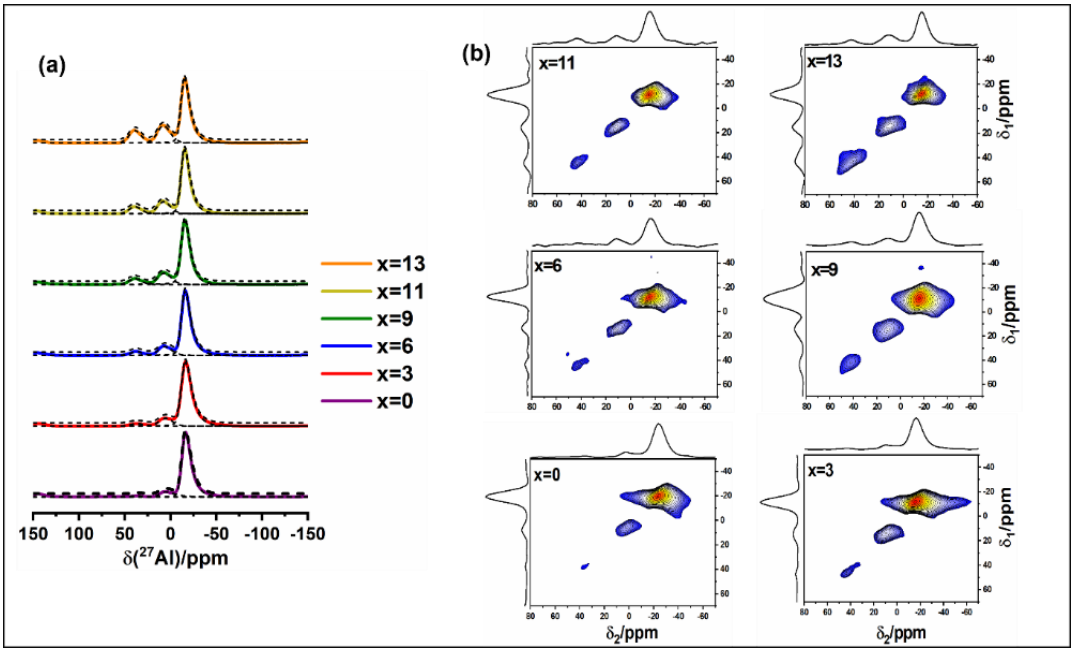

Figure 56 - (a) ^{27}Al MAS NMR spectra of $xSiO_2 – (59\text{-}x)\ P_2O_5 – 13Al_2O_3 – 28\ Na_2O$. Dashed curves fit the Czjzek distribution regarding Al(IV), Al(V) and Al(VI) units. The dash lines represent the deconvolutions whereas the coloured curves represent the spectra. (b) Triple Quantum ^{27}Al NMR spectra of $xSiO_2 – (59\text{-}x)\ P_2O_5 – 13Al_2O_3 – 28\ Na_2O$ glasses.
Source: Adapted from LOGRADO *et al.*[104]

Table 22 - Percentage area A occupied by the simulation of central peak distribution, where the total area of the peak is normalized to 1, Average Isotropic ^{27}Al Chemical Shift and Quadrupolar Coupling $\langle|C_Q|\rangle$ (extracted from One Pulse spectra), site selective second Moment $M_{2(Al\text{-}P)}$ and total second moment $M_{2(Al\text{-}P)}{}^t$ as analyzed from dipolar dephasing of the entire signal (extracted from REDOR).

Sample	A ±1 (%)	δ_{iso} ±0.5 (ppm)	$\langle\|C_Q\|\rangle$ ±0.5 (MHz)	$M_{2(Al\text{-}P)}$ ±10% (10^6 rad^2/s^2)	$M_{2(Al\text{-}P)}{}^t$ ±10% (10^6 rad^2/s^2)
x = 0	2	39.0	3.0	-	5.28 (3.64)
	8	7.6	3.0	5.25 (3.62)	
	90	-12.7	4.6	5.43 (3.75)	
x = 3	4	39.0	4.4	-	5.09 (3.51)
	12	8.3	3.4	4.67 (3.24)	
	84	-12.2	5.0	5.22 (3.60)	
x = 6	5	40.7	3.2	3.35 (2.31)	4.54 (3.13)
	14	10.0	3.9	3.57 (2.46)	
	81	-12.3	4.7	4.68 (3.35)	
x = 9	9	41.0	3.3	4.39 (3.03)	4.93 (3.40)
	18	10.3	3.9	4.23 (2.92)	
	73	-12.0	4.6	5.29 (3.65)	
x = 11	10	41.0	3.0	4.90 (3.38)	4.67 (3.22)
	18	10.6	3.6	4.13 (2.85)	
	72	-11.6	4.6	4.96 (3.42)	
x = 13	15	41.6	3.3	4.96 (3.42)	4.38 (3.02)
	22	11.0	3.7	3.86 (2.66)	
	63	-11.8	4.7	4.79 (3.31)	
$Al(PO_3)_3$	-	-	-	6.80 (4.70)	6.80 (4.70)

Source: By the author

Table 23 - Average Isotropic ^{27}Al Chemical Shift and Quadrupolar Product P_Q extracted from MQMAS.

Sample	δ_{iso} ± 0.5 / (ppm)	P_Q ±0.5 / (MHz)
x = 0	-	-
	12.0	3.9
	-14.1	4.3
x = 3	41.8	3.0
	-11.4	4.0
	-13.4	3.7
x = 6	42.1	3.3
	12.4	3.4
	-13.3	4.0
x = 9	41.0	3.2
	12.2	4.2
	-13.9	4.1
x = 11	42.4	3.0
	13.6	4.0
	-11.9	4.2
x = 13	42.0	3.3
	13.3	3.9
	-12.6	4.0

Source: By the author

The trend, regarding the conversion of Al(VI) to Al(IV) with increasing *x*, presented in the previous paragraph is shown in Figure 57, with green dots representing the NAPS glasses. Based on the simulations of the central peak in each spectrum, it was possible to determine the percentage occupied by each distribution within the central peak, thereby extracting the average coordination number. The trend indicates that as the O/P ratio increases from 3.06 to 3.51 (due to the addition of silica into the network), the P-O-Al(VI) structure may not balance the charge of oxygen, resulting in an underbonded oxygen. Consequently, the average coordination number of aluminum decreases with increasing silica concentration. [29,33-34] The figure compares the effect observed in the current work with the effect observed in ternary alkali aluminophosphate glasses investigated by Brow *et al*.[34] It is noteworthy that within the range $3.06 \leq O/P \leq 3.51$, the ^{27}Al coordination number shows a behavior like that found in pure ternary sodium aluminophosphate glasses. [34]

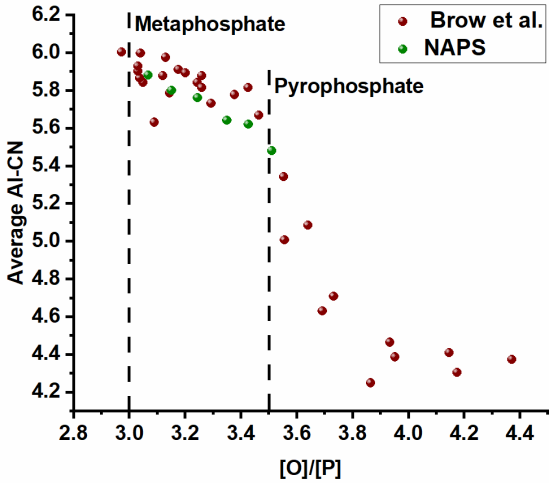

Figure 57 - Correlation between the ^{27}Al average coordination number (extracted using the simulation of the central peak) and theoretical O/P ratio observed in the glasses studied here, and in the work done by Brow *et al.* [34]

Source: By the author.

Regarding the change from Al(VI) to Al(IV) and Al(V), it might happen through two different concomitant and independent MRO rearrangements. On the one hand, phosphorus may be able to maintain itself as the main neighbor of aluminum through the formation of P-O-Al(IV) and P-O-Al(V) connectivities. On the other hand, silica could drive the reorganization, competing successfully in the network and bringing aluminum to its vicinities. To shed light on the environment around aluminum, ^{27}Al/^{31}P double resonance experiments were performed.

The ^{27}Al local structure motifs were investigated by performing ^{27}Al(^{31}P) REDOR experiments, and spectra S and S_0 were deconvoluted through two distinct methods. First, each AlO_x curve was deconvoluted with two Gaussian lines (data not shown) and, second, each AlO_x curve was deconvoluted with a single Czjzek curve, which is the more rigorous method. The dephasing curve resulting by applying the latter method is shown in Figure 58, where it is possible to observe that the scattering of the points in the dephasing curve has only minor fluctuations. By using the first points of dephasing curve to fit the Equation (67), $M_{2(Al-P)}$ values were extracted. The same procedure was done for the double Gaussian per (AlO_x) analysis. It is important to highlight that, although deconvoluting the ^{27}Al MAS NMR into distinct Gaussian lines is conceptually wrong, when the single porpoise is sole extracting the area that each distribution occupies (and not modelling the behavior of the spectrum), the method resulted in great agreement with the more laborious multiple Czjzek curves, as will be shown in short. The parameters are summarized in Table 22.

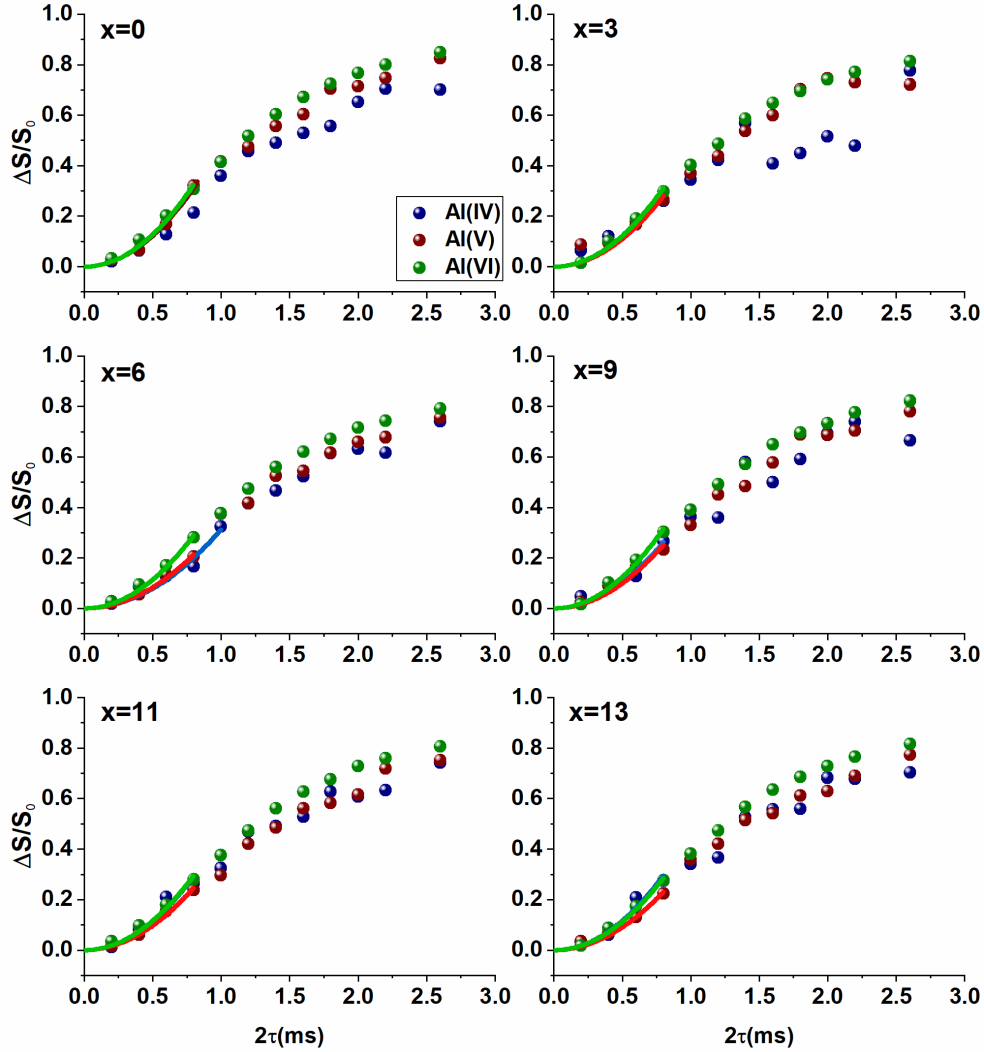

Figure 58 - $^{27}Al(^{31}P)$ REDOR dephasing of the Czjzek distributions used to deconvolute each spectrum of x SiO_2 – (59-x)P_2O_5 – 13Al_2O3 – 28Na_2O glasses. The parabolic curves were fitted within the range $\Delta S/S_0 <$ 0.3 to yield the $M_{2(Al-P)}$ value.

Source: By the author.

Figure 59 illustrates the $M_{2(Al-P)}$ calculated by the distinct methods plotted against the concentration of silicon in the network: (a) using the single Czjzek model and (b) using the double Gaussian method. The black dots represent $M_{2(Al-P)}$ of ^{27}Al spectra (sum of 3 sites), the green dots represent the $M_{2(Al-P)}$ of Al(V), and the red dots represent the $M_{2(Al-P)}$ of Al(VI). Since Al(IV) represents a minor portion of the spectrum, its contribution to explaining structural effects might be negligible, and the error associated with the calculation of its $M_{2(Al-P)}$ might be considerably larger. Due to this, the analysis done for the Al(IV) is omitted in Figure 59. It is also worth noting that both results showed a similar curve with a minimum seen in the sample x = 6. This dip represents, in terms of the aluminum vicinity, the minimal through-space dipolar interaction between ^{31}P and ^{27}Al.

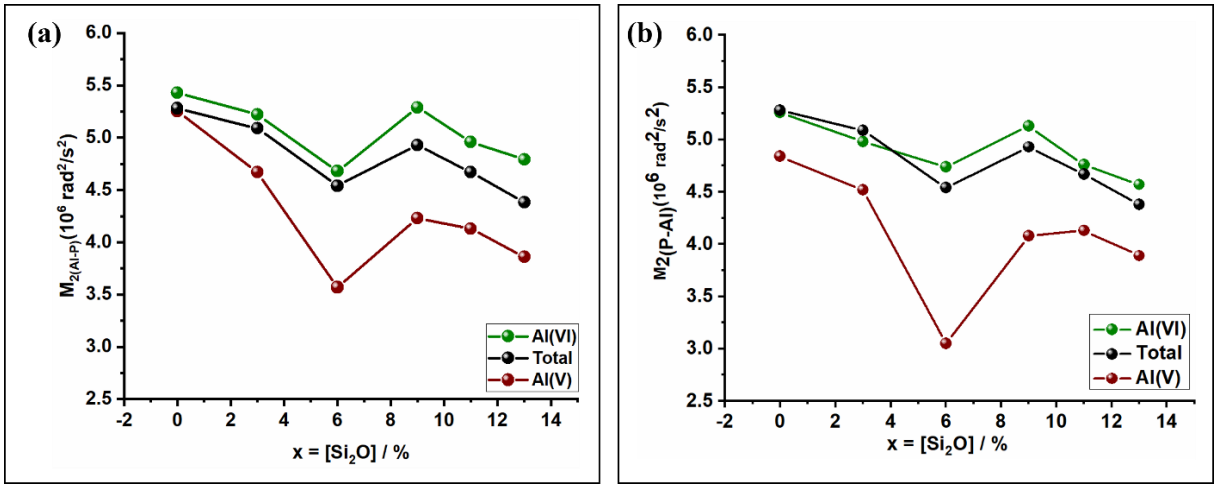

Figure 59 - $M_{2(Al\text{-}P)}$ values of each sample plotted against the concentration of silica of SiO_2 – (59-x)P_2O_5 – 13Al_2O_3 – 28Na_2O glasses. $M_{2(Al\text{-}P)}$ values were extracted by using $^{27}Al(^{31}P)$ REDOR experiment and simulating the dephasing of each AlO_x polyhedra separately using (a) one Czjzek curve in each site and (b) two Gaussians distributions to simulate each site S and S_0 spectra.
Source: By the author.

In principle, it would be reasonable to expect that, the higher the amount of silica, the lesser the phosphorus available in the network, and the smaller the probability of finding ^{31}P in ^{27}Al surroundings would be, as the P/Al ratio decreases with increasing x. However, this expectation was not confirmed. Rather, Figure 59 shows that this correlation is not monotonic, and the second moment of the x = 6 sample presents a value particularly slightly out of the expected trend. This result can be understood in terms of connectivity: in a glass composition with increased concentration of aluminum as a network-former, if Al showed to be less connected to P, and Lowenstein's rule is obeyed, Al nuclei might be more connected with silica.[138]

Based on some studies, it has been hypothesized that the higher the weathering resistance, the lower the number of P-O-P linkages.[21,130-131] As it will be discussed in the subsection dedicated to ^{31}P, such evidence was not verified by NMR experiments investigating ^{31}P homonuclear interactions. The current study indicates that, in quaternary alkali silica-aluminophosphate glasses, the glass properties might not be attributed to a single structural origin, and other connectivities might play a role in enhancing chemical durability.

Accordingly, Hamilton *et al.* showed for aluminosilicate nepheline, jadeite, and albite glasses that dissolution rate values increased with increasing [Al]/[Si] ratio, which partially explain the initial trend of the current study observed in both $M_{2(Al\text{-}P)}$ values and weathering stability vs. silica concentration.[21,132] With the addition of silica into the network, it is expected that more Si-O-Al connections are being formed. This drives $M_{2(Al\text{-}P)}$ to lower values and moves

the chemical shifts of ^{29}Si towards higher frequencies. Finally, the systematic decrease in the number of Al atoms per Si tetrahedron would also systematically decrease the dissolution rate.

However, for the sample x = 9, $M_{2(Al\text{-}P)}$ increases concomitantly with the chemical shift of ^{29}Si, which is hypothesized as the formation of silica-rich nano domains.[115] Through the formation of Si-O-Si linkage owing to the segregation of silica, aluminum may be available to recover part of the Al-O-P bonds; at the same time, Si-O-Si bonds would shift the resonance frequency towards lower values, in agreement with the ^{29}Si MAS-NMR result.

6.2.3 ^{31}P MAS -NMR and ^{31}P static-NMR

Figure 60 (a) illustrates ^{31}P MAS-NMR and (b) ^{31}P static NMR spectra. Both experiments reveal broad spectra and distinct sites could not be resolved by the regular MAS technique. Indeed, the simultaneous presence of different phosphorus environments, such as P-O-P, P-O-Si and P-O-Al linkages, covers a wide range of chemical shifts, broadening the spectra. For instance, the chemical shifts difference of $P^{n}_{m(Al)}$ and $P^{n-1}_{(m+1)(Al)}$ is too small to be unambiguously distinguished when investigating amorphous material.[55,139-140] Consequently, the unambiguous assignments of ^{31}P resonance lines are a hard task and should be done with more constraints to avoid the arbitrariness.

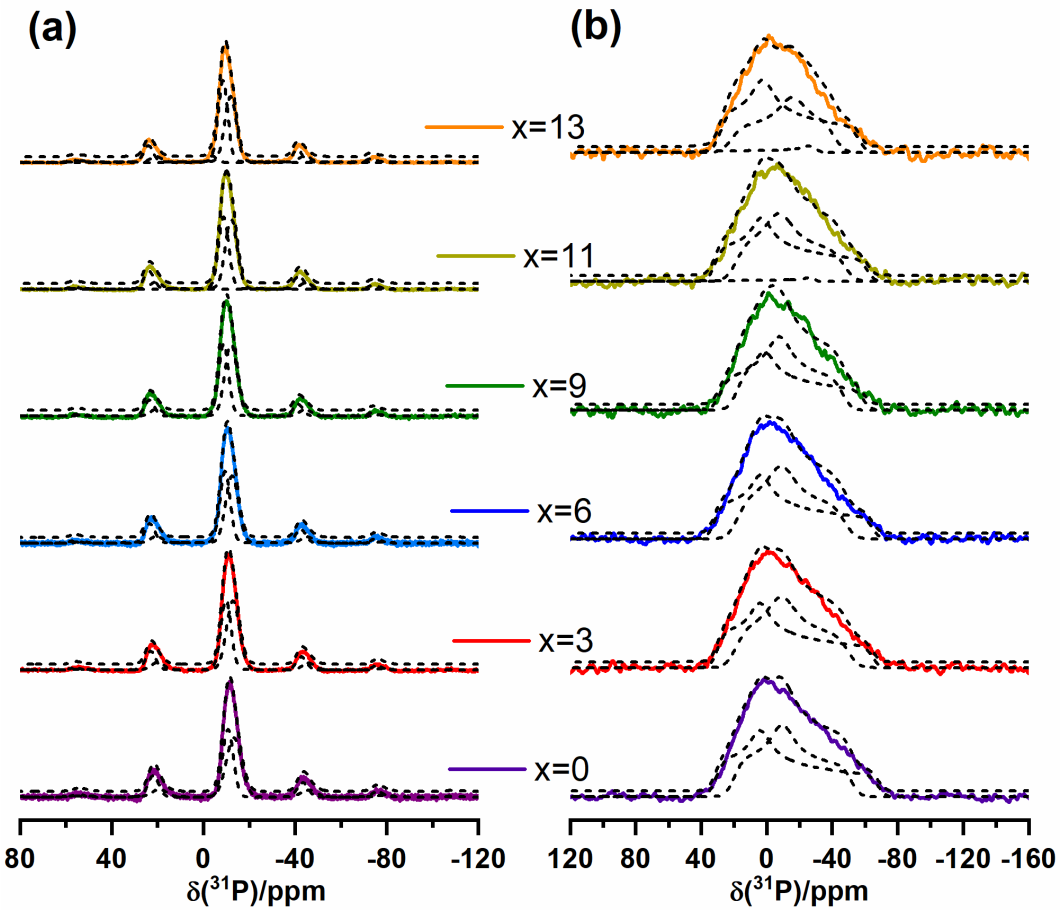

Figure 60 - For (a) ^{31}P MAS spectra and (b) ^{31}P static spectra of $xSiO_2 – (59\text{-}x)P_2O_5 – 13Al_2O3 – 28Na_2O$ glasses with x = 0, 3, 6, 9, 11 and 13. In both parts of the figure, lineshape deconvolutions are indicated by dashed curves. In both cases the dash lines represent the deconvolutions whereas the coloured curves represent the spectra. These spectra were acquired under 5.7T and (a) also under a MAS speed of 8KHz.

Source: By the author.

In order to find constraints to ^{31}P static and MAS deconvolutions, S and S_0 lineshapes corresponding to a 1.6 ms dipolar recoupling evolution time of $^{31}P(^{23}Na)$ and $^{31}P(^{27}Al)$ REAPDOR experiments were analyzed. Figure 61 shows the results for $^{31}P(^{23}Na)$ REAPDOR experiment for sample x = 0, 9 and 13. By the comparison between S_0 and S total intensities, single point $^{31}P(^{23}Na)$ REAPDOR confirms that sodium is a charge balancer for ^{31}P units. However, when the ^{23}Na dipolar recoupling was turned on, changes in the lineshape were detected, resulting in a displacement of isotropic chemical shifts toward lower frequencies. This latter observation shows that ^{31}P nuclei resonating at higher chemical shifts were more affected by ^{23}Na dipolar recoupling than ^{31}P nuclei resonating at lower chemical shifts. Fully consistent with the $^{31}P(^{23}Na)$ REAPDOR experiment is the result of the $^{31}P(^{27}Al)$ REAPDOR (single point data not shown). Therefore, Figure 61 shows the low frequency (LF), which shows a stronger dipolar interaction with sodium in comparison with the high freqeuncy componenent (HF).

Complementarily, the latter experiments indicated that HF component dephased to a lesser extent due to ^{27}Al dipolar recoupling, than ^{31}P nuclei resonating at lower frequencies. Thus, the latter represents the phosphate species connected more strongly (and charge balanced) by ^{27}Al.

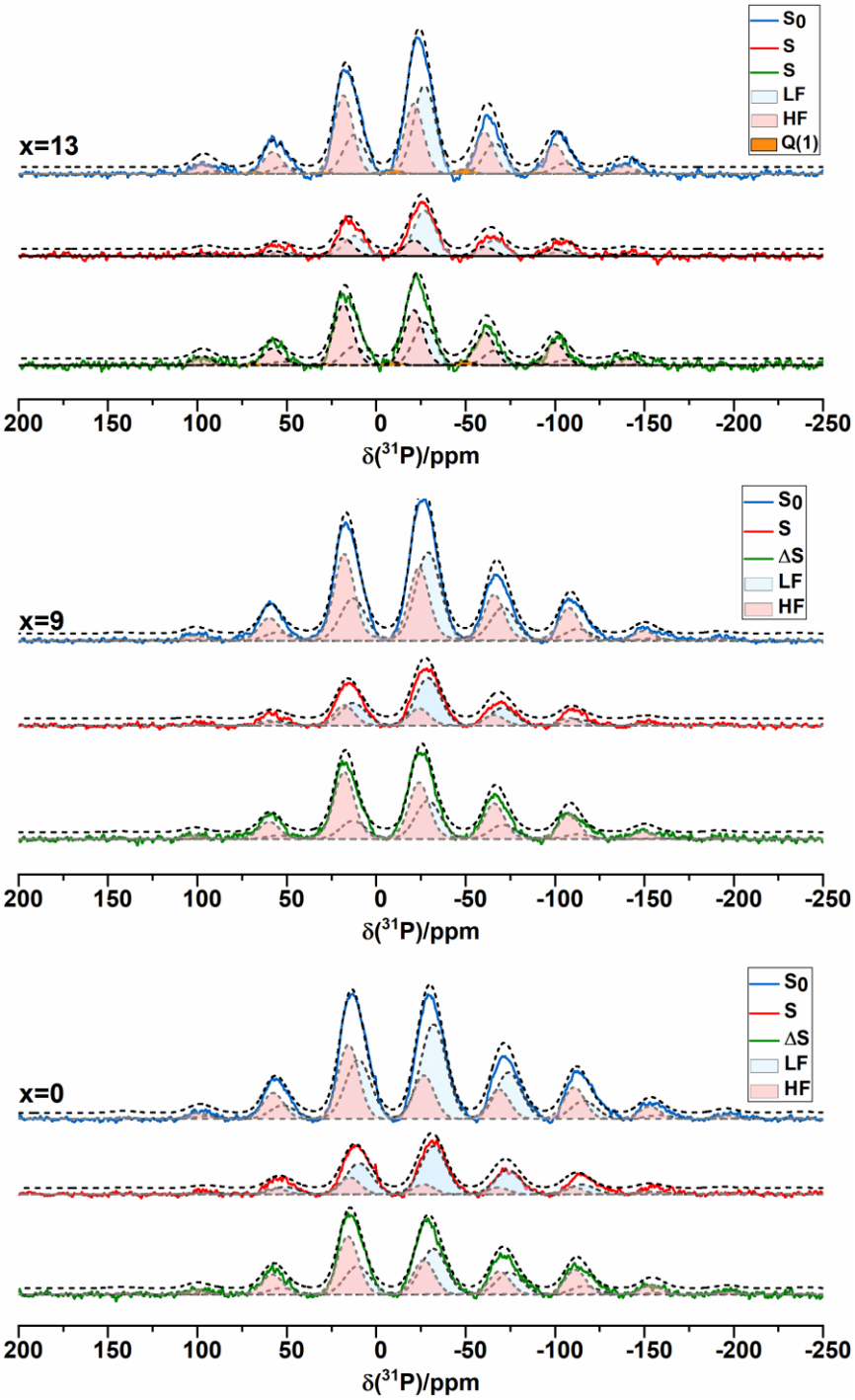

Figure 61 - The S_0 (blue curves), S (red curves) and ΔS (green curves) corresponding to a 1.6ms evolution time of ^{31}P(^{23}Na) REAPDOR experiment for samples x = 0, 9 and 13. Note the spectral deconvolution with two components. The higher-frequency site (solid pink) has its intensity more affected by ^{23}Na dipolar recoupling than the lower-frequency site. These spectra were acquired in a 14.1T field under a MAS speed of 10KHz.

Source: By the author.

Based on the behavior of the three samples exposed, a rationalized deconvolution model was proposed. The most reasonable deconvolutions would be achieved by simulating the central peak as well as the area corresponding to the sidebands (in MAS and REAPDOR spectra) with the same parameters (δ_{iso}, δ_{aniso}, η and the relation of area are the same for all three distinct spectra,) used in ^{31}P -Static spectra. For each glass, all the spectra (MAS, S and S_0 REAPDOR and Static) should be consistent with same set of parameters, within the experimental error. The best parameters found to ^{31}P -Static, -MAS as well as 1^{st} S_0 REAPDOR $^{31}P(^{27}Al)$ are summarized in Table 24, and single-point $^{31}P(^{23}Na)$ REAPDOR experiments are summarized in Table 25.

Table 24 - Total area occupied by the Gaussian distributions (A), average isotropic ^{31}P chemical shift (δ_{iso}), anisotropic ^{31}P chemical shift (δ_{aniso}), asymmetry parameter (η) and homonuclear second moment ($M_{2(P-P)}$).

Sample	Pulse Sequence	A ±1 (%)	δ_{iso} ±1 (ppm)	δ_{aniso} ±5 (ppm)	η_{Hae} ± 0.05	$M_{2(P-P)} \pm 0.6$ (10^6 rad^2/s^2)
0	Static	48	-34	-94	0.78	10.1
		52	-27	-141	0.48	
	MAS	49	-33	-94	0.78	
		51	-27	-141	0.48	
	1^{st} S_0 REAPDOR	51	-32	-94	0.78	
	$^{31}P(^{27}Al)$	49	-27	-141	0.48	
3	Static	49	-33	-90	0.77	10.0
		51	-25	-135	0.48	
	MAS	49	-32	-90	0.77	
		51	-25	-135	0.48	
6	Static	48	-32	-86	0.77	9.1
		52	-24	-136	0.51	
	MAS	48	-31	-86	0.77	
		52	-24	-136	0.51	
9	Static	51	-30	-85	0.75	9.5
		49	-24	-122	0.56	
	MAS	51	-30	-85	0.75	
		49	-22	-122	0.56	
	1^{st} S_0 REAPDOR	50	-28	-85	0.75	
	$^{31}P(^{27}Al)$	50	-22	-134	0.56	
11	Static	50	-30	-87	0.75	5.9
		49	-22	-130	0.55	
		1	-10	120	0.00	
	MAS	46	-30	-87	0.75	
		52	-22	-130	0.55	
		2	-10	120	0.00	

(continued)

(continuation)

Table 24 - Total area occupied by the Gaussian distributions (A), average isotropic ^{31}P chemical shift (δ_{iso}), anisotropic ^{31}P chemical shift (δ_{aniso}), asymmetry parameter (η) and homonuclear second moment ($M_{2(P-P)}$).

Sample	Pulse Sequence	A ±1 (%)	δ_{iso} ±1 (ppm)	δ_{aniso} ±5 (ppm)	η_{Hae} ± 0.05	$M_{2(P-P)}$ ±0.6 (10^6 rad^2/s^2)
13	Static	41	-29	-83	0.77	
		56	-21	-118	0.55	6.6
		3	-10	120	0.00	
	MAS	43	-29	-83	0.77	
		53	-21	-118	0.55	
		3	-10	120	0.00	
	1^{st} S_0 REAPDOR	40	-29	-83	0.77	
	$^{31}P(^{27}Al)$	57	-21	-118	0.55	
		3	-10	120	0.00	

Source: By the author

Table 25 - Total area occupied by the Gaussian distributions (A) in $^{31}P(^{23}Na)$ REAPDOR experiments, average isotropic ^{31}P chemical shift (δ_{iso}), anisotropic ^{31}P chemical shift (δ_{aniso}) and asymmetry parameter (η), both from static lineshapes, and s homonuclear second moment ($M_{2(P-P)}$) from SED experiments

Sample	S_0 ±2 (%)	S ±2 (%)	ΔS ±2 (%)	δ_{iso} ±1 (ppm)	δ_{aniso} ±5 (ppm)	η_{Hae} ±0.05
0	56	74	43	-32	-95	0.78
	44	26	57	-27	-145	0.48
9	44	64	31	-29	-85	0.75
	56	36	59	-24	-122	0.56
13	43	64	31	-29	-76	0.75
	55	36	66	-21	-111	0.55
	2	0	3	-10	120	0.00

Source: By the author

Finally, Figure 60 and Figure 61 exhibt the final result of the deconvolutions, based on dipolar recoupling experiments. The higher frequency components were found in the range of [-25,-21] ppm and were interpreted as P^2 units more strongly charge-balanced by the Na^+ ions charge. The low frequency components, observed in the range of [-33,-29] ppm, were attributed as, also, $P^2_{m(Al)}$ units more strongly bonded to Al (also balanced in the case by Al(VI) species).

In order to quantify the 'm' number of bonds between P and Al isotopes, the deconvolutions were used in the extension of whole $^{31}P(^{27}Al)$ REAPDOR curve. In other words, S_0 and S spectra were dencovoluted with the same set of parameters, whereas only the amplitude was allowed to vary freely for each S_0 and S spectra in each evolution time. The result for samples x = 0 (in yellow), x = 9 (in green) and x = 13 (in purple) were exposed in Figure 62. The low frequency (LoF) components are marked with triangle symbols whereas the high frequency (HF) components are depicted by circles. For comparison the result for $Al(PO_3)_3$ is

shown. According to its crystalline structure, the two shortest P-Al distances are 3.13 Å and 3.42 Å.[92] The red line represents the simulation of ^{31}P dephasing curve, of a structure with single P-O-Al bond, whose length corresponded to $d_{P\text{-}Al}$ = 3.13 Å (Sim1). The black curve represents the simulation of the ^{31}P dephasing curve of a structure with two P-O-Al bonds, whose lengths corresponded to $d_{P\text{-}Al}$ = 3.13 Å and $d_{P\text{-}Al}$ = 3.42 Å (Sim2) and whose angle $\theta_{Al\text{-}P\text{-}Al}$ = 94.97º. These simulations were done using the SIMPSON package.[141]

Consistently, the LoF components dephased as intense as $Al(PO_3)_3$ in the whole set of experimental data points and in-between of Sim1 (P_{1Al}) and Sim2 (P_{2Al}). Therefore, we can conclude that the LoF site is composed of P nuclei having between 1 and 2 linkages to Al. On the other hand, the HF component, already demonstrated as exhibiting stronger Na-P connections, showed a weaker dephasing under ^{27}Al dipolar recoupling. Its dephasing curve, located under the Sim1 (P_{1Al}), proves that the HF component is represented by P nuclei with between 0 and 1 linkages to aluminum.

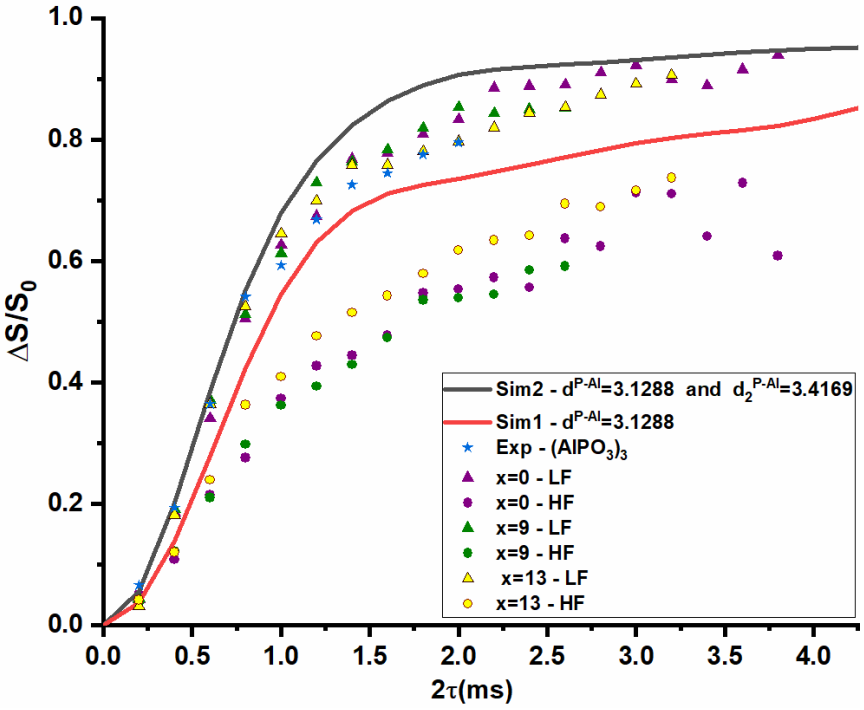

Figure 62 - $^{31}P(^{27}Al)$ REAPDOR experiment for samples x = 0 (in purple), 9 (in green) and 13 (in yellow). Low frequency (LoF) components are marked with triangle symbols whereas high frequency (HF) components are indicated with circle symbols. The solid red curve represents the simulation of ^{31}P dephasing due to a single internuclear of $d_{P\text{-}Al}$ = 3.13 Å with Al. The solid dark line represents the simulation of the ^{31}P dephasing curve in a three-spin system having $d_{P\text{-}Al}$ = 3.13 Å and $d_{P\text{-}Al}$ = 3.42 Å with Al and an angle of 94.97° between the dipolar vectors. Marked as blue stars are the experimental data of $Al(PO_3)_3$, which have a crystalline structure corresponding to the two closest P-Al distances being 3.13 Å and 3.42 Å.

Source: By the author.

As a result of dipolar recoupling experiments, the spectra shown in Figure 60 can be explained as having two components: first, a $P^2_{[0,1](Al)}$ unit, whose charge is more strongly balanced by Na ions; second, a $P^2_{[1,2](Al)}$ unit, whose vicinity is coordinated more strongly by Al. Also, in ^{31}P MAS-NMR a clear trend of the overall chemical shifts towards higher frequencies can be observed with increasing x, which may be understood based on successive replacement of P-O-P linkages with P-O-Si and P-O-Al linkages. In phosphate glasses, ^{31}P isotropic chemical shifts do normally resonate at lower values in comparison with those found in mixed oxide glasses containing Al_2O_3 and/ or SiO_2. Systematic substitution of P-O-P by P-O-Al and P-O-Si linkages tends to gradually deshield phosphorus environments,[117] as this trend is compatible with both, the ^{29}Si- and ^{27}Al MAS-NMR results. The decreased concentration of phosphorus in the network resulted in higher concentration of silicon and aluminum in phosphorus vicinity, which means to say a higher probability of P-O-Al and P-O-Si linkages at the expense of P-O-P linkages. In samples x = 11 and x = 13 a smaller shoulder (see Figure A6 – Appendix A) at x = -10 ppm was observed, which is consistent with the formation of a $P^{(1)}$ unit (phosphorus bonded with one network former).

For this project, it would be particularly interesting to investigate if the $P^{(1)}$ unit is connected in the network thought a P-O-P linkages or to another network former. The formation of P-O-P could trigger the hydrolysis, since this connectivity is often reported as having a central role in lowering the weathering stability and in increasing the dissolution rate.[21,22,129,131] In the INADEQUATE experiment, it is possible to use the double quantum excitation through the manipulation of through-bond spin-spin interaction as a filtering technique that allows selective detection of P atoms associated with of P-O-P linkages. Due to the increased [Na]/[P] ratio, sample x = 13 was used to test for the P-O-P linkages. The result is shown in Figure 63. No lineshape change was identified, proving that all $P^{(2)}$ units detected in previous experiment have at least one P-O-P linkage.

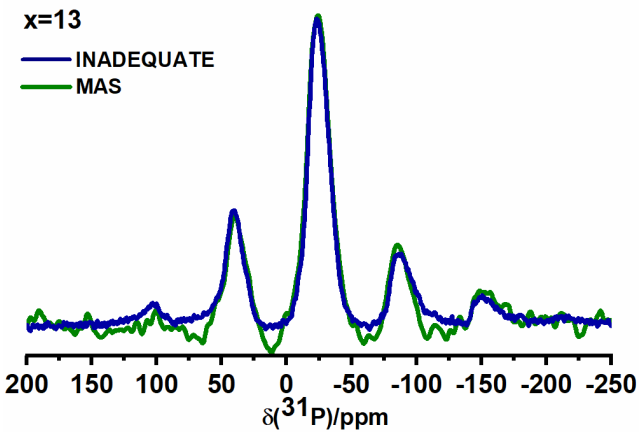

Figure 63 - Comparison between ^{31}P INADEQUATE and ^{31}P MAS.
Source: By the author.

However, the decrease of P-O-P linkage numbers would still be happening if the P-O-P bonds would have decreased the number from 2 to 1 bond, and this change would not be detectable by 1D INADEQUATE. To complement the latter result, a Spin Echo Decay static experiment was conducted to probe ^{31}P homonuclear though-space dipolar interaction, which is directly connected to the distance distribution of phosphorus in the network. Figure 64 (a) shows the SED data points and their respective Gaussian fittings, from where the average second moments $M_{2(P-P)}$ were extracted. Figure 64 (b) shows these $M_{2(P-P)}$ values plotted against SiO_2 concentration. Only a slight decrease of $M_{2(P-P)}$ values is seen within the region $0 \leq x \leq 9$. Although that is the expected trend, it is also hard to validate, as the data points are found equal within the experimental error ($0.6 \cdot 10^6$ rad^2/s^2). However, for samples x = 11 and x = 13, a significant decrease in $M_{2(P-P)}$ was observed, indicating a reduction of the average number of P-O-P linkages. This result agrees with the previously mentioned idea that the weathering resistance might not be traced to a single structural origin such P-O-P linkages causing the lack of weathering durability, but rather multiple structural origins should be considered.

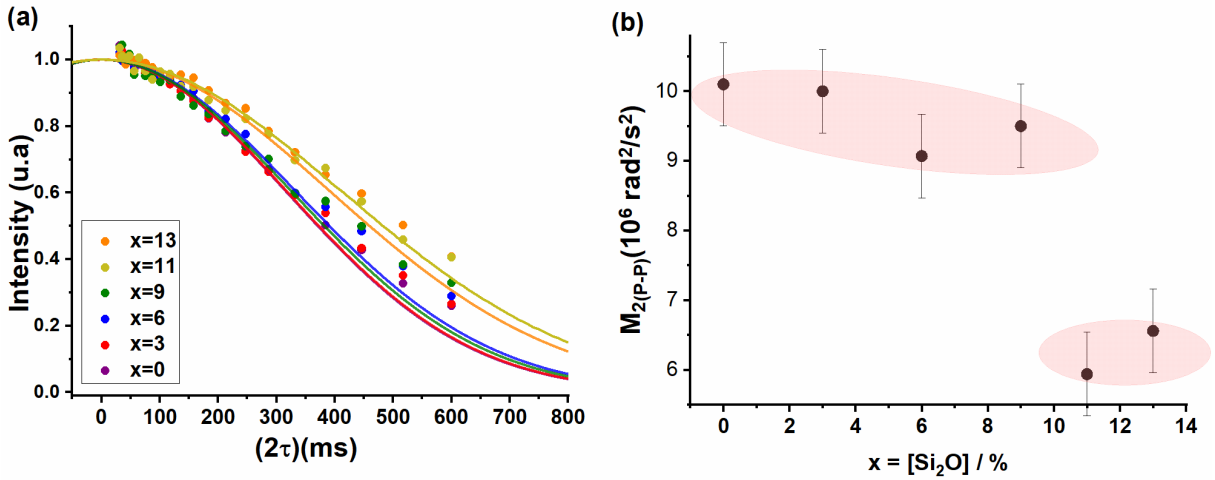

Figure 64 - (a) ^{31}P SED data points marked as circle symbols and simulated by Gaussian lineshapes, from which the average second moments $M_{2(P-P)}$ are extracted. (b) Average second moment $M_{2(P-P)}$ plotted against silica concentration.

Source: By the author.

6.2.4 ^{23}Na MAS-NMR

One common weathering mechanism observed in glasses is via the interaction of the network modifiers of the glasses with water. Cations of the glass, such as Na^+ balancing NBOs of the network, reacting with H_2O of the atmosphere is one of most prevalent mechanisms to start the glass deterioration process.[22,130] Due to this fact, an analysis of the ^{23}Na MAS-NMR spectra is of interest.

Figure 65 (a) illustrates ^{23}Na MAS spectral deconvolution, from where the isotropic chemical shift and average quadrupolar constants were extracted. The parameters are listed in Table 26. From the MAS result, no systematic effect on ^{23}Na spectra was observed as a result of the addition of Si into the network. For further investigation in sodium environment, ^{23}Na(^{31}P) REDOR experiments were performed to detect possible structural change of phosphorus in the vicinity of ^{23}Na. Figure 65 (b) shows that, within the experimental error, no change was observed. The considerable high values (values comparable to $Na_5B_2P_3O_{13}$) agree with the fact that sodium ions act as a charge balancer for $P^{(2)}$ units along the entire composition line and, $P^{(2)}$ units dominate sodium environment. Because no particular compositional trend was found, it seems that Na exhibits no protagonism in probing the changes of environment upon the addition of silica, consequently, did no probe particularities regarding the weathering resistant properties.

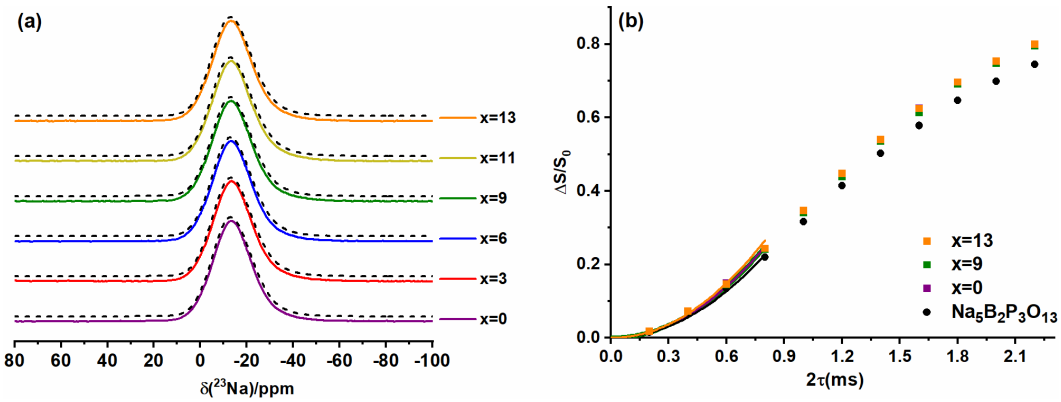

Figure 65 - (a) ^{23}Na MAS-NMR spectra of x SiO_2 – (59-x)P_2O_5 – 13Al_2O3 – 28Na_2O glasses. The dash lines represent the deconvolutions whereas the coloured curves represent the spectra. (b) ^{23}Na(^{31}P) REDOR dephasing data points for samples x = 0, x = 9 and x = 13. Parabolic curves according to Equation (67) curves were simulated for short evolution times. Comparatively, data are shown for the model calibration compound $Na_5B_2P_3O_{13}$.

Source: Adapted from LOGRADO *et al.*[104]

Table 26 - Parameters regarding ^{23}Na deconvolutions using the Czjzek distribution: average isotropic ^{23}Na chemical shift (δ_{iso}), average quadrupolar moment constant ($\langle|C_Q|\rangle$) and average second moment extracted from ^{23}Na(^{31}P) REDOR experiments ($M_{2(Na-P)}$). Inside the parenthesis, the experimental second moment is expressed, and outside the value accounting the calibration factor (Equation (67)).

Sample	δ_{iso} ±1 (ppm)	$\langle\|C_Q\|\rangle$ ±0.2 (MHz)	$M_{2(Na-P)}$ ±10% (10^6 rad^2/s^2)
x = 0	-8	2.4	5.8 (2.9)
x = 3	-8	2.4	-
x = 6	-8	2.4	-
x = 9	-8	2.4	5.8 (2.9)
x = 11	-7	2.5	-
x = 13	-8	2.4	6.2 (3.1)
$Na_5B_2P_3O_{13}$	-	-	5.2 (2.6)

Source: By the author

6.2.5 Discussion

In summary, structural details of quaternary xSiO_2 – (59-x)P_2O_5 – 13Al_2O_3 – 28Na_2O glasses were presented based on solid-state NMR spectroscopy. The network is formed through an abundant number of P-O-P linkages, as well as a significant contribution of P-O-Al connections. Based on a detailed analysis of REAPDOR data, the poorly resolved ^{31}P MAS-NMR spectra could be deconvoluted in terms of: (1) anionic P^2 units, resonating at higher frequency, whose charges are dominantly balanced by Na^+ ions; (2) metaphosphate P^2 units, resonating at lower frequency, showing stronger interactions with Al. The increased amount of Si in the network caused the ^{31}P isotropic chemical shift to displace towards higher frequencies and was interpreted as an increasing number in both P-O-Si and P-O-Al connectivities.

Particularly interesting results were found regarding Al vicinity. Upon the increased Si content into the network, a decreased average coordination number of Al was observed, which meant a change in Al-role from charge balancer (Al(V), Al(VI)) to network former (Al(IV)) due to Si-O-Al bond formation. Associated with this, the trend in $M_{2(Al-P)}$ values do not bear out the statistically expected decrease of Al-O-P connectivities. Rather, $M_{2(Al-P)}$ shows a minimum for the sample x = 6 meaning the smallest number of P-O-Al connectivities at this particular concentration. This non-linear effect was hypothesized to be due the formation of ^{29}Si nanodomains starting from x = 9. The formation of Si nanodomains would produce $Si^{(4)}$ units with a substantially higher fraction of Si-O-Si linkages that, in principle, would also reduce the fraction of Si-O-P linkages. This result might be correlated with the maximum weathering resistance of sample x = 6, however, the non-linear behavior in M_2 values is in limit of experimental error, therefore, it is hard to unambiguously point this as the motifs behind this macroscopic property.

This result agrees with the ^{29}Si MAS-NMR results, which show a continuous displacement towards higher frequency with increasing x which can be interpreted as strengthening relative increase in the fraction Si-O-Si connections per Si NFU. The formation of Si-rich nano-domains in the sample x = 9 is in good agreement with all the results found by NMR investigation. The lack of this domain might be a structural reason for the higher weathering resistance of sample x = 6 in comparison with the other samples with lower $M_{2(P-P)}$ values.

Finally, the formation of hexa-coordinated silicon species was not observed, presumably because it is suppressed by the strong P-O-Al interactions. Thus, the overall scenario sheds light on the weathering resistant glasses, regarding how the network connectivity might affect this macroscopic property.

6.3 Cold-pressurized sodium borosilicate glasses

As discussed in the Introduction, the study of room-temperature-pressurized samples has provided information regarding the structural changes in glasses that suffered an impact or were subjected to intense mechanical stress.[4,10-11] High-pressurized and densified glasses might mimic the stress suffered by the glasses in experimentally controlled situations. According to Kato *et al*., crack resistant glasses might those whose structure changes more easily under pressure, promoting an accommodation of the pressure without the forming cracks under

loads.[8-9] Table 27 illustrates the densification of the samples: after being submitted to 25GPa pressure, the density increases between 1.4% and 1.9%.

Table 27 - Compsition and density of the samples. ρ and ρ' are the densities of unpressurized and pressurized samples. Densities were measured using the sink float method (ASTM Standards C 729-75 (2000)).[142]

x	Na_2O	B_2O_3	SiO_2	ρ	ρ'
10	20	10	70	2.503	2.543
20	20	20	60	2.516	2.552
30	20	30	50	2.494	2.541

Source: Adapted from LOGRADO *et al.*[142]

One initial concern with measuring high-pressurized samples is that the pressure applied during the grinding process (which is a necessary step before NMR measurements) may result in undesired structural changes. To address this issue properly, we first initiated the measurements of the samples as whole pieces, managing to spin them in 7.5 mm rotors to acquire the MAS spectra. Then, the experiment was repeated (and other measurements were performed as well) with ground samples. Because of this, the spectra and the results in the tables are divided into unground vs. ground states. Therefore, the work is divided in four stages: (i) unground high pressurized (HP) samples, (ii) ground high pressurized (HPG) samples, (iii) annealed high pressurized – or ground and heated high pressurized (HPGH) samples, where the annealing at T_g was done with the objective of reversing the pressurization effect, and (iv) ground unpressurized samples – or ambient-pressure (AP) samples.

6.3.1 ^{29}Si MAS NMR

In Figure 66, the results of ^{29}Si MAS-NMR are presented with the HP samples on the left and AP samples on the right. The deconvolution of samples x = 10 (HP and AP) was performed with three Gaussian components whereas the other featureless spectra were modelled by single Gaussians. The parameters are outlined in Table 28.

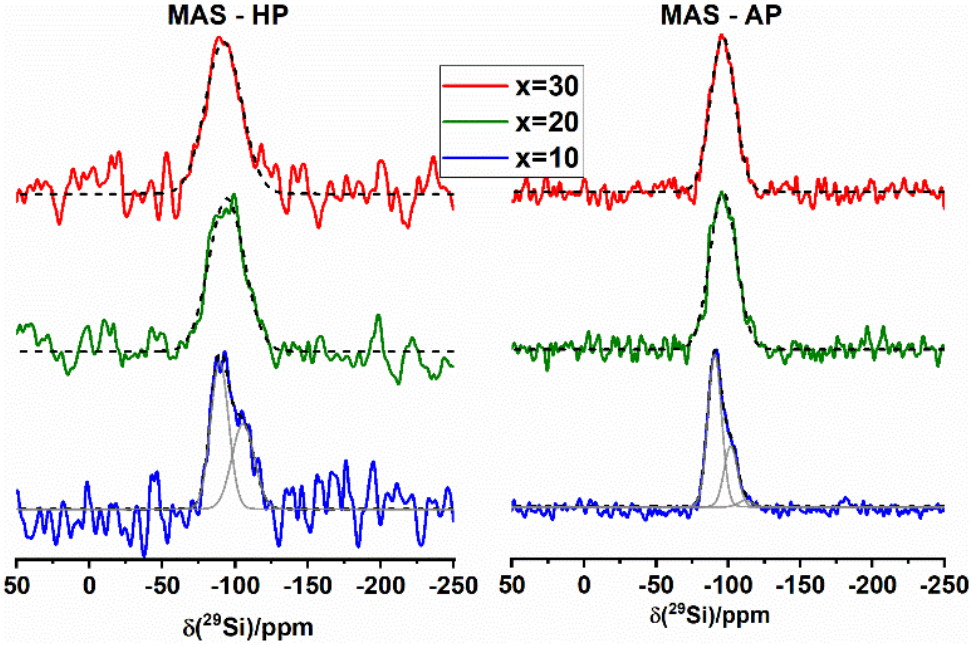

Figure 66 - ^{29}Si MAS-NMR spectra of HP and AP samples composed of (80-x)SiO_2-xB_2O_3-20Na_2O (x = 10,20,30). The dash lines represent the deconvolutions whereas the colored curves represent the spectra.
Source: Adapted from LOGRADO *et al.*[142]

Table 28 - ^{29}Si MAS-NMR Gaussian parameters: area under each distribution relative to the total area of each spectrum, the chemical shift values, and the width of the distributions. Values between the parenthesis correspond to the average chemical shift of the deconvolutions, when applicable.

Sample	Area/% (±3)	δ_{iso}/ppm HP (±3) AP (±1)	Width/ppm HP (±3) AP (±1)
10B_2O_3	63/37	-94(-88/- 104)	15/18
	68/27/4	-94 (-91/-102/-112)	11/11/11
20B_2O_3	100	-94	30
	100	-97	22
30B_2O_3	100	-92	29
	100	-96	20

Source: Adapted from LOGRADO *et al.*[142]

Due to the limited quantity of HP samples available the spectra of the HP samples are observed with considerably lower signal to noise (S/N) ratios in comparison with the spectra of the AP samples.

Although HP samples appear at slightly higher chemical shifts and with broader linewidth in comparison with AP samples, no detectable change was observed within the experimental error. In a study of sodium silicate glasses, Maekawa *et al*. found that chemical shifts around -90 ppm corresponded to $Si^{(3)}$, while those around -110 ppm to $Si^{(4)}$; which shows that increased number of NBOs in silica results in higher shifts towards positive values.[143] In

borosilicate glasses the scenario looks more complex. In Si-O-B linkages, the proximity between boron and silica deshields the silica environment, resulting in the displacement of silica resonance positions towards higher frequencies.[144] For instance, units such as $Si_{3Si}^{(3)}$ and $Si_{1B,3Si}^{(4)}$ would be hard to discriminate based exclusively on their chemical shifts, consequently the spectra might appear as featureless band. This ambiguity is observed in the spectra of Figure 66, for which with exception of sample x = 10, only the average chemical shift is reported in Table 28.

6.3.2 ^{11}B MAS NMR

Figure 67 and Figure 68 show the ^{11}B NMR spectra measured, respectively, with a 5.7 T and 14.1 T spectrometer. The spectra display at least two distinct boron sites: planar and tetrahedral boron. Planar species show a strongly field-dependent lineshape characterized by the anisotropy of the interaction between the EFG and the ^{11}B electric quadrupole moment. Tetrahedral boron lineshapes result in a Gaussian lineshape due to the symmetric charge distribution, resulting in the EFG of B(IV) being close to zero.[126,145-147] The distribution of internuclear distances and bond angles in polycrystalline samples leads to distribution in EFGs, causing a broadening of the B(III) lineshape.

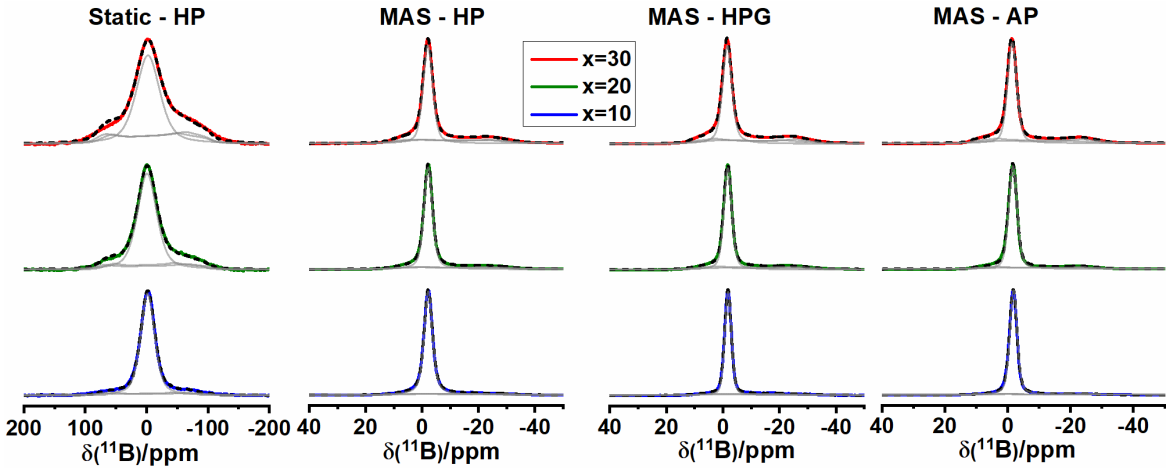

Figure 67- Comparison of the ^{11}B NMR spectra measured at 5.7 T. From left to right: the static Hahn echo acquired from HP (7.5 mm probe), MAS of HP (7.5 mm probe), MAS of HPG (4.0 mm probe), and MAS of AP samples (4.0 mm probe).

Source: Adapted from LOGRADO *et al.*[142]

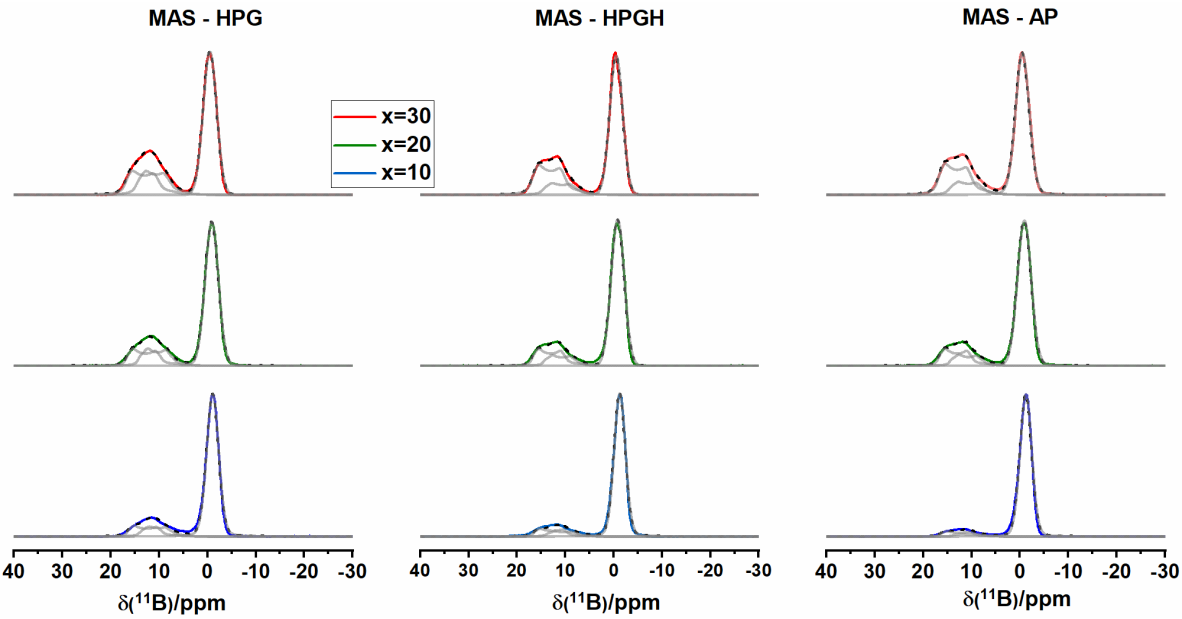

Figure 68 - Comparison of the ^{11}B NMR spectra measured at 14.1 T. The samples were measured with a 2.5 mm probe, and, at this stage, the HP samples are already ground. From left to right: spectra corresponding HPG, HPGH, and AP.
Source: Adapted from LOGRADO *et al.*[142]

For an analysis of the spectra, an inspection of their magnetic field dependence is helpful. As the second order quadrupolar effect depends on the inverse of Larmor Frequency (Equation (51)), asymmetry parameter (η) and quadrupolar coupling constant (C_Q) for the B(III) units obtained from simulation spectra acquired at 5.7 T gives more accurate results. Under higher magnetic-field, the lineshape seems featureless and approximates to a Gaussian-shape apearence.[69] On the other hand, the broadening caused by the quadrupolar interaction is reduced in spectra acquired at 14.1 T, and the signals due to B(III) and B(IV) are well separated. Therefore, the spectra acquired at high field can be accurately used to determine the proportion of each site, while the low field might be better way to analyze the η and C_Q of each site.

To obtain consistent simulations of the ^{11}B lineshapes, one approach was to use the same set of parameters to simulate both the high- and the low-field spectra. A simulation of the lineshape using a single curve for B(III) creates unrealistic values for the η parameter, whereas a consistent simulation for both fields was achieved by using two B(III) species. Table 29 and Table 30 summarize the parameters used for the distributions. Figure 69 displays the good adjustment of the fitting for B(III) species.

Table 29 - Parameters extracted from deconvolutions of ^{11}B NMR spectra obtained at 5.7 T. The spectra refer to Static Hahn Echo NMR on HP, and regular MAS NMR of HP, HPG and AP samples.

	B(IV)			B(III)			
	A ±1 (%)	δ_{iso} ±0.5 (ppm)	Width ±0.5 (ppm)	A ±1 (%)	δ_{iso} ±0.5 (ppm)	C_Q ±0.05 (MHz)	η ±1
			Samples x = 30				
HP Static	60	-2.5	45.7	21	19.0	2.72	0.2
				19	15.6	2.60	0.3
HP 5.5 kHz	61	-2.0	4.0	20	19.0	2.67	0.2
				19	15.6	2.54	0.3
HPG 8 kHz	60	-1.4	3.9	22	18.8	2.70	0.2
				18	16.2	2.53	0.3
AP 8 kHz	63	-1.0	3.4	23	18.8	2.64	0.2
				14	16.6	2.47	0.3
			Samples x = 20				
HP Static	73	-1.0	36.9	14	18.1	2.74	0.2
				13	14.9	2.50	0.3
HP 5.5 kHz	73	-2.1	3.5	13	18.1	2.71	0.2
				14	14.9	2.49	0.3
HPG 8 kHz	70	-1.7	3.3	16	18.1	2.70	0.2
				14	14.9	2.49	0.3
AP 8 kHz	78	-1.6	3.2	12	17.8	2.60	0.2
				10	14.9	2.52	0.3
			Samples x = 10				
HP Static	85	-1.8	27.0	8	17.0	2.72	0.2
				7	14.0	2.45	0.3
HP 5.5 kHz	86	-2.2	3.0	7	17.0	2.68	0.2
				7	14.0	2.45	0.3
HPG 8 kHz	83	-1.8	2.8	9	16.0	2.68	0.2
				8	14.5	2.45	0.3
AP 8 kHz	90	-1.7	2.8	5	17.5	2.67	0.2
				5	14.6	2.45	0.3

Source: Adapted from LOGRADO *et al.*[142]

Table 30 - Parameters of deconvolutions of ^{11}B NMR spectra obtained with at 14.1 T. The spectra are relative to regular MAS of (i) HPG (ii) HPGH and (iii) AP samples.

	B(IV)			B(III)			
	A ±1 (%)	δ_{iso} ±0.5 (ppm)	Width ±0.5 (ppm)	A ±1 (%)	δ_{iso} ±0.5 (ppm)	C_Q ±0.05 (MHz)	η ±0.1
			Samples x = 30				
HPG 15 kHz	57	-0.5	3.3	22	18.1	2.67	0.2
				21	15.6	2.60	0.3
HPGH 15 kHz	59	-0.4	3.3	30	18.1	2.67	0.2
				11	15.6	2.60	0.3
AP 15 kHz	60	-0.5	3.3	28	18.1	2.67	0.2
				12	15.6	2.60	0.3
			Samples x = 20				
HP G15 kHz	68	-0.9	3.3	16	18.0	2.71	0.2
				16	15.2	2.60	0.3
HPGH 15 kHz	73	-0.8	3.2	17	18.1	2.67	0.2
				10	15.4	2.68	0.3
AP 15 kHz	73	-0.9	3.3	16	18.1	2.67	0.2
				11	15.4	2.68	0.3
			Samples x = 10				
HPG 15 kHz	76	-1.0	2.9	11	17.8	2.70	0.2
				12	14.8	2.51	0.3
HPGH 15 kHz	83	-1.2	2.9	10	17.8	2.70	0.2
				7	14.8	2.51	0.3
AP 15 kHz	89	-1.2	2.9	7	17.8	2.70	0.2
				4	14.8	2.51	0.3

Source: Adapted from LOGRADO *et al.*[142]

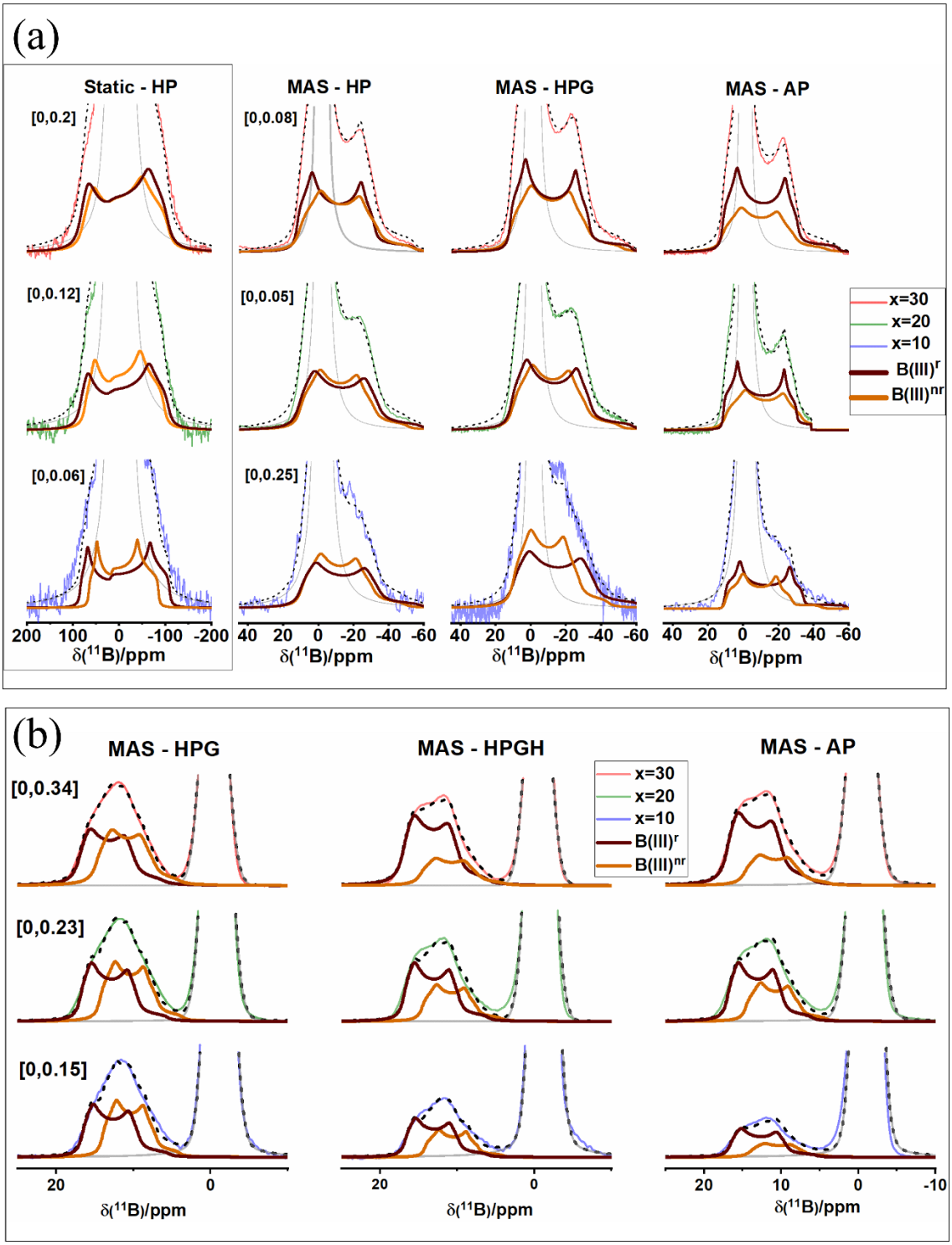

Figure 69 - Comparison the ^{11}B resonances pertaining to B(III) units obtained at magnetic flux densities of (a) 5.7 T and (b) 14.1 T. The zoom scale is provided in the top left corner of the figure, and if no value is shown, the level is the same as the last value displayed in the same line.
Source: Adapted from LOGRADO *et al.*[142]

The B(IV) unit exhibits a chemical shift at around -2.0 ppm, which is in line with resonance frequencies corresponding to B-O-Si linkages.[145–147] The two sites B(III) show isotropic chemical shifts at approximately 17-19/14-16 ppm, with quadrupolar coupling

constants at around 2.65/2.52 MHz and η values of 0.2/0.3, corresponding well with the ring and the non-ring triagonal boron units, labeled as $B(III)^{r}$ and $B(III)^{nr}$.[145–147] The absence of higher η values suggests a lack of evidence for anionic B(III), i.e., meta- or pyroborate units. Additionally, TQMAS was performed on HPG and AP samples to further explore ^{11}B environments, as illustrated by Figure 70. Parameters extracted from TQMAS are summarized in Table 31. However, the resolution of the two B(III) sites could not be improved. The isotropic chemical shift extracted from both MQMAS and MAS-NMR shows a displacement of B(IV) and B(III) units towards higher frequencies with increasing boron content. According to the literature,[148] boron units exhibit lower resonance frequencies due to the shielding effect of silica on its neighborhood, compared to the chemical shift observed when B-O-B linkages dominate the boron environment. Thus, the effect observed here explains the increased number of B-O-B linkages at the expense of B-O-Si connectivities.

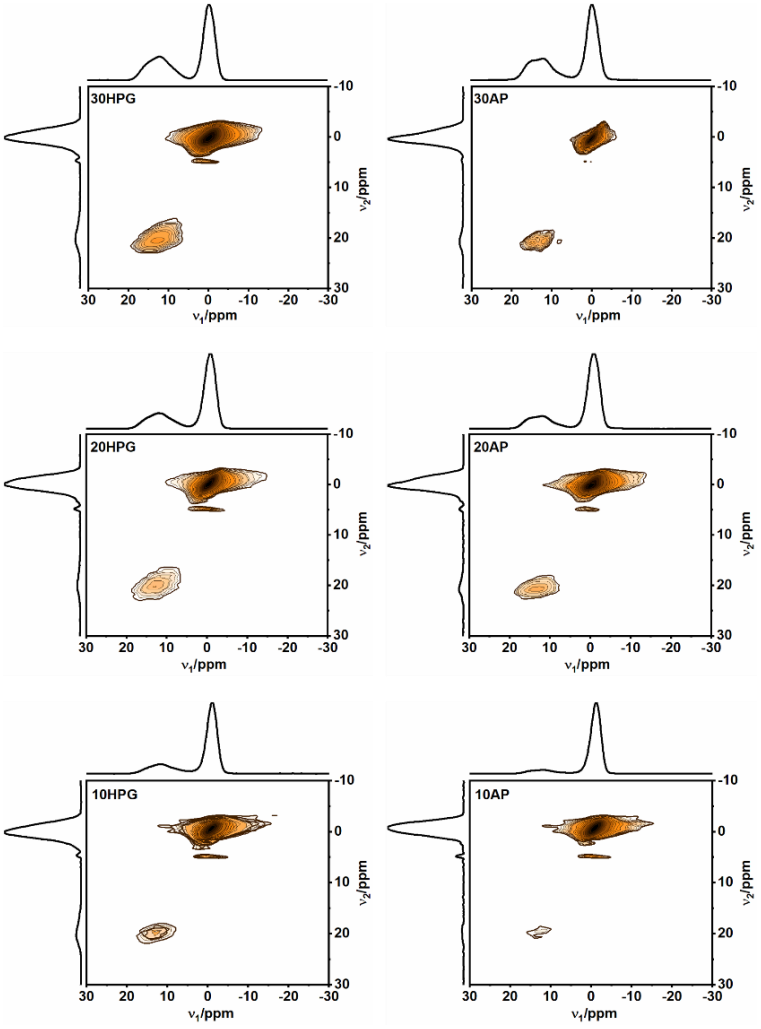

Figure 70 - ^{11}B MQMAS NMR spectra measured at 14.1 T of HPG and AP samples. The resolution of two sites were observed: one B(III) unit and one B(IV) unit. A smaller artifact can be observed closer to B(IV). Source: Adapted from LOGRADO *et al.*[142]

Table 31 - Parameters of ^{11}B MQMAS obtained at 14.1 T for (i) HPG and (ii) AP samples. The parameters were obtained based on the isotropic resonance frequency of the indirect dimension δ_1 and the center of gravity of the direct dimension δ_2. *Poor resolution

	δ_{iso} - B(IV) ±0.5 (ppm)	P_Q - B(IV) ±0.1 (MHz)	δ_{iso} - B(III) ±0.5 (ppm)	P_Q - B(III) ±0.1 (MHz)
30AP	0.1	0.1	18.6	2.5
			3.7*	1.8*
20AP	0.1	0.1	17.9	2.5
			3.1	2.1
10AP	-0.9	0.1	16.9	2.6
			2.8	2.2
30HPG	0.2	0.5	17.3	2.6
			3.3	2.0
20HPG	-0.3	0.5	17.5	2.6
			3.0	2.2
10HPG	-0.6	0.4	17.3	2.6
			3.2	2.1

Source: Adapted from LOGRADO *et al.*[142]

Figure 67 display the deconvolution of (i) Static –HP, (ii) MAS –HP, and (iii) MAS-HPG spectra. Within the experimental errors, these three distinct conditions produce the same set of chemical shifts and quadrupolar coupling constant, as summarized in Table 29. Thus, no significant change was observed after the samples were ground, indicating that grinding did not result in any undesired structural changes. The proportion of B(IV), referred to as N_4, is one crucial parameter for the characterization of boron-containing glasses. N_4 is expressed as:

$$N_4 = \frac{B(IV)}{B(III) + B(IV)} \quad (75)$$

Within the experimental error, no change was observed upon grinding the samples. However, the (iv) MAS-AP spectral simulation resulted in smaller amounts of both units $B(III)^r$ and $B(III)^{nr}$, and increased B(IV), in all the three samples (x = 10, 20 and 30), as illustrate in Figure 71. While many NMR studies in borosilicate,[10,49] aluminosilicate[10,44,149] and aluminoborosilicate[10] glasses show that under pressure the coordination number increases, the current study produced the opposite effect, showing that the coordination number of (80-x) SiO_2 – xB_2O_3 – $20Na_2O$ (x = 10,20,30) glasses decreased under pressure. To confirm this behavior, the HPG samples were annealed for 2 hours at T_g (glass transition temperature), using the values of Kato *et al.*[8] with the annealing process, the memory of the pressure is lost because of the structural relaxation caused by the temperature. After the HPG samples were annealed, the amount of $B(III)^r$ had risen, and that of $B(III)^{nr}$ had diminished, resulting in similar or identical lineshape found in AP samples, as shown in the HPGH column in Figure 68 and Figure 69 (b).

This result indicates a counter-intuitive effect, contradicting the commonly held assumption that high-pressure samples always exhibit an increased average boron coordination number.

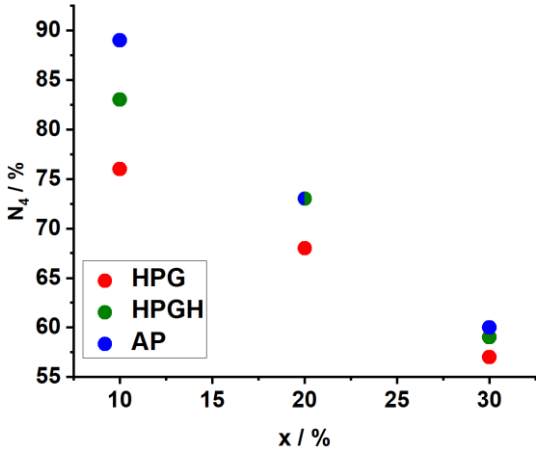

Figure 71 - Plot of N_4 vs. concentration of boron oxide in the network for HPG, HPGH and AP measured at 14.1T. The datapoint half blue and half green in coordinate line x = 20 represents a superposition of HPGH and AP N_4 values.

Source: By the author

Another change in the lineshape reflects an increased $B(III)^{r}/B(III)^{nr}$ ratio upon pressurization. As shown in Figure 69 (a) and (b), the amount of $B(III)^{r}$ is equivalent to the amount of $B(III)^{nr}$ for HPG samples, while the spectral deconvolution of AP samples shows that the $B(III)^{r}$ proportion is significantly higher than the $B(III)^{nr}$ proportion. This result agrees with the literature, [4,10] which shows that due to the free volume of the $B(III)^{r}$ unit can better accommodate the pressure than $B(III)^{nr}$ units, resulting in conversion of $B(III)^{r}$ to other units, such as the $B(III)^{nr}$.

6.3.3 ^{23}Na MAS NMR

Figure 72(a) shows the ^{23}Na MAS-NMR results using 5.7 T and 14.1 T spectrometers. These experiments were initiated with the measurements of HP samples in a 5.7 T spectrometer using a 7.5 mm probe, in which the maximum MAS speed available is 6 kHz. Quadrupolar nuclei show a spectral broadening caused by second order quadrupolar interaction, which is inversely proportional to the static magnetic field B_0. Thus, the weaker the magnetic field, the broader the lineshape. The combination of low field with the maximum available spinning speed of 6 kHz results in the central transition peak not completely separated from the multiple spinning sidebands. These lines were simulated using the Ssnake software to also calculate the intensity of spinning side bands arising in Czjzek in the finite spinning speeds case. No

Chemical Shift Anisotropy is considered in this case. The parameters extracted from the simulations are listed in Table 32.[103]

The right side of Figure 72(a) shows the spectra of HPG samples measured at 14.1 T. Even though the phasing of the spectra at low field may have been an additional source of error (due to the reasons explained above), the deconvolutions of spectra acquired with low and high field spectrometers result in the same set of parameters (within experimental errors). In agreement with the ^{11}B MAS-NMR results, no structural change could be observed upon grinding the sample.

Figure 72 (b) compares the spectra of HPG samples (dashed curves) with HPGH in the left side and HPG samples (dashed curves) and AP samples in the right side. It is possible to note the effect on the isotropic chemical shifts (see Table 30) caused by the relaxation due to annealing these samples at T_g. This results in the recovery of the short-range structure of the pressurized glasses, in agreement with the expectation. It highlights the fact that pressurization at room temperature has a clear role in permanently changing not only the structure of boron, but that of sodium as well.

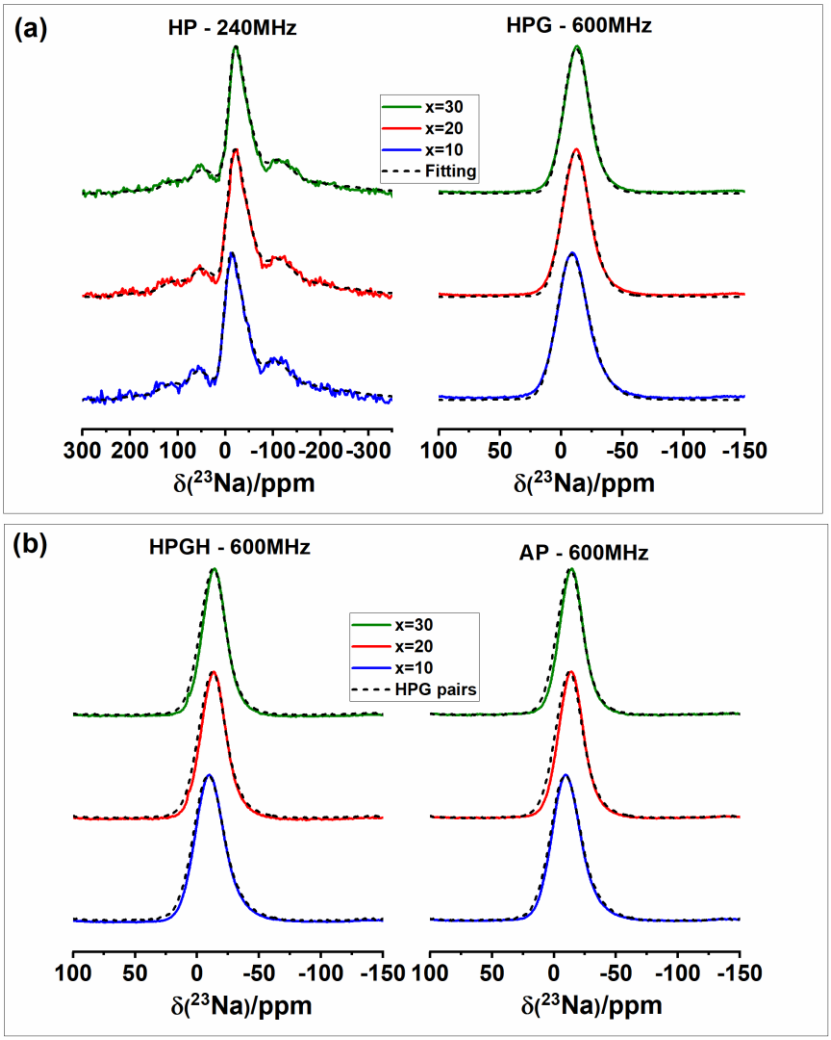

Figure 72 - ^{23}Na MAS-NMR spectra. (a) Column from left to right: HP samples measured at 5.7 T and HPG samples measured with at 14.1 T. In this figure, the dash lines represent the deconvolutions whereas the colored curves represent the spectra. (b) Column from left to right: HPGH and AP samples, both measured at 14.1 T. In this figure, the colored curves represent the spectra whereas the dash lines represent the spectra of respective HPG pair (spectra of HPG sample with same concentration of boron).

Source: Adapted from LOGRADO *et al.*[142]

The simulations show that ^{23}Na chemical shifts decrease when the concentration of boron increases. A well-reported behavior of Na in sodium borate glasses is the decrease in chemical shift values upon the decreases of Na/B ratio.[148,150,151] This can be explained by longer average Na-O distances resulting in resonance positions shifted towards lower frequencies, as in the case of sodium ions balancing the charge of $[BO_4]^-$ units. Also observed is the displacement of ^{23}Na chemical shifts towards higher values upon the pressurization of the samples. This result was interpreted as shorter average Na-O distances, as a consequence of more NBO, indicating the formation of NBOs though the $Si^{(3)}$ or $Si^{(2)}$ units. The HP samples also presented a larger average magnitude of the ^{23}Na quadrupolar coupling constant, reflecting

a less symmetric local environment. After the annealing the parameters found in HPGH samples are close to those measured on the AP samples.

Table 32 - Parameters of deconvolutions of the ^{23}Na MAS-NMR spectra. The spectra are relative to regular MAS of (i) HPG, (ii) annealed HP and (iii) AP samples. *Simulation performed in Ssnake, whereas unmarked parameters were simulated with Dmfit.

Sample	δ_{iso}/ppm HP – 5.7 T (±3) HPG – 14.1 T (±0.5) HPGH – 14.1 T (±0.5) AP – 14.1 T (±0.5)	C_Q/MHz HP – 5.7 T (±3) HPG – 14.1 T (±0.5) HPGH – 14.1 T (±0.5) AP – 14.1 T (±0.5)
$10B_2O_3$	4.0*	2.6*
	0.3	3.1
	-1.3	3.0
	-0.8	3.0
$20B_2O_3$	-2.1*	2.6*
	-4.5	2.7
	-6.6	2.5
	-6.8	2.6
$30B_2O_3$	-4.5*	2.5*
	-5.9	2.6
	-7.8	2.4
	-7.7	2.5

Source: Adapted from LOGRADO *et al.*[142]

6.3.4 Discussion

The extensive studies published on borosilicate structural characterization can be used as a background to promote further discussion about the current sodium borosilicate glasses, bringing more elucidative insights. For instance, the theoretical Dell, Yun, and Bray (DYB) model investigated and predicted the proportion of N_4 for $KSiO_2 – B_2O_3 – RNa_2O$ glasses based on quantitative ^{11}B NMR-MAS, dividing the compositional space into four regions. [152–154] According to these studies, the glasses under investigation belong to Region 3, characterized by $R^* \leq R \leq (0.5+K/4)$, where $R^* = 0.5 + K/16$. For this region, the predicted values of N_4 are $N_4 = R^*$ and the sodium ions act in a dual role as balancers of the tetrahedral $(BO_4)^-$ unit and also of NBOs bonded to $Si^{(n)}$ species. Also, in this region, the DYB model predicts no $B^{(2)}$ units being formed. This result is in very good agreement with the MAS- and the TQMAS-NMR data reported in this work. Table 33 illustrates the comparison between R^* and N_4, which within the experimental error of ±0.01 agrees with the model.

Table 33 - Composition of $KSiO_2 – B_2O_3 – RNa_2O$ current under investigation and the comparison between the proportion of B(IV) units predicted by DYB model (*R**) and the values measured by NMR (N_4-NMR) on the AP samples.

Na_2O	B_2O_3	SiO_2	*K*	0.5+*K*/4	*R*	*R**	N_4-NMR (± 0.01)
20	10	70	7	2.25	2	0.94	*0.89*
20	20	60	3	1.25	1	0.69	0.73
20	30	50	1.6	0.9	0.66	0.60	0.60

Source: By the author

This work also illustrates the permanent effect of densification. The pressurized samples showed a decreased boron coordination number, which seems like a counter intuitive effect due to the general assumption that the coordination number of glasses generally increases under high pressure. In the current work, the opposite trend was observed. This outcome might be understood as the strengthening of the bonds between sodium ions and the NBOs promoted by high pressure. The following reaction equations might express the structural changes occurring under pressure:

$$Na^+ {}^-\{BO_{3/2}\text{-}O\text{-}SiO_{3/2}\} \rightarrow BO_{3/2} + Na^+ {}^-O\text{-}SiO_{3/2} \quad (76)$$

$$Na^+ {}^-\{BO_{3/2}\text{-}O\text{-}BO_{2/2}\} \rightarrow BO_{3/2} + Na^+ {}^-O\text{-}BO_{2/2} \quad (77)$$

The structural changes can be interpreted on the basis of dual role of sodium. The pressure induces a closer proximity between linkages of $B^{(4)}$ structures balanced by Na^+, such as $B^{(4)}$-O-$B^{(3)}$ and $B^{(4)}$-O-$Si^{(4)}$. The breakage of this connectivity produces either the anionic $B^{(3)}$ or anionic $Si^{(3)}$ (or $Si^{(2)}$) species with NBO charges compensated by sodium. No detectable change was observed within experimental error by ^{29}Si MAS-NMR due to the low amount of HP samples and to the low abundance of the ^{29}Si isotope. On the other hand, ^{11}B MAS-NMR results reinforce the idea behind these reaction equations resulting in a clear decrease of N_4. Upon pressurization ^{23}Na MAS-NMR spectra also corroborate this hypothesis, as the shifts towards higher frequency in the pressurized samples reveal an increased number of NBOs compensating the charge. Additionally, the literature reports reduced numbers of ring-B(III) units in densified *in-situ* cold pressed samples and *ex-situ* hot pressed ones.[42–44,155–158] The NMR results of the current work agree with this reduction. Equations (76) and (77) suggest further that, for understanding high-pressure structural effects, one also must also take into account a medium-range order phenomena such as the network former connectivity and the network former/network modifier interactions.

It is important to note that the literature has reported increased coordination numbers following the application of pressure on a range of borate, alkali borate, silicate and

aluminosilicate glasses.[10,44,46] However, there have been limited studies performed on relaxed cold-pressed samples, [42,49,155-156,159] mainly in ssNMR, as in-situ NMR studies at high pressures are not possible using standard instrumentation. Hot pressed samples may differ significatively from the structure found in pressure-relaxed glasses, which reveal a non-relaxed state of the glass. The hot-pressurized samples undergo the glass transition at high pressure; therefore, it represents the melt-structure of the equilibrium state at T_g and under high pressure. The investigation of cold-pressed samples sheds light on the permanent effect caused by the pressure induced in the frozen state. Also, such investigations might impact the study of crack resistant glasses. The resulting structure of densified glasses at room temperature might mimic how the glasses respond to impacts and how their structure is rearranged to avoid the crack formation.

7 CONCLUSION

In summary, the structures of two quaternary sodium aluminum phosphosilicate glass systems were investigated by solid-state Nuclear Magnetic Resonance: (i) NAPS: x Na_2O – (22.5-x)Al_2O_3 – 7.5P_2O_5 – 70SiO_2, (2.50 ≤ x ≤ 17.5), (ii) SPAN: xSiO_2-(59-x)P_2O_5–13Al_2O_3–28Na_2O, (0 ≤ x ≤ 13). In addition, the effect of cold pressurization in a sodium borosilicate glass system(iii) (80-x)SiO_2 – xB_2O_3 -20Na_2O (x = 10, 20, 30) was investigated.

7.1 NAPS glass system

Study (i) elucidates changes in the NAPS network interpreted as three distinct compositional regimes concerning the structural role of the sodium ions. The first regime is characterized by the changes due to the sodium attack to higher coordinate Al(V) in a tricluster $Al^{+3}(V)(AlPO_4)_n^-$ structure, which promotes formation of $Si^{(4)}$-O-Al(IV) linkages. After $Al^{+3}(V)$ units are completely converted to $(AlO_4)^-$ units balanced by Na^+, samples with composition 10.00 ≤ x < 15.00, sodium oxide successively leads to the breakage of $P^{(4)}$-O-Al(IV) linkages, causing initially the formation of neutral $P^{(3)}$ units, and subsequently $P^{(2)}$ and $P^{(1)}$ units. Within this regime, two types of sodium ions are present: one Na^+ compensating the NBOs formed on the phosphate NFUs, the other balancing the charge of the tetrahedral $(AlO_4)^-$ units. This picture clearly illustrates the dual role of sodium. In this regime silica seems to form proportionally more $Si^{(4)}$-O-$Si^{(4)}$ linkages (than $Si^{(4)}$-O-Al(IV)), owing to the decreased [Al]/[Si] ratio. The third regime represents the samples dominant ^{23}Na-^{31}P dipolar interactions, eventually leading to the crystallization of $Na_4P_2O_7$.

7.2 SPAN glasses

Study (ii) investigated structural reasons for the non-linear properties of weathering-resistant SPAN glasses. This study shows that the network is dominated by P-O-P linkages. By using ^{31}P(^{27}Al) and ^{31}P(^{23}Na) REAPDOR experiments, two distinct ^{31}P sites could be differentiated: $P^{(2)}$ units resonating at higher frequencies are preferentially charge balanced by Na^+ and were identified by $P^{(2)}_{[0,1]Al}$ unit, whereas the $P^{(2)}$ units resonating at lower frequencies interact more strongly with aluminum, and were identified as $P^{(2)}_{[1,2]Al.}$ The structural origins for the higher weathering stability near x = 6 might have a basis on the balance of Si-O-Si, Si-

O-Al, and P-O-P connectivities. ^{27}Al MAS-NMR indicates a gradual change of the role from network modifier to network former with increasing Si content, which implies a monotonically decreased Al$^{(5,6)}$-O-P interaction due to decreased [P]/[Al] ratio. However, this trend is non-linear and displays a minimum at sample x = 6.

The strengthening in the interaction for samples with $x \geq 9$ was understood to be related to the hypothesized formation of Si-rich nanodomains. The weathering resistant property might further be influenced by the concentration of P-O-P linkages.

By using Spin Echo Decay experiments, samples for $0 \leq x \leq 6$ displays successive decreased interaction, followed by slightly increase in ^{31}P-^{31}P dipolar interaction at sample x = 9, which reinforce that Si-O-P linkages might be under-represented owing to the formation of Si-rich nanodomains. Even though the conclusions of the static SED experimental results might be limited by the precision of the measurements, it fully supports the discussed hypothesis. Finally, this NMR-based study documented multiple structural changes in the network; thus, the trend observed in Figure 53 and Figure 54 might not be due to a single structural origin but may be the composite effect of multiple structural underpinnings.

7.3 Cold-pressurized sodium borosilicate glasses

Study (iii) investigated ternary sodium borosilicate structural changes after being compressed at 25GPa at room temperature. A counter-intuitive effect of decreasing the average coordination of boron upon pressurization was observed. This change was elucidated on the basis of a small change in the role of sodium ions, as indicated by ^{23}Na MAS-NMR. The structural hypothesis formulated by this trend involves a breakage of Si-O-B linkages, with a concomitant increase in the concentration of non-bridging oxygen atoms.

The results obtained in this part of the work further illustrate that a local densification of the sodium ion environment (creation of shorter Na···O distances) and medium-range order aspects regarding NFU connectivity and NFU-modifier interactions may be more important than merely the coordination number of the NFUs.

To further clarify the effects reported in this work, our laboratory is conducting experiments on the same sodium borosilicate samples with ^{17}O enrichment. Finally, studies focused on permanent densification in cold-pressed glasses can be of fundamental importance in

Overall, the results presented in this thesis illustrate the power and potential of single- and double resonance NMR studies in elucidating the network former, modifier, and intermediate oxides in this series of inorganic ternary and quaternary glass structure.

REFERENCES

1 PYE, L. D. Arrival of the glass age affirmed. **International Journal of Applied Glass Science,** v. 07, n. 4, p. 407-408, 2016.

2 MORSE, D. L.; EVENSON, J. W. Welcome to the glass age. **International Journal of Applied Glass Science,** v. 07, n. 4, p. 409-412, 2016.

3 KURKJIAN, C. R.; PRINDLE, W. R. Perspectives on the history of glass composition. **Journal of the American Ceramic Society,** v. 81, n. 4, p. 795-813, 1998.

4 JANUCHTA, K.; SMEDSKJAER, M. M. Indentation deformation in oxide glasses: Quantification, structural changes, and relation to cracking. **Journal of Non-Crystalline Solids:** X, v. 01, n. 1, p.100007-100027, 2019.

5 KE, X. *et al.* Toward hard and highly crack resistant magnesium aluminosilicate glasses and transparent glass-ceramics. **Journal of the American Ceramic Society,** v. 103, n. 6, p. 3600-3609, 2020.

6 ROSALES-SOSA, G. A. *et al.* Crack-resistant Al_2O_3-SiO_2 glasses. **Scientific Reports,** v. 06, n. 1, p. 23620, 2016.

7 GROSS, T. M. *et al.* Crack-resistant glass with high shear band density. **Journal of Non-Crystalline Solids,** v. 494, n. 1, p. 13-20, 2018.

8 KATO, Y. *et al.* Effect of B_2O_3 content on crack initiation under Vickers indentation test. **Journal of the Ceramic Society of Japan,** v. 118, n. 1381, p. 792-798, 2010.

9 KATO, Y. *et al.* Effect of densification on crack initiation under Vickers indentation test. **Journal of Non-Crystalline Solids,** v. 356, n. 35-36, p. 1768-1773, 2010.

10 JANUCHTA, K. *et al.* Discovery of ultra-crack-resistant oxide glasses with adaptive networks. **Chemistry of Materials,** v. 29, n. 14, p. 5865–5876, 2017.

11 GROSS, T. M.; PRICE, J. J. Vickers indentation cracking of ion-exchanged glasses: quasi-static vs. dynamic contact. **Frontiers in Materials,** v. 04, n. 4, p. 1-14, 2017.

12 BALLATO, J. *et al*. Glass and process development for the next generation of optical fibers: a review. **Fibers,** v. 5, n. 11, 2017.

13 JIANG, S.; MYERS, M.; PEYGHAMBARIAN, N. Er^{3+} doped phosphate glasses and lasers. **Journal of Non-Crystalline Solids,** v. 239, n. 3, p. 143-148, 1998.

14 CAMPBELL, J. H.; SURATWALA, T. I. Nd-doped phosphate glasses for high-energy/high-peak-power lasers. **Journal of Non-Crystalline Solids,** v. 263–264, n. 1. p. 318-341, 2000.

15 WEBER, M. J. Science and technology of laser glass. **Journal of Non-Crystalline Solids,** v. 123, n. 1-3. p. 208-222, 1990.

16 BUNKER, B. C.; ARNOLD, G. W.; WILDER, J. A. Phosphate glass dissolution in aqueous solutions. **Journal of Non-Crystalline Solids,** v. 64, n. 3, p. 291-316, 1984.

17 SEN, S.; STEBBINS, J.F. Structural role of Nd^{3+} and Al^{3+} cations in SiO_2 glass: a ^{29}Si MAS-NMR spin-lattice relaxation, ^{27}Al NMR and EPR study. **Journal of Non-Crystalline Solids,** v. 188, n. 1-2. p. 54-62, 1995.

18 WALTERS, H. V.; ADAMS, P. B. The chemical durability of optical glass. **Applied Optics,** v. 07, n. 5, p. 845-845, 1968.

19 DIGIOVANNI, D.J.; MACCHESNEY, J.B.: KOMETANI, T.Y.; Structure and properties of silica containing aluminum and phosphorus near the $AlPO_4$ join. **Journal of Non-Crystalline Solids** v. 113, n. 1, p. 58-64, 1989.

20 AITKEN, B. G. *et al*. Structure−property relations in mixed-network glasses: multinuclear solid state NMR investigations of the system xAl_2O_3:$(30-x)P_2O_5$:$70SiO_2$. **Journal of Physical Chemistry C,** v. 113, n. 8, p. 3322-3331, 2009.

21 MASCARAQUE, N.; BAUCHY, M.; SMEDSKJAER, M. M. Correlating the network topology of oxide glasses with their chemical durability. **Journal of Physical Chemistry B,** v. 121, n. 5, p. 1139-1147, 2017.

22 LIMA, C. J. *et al.* Effects of composition on the durability and weathering of flat glass. **Glass Structures and Engineering,** v. 07, n. 2, p. 139-155, 2022.

23 KLEIN, L. C.; GRAI, P. E. Tie chemical durability of sodium ultraphosphate glasses. **Glass Technology,** v. 24, n. 4. P. 202-206, 1983.

24 MINAMF, T.; MACKENZIE, J. D. Thermal expansion and chemical durability of phosphate glasses. **Journal of the American Ceramic Society,** v. 60, n. 5-6, p. 232-235, 1977.

25 KROEKER, S. Nuclear magnetic resonance spectroscopy of glasses. *In*: AFFATIGATO, M. (ed.). **Modern glass characterization.** New Jersey: Wiley, 2015. p.315–344.

26 ECKERT, H. Advanced dipolar solid state NMR spectroscopy of glasses. *In*: AFFATIGATO, M. (ed.). **Modern glass characterization.** New Jersey: Wiley, 2015. p.345–390.

27 YOUNGMAN, R. NMR spectroscopy in glass science: a review of the elements. **Materials,** v. 11, n. 4, p. 476-499, 2018.

28 ECKERT, H. Structural characterization of non-crystalline solids and glasses using solid state NMR. **Progress in Nuclear Magnetic Resonance Spectroscopy,** v. 24, n. 3, p. 159-293, 1992.

29 NIZAMUTDINOVA, A. *et al*. The structural role of alumina in alkali phosphosilicate glasses: A multinuclear solid state NMR study. **Physics and Chemistry of Glasses**: european journal of glass science and technology part b, v. 59, n. 6, p. 267-276, 2018.

30 NIZAMUTDINOVA, A. *et al*. Structural role of phosphate in metaluminous sodium aluminosilicate glasses as studied by solid state NMR spectroscopy. **Journal of Physical Chemistry B,** v. 124, n. 13, p. 2691-2701, 2020.

31 SCHALLER, T. *et al*. TRAPDOR NMR investigations of phosphorus-bearing aluminosilicate glasses. **Journal of Non-Crystalline Solids**. v. 248, n. 1, p. 19−27, 1999.

32 TOPLIS, M. J.; SCHALLER, T. A. P-31 MAS NMR study of glasses in the system xNa_2O-(1- x)Al$_2O_3 - 2SiO_2 - yP_2O_5$. **Journal of Non-Crystalline Solids**, v. 224, n. 1, p. 57−68, 1998.

33 BROW, R. K.; KIRKPATRICK, R. J.; TURNER, G. L. Nature of alumina in phosphate glass: ii, structure of sodium aluminophosphate glass. **Journal of the American Ceramic Society,** v. 76, n. 4, p. 919-928, 1993.

34 BROW, R. K. Nature of alumina in phosphate glass: i, properties of sodium aluminophosphate glass. **Journal of the American Ceramic Society,** v. 76, n. 4, p. 913-918, 1993.

35 KREIDLT, N. J.; WEYL, W. A. Phosphate in ceramic ware: IV, phosphate glasses. **Journal of the American Ceramic Society,** v. 24, n. 11, p. 372-378, 1941.

36 EGAN, J. M.; WENSLOW, R. M.; MUELLER, K. T. Mapping aluminum/phosphorus connectivities in aluminophosphate glasses. **Journal of Non-Crystalline Solids,** v. 261, n. 1-3, p. 115-126, 2000.

37 LANG, D. P.; ALAM, T. M.; BENCOE, D. N. Solid-state $^{31}P/^{27}AI$ and $^{31}P/^{23}Na$ TRAPDOR NMR investigations of the phosphorus environments in sodium aluminophosphate glasses. **Chemistry of Materials,** v. 13, n. 2, p. 420-428, 2001.

38 WENSLOW, R. M.; MUELLER, K. T. Structural details of aqueous attack on a phosphate glass by $^{1}H/^{31}P$ cross-polarization NMR. **Journal of Physical Chemistry B,** v. 102, n. 45, p. 9033-9038, 1998.

39 SONNEVILLE, C. *et al.* Progressive transformations of silica glass upon densification. **Journal of Chemical Physics,** v. 137, n. 124501, p. 1-7, 2012.

40 SAMPATH, S. *et al.* Intermediate-range order in permanently densified GeO_2 glass. **Physical Review Letters,** v. 90, n. 11, p. 115502-1-115502-4, 2003.

41 GUERETTE, M. *et al.* Structure and properties of silica glass densified in cold compression and hot compression. **Scientific Reports,** v. 5, n. 15343, p. 1-10, 2015.

42 LEE, S. K. *et al.* Probing of bonding changes in B_2O_3 glasses at high pressure with inelastic X-ray scattering. **Nature Materials,** v. 4, n. 1, p. 851-854, 2005.

43 LEE, S. K. *et al.* Probing and modeling of pressure-induced coordination transformation in borate glasses: Inelastic x-ray scattering study at high pressure. **Physical Review B,** v. 78, n. 21, p. 2014203-1-2014203-6, 2008.

44 LEE, S. K.; LEE, A. C.; KWEON, J. J. Probing medium-range order in oxide glasses at high pressure. **Journal of Physical Chemistry Letters,** v. 12, n. 4, p. 1330-1338, 2021.

45 ALLWARDT, J. R. *et al.* Aluminum coordination and the densification of high-pressure aluminosilicate glasses. **American Mineralogist,** v. 90, n. 7, p. 1212-1222, 2005.

46 KAPOOR, S. *et al.* Permanent densification of calcium aluminophosphate glasses. **Frontiers in Materials,** v. 6, n. 63, p. 1-13, 2019.

47 AMIN, S. A. *et al.* Characterizing pressure-induced coordination changes in $CaAl_2O_4$ glass using ^{27}Al NMR. **Journal of Physical Chemistry C,** v. 116, n. 3, p. 2068-2073, 2011.

48 TREASE, N. M. *et al*. Bond length-bond angle correlation in densified silica - results from ^{17}O NMR spectroscopy. **Journal of Chemical Physics,** v. 146, n. 18, p. 184505-1-184505-9, 2017.

49 LEE, S. K. *et al.* Degree of permanent densification in oxide glasses upon extreme compression up to 24 GPa at room temperature. **Journal of Physical Chemistry Letters,** v. 11, n. 8, p. 2917-2924, 2020.

50 AMOUREUX, J. P.; FERNANDEZ, C.; STEUERNAGEL, S. Z Filtering in MQMAS NMR. **Journal of Magnetic Resonance A,** v. 123, n.1, p. 116-118, 1996.

51 GULLION, T. Measurement of dipolar interactions between spin-1/2 and quadrupolar nuclei by rotational-echo, adiabatic-passage, double-resonance NMR. **Chemical Physics Letters,** v. 246, n. 3, p. 325-330, 1995.

52 GULLION, T.; SCHAEFER, J. Rotational-echo double-resonance NMR. **Journal of Magnetic Resonance,** v. 81, n. 1, p. 196-200, 1989.

53 ECKERT, H.; LETZ, M. Ultra-strong glasses and glass-ceramics and bioactive materials (and therein). *In:* PÖTTGEN, R.; JÜSTEL, T.; STRASSERT, C. A. (ed.). **Construction materials to technical gases.** Berlin: De Gruyter, 2023. p. 271-293.

54 VARSHNEYA, A. K. **Fundamentals of inorganic glasses.** Cambridge: Academic Press, 1993.

55 BROW, R. K.; KIRKPATRICK, R. J.; TURNER, G. L. Local structure of $xAl_2O_3{\cdot}(1-x)NaPO_3$ glasses: an NMR and XPS Study. **Journal of the American Ceramic Society,** v. 73, n. 8, p. 2293-2300, 1990.

56 ZACHARIASEN, H. The atomic arrangement in glass. **Journal of the American Chemical Society**. v. 54, n. 10, p. 3841-3851, 1932.

57 DUER, M. J. **Introduction to solid-state NMR spectroscopy.** New Jersey: Wiley, 2005.

58 SLICHTER, C. P. **Principles of magnetic resonance.** Berlin: Springer, 1996.

59 ERNST, R. R.; BODENHAUSEN, G.; WOKAUN, A. **Principles of nuclear magnetic resonance in one and two dimensions.** Oxford: Oxford University Press, 1997.

60 LEVITT, M. H. **Spin dynamics:** basics of nuclear magnetic resonance. New Jersey: Wiley, 2009.

61 SCHMIDT-ROHR, K.; SPIESS, H. W. Principles of NMR of organic solids. *In*: SCHMIDT-ROHR, K.; SPIESS, H. W. (ed.). **Multidimensional solid-state NMR and polymers.** Cambridge: Academic Press, 1991. p. 13-68.

62 OLIVEIRA JÚNIOR, M., AITKEN, B.; ECKERT, H. Structure of P_2O_5–SiO_2 pure network former glasses studied by solid state NMR spectroscopy. **Journal of Physical Chemistry C,** v. 122, n. 34, p. 19807-19815, 2018.

63 VLECK, J. H. The dipolar broadening of magnetic resonance lines in crystals. **Physical Review,** v. 74, n. 9, p. 1168-1183, 1948.

64 ABRAGAM, A. **The principles of nuclear magnetism.** Oxford: Clarendon Press, 1967.

65 VANDERHART, D. L.; GUTOWSKY, H. S.; FARRAR, T. C. Dipole-dipole interactions of a spin-1/2 nucleus with a quadrupole-coupled nucleus**. Journal of the American Chemical Society,** v. 89, n. 19, p. 5056-5057, 2002.

66 COHEN, M. H.; REIF, F. Quadrupole effects in nuclear magnetic resonance studies of solids. **Solid State Physics**: advances in research and applications, v. 5, n. 1, p. 321-438, 1957.

67 RAMSEY, N. F. H. **Nuclear moments**. New York: John Wiley & Sons, 1953.

68 GOLDBOURT, A.; MADHU, P. K. Multiple-quantum magic-angle spinning: high-resolution solid-state NMR of half-integer spin quadrupolar nuclei. **Annual Reports on NMR Spectroscopy,** v. 54, n. 1, p. 81-153, 2004.

69 GAN, Z. *et al.* Seeking higher resolution and sensitivity for NMR of quadrupolar nuclei at ultrahigh magnetic fields. **Journal of the American Chemical Society,** v. 124, n. 20, p. 5634-5635, 2002.

70 FUKUSHIMA, E.; ROEDER, S. B. W. **Experimental pulsed NMR:** a nuts and bolts approach. Boca Raton: CRC, 1981.

71 POZAR, D. M. **Microwave engineering.** New Jersey: Wiley, 2012.

72 MISPELTER, J.; LUPU, M.: BRIGUET, A. **NMR probeheads for biophysical and biomedical experiments:** theoretical principles and practical guidelines**.** London: Wiley, 2015.

73 CROSS, V. R.; HESTER, R. K.; WAUGH J. S. Single coil probe with transmission-line tuning for Nuclear Magnetic double resonance. **Review of Scientific Instruments,** v. 47, n. 12, p. 1486-1488, 1976.

74 ARFKEN, G. **Mathematical methods for physicists.** Cambridge: Academic Press Inc., 1958.

75 MEDEK, A.; FRYDMAN, L. Multiple quantum magic angle spinning NMR: a new technique for probing quadrupolar nuclei in solids. **Journal of the Brazilian Chemical Society,** v. 10, n. 4, p. 263-277, 1999.

76 SAMOSON, A.; LIPPMAA, E.; PINES, A. High resolution solid-state N.M.R. **Molecular Physics**. v. 65, n. 4, p. 1013-1018, 1988.

77 LLOR, A.; VIRLET, J. Towards high-resolution NMR of more nuclei in solids: sample spinning with time-dependent spinner axis angle. **Chemical Physics Letters.** v. 152, n. 2–3, p. 248-253, 1988.

78 CHMELKA, B.F. *et al*. Oxygen-17 NMR in Solids by dynamic-angle spinning and double rotation. **Nature**, v. 339, p. 42-43, 1989.

79 FRYDMAN, L.; HARWOOD, J. S. Isotropic spectra of half-integer quadrupolar spins from bidimensional magic-angle spinning NMR. **Journal of the American Chemical Society.** v. 117, n. 19, p. 5367–5368, 1995.

80 MADEK, A.; FRYDMAN, L.; HARWOOD, J. S. Multiple-quantum magic-angle spinning NMR: a new method for the study of quadrupolar nuclei in solids. **Journal of the American Chemical Society.** v. 117, n. 51, p. 12779–12787, 1995.

81 KENTGENS, A. P. M. A practical guide to solid-state NMR of half-integer quadrupolar nuclei with some applications to disordered systems. **Geoderma,** v. 80, n. 3-4, p. 271-306, 1997.

82 LACAILLERIE, J. B. E.; FRETIGNY, C.; MASSIOT, D. MAS NMR spectra of quadrupolar nuclei in disordered solids: the Czjzek model. **Journal of Magnetic Resonance,** v. 192, n. 2, p. 244-251, 2008.

83 LESAGE, A.; BARDET, M.; EMSLEY L. Through-bond carbon-carbon connectivities in disordered solids by NMR. **Journal of the American Chemical Society,** v. 121, n. 47, p. 10987-10993, 1999.

84 CADARS, S. *et al.* The refocused INADEQUATE MAS NMR experiment in multiple spin-systems: interpreting observed correlation peaks and optimizing lineshapes. **Journal of Magnetic Resonance,** v. 188, n. 1, p. 24-34, 2007.

85 LARINK, D.; REN, J.; ECKERT, H. Spectral editing based on scalar spin–spin interactions: new results on the structure of metathiophosphate glasses. **Solid State Nuclear Magnetic Resonance,** v. 45–46, n. 1, p. 30-35, 2012.

86 GUERRY, P.; SMITH, M. E.; BROWN, S. P. ^{31}P MAS refocused INADEQUATE spin-Echo (REINE) NMR spectroscopy: revealing J coupling and chemical shift two-dimensional correlations in disordered solids. **Journal of the American Chemical Society,** v. 131, n. 33, p. 11861-11874, 2009.

87 LATHROP, D. *et al.* Dipolar ^{31}P NMR spectroscopy of crystalline inorganic phosphorus compounds. **Solid State Nuclear Magnetic Resonance,** v. 1, n. 2, p. 73-83, 1992.

88 PAN, Y.; GULLION, T.; SCHAEFER, J. Determination of C N internuclear distances by rotational-echo double-resonance NMR of solids. **Journal of Magnetic Resonance,** v. 90, n. 2, p. 330-340, 1990.

89 GULLION, T.; VEGA, A. J. Measuring heteronuclear dipolar couplings for I=1/2, S>1/2 spin pairs by REDOR and REAPDOR NMR. **Progress in Nuclear Magnetic Resonance Spectroscopy,** v. 47, n. 3, p. 123-136, 2005.

90 BERTMER, M.; ECKERT, H. Dephasing of spin echoes by multiple heteronuclear dipolar interactions in rotational echo double resonance NMR experiments. **Solid State Nuclear Magnetic Resonance,** v. 15, n. 3, p. 139-152, 1999.

91 FRIEDRICH, T.; HAUF, C.; KNIEP, R. Crystal structure of pentasodium catiborateorato-triphosphate), $Na_5[B_2P_3O_{13}]$. **Zeitschrift fuer Kristallographie,** v. 210, n. 6, p. 446-446, 1995.

92 PAULING, L.; SHERMAN, J. The crystal structure of aluminum metaphosphate, $Al(PO_3)_3$. **Zeitschrift fuer Kristallographie,** v. 96, n.1-6, 481-487, 1937.

93 STROJEK, W. *et al*. Site discrimination in the crystalline borophosphate $Na_5B_2P_3O_{13}$ using advanced solid-state NMR techniques **Solid State Nuclear Magnetic Resonance,** v. 32, n. 3, p. 89-98, 2007.

94 GREY, C. P.; VEGA, A. J. Determination of the quadrupole coupling constant of the invisible aluminum spins in zeolite HY with $^{1}H/^{27}Al$ TRAPDOR NMR. **Journal of the American Chemical Society,** v. 117, n. 31, p. 8232-8242, 2002.

95 BA, Y. *et al.* Optimizing the $^{13}C–^{14}N$ REAPDOR NMR experiment: a theoretical and experimental study. **Journal of Magnetic Resonance,** v. 133, n. 1, p. 104-114, 1998.

96 ASHBROOK, S. E.; DUER, M. J. Structural information from quadrupolar nuclei in solid state NMR. **Concepts in Magnetic Resonance Part A,** v. 28, n. 3, p. 183-248, 2006.

97 HUGHES, E. *et al*. Internuclear distance determination of S=1, I=1/2 spin pairs using REAPDOR NMR. **Journal of Magnetic Resonance,** v. 156, n. 2, p. 230-241, 2002.

98 GOLDBOURT, A.; *et al*. Interatomic distance measurement in solid-state NMR between a spin-1/2 and a spin-5/2 using a universal REAPDOR curve. **Journal of the American Chemical Society,** v. 125, n. 37, p. 11194-11195, 2003.

99 KALWEI, M.; KOLLER, H. Quantitative comparison of REAPDOR and TRAPDOR experiments by numerical simulations and determination of H–Al distances in zeolites. **Solid State Nuclear Magnetic Resonance,** v. 21, n. 3-4, p. 145-157, 2002.

100 MQMAS processing in SSNAKE. San Francisco, 2019. Available from: https://github.com/smeerten/ssnake_tutorials/blob/master/MQMAS/MQMAS.pdf. Accessible at: 04 Mar. 2023

101 AMOUREUX, J. P.; FERNANDEZ, C.; FRYDMAN, L. Optimized multiple-quantum magic-angle spinning NMR experiments on half-integer quadrupoles. **Chemical Physics Letters,** v. 259, n. 3-4, p. 347-355, 1996.

102 MASSIOT, D. *et al.* Modelling one- and two-dimensional solid-state NMR spectra. **Magnetic Resonance in Chemistry,** v. 40, n. 1, p. 70-76, 2002.

103 VAN MEERTEN, S. G. J.; FRANSSEN, W. M. J.; KENTGENS, A. P. M. ssNake: a cross-platform open-source NMR data processing and fitting application. **Journal of Magnetic Resonance,** v. 301, n. 1, p. 56-66, 2019.

104 LOGRADO, M. *et al*. Silica incorporation into sodium aluminum phosphate glasses: structural characterization by Raman spectroscopy and multinuclear solid-state NMR. **Journal of Non-Crystalline Solids,** v. 579, n. 1, p. 121366, 2022.

105 HAYDEN, J.S. *et al.* Surface tensile layer generation during thermal annealing of phosphate glass. **Journal of Non-Crystalline Solids,** v. 263-264, n. 1, p. 228-239, 2000.

106 CHOI, H.; LEE, J.; KIM, Y. High temperature strength and oxidation behaviour of hot-pressed silicon nitride-disilicate ceramics. **Journal of Materials Science,** v. 32, p. 1937-1942, 1997.

107 Li, Y.M.; Bian, J.J. Effects of reoxidation on the dielectric and energy storage properties of Ce-doped (Ba,Sr)TiO3 ceramics prepared by hot-pressed sintering. **Journal of the European Ceramic Society,** v. 40, n. 15, p. 5441-5449, 2020.

108 SCHOLZE, H.; KREIDL, N. J. Technological aspects of viscosity. *In*: UHLMANN, D.R.; KREIDL, N. J. (ed.). **Glass:** science and technology. London: Academic Press, 1986. p 233-273.

109 ANGELI, F. *et al.* Influence of glass chemical composition on the Na-O bond distance: a ^{23}Na 3Q-MAS NMR and molecular dynamics study. **Journal of Non-Crystalline Solids,** v. 276, n. 1-3, p.132-144, 2000.

110 LEE, S. K.; STEBBINS, J. F. The distribution of sodium ions in aluminosilicate glasses: a high-field Na-23 MAS and 3Q MAS NMR study. **Geochimica et Cosmochimica Acta,** v. 67, n. 9, p.1699-1709, 2003.

111 XIN, S. *et al.* Heteronuclear correlation experiments of ^{23}Na-^{27}Al in rotating solids. **Solid State Nuclear Magnetic Resonance,** v. 84, n. 1, p. 103-110, 2017.

112 HAASE, J.; CURRO, N. J.; SLICHTER, C. P. Double resonance probes for close frequencies. **Journal of Magnetic Resonance,** v. 135, n. 2, p. 273-279, 1998.

113 JOHNSON, R. A.; WICHERN, D. W. **Applied multivariate statistical analys^{is}.** 6th ed. London: Pearson Prentice Hall, 2007.

114 KOLLER, H. *et al.* ^{23}Na NMR Spectroscopy of solids: interpretation of quadrupole interaction parameters and chemical shifts. **Journal of Physical Chemistry,** v. 98, n. 6, p. 1544-1551, 2002.

115 ZHAO, Y. *et al.* A modified random network model for P_2O_5-Na_2O-Al_2O_3-SiO_2 glass studied by molecular dynamics simulations. **RSC Advances,** v. 11, n. 12, p. 7025-7036, 2021

116 SCHNEIDER, J. *et al*. Local structure of sodium aluminum metaphosphate glasses. **Journal of the American Ceramic Society,** v. 86, n. 2, p. 317-324, 2003.

117 XUE, X.; STEBBINS, J. F. ^{23}Na NMR Chemical shifts and local Na coordination environments in silicate crystals, melts and glasses. **Physics and Chemistry of Minerals,** v. 20, n. 1, p. 297-307,1993.

118 WONG, A.; WU, G. Solid-state ^{23}Na nuclear magnetic resonance of sodium complexes with crown ethers, cryptands, and naturally occurring antibiotic ionophores: a direct probe to the sodium-binding sites. **Journal of Physical Chemistry A,** v. 104, n. 51, p. 11844-11852, 2000.

119 STEBBINS, J. F. Cation sites in mixed-alkali oxide glasses: correlations of NMR chemical shift data with site size and bond distance. **Solid State Ionics,** v. 112, n. 1-2, p. 137-141, 1998.

120 KOBERA, L. *et al*. The nature of chemical bonding in Lewis adducts as reflected by ^{27}Al NMR quadrupolar coupling constant: combined solid-state NMR and quantum chemical approach. **Inorganic Chemistry,** v. 57, n. 12, p. 7428-7437, 2018.

121 CODY, G. D. *et al*. Silicate-phosphate interactions in silicate glasses and melts: I. A multinuclear, ^{27}Al,^{29}Si,^{31}P) MAS NMR and ab initio chemical shielding, ^{31}P) study of phosphorous speciation in silicate glasses. **Geochimica et Cosmochimica Acta,** v. 65, n. 14, p. 2395-2411, 2001.

122 STRUCTURE and properties of phase-separated borosilicates containing P_2O_5. Berlin, 2007. Available from: https://www.researchgate.net/publication/281303490. Accessible at: 23 Feb. 2023.

123 MÜLLER, D. *et al*. High-resolution solid-state ^{27}Al and ^{31}P NMR: correlation between chemical shift and mean Al-O-P angle in $AlPO_4$ polymorphs. **Chemical Physics Letters,** v. 109, n. 4, p. 332-336, 1984.

124 GAMBUZZI, E. *et al*. Probing silicon and aluminum chemical environments in silicate and aluminosilicate glasses by solid state NMR spectroscopy and accurate first-principles calculations. **Geochimica et Cosmochimica Acta,** v. 125, n. 1, p. 170-185, 2014.

125 HAOUAS, M.; TAULELLE, F.; MARTINEAU, C. Recent advances in application of ^{27}Al NMR spectroscopy to materials science. **Progress in Nuclear Magnetic Resonance,** v. 94-95, n. 1, p. 11-36, 2016.

126 LOGRADO, M. *et al*. Structure-property relations in crack-resistant alkaline-earth aluminoborosilicate glasses studied by solid state NMR. **Journal of the American Ceramic Society,** v. 104, n. 5, p. 2250-2267, 2020.

127 SEN, S.; E. YOUNGMAN, R. High-resolution multinuclear NMR structural study of binary aluminosilicate and other related glasses. **Journal of Physical Chemistry B,** v. 108, n. 23, p. 7557-7564, 2004.

128 MORIN, E. I.; WU, J.; STEBBINS, J. F. Modifier cation (Ba, Ca, La, Y) field strength effects on aluminum and boron coordination in aluminoborosilicate glasses: the roles of fictive temperature and boron content. **Applied Physics A,** v. 116, n. 1, p. 479-490, 2014.

129 MINAMI, T.; MACKENZIE, J. D. Thermal expansion and chemical durability of phosphate glasses. **Journal of American Ceramics Society,** v. 60, n. 5-6, p. 232-236, 1977.

130 GRAY, P. E.; KLEIN, L. C. The chemical durability of sodium ultraphosphate glasses. **Glass Technology,** v. 24, n. 4, p. 202-206, 1983.

131 BUNKER, B. C.; ARNOLD, G. W.; WILDER, J. A. Phosphate glass dissolution in aqueous solutions. **Journal of Non-Crystalline Solids,** v. 64, n. 3, p. 291-316, 1984.

132 HAMILTON, J. P. *et al*. Dissolution of nepheline, jadeite and albite glasses: toward better models for aluminosilicate dissolution. **Geochimica et Cosmochimica Acta,** v. 65, n. 21, p. 3683-3702, 2001.

133 MACKENZIE, K. J. D.; SMITH, M. E. **Multinuclear solid-state NMR of inorganic materials.** London: Pergamon,2002.

134 SCHNEIDER, J. *et al*. Q^n distribution in stoichiometric silicate glasses: thermodynamic calculations and ^{29}Si high resolution NMR measurements. **Journal of Non-Crystalline Solids,** v. 325, n. 1-3, p. 164-178, 2003.

135 REN, J.; ECKERT, H. Superstructural units involving six-coordinated silicon in sodium phosphosilicate glasses detected by solid-state NMR spectroscopy. **Journal of Physical Chemistry C,** v. 122, n. 48, p. 27620-27630, 2018.

136 MIYABE, D. *et al*. Structure and formation mechanism of six-fold coordinated silicon in phosphosilicate glasses. **Physical Review B,** v. 71, n. 17, p. 17202, 2005.

137 DUPREE, R. *et al*. Magic angle spinning NMR of alkali phospho-alumino-silicate glasses. **Journal of Non-Crystalline Solids,** v. 112, n. 1-3, p. 111-119, 1989.

138 LOEWENSTEIN, W. The distribution of aluminum in the tetrahedra of silicates and aluminates. **American Mineralogist,** v. 39, n. 1-2, p. 92-96, 1954.

139 DOLLASE, W. A.; MERWIN, L. H.; SEBALD, A. Structure of $Na_{3-3x}Al_xPO_4$, x = 0 to 0.5. **Journal of Solid-State Chemistry,** v. 83, n. 1, p. 140-149, 1989.

140 M. WENSLOW, R.; FISKE, K.; MUELLER, K. T. An overview of solid-state NMR correlation experiments in phosphate glass systems. **Solid-State NMR Spectroscopy of Inorganic Materials,** v. 717, n. 6, p. 228-241, 2009.

141 BAK, M.; RASMUSSEN, J. T.; NIELSEN, N. C. SIMPSON: a general simulation program for solid-state NMR spectroscopy. **Journal of Magnetic Resonance,** v. 147, n. 2, p. 296-330, 2000.

142 LOGRADO, M. *et al*. Densification of sodium borosilicate glasses at ambient temperature: structural investigations by solid-state nuclear magnetic resonance and Raman scattering. **Journal of Physical Chemistry Letters,** v. 14, n. 19, p. 4471-4481, 2023.

143 MAEKAWA, H. *et al*. The structural groups of alkali silicate glasses determined from ^{29}Si MAS-NMR. **Journal of Non-Crystalline Solids,** v. 127, n. 1, p. 53-64, 1991.

144 NANBA, T.; NISHIMURA, M.; MIURA, Y. A theoretical interpretation of the chemical shift of ^{29}Si NMR peaks in alkali borosilicate glasses. **Geochimica et Cosmochimica Acta,** v. 68, n. 24, p. 5103-5111, 2004.

145 DU, L. S.; STEBBINS, J. F. Solid-state NMR study of metastable immiscibility in alkali borosilicate glasses. **Journal of Non-Crystalline Solids,** v. 315, n. 3, p. 239-255, 2003.

146 DU, L. S.; STEBBINS, J. F. Nature of silicon−boron mixing in sodium borosilicate glasses: a high-resolution ^{11}B and 17O NMR study. **Journal of Physical Chemistry B,** v. 107, n. 37, p. 10063-10076, 2003.

147 LEE, S. K. *et al*. Structure of B_2O_3 glass at high pressure: A ^{11}B solid-state NMR study. **Physical Review Letters,** v. 94, n. 16, p. 165507, 2005.

148 MARTENS, R.; MÜLLER-WARMUTH, W. Structural groups and their mixing in borosilicate glasses of various compositions - an NMR study. **Journal of Non-Crystalline Solids,** v. 265, n. 1-2, p. 167-175, 2000.

149 LEE, S. K. *et al.* Effect of network polymerization on the pressure-induced structural changes in sodium aluminosilicate glasses and melts: ^{27}Al and ^{17}O solid-state NMR study. **Journal of Physical Chemistry C,** v. 116, n. 3, p. 2183-2191, 2011.

150 YU, Y.; STEVENSSON, B.; EDÉN, M. A unified ^{23}Na NMR chemical shift correlation with structural parameters in multicomponent silicate-based glasses. **Journal of the American Ceramic Society,** v. 103, n. 2, p. 762-767, 2020.

151 YU, Y.; STEVENSSON, B.; EDÉN, M. Structural role of sodium in borosilicate, phosphosilicate, and borophosphosilicate glasses unveiled by solid-state NMR and MD simulations. **Journal of Physical Chemistry C,** v. 123, n. 42, p. 25816-25832, 2019.

152 YUN, Y. H.; BRAY, P. J. Nuclear magnetic resonance studies of the glasses in the system Na_2O B_2O_3 SiO_2. **Journal of Non-Crystalline Solids,** v. 27, n. 3, p.363–380, 1978.

153 YUN, Y. H.; FELLER, S. A.; BRAY, P. J. Correction and addendum to "Nuclear Magnetic Resonance studies of the glasses in the system Na_2O B_2O_3 SiO_2". **Journal of Non-Crystalline Solids,** v. 33, n. 2, p. 273–277, 1979.

154 DELL, W. J.; BRAY, P. J.; XIAO, S. Z. ^{11}B NMR studies and structural modeling of Na_2O B_2O_3 SiO_2 glasses of high soda content. **Journal of Non-Crystalline Solids,** v. 58, n. 1, p. 1–16, 1983.

155 HUANG, L. *et al*. Polyamorphic transitions in vitreous B_2O_3 under pressure. **Journal of Physics**: condensed matter, v. 20, n. 7, p. 075107, 2008.

156 ZEIDLER, A. *et al*. Density-driven structural transformations in B_2O_3 glass. **Physical Review B,** v. 90, n. 2, p. 024206, 2014.

157 SVENSON, M. N. *et al*. Raman spectroscopy study of pressure-induced structural changes in sodium borate glass. **Journal of Non-Crystalline Solids,** v. 443, n. 1, p.130-135, 2016.

158 YOSHIDA, S. *et al.* Indentation induced densification of sodium borate glasses. **Physics and Chemistry of Glasses**: european journal of glass science and technology part b, v. 50, n. 1, p. 63-70, 2009.

159 BRAZHKIN, V. V. *et al*. Nature of the structural transformations in B_2O_3 glass under High Pressure. **Physical Review Letters,** v. 101, n.3, p. 035702, 2008.

APPENDIX A

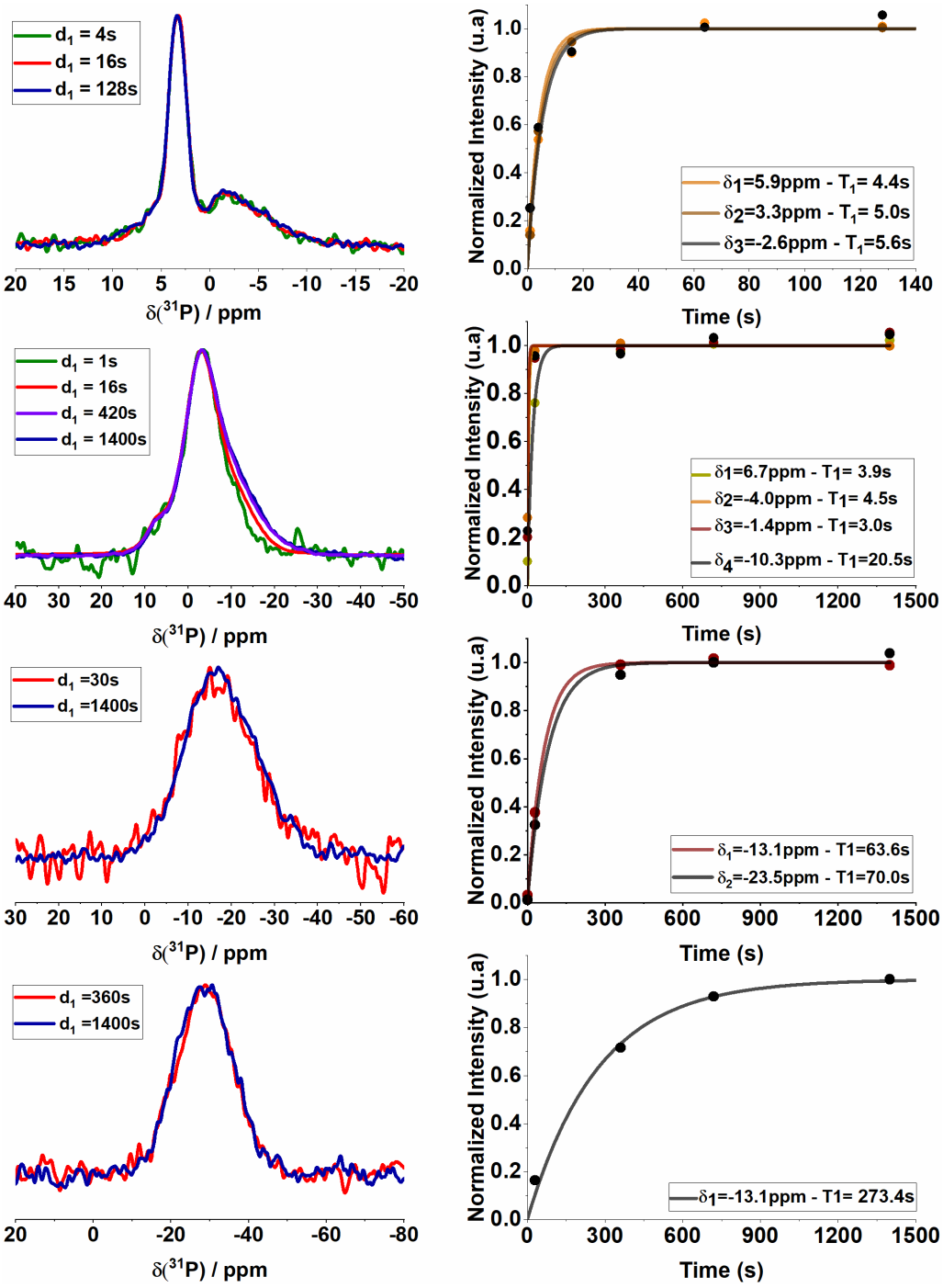

Figure A1 - Left: Fourier Transform of ^{31}P MAS-NMR FIDs measured under distinct relaxation delays d_1 of samples x=17.50, x=15.00, x=11.25 and x=2.50, from the top to the bottom, respectively. **Right:** The intensity of the magnetization for each deconvolution of ^{31}P spectra as a function of distinct relaxation in a saturation recovery experiment. Solid curves show the function $M(t) = M_0(1\text{-exp-}t/T_1)$, fitted to datapoints, where M_0, representing the value of the magnetization at thermal equilibrium, was normalized.

Source: By the author.

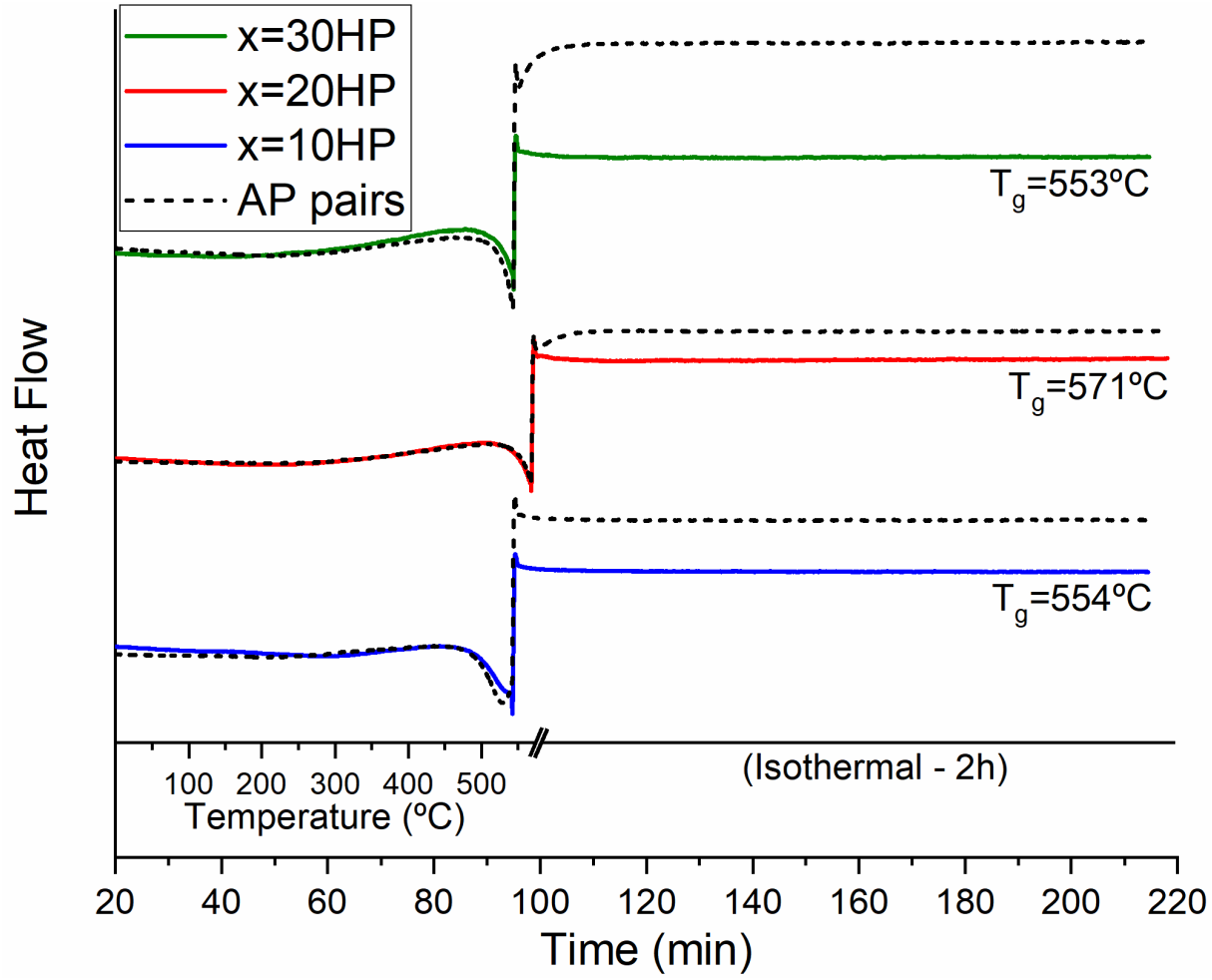

Figure A2 - DSC curves of high pressurized $xB_2O_3 – 20Na_2O – (80\text{-}x)SiO_2$ samples. Dash curves show their respective unpressurized curves pairs. The samples were heated using a rate of 5k/s until T_g temperatures, according to Kato *et al*,[8,9] afterwards annealed for 2 hours.
Source: By the author.

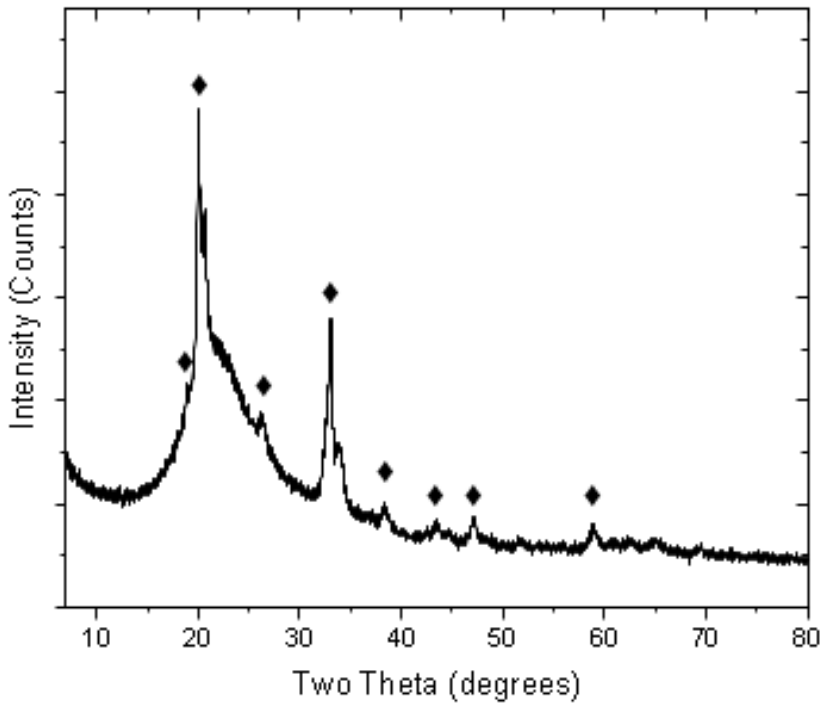

Figure A3 - XRD data of the sample x = 17.50. The data was obtained using Cu radiation on a Bruker D8 diffractometer equipped with a LYNXEYE-2 compound silicon strip detector. Diffraction data was acquired with a 0.013-degree step size and 0.09 degree per second scan rate. The marked peaks correspond to orthorhombic $Na_4P_2O_7$ (PDF#04-018-4331).

Source: Corning Incorporated collaborators.

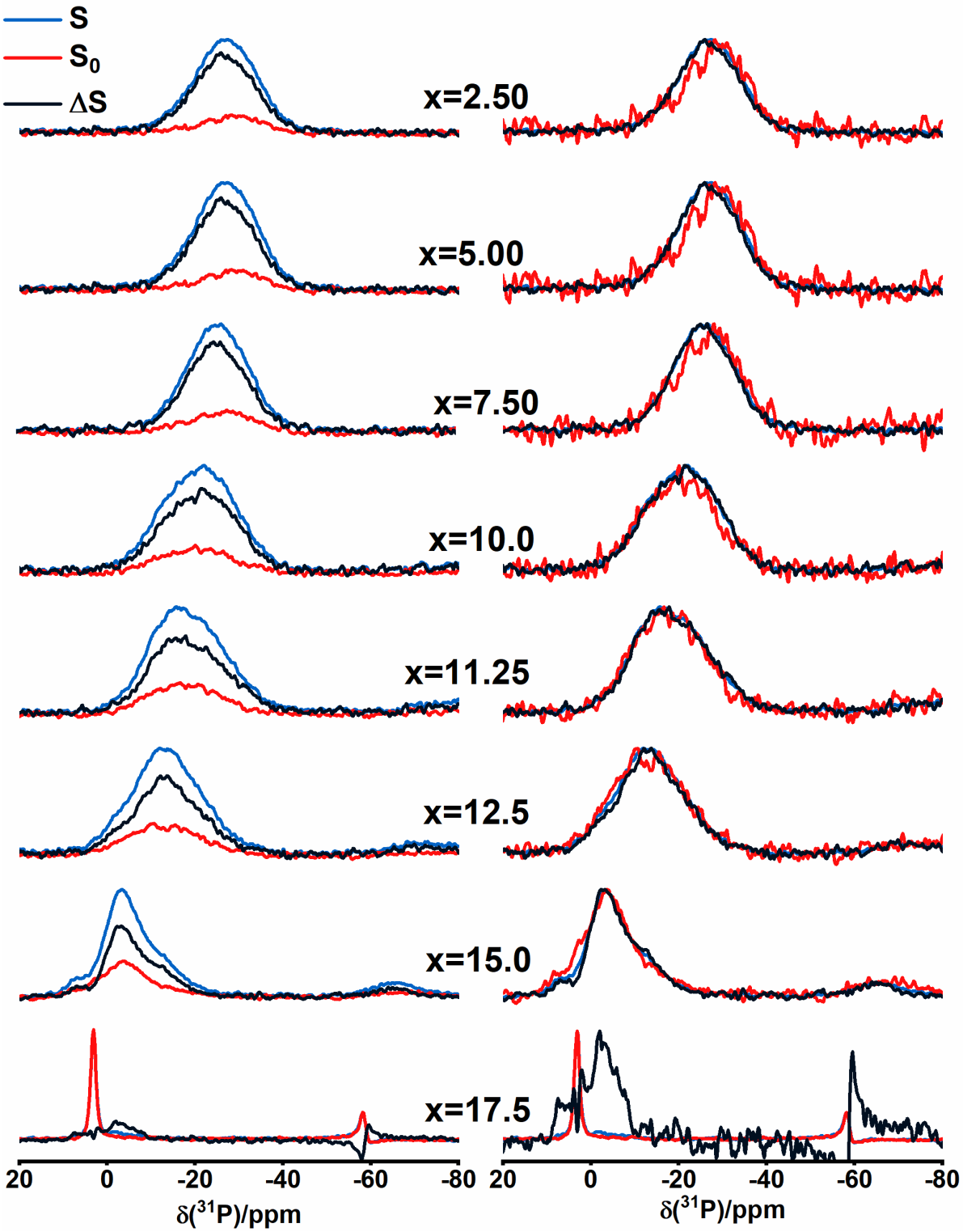

Figure A4 - On the left, Fourier Transforms from single point $^{31}P(^{23}Al)$ REAPDOR spectra measured at 1.2 ms of dipolar evolution of the glasses xNa_2O–- $(22.5\text{-}x)Al_2O_3$ – $7.5P_2O_5$–- $70SiO_2$. On the right same spectra with normalized intensities.

Source: By the author.

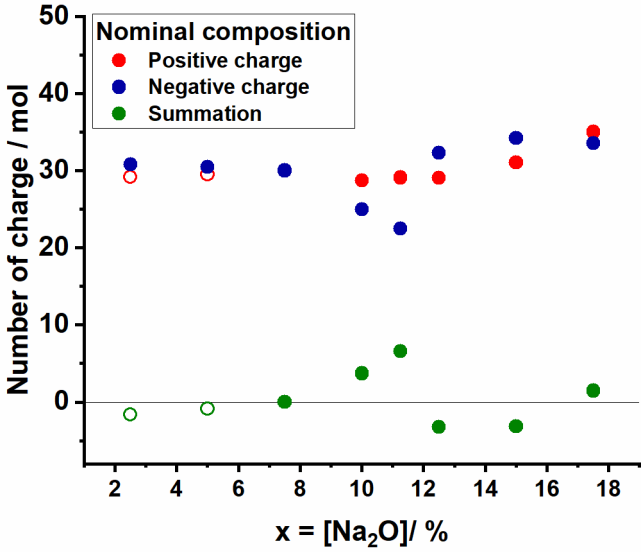

Figure A5 - Sum of positive charges of the network in red - $P^{(4)}$, Na^{+} and assumed Al^{+3}(V) with formal compensating charge of +1, sum of negatives charges of the network - $P^{(n)}$, with n < 4 and $(AlO4)^{-}$, and the total summation.

Source: By the author.

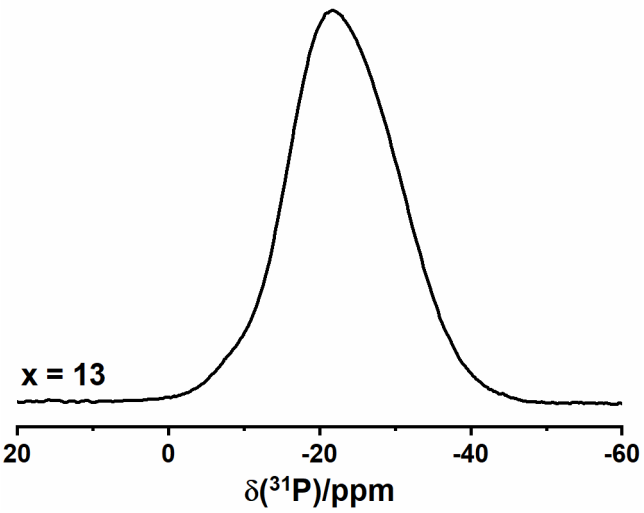

Figure A6 - Zoom in the central transition of samples the sample $13SiO_2 – 46P_2O_5 – 13Al_2O3 – 28Na_2O$ glass (x = 13) to illustrate the appearance of shoulder in higher frequencies.

Source: By the author.